NASA/TM—2015–218216

Marshall Space Flight Center Faculty Fellowship Program

N.F. Six, Program Director/Compiler
Marshall Space Flight Center, Huntsville, Alabama

December 2015

The NASA STI Program…in Profile

Since its founding, NASA has been dedicated to the advancement of aeronautics and space science. The NASA Scientific and Technical Information (STI) Program Office plays a key part in helping NASA maintain this important role.

The NASA STI Program Office is operated by Langley Research Center, the lead center for NASA's scientific and technical information. The NASA STI Program Office provides access to the NASA STI Database, the largest collection of aeronautical and space science STI in the world. The Program Office is also NASA's institutional mechanism for disseminating the results of its research and development activities. These results are published by NASA in the NASA STI Report Series, which includes the following report types:

- TECHNICAL PUBLICATION. Reports of completed research or a major significant phase of research that present the results of NASA programs and include extensive data or theoretical analysis. Includes compilations of significant scientific and technical data and information deemed to be of continuing reference value. NASA's counterpart of peer-reviewed formal professional papers but has less stringent limitations on manuscript length and extent of graphic presentations.

- TECHNICAL MEMORANDUM. Scientific and technical findings that are preliminary or of specialized interest, e.g., quick release reports, working papers, and bibliographies that contain minimal annotation. Does not contain extensive analysis.

- CONTRACTOR REPORT. Scientific and technical findings by NASA-sponsored contractors and grantees.

- CONFERENCE PUBLICATION. Collected papers from scientific and technical conferences, symposia, seminars, or other meetings sponsored or cosponsored by NASA.

- SPECIAL PUBLICATION. Scientific, technical, or historical information from NASA programs, projects, and mission, often concerned with subjects having substantial public interest.

- TECHNICAL TRANSLATION. English-language translations of foreign scientific and technical material pertinent to NASA's mission.

Specialized services that complement the STI Program Office's diverse offerings include creating custom thesauri, building customized databases, organizing and publishing research results…even providing videos.

For more information about the NASA STI Program Office, see the following:

- Access the NASA STI program home page at <http://www.sti.nasa.gov>

- E-mail your question via the Internet to <help@sti.nasa.gov>

- Phone the NASA STI Help Desk at 757–864–9658

- Write to:
  NASA STI Information Desk
  Mail Stop 148
  NASA Langley Research Center
  Hampton, VA 23681–2199, USA

NASA/TM—2015–218216

Marshall Space Flight Center Faculty Fellowship Program

N.F. Six, Program Director/Compiler
Marshall Space Flight Center, Huntsville, Alabama

National Aeronautics and
Space Administration

Marshall Space Flight Center • Huntsville, Alabama 35812

December 2015

Acknowledgments

Appreciation to those who brought this 2015 Faculty Fellowship program together include John Brunson, Steve Cash, Todd May, Chris Singer, and Jim Turner, along with Tina Atchley, Rachael Damiani, Judy Drinnon, Katie Hayden, Jerry Karr, Mona Miller, Ann Mix, Deborah Nielson, and Tammy Rowan.

Available from:

NASA STI Information Desk
Mail Stop 148
NASA Langley Research Center
Hampton, VA 23681–2199, USA
757–864–9658

This report is also available in electronic form at
<http://www.sti.nasa.gov>

EXECUTIVE SUMMARY

The Faculty Fellowship program was revived in the summer of 2015 at NASA Marshall Space Flight Center, following a period of diminished faculty research activity here since 2006 when budget cuts in the Headquarters' Education Office required realignment. Several senior Marshall managers recognized the need to involve the Nation's academic research talent in NASA's missions and projects to the benefit of both entities. These managers invested their funds required to establish the renewed Faculty Fellowship program in 2015, a 10-week residential research involvement of 16 faculty in the laboratories and offices at Marshall. These faculty engineers and scientists worked with NASA collaborators on NASA projects, bringing new perspectives and solutions to bear.

This Technical Memorandum is a compilation of the research reports of the 2015 Marshall Faculty Fellowship program, along with the Program Announcement (appendix A) and the Program Description (appendix B). The research touched on seven areas—propulsion, materials, instrumentation, fluid dynamics, human factors, control systems, and astrophysics.

The propulsion studies included green propellants, gas bubble dynamics, and simulations of fluid and thermal transients. The materials investigations involved sandwich structures in composites, plug and friction stir welding, and additive manufacturing, including both strength characterization and thermosets curing in space. The instrumentation projects involved spectral interferometry, emissivity, and strain sensing in structures. The fluid dynamics project studied the water hammer effect. The human factors project investigated the requirements for close proximity operations in confined spaces. Another team proposed a controls system for small launch vehicles, while in astrophysics, one faculty researcher estimated the practicality of weather modification by blocking the Sun's insolation, and another found evidence in satellite data of the detection of a warm-hot intergalactic medium filament.

Our goal is to continue the Faculty Fellowship effort with Center funds in succeeding summers.

TABLE OF CONTENTS

TABLE OF CONTENTS (Continued)

2015 Marshall Faculty Fellows

From Left to Right:

Row 1—V. Coverstone, K. Zuo

Row 2—G. Karr, F. Six, P. Reardon, J. Schneider, C. Wu, J. Odutola, S. Ravindran, A. Bandyopadhyay, A. Carton

Row 3—Z. Deng, T. Stockman (Student), A. Adams, S. Whitmore, L. Berhan, A. Gleich (Student), R. Damiani

Not shown: M. Bonamente, G. Wang, A. Mazzeo

3D Printed ABS Plastic Strength Improvement

A.Adams[1]
Alabama A &M University, Department of Civil and Mechanical Engineering, Normal, AL 35762, USA

W. Guin[2]
The University of Alabama, Department of Civil, Construction, and Environmental Engineering, Tuscaloosa, AL 35487, USA

and

R. Kaul.[3]
NASA Marshall Space Flight center, Huntsville, Alabama, 35812, USA

Nomenclature

ABS	=	Acrylonitrile Butadiene Styrene
SiC	=	Silicon carbon
3D	=	Three dimensional
MWCNT	=	multi-walled carbon nanotubes
MSFC	=	Marshall Space Flight Center
SEM	=	Scanning Electron Microscope
ASTM	=	American Standards for Testing and Materials

I. Introduction

Additive manufacturing has become increasingly attractive by material scientists and engineers to improve the mechanical properties of acrylonitrile butadiene styrene (ABS) plastics. The augmented ABS plastic exhibits improved mechanical properties that make it ideal for human spaceflight operations. Currently, the International Space Station (ISS) has an additive manufacturing machine, more commonly known as a three-dimensional (3D) printer. 3D printing is a technology that has been vastly researched since the early 1990s. It is a technology that allows a three-dimensional object to be produced from a digital file. Sometimes referred to as "additive manufacturing," because the process consists of adding one layer of material on top of another until it formed into a three-dimensional object. The rise of popularity of this technology is due to its ability to quickly manufacture parts that have a high degree of complexity and do not require molds or specific tooling to create parts. This provides key economic advantages by reducing prototyping time and also eliminates prototype tooling, which are large factors that when dealing small volume production. Due to the mechanical integrity, surface quality, and the ability to be rapidly produced industries that are known for adapting this technology are automotive, bioengineering, and aerospace.

The preferred material used in 3D printing is acrylonitrile butadiene styrene (ABS) plastic, which is also used to create the popular child's toy, the Lego® brick. ABS plastics have inherent limitations of limited weathering resistance, moderate heat, moisture, and chemical resistance and are flammable, thus making it an unattractive choice for certain applications. NASA's interest is in allowing astronauts to create components and mechanisms on demand, and reduces the existing logistical requirements associated with the transportation of necessary materials. Another added asset is the ability to evolve procedures as NASA's current mission to commission human life on the moon, insuring that once there mechanisms and components can be manufactured if needed on demand and recycled and reused if a mechanism requires to be converted into a new tool. The ability to remanufacture on demand while in space will significantly reduce the amount of payload on the launch vehicle and eliminate the need for duplication of backup fixtures for later use. The progression of this technology will enhance the likelihood of manufacturing entire large-scale systems while

[1] Assistant Professor, Civil and Mechanical Engineering, Alabama A&M University.
[2] PhD Candidate, Department of Civil, Construction, and Environmental Engineering, The University of Alabama, Tuscaloosa, AL 35487, USA
[3] Research Scientist, Materials and Processes Lab, EM42, NASA MSFC.

in space, and could even kickoff space architecture. Engineers could design systems for space and not focus on the constraints and confinements of gravity and other elements. A modern design and manufacturing process without the constrictions of Earth's and zero gravity could be a new phenomenon for space exploration. Launch related stresses would become obsolete as there would be no gravitational restrictions, and would not have to account for other complications that are involved when launching spacecraft in to space.

The current state of the 3D technology demonstrates the substantial gaps between the vision of 3D manufacturing in space and the limitations of the additive manufacturing technology. Currently ground-based additive manufacturing has established the technical basis, and has great potential for long-term impact by reducing cost and increase performance of space systems of later for space-based additive manufacturing. When 3D printing full matures as a technology, it has the potential to be a paradigm-changing approach to designing hardware for in-space activities. Additive manufacturing also offers economic incentives when compared to conventional manufacturing processes. 3D manufacturing from a raw materials perspective, creates a far less manufacturing byproducts (waste). From a bill of materials perspective a cost savings of 75 percent can be realized by using 3D additive manufacturing rather than milling methods of material removal. The speed in which parts and tools can be manufactured can be improved by 40 percent. However, currently, the variety of materials (ABS plastics) available to support additive manufacturing is only a small subset of those used in conventional manufacturing.

Government agencies, universities, nonprofit organizations and commercial aerospace industries are currently developing new research efforts that involve sophisticated hybrid materials. These hybrid materials would be able to withstand environmental impacts as well withstand previous factors that they could not have before additive manufacturing. The improved technology has become an intriguing concept for NASA, as the technology can be used to potentially create a combination of materials that can support a diverse amount of material properties. The additive materials can be designed to have localized, specific values of selected physical characteristics, making parts tailored for performance under various structural load and temperature conditions such as an artifact's hardness, rigidity, and/or electrical and thermal conductivities. To form a resolution that would expand 3D printing in respect to additive manufacturing, the limitations of ABS based materials must be addressed. In this paper a preliminary study has been explored by in infusing multi-walled carbon nanotubes (MWCNTs), silicon carbon (SiC), and carbon fiber into ABS plastics to improve the feedstock material.

II. Experimental Setup / Material Methods

The materials used in this study were purchased from several sources. Acrylonitrile Butadiene Styrene (ABS) plastic pellets and filaments were purchased from Filabot (Vermont, USA) and Stratasys (Minnesota, USA) respectively. Silicon carbide whiskers of 1.5-micron diameter and approximately 18 micron in length with the purity of greater than 99% were purchased from Alfa Aesar. Carbon fiber filament was acquired from 3DXTECH.

The ABS pellets were separated by aluminum dishes by weight and placed into plastic bags so that they could be easily and readily accessed when administering additional experiments. The first procedure of the experimental process begins with fabricating a baseline solution cast, an acetone-ABS pellet mixture. In the solution, 30 grams of the ABS pellets and dissolved in 90 grams acetone to form a solution of ABS in acetone. To ensure a homogenous mix that is not imbalanced, the room temperature baseline solution is placed onto a magnetic stirrer for approximately four hours.

After a complete analogous mixture of new acetone-ABS pellet solution, the new compound is then cast into aluminum dishes of approximately 2.5 inches in diameter. The aluminum dished that contains the mixtures is then transported and arranged beneath a fume hood in which the liquid is allowed to solidify for 24 hours. Following the 24 hour drying process, the solution had become completely solidified within the aluminum plate. The new acetone-ABS discs wafers were removed from the aluminum plate and compiled into three assortments to be transported to a heated press. The heated press was plunged onto each ABS disk pack, to allow the acetone to be removed and flashed off for an approximated four hours. Since acetone can be removed through evaporation at an accelerated speed, it was assumed that nearly all of the chemical had been removed from the ABS disc. The newly compressed ABS discs are then cut and divided into 5 mm x 5 mm squares. The squares are loaded inside the extruder in which the production of filament that will be later used within the 3D printer. Preliminary tension tests were carried out to determine the mechanical properties of the newly extruded filament.

Figure 1. (A) 30 grams of ABS pellets separated into aluminum dishes before being added into the vial of Acetone (B) 90 grams of acetone in vials before mixing with ABS pellets.

Figure 2. (A) 30 grams of ABS pellets before being fully dissolved into 90 grams of acetone. (B) ABS acetone mixture before being magnetically stirred dissolved in 90 grams of acetone.

Figure 3. (A) The ABS acetone mixture placed in beaker before placement on the mechanical stirring heat plate. (B) Beaker placed on magnetic stirring heat plate for eight hours. (C) Overall experiment setup for ABS pellet material modifications infusion process.

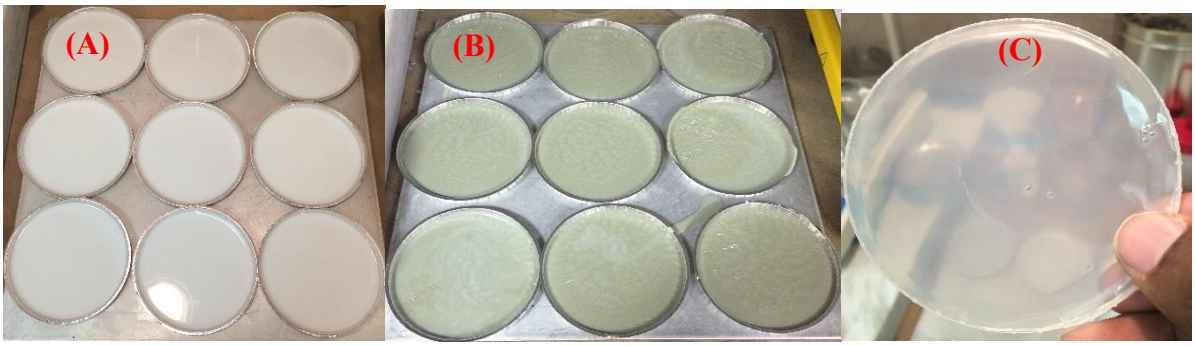

Figure 4. (A) The ABS acetone mixture after being cast in aluminum dish for 24 hours. (B) ABS acetone SiC mixture after being cast for 24 hours. (C) The solution cast ABS wafer after removal from aluminum dish.

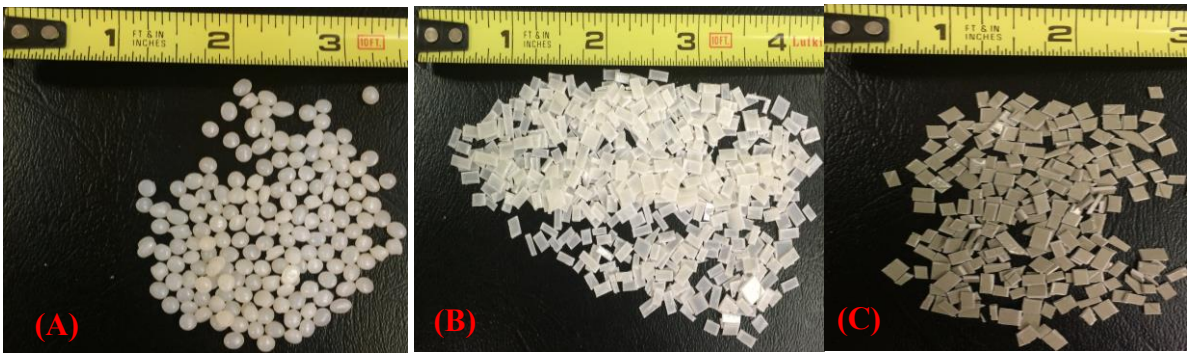

Figure 5. (A) ABS pellets before acetone addition. (B) Solution cast ABS wafer after being dissected into chips for insertion into the Filabot hopper. (C) Solution cast ABS and SiC infusion wafer after being dissected into chips for insertion into the Filabot hopper.

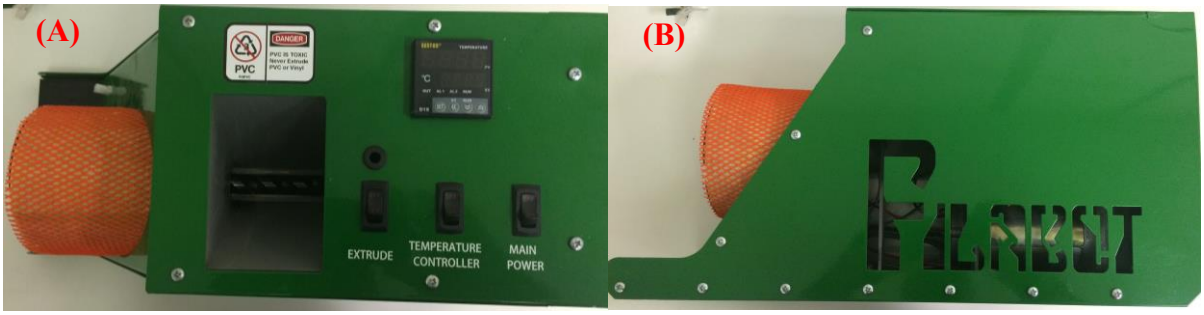

Figure 6. (A) Top view of the Filabot filament maker used to make experimental filament. (B) Side view of the Filabot filament maker

This procedure proceeds with the replication of previous steps in which several different additives are added into the baseline solution. Silicon carbide (SiC) whiskers were dissolved into the ABS-pellets at incremental intervals of 1% by weight, 3% by weight and 6% by weight, respectively. The homogenous SiC mixture is evaluated by the same procedure as the previously explored blend. Through tension tests were also administered for both multi-walled carbon nanotubes (MWCNTs) and carbon fiber into ABS plastics, both filaments were purchased from University of Delaware and 3DXTECH respectively. After completion of the tensile test the new mixed filament was used to construct an ASTM D638 Type IV specimen for testing to obtain results that can be used in publications and can begin the process of establishing a material that will satisfy all the specific requirements of NASA for 3D printing in space.

III. Results

These experimental results offer a better understanding of the complex parameter that are involved in the process of adding additives to ABS plastics for the purpose of improving their mechanical properties. Figure 10 through Figure 12 show micrographs of ABS filaments that have been infused with 1%, 3%, 6% of SiC by volume respectively. The pictures shows micrographs of the samples at 50,100,250,500, and 1000 magnifications levels. Figure 13 shows filament that has been infused with multi-walled carbon nanotubes filament. The 1% SiC filament showed an ultimate stress of 5,800 PSI a tensile module of 3100 PSI and a failure stress percentage of 42%. The 3% SiC filament showed an ultimate stress of 4,900 PSI, tensile modules of 22,500 PSI and a failure stress percentage of 49%. The 6% SiC filament showed an ultimate stress of 58,500 PSI, tensile modules of 41,000 PSI and a failure stress percentage of 32%. A comparisons of these results is shown graphical in Figures 7 through figure 9.

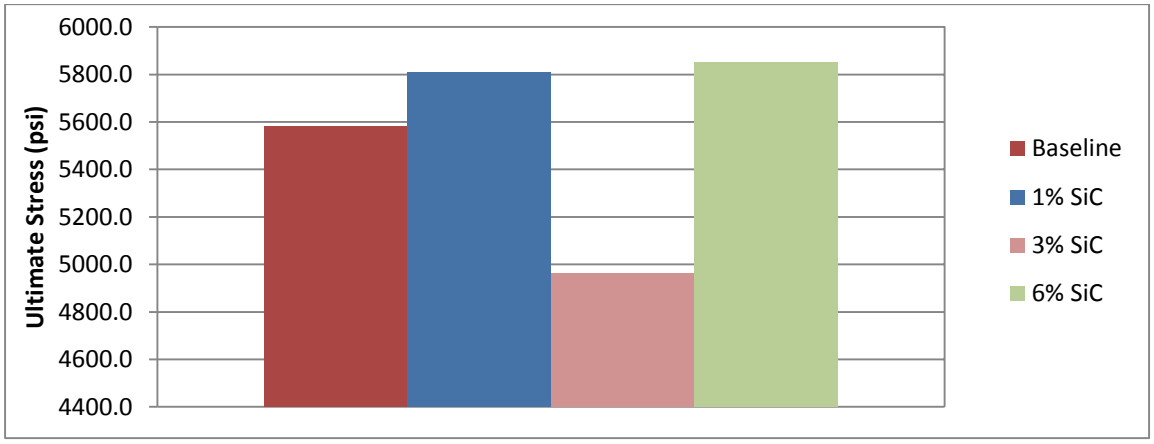

Figure 7. Comparison of ultimate stress for all ABS SiC filament strands created with the various percentages.

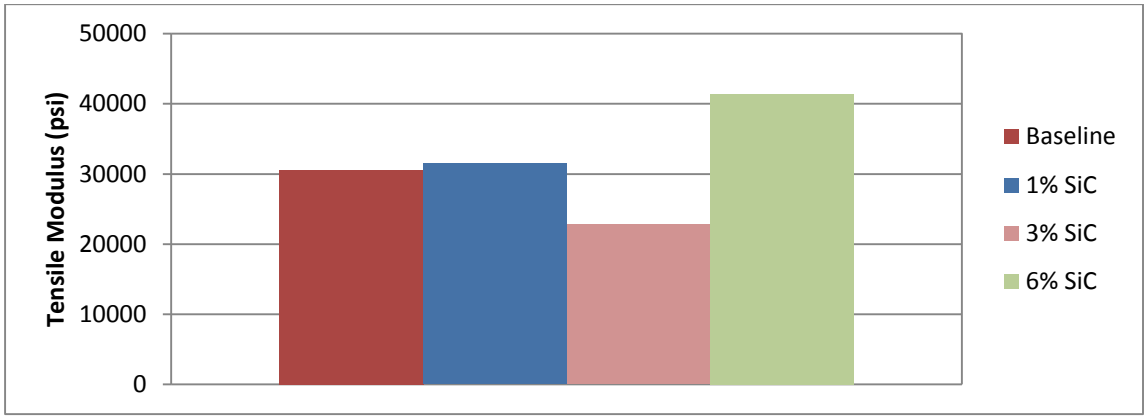

Figure 8. Comparison of Tensile Modulus for all ABS SiC filament strands created with the various percentages.

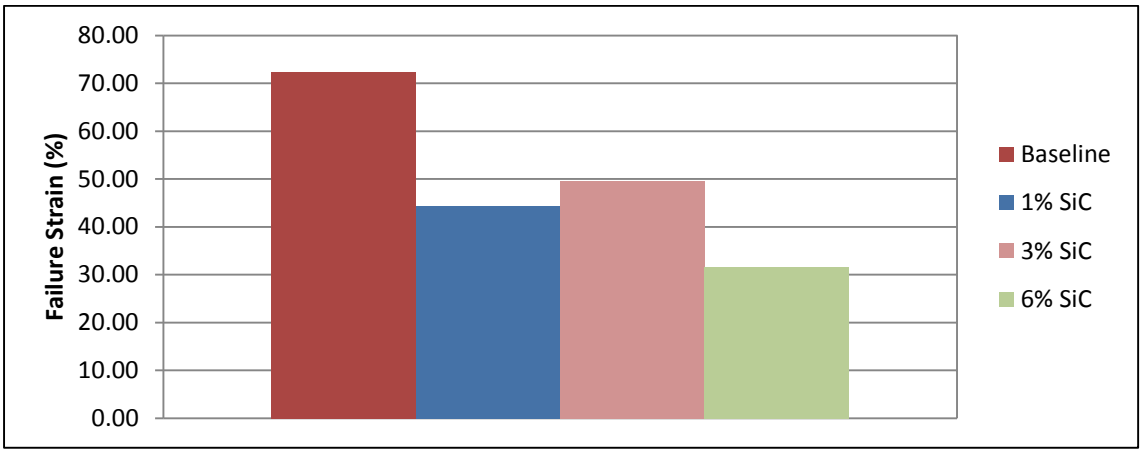

Figure 9. Comparison of Failure Strain for all ABS SiC filament strands created with the various percentages.

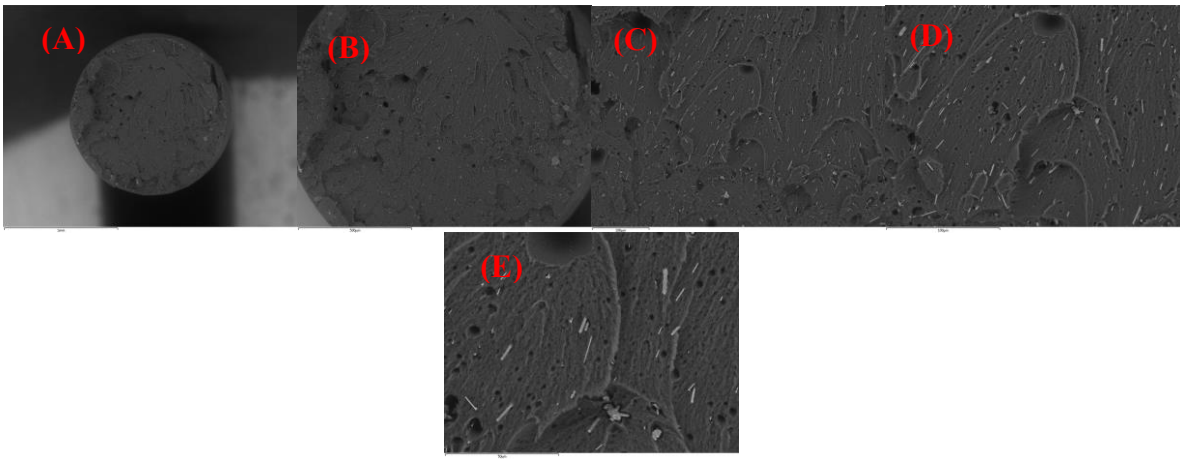

Figure 10. Micrograph of ABS filament with 1% by volume of SiC shown at different magnifications (A) is shown at x50, (B) is shown at x100 (C) is shown at x250 (D) is shown at x500 and (E) is shown at x1000.

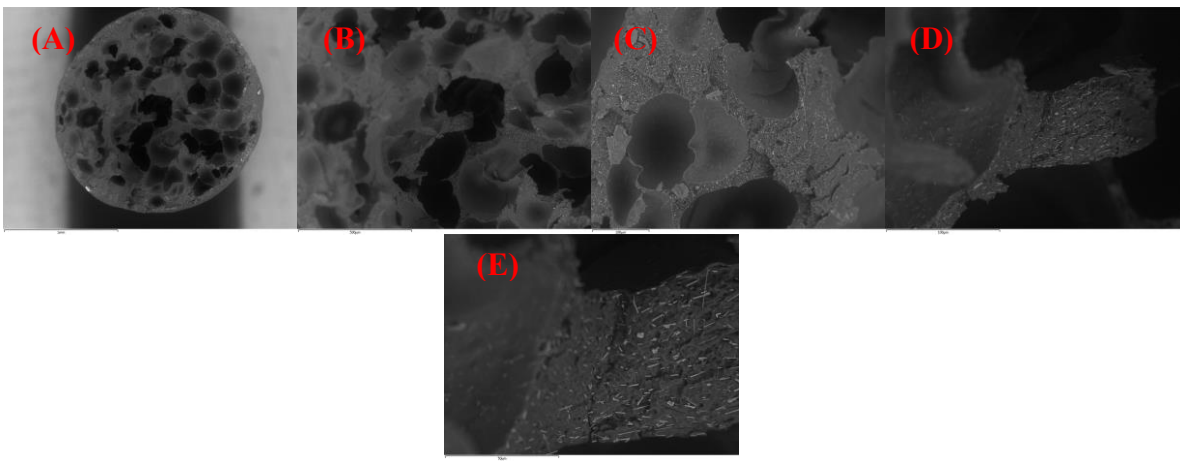

Figure 11. Micrograph of ABS filament with 3% by volume of SiC shown at different magnifications (A) is shown at x50, (B) is shown at x100 (C) is shown at x250 (D) is shown at x500 and (E) is shown at x1000.

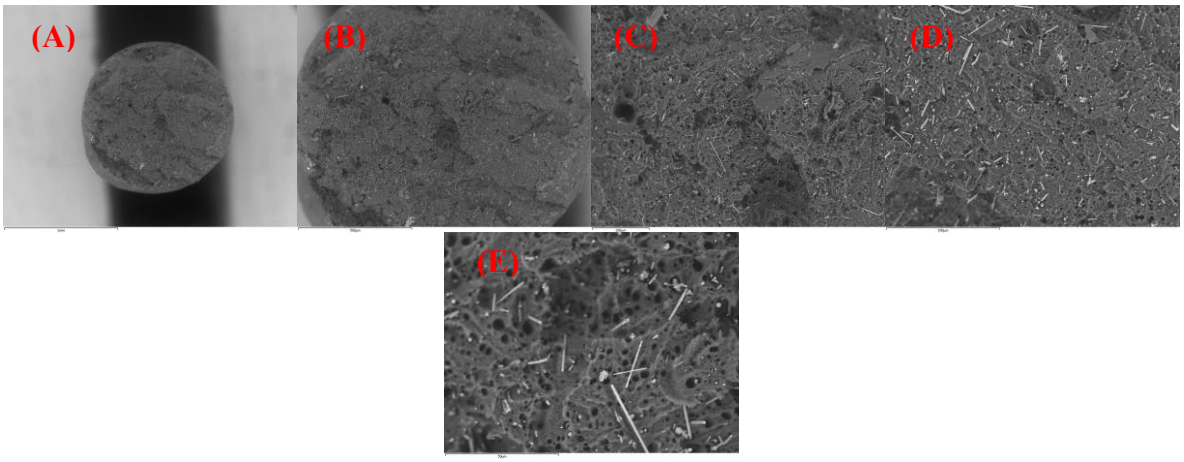

Figure 12. Micrograph of ABS filament with 6% by volume of SiC shown at different magnifications (A) is shown at x50, (B) is shown at x100 (C) is shown at x250 (D) is shown at x500 and (E) is shown at x1000.

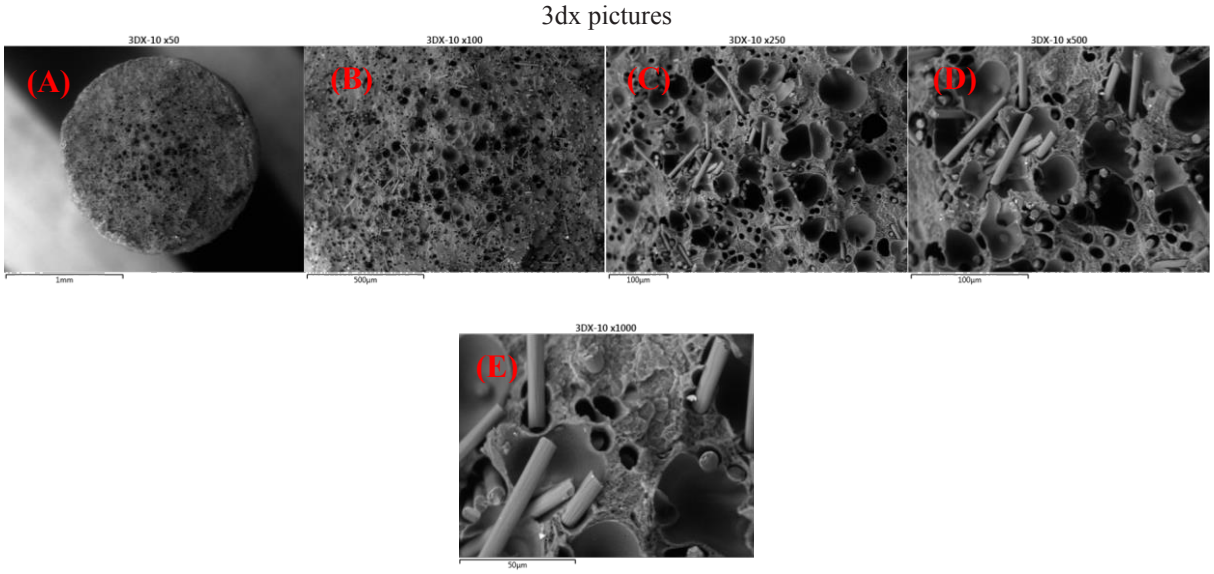

Figure 13. Micrograph of ABS filament with multi-walled carbon nanotubes shown at different magnifications (A) is shown at x50, (B) is shown at x100 (C) is shown at x250 (D) is shown at x500 and (E) is shown at x1000.

IV. Conclusion

The results show that adding an additional element to ABS plastics for the purpose of improving their mechanical properties is a viable solution to solving the current limitations of ABS plastics. This new material may be key to helping NASA reach it going of getting to Mars and decreasing the dependence on cargo flights to the International Space Station. Further experiments are need to determine the multi-variable correlation between the volume of the additive to the volume of the matrix of the base ABS, as well as the best way to develop a homogenous mixture of the additive material.

Appendix

Group	Specimen	Yield Load (lbf)	Yield Extension (in)	Peak Load (lbf)	Failure Load (lbf)	Failure Extension (in)	P-Δ Slope (lbf/in)
1MWCNT	1			17.081	15.275	1.188	43.827
Stratasys	3	16.185	0.56	20.087	20.087	3.387	45.48
1SiCUTSC	1			16.104	14.896	1.197	43.973
3SiCTSC	1	17.756	0.84	17.913	15.776	1.018	43.88
3SiCUTSC	1			25.063	24.042	0.384	90.03
6SiCUTSC	1			17.295	17.076	0.513	66.042
3SiCUTSC Baseline	1			46.35	24.042	0.384	90.03
ABS CarbonFiber	2			24.136	24.136	0.163	275.4

Acknowledgments

This work was done at NASA Marshall Space Flight Center, and has been supported by the MSFC's Dr. Frank Six, director of the Office of University Affairs and Majid Babai and Scotty Sparks Division Directors at MSFC's EM 42 division. The United States Government retains, and by accepting the article for publication, the publisher acknowledges that the United States Government retains, a non-exclusive, paid-up, irrevocable, worldwide license to publish or reproduce the published form of this work, or allow others to do so, for United States Government purposes.

The primary author would like to give a special thank you to the co-authors Dr. Raj Kaul, and Mr. William Guin. I would also like the thank the entire staff of NASA MSFC building 4707, for providing their expertise and access to their facilities, raw material and equipment used in this study.

References

Jones, R, *Mechanics of Composite Materials*, 1nd ed., McGraw–Hill, Washington D.C., 1983,

Committee on Space-Based Additive Manufacturing, *3D Printing in Space*, The National Academics Press, Washington D.C., 2014,

G. Postiglione, G.Natale, G.Griffini, M.Levi, and S.Turri ., "*Conductive 3D microstructures by direct 3D printing of polymer/carbon nano tube nanocomposites via liquid deposition modeling*," Journal of Composites, 2014 pp. 110-113.

R.D. Goodridge, M.L. Shofner, R.J.M. Hague, M. McClelland, M.R. Schlea and R.B. Johnson, C.J. Tuck., "*Processing of a Polyamide-12/carbon nanofiber composite by laser sintering," Journal of Polymer Testing Composites*, 2011 pp. 94-100.

Effect of Structural Deformation and Unsteady Friction Factor to Improve Water Hammer Results using GFSSP

Alak Bandyopadhyay
Associate Professor, Computer Science, Alabama A & M University

and

Alok Majumdar
Engineer, Thermal and Combustion Analysis Branch, NASA Marshall Space Center, Huntsville, AL

ABSTRACT

This paper presents a numerical study of fluid transients in a pipeline with the sudden opening of a valve. The network flow simulation software (Generalized Fluid System Simulation Program) based on the finite volume method has been used to predict the pressure surges in a pipeline that has entrapped air at one end of the pipe. The mathematical model is formulated by involving the flow equations in the liquid (water) zone and compressibility of the entrapped air, the structural deformation of the pipe and unsteady friction factor effect. The numerical results are compared with the experimental data available in the literature. The study shows a reasonable good agreement of computed results with the experimental data when the percentage of entrapped air is reasonably high, about 50%. However, as the pressure amplitudes go higher when there is relatively low volume of entrapped air is present, the computed results differ from experimental data both in amplitude of the pressure oscillations and corresponding frequencies. Use of structural deformation modeling coupled with the fluid dynamics problem reduces difference for much better comparisons with the experimental data. The unsteady friction factor model helps in bringing a damping effect as shown in experimental study.

NOMENCLATURE

A	=	area (ft^2)
C	=	Courant number
C_L	=	flow coefficient
D	=	diameter of the pipe (ft)
f	=	friction factor; frequency in cycles per second (Hz)
g_c	=	conversion factor for engineering unit
$H(f)$	=	frequency domain function
h	=	enthalpy (Btu/lb)
$h(\tau)$	=	time domain function
J	=	mechanical equivalent of heat (=778 lb_f-ft/Btu)
K_f	=	flow resistance coefficient (lb_f-s^2/(lb_m-ft)^2)
L	=	length of the tube (ft)
L_1	=	initial length for the water volume in the pipe
L_g	=	initial length of air column in the pipe
L_T	=	initial total length of liquid and air column = $L_l + L_g$
m	=	nodal mass (lb_m)
$\dot{m}$	=	mass flow rate (lb_m/s)
$(m_{air})^0$	=	initial air mass
N	=	number of internal nodes; number of data points for Fast Fourier Transform calculation
P_R	=	pressure ratio
p	=	pressure (lb_f/ft^2)
p_R	=	reservoir pressure
R	=	gas constant (lb_f-ft/ lb_m-R)
Re	=	Reynolds number
S	=	source term
T	=	temperature (ºF)
t_k	=	kth time value (s)
U	=	characteristic velocity

u = fluid velocity (ft/s)
V = volume (ft^3)
V^0 = initial total volume (ft^3)
x = spatial coordinate along the pipe length (ft)
Z = compressibility factor
α = void fraction of air
ε = surface roughness of pipe (ft)
ε/D = surface roughness factor
θ = valve angle
μ = dynamic viscosity (lb_m/ft-s)
ρ = density (lb/ft^3)
ρ_u = density of fluid at upstream node lb_m/ft^3
τ = time (s)
$\Delta\tau$ = time step (s)

Subscripts

f = liquid state
g = vapor state
i = ith node
ij = branch connecting nodes i and j
j = jth node
N = for the Nth node
w = water

I. Introduction

In pipeline systems, the flow control is an integral part of the operation, for instance, opening and closing of valves, starting and stopping of pumps. When these operations are performed very quickly, they cause the hydraulic transient phenomena in the pipelines which may cause pump and valve failures and catastrophic pipe ruptures. These fluid transients (also known as water hammer) have significant impact in design and operation of spacecraft and launch vehicle propulsion systems. The pressure rise due to the sudden opening and closing of valves of a propulsion feed line can cause serious damage during activation and shutdown of propulsion systems. Pressure surge occurs when either a propellant feed line system is opened or closed suddenly by using control valves. The accurate prediction of pressure surge is very important from a structural integrity point of view of the propulsion systems. The water hammer pressure rise can be even higher if there is a presence of entrapped gas in the pipe line. The problem of fluid transients in pipeline have been studied by many researchers both experimentally and numerically [1, 2, 3, 4]. However, most of the numerical work has been confined to use of method of characteristics and lumped model [5, 6]. Many often the pipe lines filled with water or other liquid might have entrapped air or some other gas. This can lead to further increase in the pipe lines causing severe damage not only to the pipe systems but also to the valves, pumps and other connected components.

Bandyopadhyay and Majumdar [7] have used Generalized Fluid System Simulation Program (GFSSP) to study the fluid transient behavior in a closed pipe filled with air and entrapped air for sudden valve opening and have compared the computed results with experimental data as obtained from literature [8]. GFSSP is a finite volume based network flow and heat transfer simulation program developed by NASA MSFC [9] which have been used for a wide variety of fluid flow and heat transfer problems. It has been found that GFSSP predicts the results very well in relatively low reservoir pressure (reservoir to ambient pressure ratio of 5 or less) and higher amount of entrapped air (initial ratio of air volume to total volume of fluids in the pipe is about

0.5). However, as pressure ratio goes up or the amount of air is lowered, then the water hammer pressure rise is very high (above 500 psi) and the computed values of pressure amplitudes and frequencies are significantly (more than 10%) different from the experimental data. One of the major reasons for this difference could be attributed to the assumption of rigid pipe.in the GFSSP model. GFSSP in its current form does not support structural deformation and needs modification to account for such deformation. A few researchers [10, 11] have also observed damping effect on the pressure fluctuation for water hammer study by including unsteady friction factor instead of only steady state friction factor.

In the current work, a simple structural model based on static deformation of the pipe diameter is used to study the effect of structural deformation on water hammer pressure transients. The damping effect due to unsteady friction factor also has been implemented in the model. The computed results are compared with the experimental data of Lee [8].

This paper describes the mathematical formulation, algorithm development and modification of GFSSP to account for two-way coupling of structural deformation and unsteady friction factor and verification of computed results parametrically with the experimental data.

1.1 Problem Description

A long pipe attached to a reservoir containing liquid water at one end and closed at the other end as shown in Figure 1. The liquid water and entrapped air regions in the pipe are separated by a ball valve located at section CD. Section AB represents the entrance of the fluid to the pipe, and this will be the starting location for the GFSSP model with appropriate boundary conditions for the reservoir pressure. Section C′ D′ represents the moved fluid-air interface location at a later time.

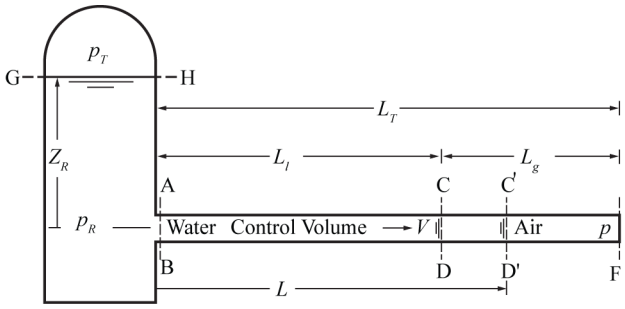

Fig. 1 Schematic of the water pipe with entrapped air [9].

The dimension of the pipe and other controlling parameters such as reservoir-to-air pressure ratio, length of air column, etc. are taken from Lee [8], so that the numerical results can be compared to the experimental data. The ball valve is opened from a 0% opening to 100% opening by controlling the angle of the ball valve and is shown in Figure 2. The reservoir pressure is considerably higher than the pressure of the entrapped air (air is assumed to be at atmospheric pressure). The ratio of reservoir pressure to the initial pressure (P_R) varies in the range of 2 to 7, i.e., the reservoir pressure (p_R) range being 29.4 psi to 102.9 psi. Apart from the initial pressure ratio, another controlling parameter is the ratio of initial length of the entrapped air column to the total length of the pipe ($\alpha = L_g/L_T$). The initial length for the water volume in

the pipe (L_l) is fixed to 20 ft., and the initial length of air column in the pipe *(*L_g*)* varies from 1.23 ft to 16.23 ft, the value of α ranging from 0.0579 to 0.448, respectively. The pipe diameter is 1.025 in. The entrapped air and water is initially at 14.7 psia and 60 ºF, respectively.

The ball valve does not open until about 0.15 s, and gradually starts opening. It opens 100% at about 0.4 s. Figure 2 shows the ball valve angle position with time; 0 deg refers to the full closed position and 90 deg refers to the full open position.

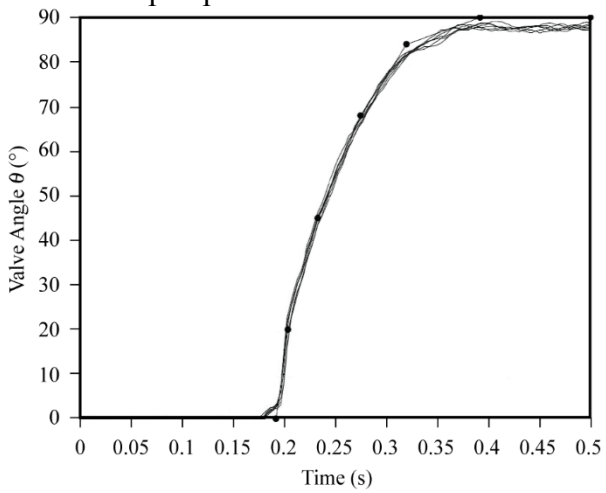

Fig. 2 Ball valve angle change with time [8].

1.2 Mathematical and Numerical Model Using Rigid Pipe Assumption

Modeling of Fluid Transient using the finite volume method requires the solution of unsteady mass, momentum, and energy conservation. In addition, the variation of the compressibility factor plays a significant role for modeling the pressure oscillations. Selection of time step to satisfy the Courant's condition is another critical factor. The mathematical formulations for solving the complete flow equations are quite complex and involve two fluids—water column and entrapped air. The numerical model has been separated into two parts: (1) solving the mass, momentum, and energy equation of the water using the finite volume method, and (2) solving the thermodynamic relations in the gas (air). The interface conditions are suitably used for the two-way coupling between water and air domain. The interface conditions are: (1) implementation of the force equilibrium by equating the pressure of the gas phase and liquid phase, and (2) implementation of thermal equilibrium by equating the temperature across the interface in two phases. The pipe is considered to be rigid.

In order to understand the mathematical and numerical model to solve this problem using GFSSP, a brief description and program structure of the simulation software (GFSSP) has been given as below.

In GFSSP, A fluid system is discretized into nodes and branches as shown in Figure 3. Mass conservation, energy conservation, and species concentration equations are solved at the nodes whereas momentum conservation equations are solved at the branches in conjunction with thermodynamic equation of state. The figure below shows only a typical node-branch system with a mixture option of three different pure species (H_2, O_2, and N_2) entering into the flow network and a mixture of H_2, O_2, and N_2 exits the network through outlet boundary nodes. However, for the current study of water hammer simulation only one fluid (water) is solved for

all the flow equations and the interaction with the other fluid (air) is done thermodynamically by suitably modifying the mass source and momentum source terms.

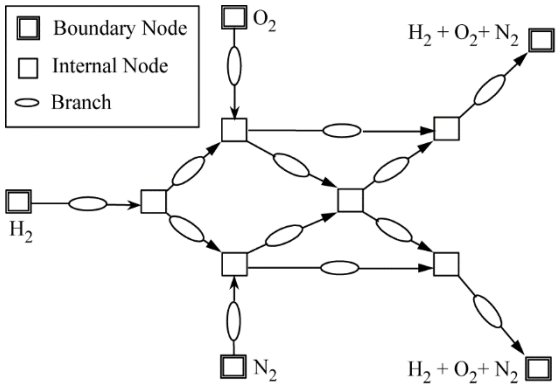

Fig. 3 A typical flow network consisting of boundary and internal nodes and branches.

GFSSP has three major parts as shown in Figure 4. The first part is the Graphical User Interface which allows users to create a flow circuit and the GFSSP input file after the completion of the model building process. The second major part of the program is the Solver and Property Module. This is the heart of the program that reads the input data file and generates the required conservation equations for all internal nodes and branches with the help of thermodynamic property data. It also interfaces with User Subroutines, the third major part of the program, to receive any specific inputs from users. This consists of several blank subroutines that are called by the Solver Module. These subroutines allow the users to incorporate any new physical model, resistance option, and nonlinear boundary conditions.

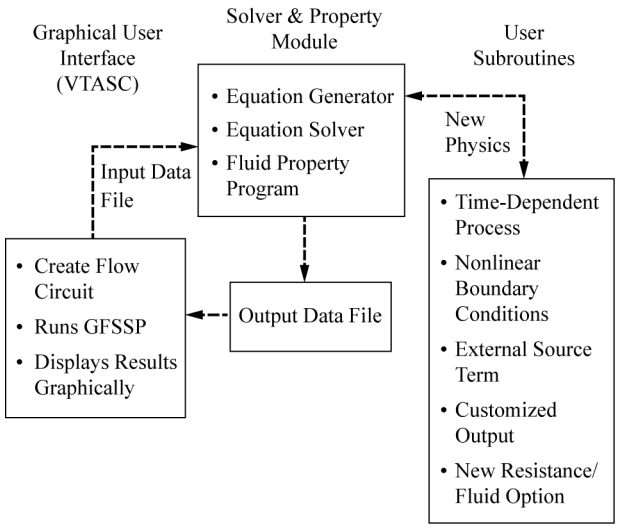

Fig. 4 GFSSP Program Structure showing the interaction of three major modules.

The entire pipe domain (Fig. 1) is split into a set of finite volume with number of segments as shown in Figure 5. Node 1 is the boundary node that represents the tank (reservoir). Node 12 has an interface with an imaginary control volume containing air only. The imaginary control volume has a fixed amount of air but the volume changes as it is pressurized due to fluctuation of pressure at node 12. Thereby, the volume of node 12 changes as the volume of the imaginary control volume changes. The entire liquid column was divided into 10 equal length pipe

volume discretization are explained in the user's manual of GFSSP [9]. However, a detailed formulation for water-air interaction due to valve opening is described here.

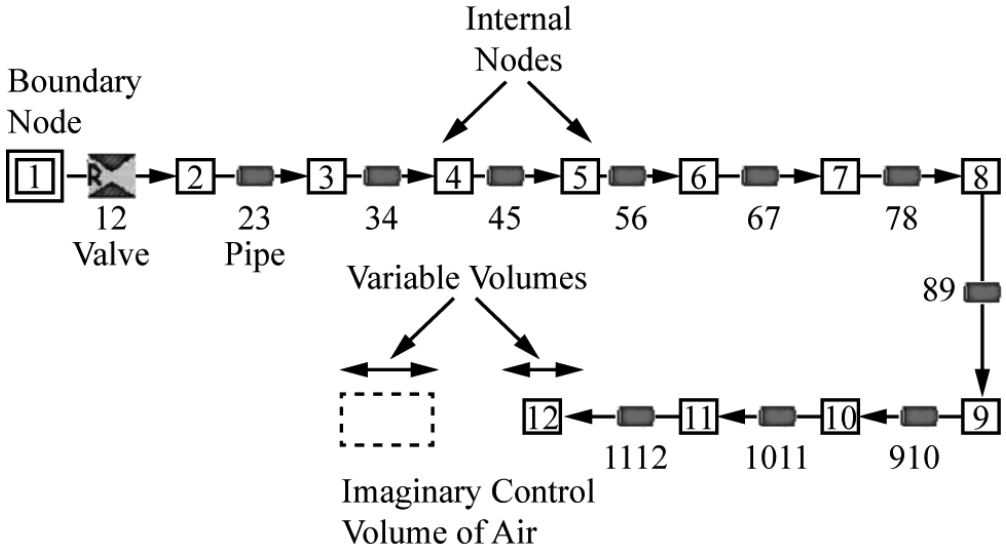

Fig. 5 Finite volume model of the flow network.

The modeling of dynamics of entrapped air and its interaction with the liquid column is critical for predicting the pressure transient of the present system. The GFSSP model (shown in Fig. 5) does not include the control volume representing entrapped air. Therefore, a separate model for entrapped air is necessary to establish the interaction between liquid and air column by calculating the volume change and the interfacial force (included as a momentum source in the momentum equation). In order to compute the volume change in the liquid and air column, it is assumed that all the volume change occurs at the last node (node 12 in Fig. 5), and the adjustments are done by using the equilibrium conditions as explained in Figure 6.

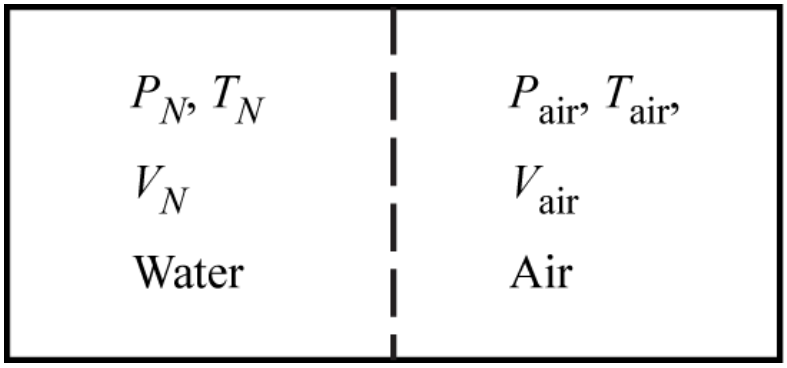

Fig. 6 Equilibrium conditions across the water-air interface.

Air mass is constant as the air is entrapped and is not going out of the pipe (closed pipe). The initial air mass, $(m_{air})^0$ is computed by using the ideal gas law for air using the initial air volume, pressure, and temperature. Air volume at any instant of time can be computed by using the ideal gas law as:

$$V_{\text{air}} = m_{\text{air}} R_{\text{air}} T_{\text{air}} / p_{\text{air}} . \quad (1)$$

Volume of liquid water in node *N* is computed using:

$$V_N = \left(m_w R_w T_N Z_N \right) / p_N , \quad (2)$$

where m, R, T, Z, p, and V represent the resident mass, gas constant, temperature, compressibility factor, pressure, and volume of liquid water, respectively, and subscript *N* implies for the Nth node. N is the last node that is node 12 in Figure 5.
Using the volume balance (change in water volume will be negative of change in air volume) as the total volume remains constant, V^0 (the initial total volume) = $(V_{air} + V_w)^0$ = V (total volume at any instant of time) = $V_{air} + V_N$, where V_N is the water volume of node *N*.
Using the expressions of V_{air} and V_N as given in equations (1) and (2), and also using the force equilibrium ($p_{air} = p_N$) and thermal equilibrium ($T_{air} = T_N$), it can be shown that:

$$V_N = V^0 / (1 + \beta) , \quad (3)$$

Where, $\beta = \dfrac{m_{\text{air}} R_{\text{air}}}{m_N R_N Z_N}$.

The momentum source for the liquid (node N) due to air pressure interaction will be:

$$\text{Momentum Source} = -\frac{1}{g_c} \rho_N \frac{\left(V_N - V_N^* \right)}{\Delta \tau} u_N , \quad (4)$$

Where u_N is the velocity at the last node, and V_N and V_N^* are the volume of the *N*th node at the current and previous time steps, respectively.

1.3 Results with Rigid Pipe Assumption

A time step of 0.005 s was found satisfactory to obtain a time-step independent numerical solution. Similarly a total number of 12 nodes were sufficient to get a grid-independent solution. These optimized values were obtained while studying the case with reservoir pressure to ambient pressure ratio of 7 and α = 0.45. Similar behavior have been found for other cases of pressure ratio and relative air column. For the numerical simulation a wide range of reservoir pressure (7 times more than atmospheric to 2 times more than atmospheric) and relative air volume ratio (α) in the range of 0.05 to 0.5 has been considered. Air volume ratio (α) of 0.05 indicates about 5% air in the pipe and 0.5 indicates 50% air in the pipe. The node volume has to be under-relaxed in some cases to 0.8 in order to get a converged solution.

In this section, numerical results obtained from the current simulation with the rigid pipe assumption are compared with the experimental data of Lee [8]. As the pressure developed in the water column is the highest at the end of the pipe (node 12 of Fig. 3), it is more appropriate to

plot this pressure (pressure at node 12), which is also the same as the bulk pressure in the entrapped air. Figures 7(a) and (b) show the transient pressure plot with about 45% entrapped air initially for (a) P_R = 7 and (b) P_R = 4 respectively. The numerical results agree reasonably well with that of the experimental data both at low (P_R = 4) and high (P_R = 7) pressure ratios. The peak pressure rise is about 272 psia from numerical computation as compared to 251 psia from the experimental data for P_R = 7 (about 8% difference) and 102 psia (numerical) to 107 psia (experimental) for P_R = 4, a difference of about 5%. As the pressure ratio (P_R) is reduced, the agreement is better. Maximum pressure occurs at the end of the pipe (node 12 of Fig. 3) and this is also the same as the bulk pressure of entrapped air.

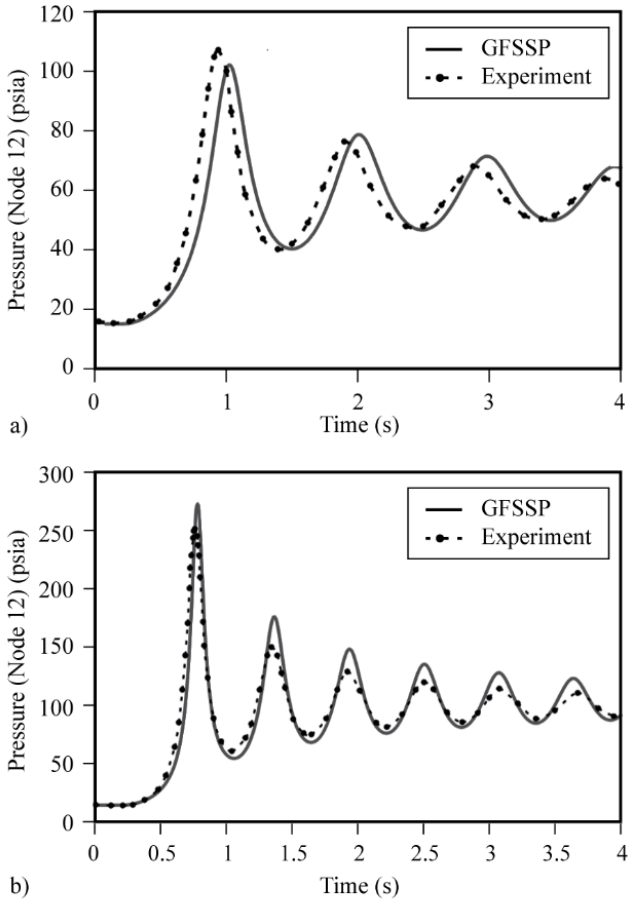

Fig. 7 Comparison of predicted and measured air pressure for a) P_R = 4 and b) P_R = 7 at about 45% initial air volume ($\alpha \approx 0.45$).

Figure 8 shows the comparisons for the relatively low void fraction of the air ($\alpha \approx 0.2$), at pressure ratios (P_R) of 2 and 5, respectively. As observed from these two plots, the numerical results match quite well with that of the experimental results at a low pressure ratio, but the difference is quite large (about 25% in the peak pressure estimate) when the pressure ratio (P_R) is 5. From Figures 7 and 8, it is observed that the numerical results predict the pressure distribution reasonably well at a higher value of α (α≈ 0.45), i.e., with more air, the peak pressure rise is relatively smaller for a particular inlet pressure ratio (PR). At a lower value of α ($\alpha \leq 0.2$), when

the pressure rise is relatively high due to less cushion effect, the difference in the peak pressure is more. Also observed that the frequencies of pressure oscillations match quite well between the computed results and the experimental results. However, a phase shift occurs in the pressure peaks, particularly after the first peak (Figure 8) for the case of low entrapped air ($\alpha = 0.2$). The overall discrepancy between numerical results and experimental data can be attributed to several factors which include (a) compliance due to structural deformation, and (b) assumption of steady state and a fully developed friction factor.

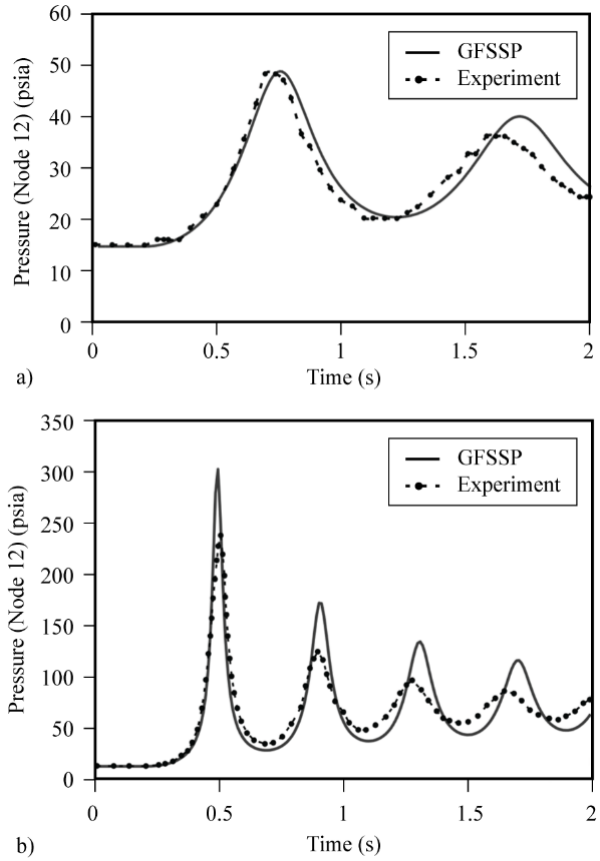

Fig. 8. Comparison of predicted and measured air pressure for a) $P_R = 2$ and b) $P_R = 5$ at about 20% initial air volume ($\alpha \approx 0.2$).

Hence in the current study the structural deformation of the pipe due to high pressure development is being considered. The pipe material is Plexiglas which has much less modulus of elasticity as compared to steel. In the next section, the structural deformation of the pipe due to very high internal pressure is considered to suitably modify the various geometric quantities in the GFSSP simulation and its mutual interaction with the fluid flow computations are considered.

2. STRUCTURAL DEFORMATION USING STATIC APPROACH

As a first attempt to incorporate the structural dimension change of the pipe for the fluid flow simulation, it is assumed that at any instant of time, the pipe is undergoing static deformation due to the pressure force the pipe is subjected to at the previous time step. The details of the static deformation due to pressure force are given in the section below.

2.1 Static Formulation

Consider the pipe as a thin pressure vessel subjected to pressure force as shown in figure 9 below. This figure shows normal stresses in circumferential (tangential, Θ) and axial (z) directions. The pressure inside the pipe (p) is considered uniform both circumferentially and axially.

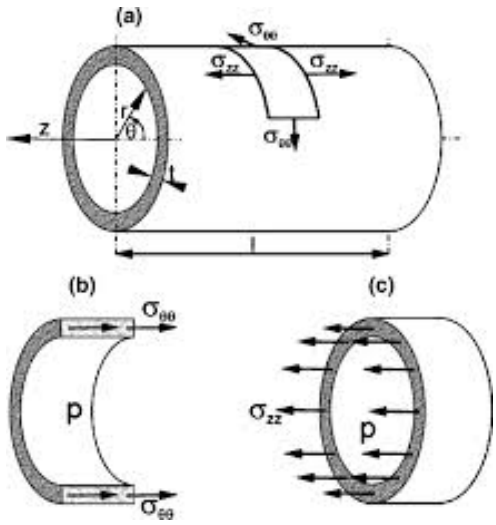

Fig. 9 Schematic of Pressure Vessel Loading and Stress

The tangential (circumferential direction) stress (σ_Θ) and the longitudinal stress (σ_z) are obtained using the thin-walled pressure vessel formulae as given below.

$$\sigma_\theta = \frac{pr}{t} \tag{5a}$$

$$\sigma_L = \frac{pr}{2t} \tag{5b}$$

p = internal pressure
r = inner radius of the pipe
t = thickness of the pipe

The normal stress in the radial direction $\sigma_r = -p$, and this is neglected as compared the other two direction stresses for thin walled pipe (i.e. t/r << 1).

The strain in the circumferential (tangent direction), is defined as:

$$\varepsilon_\theta = \frac{2\pi\Delta r}{2\pi r} = \frac{1}{E}\left(\sigma_\theta - \upsilon\sigma_z\right) \tag{6}$$

Where E is the Young's modulus of the pipe material and ν is the Poisson's Ratio.

Using equations 1(a) and 1(b) into the above equation, one gets

$$\frac{\Delta r}{r} = \frac{(p - p_{amb})r}{Et}\left(1 - \upsilon/2\right) \tag{7}$$

This equation will lead to computing the radius (r) at any instant of time as below.

$$(\Delta r)_{\tau+\Delta\tau} = \frac{\left(1-\frac{\upsilon}{2}\right) r_\tau^2 (p - p_{amb})}{Et} \tag{8a}$$

And $r_{\tau+\Delta\tau} = r_\tau + (\Delta r)_{\tau+\Delta\tau}$ (8b)

2.2 Testing of Static Formulation Using GFSSP Pressure Data

A FORTRAN program is written to compute the static deformation of the pipe subjected to the pressure oscillation obtained using rigid pipe assumption as given in Figure 7(b). Figure 10 shows the pipe diameter as a function of time as computed by using the static deformation formulation as given in equations 8(a) and 8(b). The solid line corresponds to applied pressure oscillation and the dotted line corresponds to fluctuation of the pipe diameter as a function of time. It may be observed the static formulation is able to capture the real phenomena.

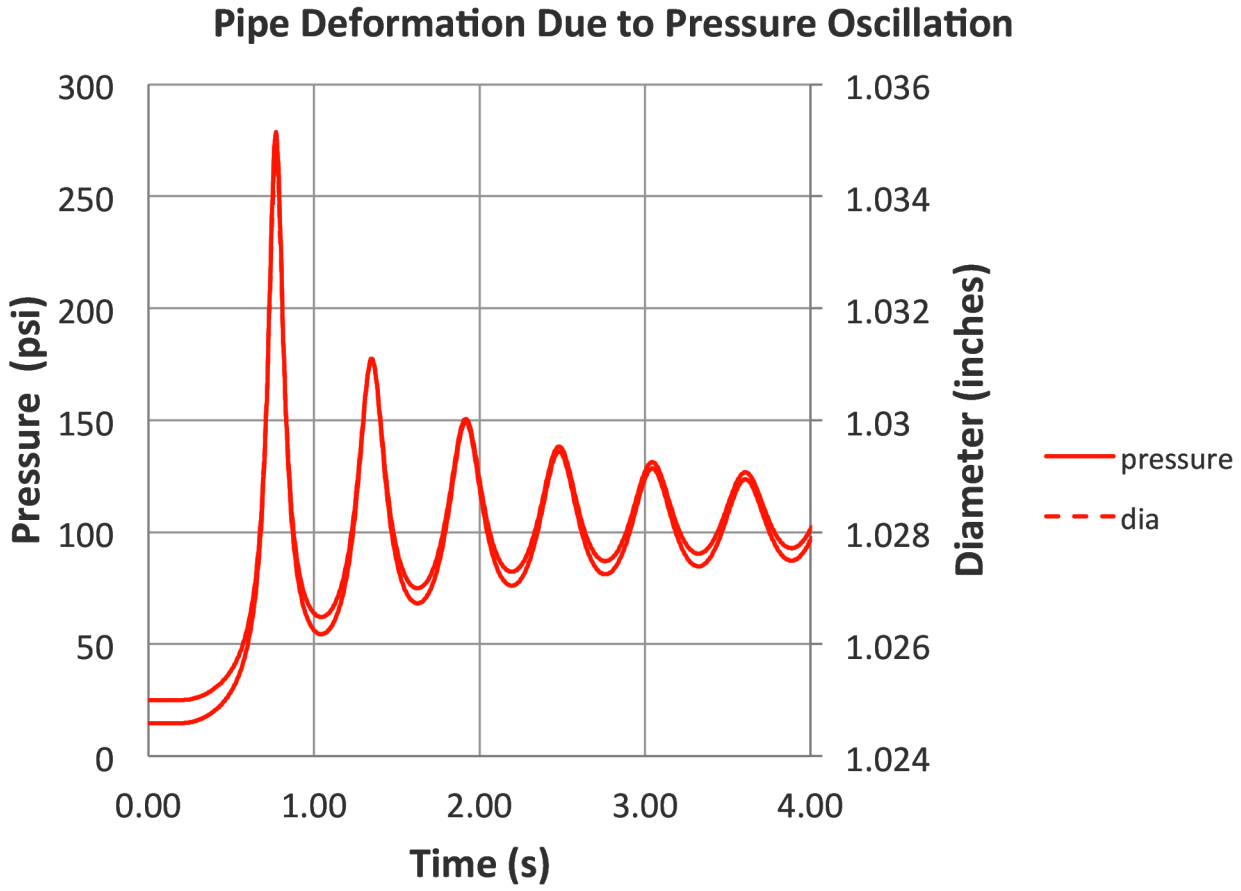

Fig. 10. Static Deformation Due to Transient Pressure Oscillation

2.3 Implementation of Structural Deformation using Static Formulation in GFSSP

In order to couple the structural deformation (in the radial direction only) with GFSSP fluid flow simulation, the following algorithm is followed.

Algorithm:

- At every iteration and for each internal node, the change in radius and new radius being computed using equations (8a) and (8b).
- The average cross-sectional area and volume for each branch are computed using the following relations:
  Area = $A_{br} = \pi(r_{new})^2$
  Volume = $V_{br} = A_{br} * L_{br}$, where L_{br} is the branch length.
- Node volumes are computed using half of the branch volumes of the connecting branches. For boundary nodes however it is computed differently as it has only one branch connected with. This is done to be consistent with GFSSP's standard formulation of computing node volumes from branch volumes.
- All of the above steps are being repeated until desirable convergence is achieved. For faster and stable convergence, a relaxation parameter is introduced for the node volume computation.

2.4 Results and Discussion

In order to observe the effect of structural deformation as compared to the rigid pipe assumption [7], the operating conditions for the pressure ratio ($P_R = p_R/p_a$) and the range of relative air length (α) are kept same as earlier work with rigid pipe assumption. Two extreme conditions of relative air column length (α) are 0.445 and 0.058. The reservoir pressure varies from 7 times atmospheric ($P_R = 7$) to 2 times more than atmospheric ($P_R = 2$). Figure 11 shows a plot of water hammer pressure at the dead end of the pipe with time with (a) rigid pipe assumption, solid line and (b) Structural Deformation (SD) of the pipe (computed using static formulation) (Dotted line). As can be observed that the results with structural deformation (SD) match much better with the experimental data (red dots) as compared to the rigid pipe assumption.

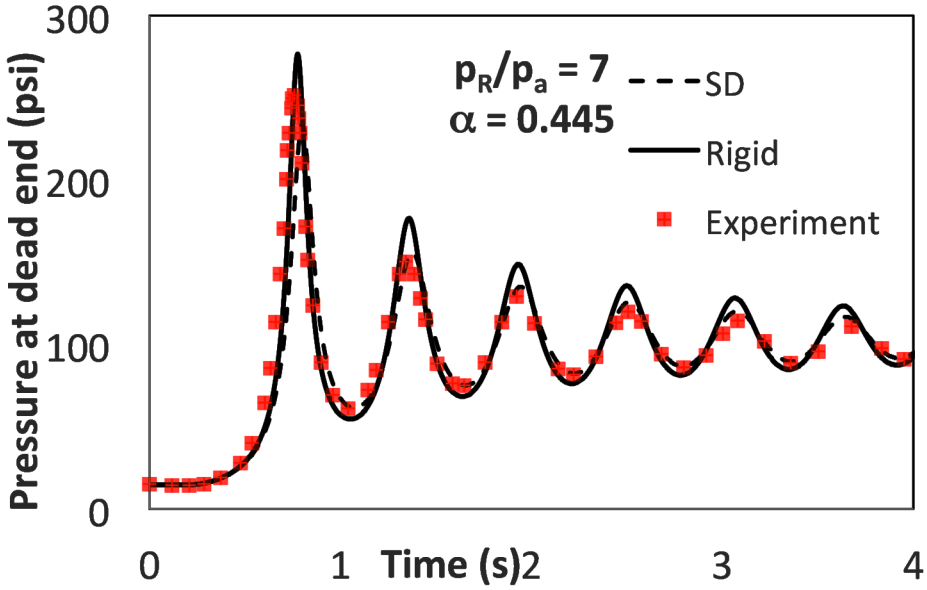

Fig. 11. Comparison of Computed results (structural deformation and rigid) with Expt.

Figure 12 (a), (b), (c) and (d) show a comparison of the GFSSP simulation for the case of low entrapped air (α = 0.058) with both structural deformation as well as rigid pipe assumption with the experimental data for P_R = 5, 4, 3 and 2 respectively.

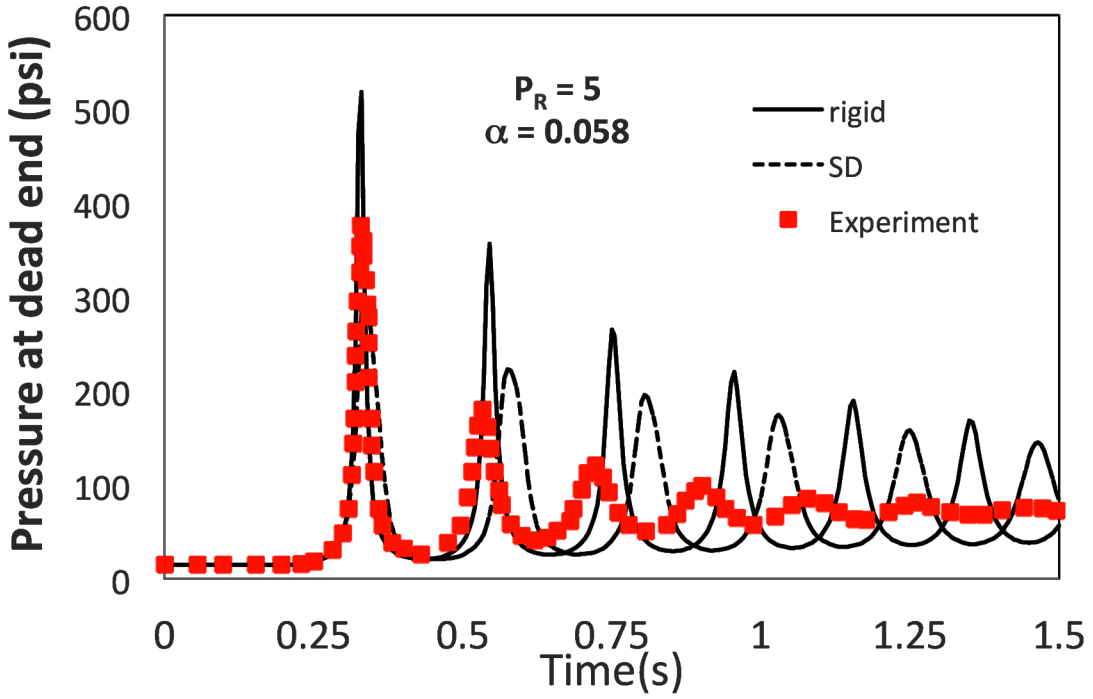

(a)

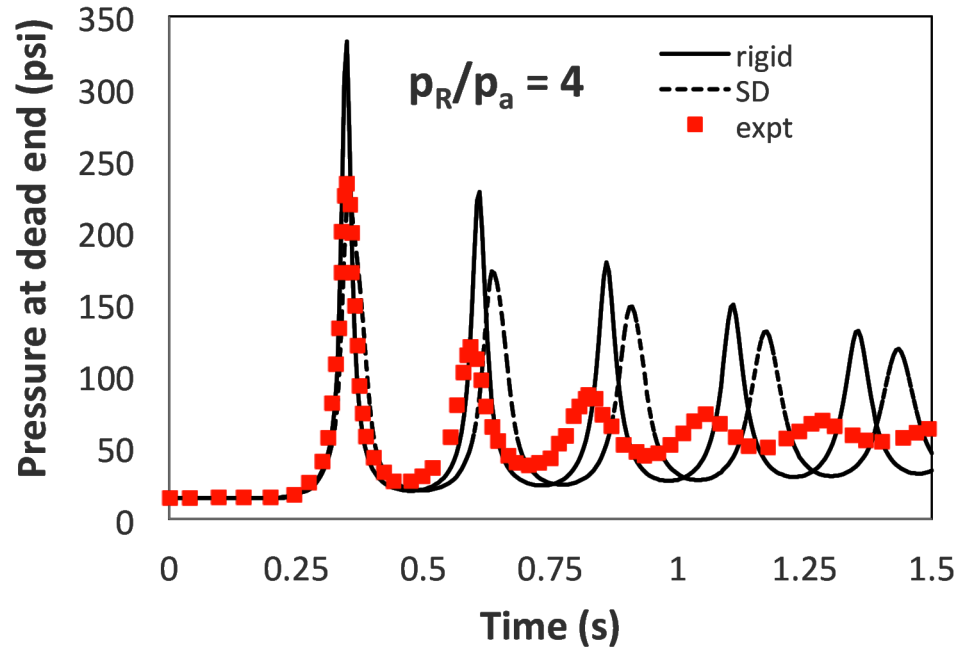
Pressure at dead end (psi)
350
300
250
200
150
100
50
0
0
0.25
0.5
0.75
1
1.25
1.5
Time (s)
$p_R/p_a = 4$
rigid
SD
expt

(b)

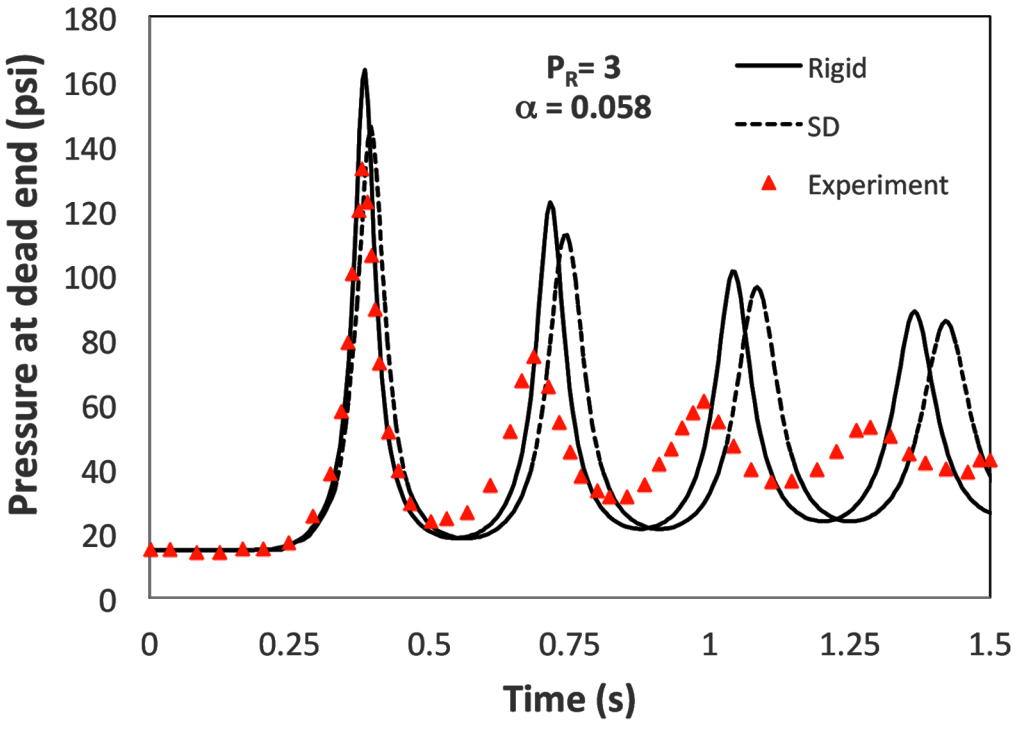
Pressure at dead end (psi)
180
160
140
120
100
80
60
40
20
0
0
0.25
0.5
0.75
1
1.25
1.5
Time (s)
P_R= 3
α = 0.058
Rigid
SD
Experiment

(c)

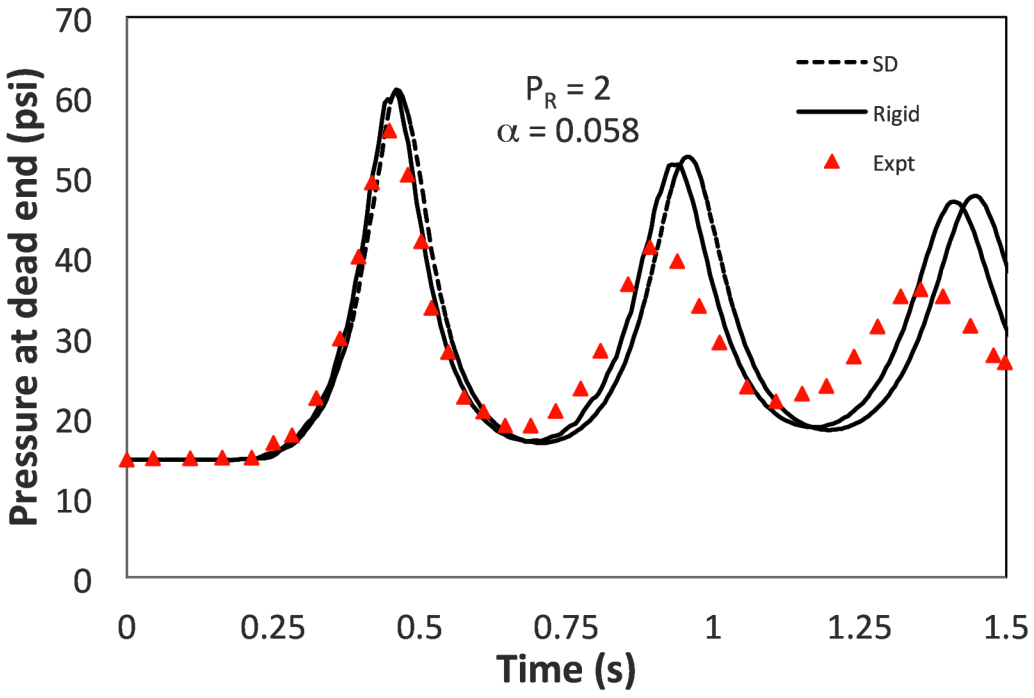

(d)

Fig. 12. Comparison of numerical simulation using lateral structural deformation of the pipe with experimental data for a) P_R = 5 (b) P_R = 4 (c) P_R = 3 and (d) P_R = 2

As observed from Figures 11 and 12, considering the structural deformation in GFSSP simulation improved the prediction as compared to the experimental data, however, the model seems like not able to have much damping effect. This can be attributed to some other modeling feature such as unsteady friction factor which has been used by a few researchers and have observed the damping effect on pressure oscillation and thereby able to predict and compare with the experimental data better [10].

3. Effect of Unsteady Friction Factor

3.1 Unsteady Friction Model

GFSSP uses a quasi-steady-state friction factor based on Moody's chart.

A more accurate model as used by some researchers is the inclusion of unsteady friction factor along with steady-state friction model as:

$f = f_s + f_u$

Where, f_s is the quasi-steady friction factor (Darcy's friction coefficient), f_u is the unsteady friction coefficient. There are a few models available for modeling the unsteady friction factor part. One of the standard model is that given by Brunone[5]. According to this model there are two components of the unsteady friction factor, one due to instantaneous local acceleration and other due to convective acceleration as given in the equation below.

$$f_u = \frac{kD}{v|v|}\left(\frac{\partial v}{\partial t} - a\frac{\partial v}{\partial x}\right) \quad (9)$$

Where $k = C^*/2$, where $C^* = 0.00476$ for laminar flow

and $C^* = \frac{7.41}{Re^{\log(14.8/Re^{0.05})}}$ for turbulent flow.

Where a is the water hammer wave speed, which is the velocity of sound in water.

There is an alternate friction-factor model modified by Vítkovský [6] corrected for back flow as below: $f_u = \frac{kD}{v|v|}\left(\frac{\partial v}{\partial t} + sign(v)c\frac{\partial v}{\partial x}\right)$ (10)

Sign(v) = + 1 when flow is in positive x-direction, otherwise it is -1.

In the current work, the original Brunone model (eq. 9) is being used and gave better results as compared to the modified model (eq. 10).

3.2 Results from Unsteady Friction Factor Model

Using constant sound velocity in water (a = 4911 ft/sec), and all other parameters as given above, the flow computations were modified using unsteady friction factor. Figure 13 given below shows the effect of unsteady friction for rigid pipe as well as for structural deformation. The case of low alpha (α = 0.058) and PR = 5 is considered, to see the effect of unsteady friction to damp the pressure oscillations. In this figure, there are five different plots representing various combinations of rigid pipe and flexible pipe (with the structural deformation model used in this study) and steady and unsteady friction factor models along with the experimental data are shown. As it could be seen the red solid line representing results with structural deformation along with unsteady friction model is able to fit most of the experimental data quite well as compared to other cases.

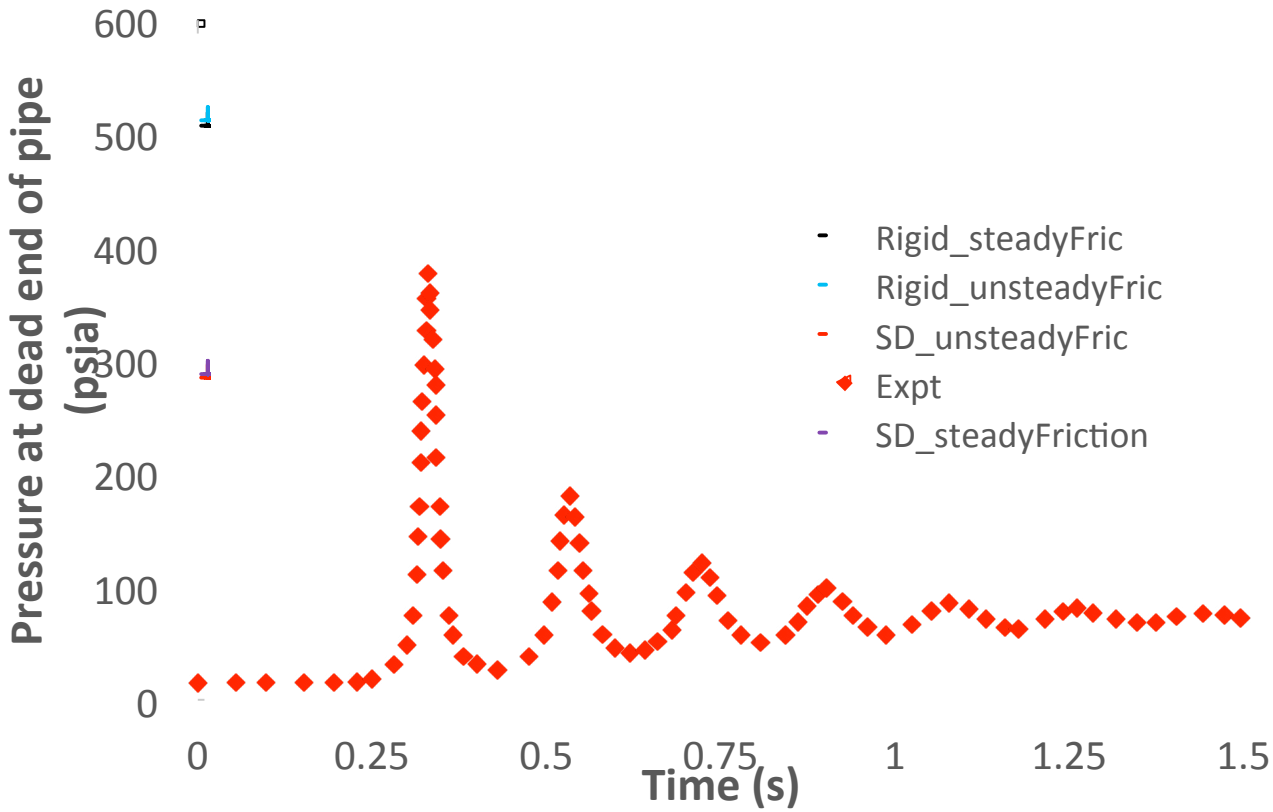

Fig. 13. Effect of unsteady friction factor on transient pressure oscillations

3 Conclusions:

Using the static formulation for computing the pipe diameter change helps in predicting the pressure better than rigid pipe formulation in regards to pressure amplitude is concerned, especially for the highest pressure developed in the pipe. However, experimental data show a faster damping of the pressure fluctuation, somehow the computation does not show this behavior. In the numerical model, inclusion of unsteady friction factor shows the damping effect. However, still there is some difference with the experimental data, and a further investigation using dynamic structural model is in progress and might improve the results further.

4 Acknowledgements

The author like to acknowledge the following person for the work possible.

1. Dr. Alok K. Majumar, Summer Faculty Mentor, ER-43, Marshall Space Center
2. Dr. Paul Schallhorn, LSPKSC.
3. Ms. Alicia Turpin, Branch Chief. Combustion and Thermal Analysis Branch, NASA MSFC
4. Dr. Andre' Leclair, ER-43/ Combustion &Thermal Analysis
5. Mr. Odric Moore, MITS
6. Dr. Frank Six, Summer Faculty Coordinator

4 References

[1] R.P. Prickett, E. Mayer, J. Hermel, Water Hammer in a Spacecraft Propellant Feed System, *Journal of Propulsion and Power*, 8(3) (May–June 1992) pp. 592–597.

[2] T.Y. Lin, D. Baker, Analysis and Testing of Propellant Feed System Priming Process, *Journal of Propulsion and Power* 11(3) (May–June 1995) pp. 505–512.

[3] H.C. Hearn, Development and application of a priming surge analysis methodology, *Proceedings of the 41st AIAA/ASME/SAE/ASEE Joint Propulsion Conference & Exhibit*, Tucson, Arizona (July 10–13, 2005) pp. 1–10.

[4] A.K Majumdar, R.H. Flachbart, Numerical modeling of fluid transients by a finite volume procedure for rocket propulsion systems, *Proceedings of the ASME FEDSM'03, 4th ASME/JSME Joint Fluids Engineering Conference*, Honolulu, Hawaii (July 6–10, 2003) pp. 1–8.

[5] E.B. Wylie, V. Streeter, *Fluid Transients*, FEB Press, Ann Arbor (1982) pp. 13–61.

[6] F.J. Moody, *Introduction to Unsteady Thermofluid Mechanics*, John Wiley & Sons (1990) pp. 408–422.

[7] Alak Bandyopadhyay and Alok Majumdar. "Network Flow Simulation of Fluid Transients in Rocket Propulsion Systems", Journal of Propulsion and Power, Vol. 30, No. 6 (2014), pp. 1646-1653.

[8] Nahm Ho Lee, "Effect of Pressurization and Expulsion of Entrapped Air in Pipelines", Ph.D. Thesis, Georgia Inst. Of Tech, August 2005.

[9] A.K. Majumdar, A.C. LeClair, R. Moore, P.A. Schallhorn, Generalized Fluid System Simulation Program, Version 6.0, NASA/TM—2013–217492 (October 2013) https://gfssp.msfc.nasa

[10] Dehkordi, M. M., and Firoozabadi, B.,"Effects of Unsteady Friction Factor on Gaseous Cavitation Model"Scientia Iranica Journal,Transaction B, Mechanical Engineering,Vol. 17, No. 1, 2010, pp. 13–24

[11] Brunone, B., Kearney, W., Mecarelli, M., and Ferrante, M.,"Velocity Profiles and Unsteady Pipe Friction in Transient Flow,"Journal of Water Resources Planning and Management,Vol. 126, No. 4, 2000,pp. 236–244.

Joining Aluminum Honeycomb Cores for Large Scale Sandwich Composite Structures: Demonstration of Splice Procedure and Mechanical Testing of Spliced Panels

Lesley N. Berhan[1]
University of Toledo, Toledo, OH, 43606

William T. King[2]
University of Alabama, Tuscaloosa, AL, 35487

and

William C. Hastings[3]
Marshall Space Flight Center, Red Stone Arsenal, AL 35812

A procedure for joining aluminum honeycomb cores using a room temperature cure, high strength epoxy adhesive was developed, and the key parameters, hardware, and conditions to be considered when splicing aluminum honeycomb cores for large scale, co-cured sandwich panels were identified. The process was demonstrated on a small scale using 2' x 2' panels, however the approach can be readily scaled up for use in the construction of large sandwich panels such as those to be manufactured in NASA's Composites for Exploration Upper Stage (CEUS) demonstration project. The desired outcomes of the joining process are that the location of splice should not be evident on the cured panel (i.e. the surface of the face sheets should be smooth and seamless on both visual and tactile inspection), and the splice should effectively transfer the transverse shear stress from one core to the other, without significant reduction in shear strength. In order to evaluate the structural integrity of the splice, mechanical tests were performed on specimens cut from sandwich panels containing the spliced core. The approach used produced splices of high quality from both an aesthetic and structural standpoint. The results of this demonstration, coupled with the ease of use of the room temperature cure adhesive, make this approach a highly attractive alternative to other methods used for core splices in large composite sandwich structures.

Nomenclature

P	=	midspan load (lb)
P_{max}	=	maximum midspan load (lb)
Δ	=	total beam midspan deflection (in.)
d	=	sandwich thickness (in.)
c	=	core thickness (in.)
b	=	sandwich width (in.)
L	=	span length (in.)
τ	=	ultimate core shear strength (psi)

I. Introduction

SANDWICH structures are composite comprised of a lightweight, low strength core (e.g. foam, balsa wood or honeycomb) sandwiched between two thin, stiff outer skins or face sheets (typically made from fiber reinforced

[1] Associate Professor, Department of Mechanical, Industrial, and Manufacturing Engineering, University of Toledo.
[2] Undergraduate Student, Mechanical Engineering, University of Alabama.
[3] Materials Engineer, Materials and Processes Laboratory, NASA-MSFC/EM42

polymer laminates). The face sheets are of high strength and stiffness and are assumed to carry the in plane loads while the core supports the facesheets and resists transverse shear stresses. Because of their high strength-to-weight and stiffness-to-weight ratios, sandwich structures are widely used in the aerospace and automotive industries, where weight is an important factor in the design process. For large sandwich structures it is not always practical or possible that the core be comprised of one continuous panel, rather the core of the sandwich structure is made up of sections of different sizes and shapes that must be joined or spliced together. Commercially available core splice adhesive products (e.g. 3M™ Core Splice Films, FM 410 Core Splice Foam, etc.) are typically foaming adhesives that are designed to expand during curing. These products are widely used throughout the aerospace industry and have been used previous on the CEUS project, including in the manufacture of the Composite Crew Module[1]. One disadvantage of the core-splice adhesives is that they must be cured at elevated temperatures. For large sandwich structures manufacturing time and costs can be reduced by using a one stage curing process, wherein the face sheets and adhesive are co-cured in a single autoclave cycle. The use of core-splice adhesive films requires that either a two stage process be employed (wherein the splice material is cured first, and the adhesive and face sheets is cured after) which drives up the manufacturing cost, or alternately the splice can be cured with the face sheets and adhesive. The disadvantage of this approach is that it does not allow for the inspection of the splice before the top facesheet is placed and cured, thus defects in the splice cannot be corrected. A preferred approach would be to use a material that cures at room temperature for splicing the cores. This would allow the splice to be inspected and any faults identified and corrected before the placement of top adhesive film and face sheet and prior to the single stage curing of the panel in the autoclave. The ability to inspect the splice while maintaining a single stage cure process leads to a more cost effective, quality controlled process. The central objective of this project was thus the development and documentation of a manufacturing process to splice aluminum honeycomb cores using a room temperature cure epoxy adhesive. The process as described in this paper was demonstrated on small panels, but it is anticipated that the same procedure can be successfully scaled up for use on large composite structures.

II. Splice Procedure

The splice procedure is outlined in Figure 1 below. Since the emphasis is on the joining of the aluminum cores, the debulking and autoclave cure stages are not described in detail and should follow the standard approaches recommended for the film adhesive and facesheet materials being used. For all demonstration panels the core material used was HexWeb® CRIII 5052 1 in. thick aluminum honeycomb with a cell size of 1/8 in. and nominal density 3.1 pcf. The film adhesive used was Cytec FM® 300, and a single layer of HexPly® 8552 A280-5H was used for each facesheet. The panels were autoclave cured. All splices were along the ribbon direction of the honeycomb core. The materials, preparation, set up, hardware, and application technique used for the splice are fully described in this section of the paper.

A. Materials, Preparation, and Setup

The material selected for the splice was Hysol® EA 939.6MD, which is a two-part syntactic epoxy adhesive that can be cured at room temperature. The manufacturer's recommendation is that Parts A and B of the uncured adhesive be stored below 40°F, but that they should be close to room temperature (77°F) before mixing. The epoxy parts must therefore be removed from freezer storage and thawed to room temperature before use, and the remainder of the material should be returned to storage after the desired amount is measured. The mix ratio by weight of Part A and Part B is 100:31. For the demonstration splices reported in this paper mixing was done manually, however other methods such as a static mixture could also be used and may be preferable for large structures. Using the procedure outlined in this paper, 131 g of material (100 g Part A and 31 g Part B) was found to be sufficient for a 4 ft. splice of one inch thick cores. The manufacturer of the epoxy adhesive recommends that the adhesive should not be mixed in amounts greater than 450 g since the excessive heat buildup can lead to decomposition of the material. In preparing the demonstration panels it was found that mixing a quantity of 262 g grams led to excessive heat buildup during splicing using the pneumatic gun at 100 psi, resulting in decomposition of the material and the initiation of an accelerated cure, rendering the product unusable. Based on these findings it is recommended that quantities of no greater than 200 g be mixed at any one time when using this core splice procedure.

In preparation for splicing, the core faces to be joined should be cleaned using isopropyl alcohol. Lint and powder free latex gloves should be worn throughout the preparation of the panels and during the splicing process to avoid contamination of the surfaces to be joined. The core parts to be joined are then positioned in contact on the uncured bottom face sheet and film adhesive layer and the assembly debulked under vacuum. The assembly is then placed in a frame or similar supporting tool to hold them in place during splicing. It is recommended that the faces to be joined

be in physical contact when placed in the frame, however a small gap between the panels (i.e. not wider than the nozzle to be used to apply the epoxy) is acceptable. Parts of the tool which are likely to come into contact with the epoxy adhesive during the splicing process should be prepared so as to avoid bonding of the core to the frame. For the demonstration panels, thin plates covered in Teflon tape were placed between the core and the frame at the ends of the splice to facilitate easy removal of the panel after curing.

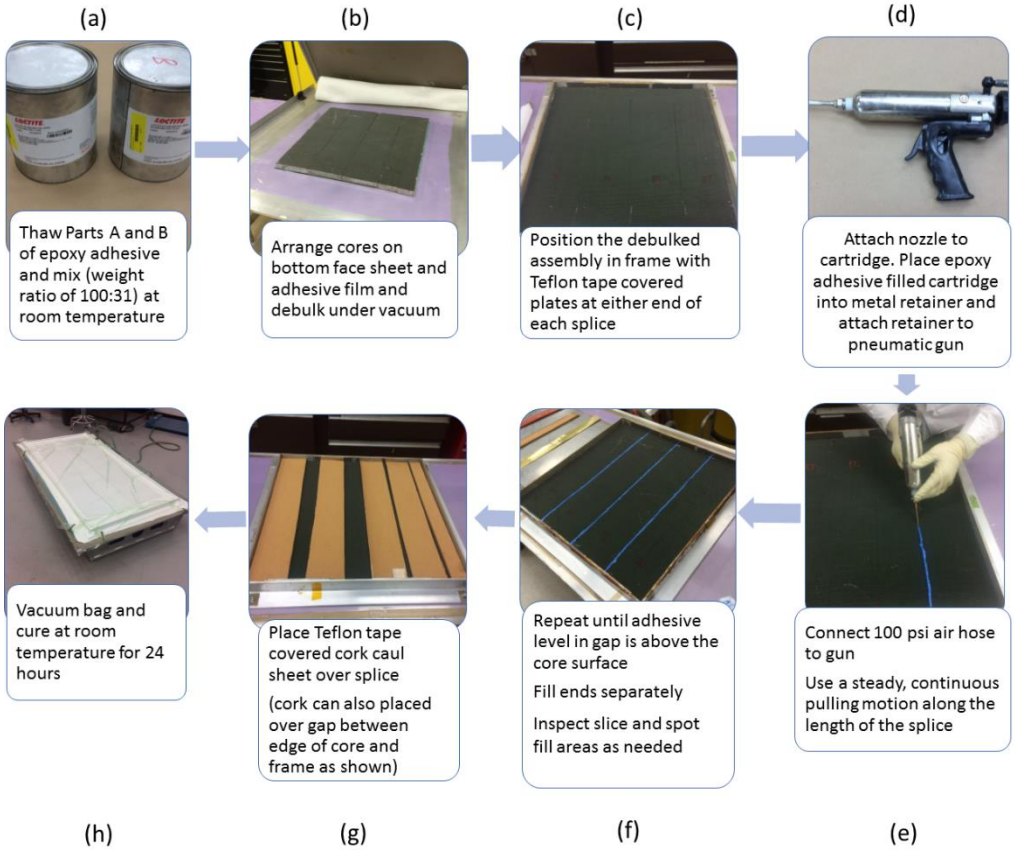

Figure 1. Step by step procedure for joining aluminum honeycomb cores with epoxy adhesive.

B. Hardware and Core Splice Procedure

The adhesive is injected between the aluminum core panels using a pneumatic gun at 100 psi pressure. Nozzle selection was based both on the ease of application and the quality of the splice produced. While it is desirable that the splice width be kept at a minimum, the viscosity of the epoxy adhesive precludes the use of very narrow nozzles (e.g. A and F in Figure 2). It was found that nozzles with a rectangular or oval cross section produced a more uniform splice than circular ones, and that metal nozzles performed better than their plastic counterparts. The nozzles selected for the splices in this paper were copper or stainless steel nozzles with internal dimensions of approximately 0.1" x 0.3" and are shown as nozzles C and D in Figure 2. A metal nozzle of similar cross section shape and dimensions is recommended for the splice procedure reported in this paper.

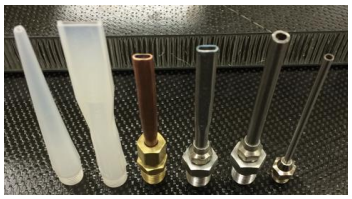

Figure 2. Nozzles considered in down selection process.

To facilitate the injection of the adhesive, prior to attachment to the gun, the nozzle should be placed between the two panels and moved from one end to the next in a continuous motion so as to create a gap between the panels the width of the nozzle. An adhesive filled canister is then installed in the pneumatic gun and the adhesive applied with the technician starting from the far end and pulling the gun towards them in a steady, continuous motion, with special care being taken at the ends of the splice to ensure that the material was distributed will in those locations. This process is to be repeated until the gap is filled to a level slightly above the top surface of the core. Overfilling the gap is necessary to ensure that the surface of the splice will be flush with that of the core after curing. The splice should be

visually inspected to ensure that the adhesive is uniformly applied and any gaps filled as needed. Finally a cork caul sheet with a layer of Teflon tape affixed to it is laid on the splice and the panel vacuum bagged and allowed to cure at room temperature for 24 hours.

For the demonstration panels spliced in this procedure development stage, the cured splices were observed to be of good quality with little or no voids and flush with the surface of the cores after the room temperature cure. To prepare sandwich panels for testing, a film adhesive layer and facesheet was placed on the top surface of each spliced panel and the panels was cured in the autoclave. In the cured panels, the facesheet was found to be smooth with no ridges or valleys in the vicinity of the splices as shown in Figure 3. Note that the blue color of the epoxy is visible in the demonstration panels since only and single layer of prepreg was used as the facesheet. In addition, while the epoxy adhesive attains handling strength after 24 hours, it takes 5 to 7 days to achieve normal performance at room temperature. The adhesive therefore was subject to an accelerated cure in the autoclave.

Figure 3. Cured 2' x 2' spliced demonstration sandwich panel.

III. Mechanical Testing

In order to evaluate the effect of the presence of the splice on the shear strength of the core material, three-point bending tests were performed on beam specimens cut from demonstration panels which were spliced using the procedure described above. Six beams were tested – three having a splice and three with continuous cores (i.e. with no splice). The experiments were conducted in accordance with the standard test method for flexural properties of sandwich constructions, ASTM C 393. A schematic of the test setup is shown in Figure 4. For the specimens with the splice, the splice was located midway between the middle of the span and the support. Metal plates were used as load spreaders at the midspan and the supports as shown in Figure 4 to prevent the local core crushing failure. The beams were tested to failure and the load and deflection data was recorded for each specimen. For the specimens tested, d = 1.03 in., c = 1.00 in., b = 2.1 in., and L = 6 in. For the three beams containing the splice therefore, the splice was located 1.5 in. from the support.

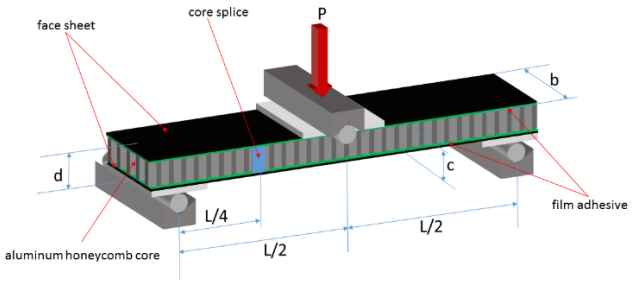

(a)

Figure 4. Schematic of test setup for bending test on sandwich beams.

The shear strength of the core in each case was calculated as follows:

$$\tau = \frac{P_{\max}}{(d+c)b} \tag{1}$$

A. Results and Discussion

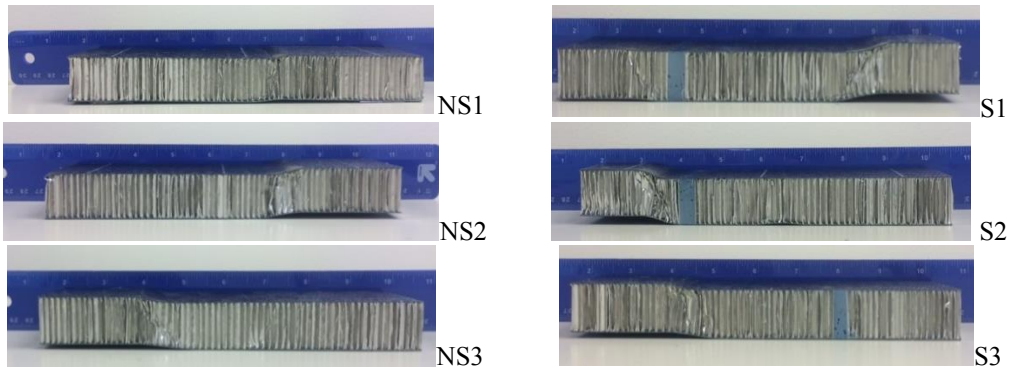

Figure 5. Photographs of the six beam specimens tested after failure showing failure modes.

Examination of the specimens with continuous cores NS1, NS2, and NS3 and those with a splice S1, S2, S3 confirms that the failure mode of all six specimens was shear failure of the core as seen in Figure 5. The location of the failure plane in both S1 and S3 was not located near the splice, and these specimens (S1 and S3) after failure appear similar to the specimens without splices (NS1 – NS3). It appears therefore that for those specimens the presence of the splice had little effect on the shear strength. This is confirmed in both the plot of midspan load P, versus midspan deflection, Δ (Figure 6) and the calculated τ values listed in the inset of Figure 6. The average shear strength of the specimens (excluding S2) was 95.67 psi with a standard deviation of 2.69. This value for shear strength is consistent with the product data sheets for the core which report typical and minimum shear strengths of approximately 120 and 83 pi respectively (after correction for a 1" thick core is applied). Figure 5 indicates that in specimen S2 the shear failure appears to have initiated at the splice, which suggests that the interface of the stiff splice material with the more compliant core material acts as a stress concentrator. This phenomenon where the splice material acts like a stiff inclusion and can potentially lead to a reduction in core strength has been reported in the literature for foam cores with epoxy splices[2]. In our experiments, the shear strength of specimen S2 while greater than the published minimum value for the core, was 14% less than the average value for the other five specimens which suggests that the presence of the splice did in fact lead to a reduction in shear strength in this case. Considering all six specimens, the average shear strength of the three specimens with the splice was 7% less than that of the specimens with continuous cores. It is worth noting that other splice methods are likely cause a reduction in core shear strength as well, and this 7% value should be compared with the experimental results from similar tests on beams spliced by other methods. The level of acceptable reduction in strength due to the presence of a splice would also depend on both the location of the splice and the loading and conditions during application of the full scale structure, however these preliminary results suggest that this method for splicing aluminum honeycomb cores is an efficient and effective alternative to other approaches.

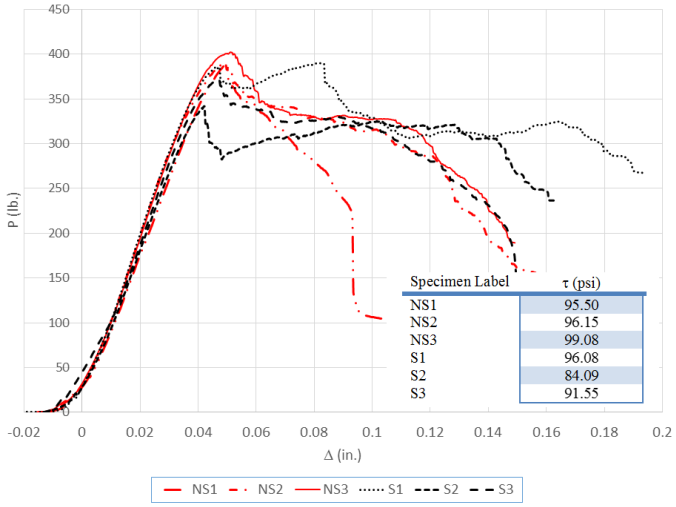

Figure 6. Plot of P vs. Δ. Inset: Core shear strength values.

IV. Conclusion

A procedure for joining aluminum honeycomb cores using a room temperature cure epoxy adhesive was developed and demonstrated. This approach appears to be an attractive alternative to traditional core splicing techniques for large scale composites given the ease of use implementation and the aesthetic quality of the resulting splices. While preliminary testing indicates that there is some reduction in core shear strength at the splice, this is not a problem unique to this method and a more comprehensive study is needed to compare the structural integrity of these splices with those produced using the foaming core-splice adhesive products. The results of such a study, coupled with a study of the manufacturing costs of the different approaches are necessary to evaluate the procedure described and fully compare it with other techniques.

Acknowledgments

L.M. Berhan gratefully acknowledges the support of a NASA Marshall Faculty Fellowship Award.

References

[1]NASA Engineering and Safety Center Technical Assessment Report. Composite Crew Module: Manufacturing, NASA NESC-RP-06-019, 2011.

[2]Goyal, V. K., Rome, J. I., Schubel, P.M., Patel, D. N., and Steckel, G. L., "Predicting and Measuring the Strength Reduction of Sandwich Structures with Spliced Foam Cores," 53rd *AIAA/ASME/ASCE/ASC Structural Dynamics and Materials Conference*, CP849, Vol. 1, AIAA, Honolulu, HI, 2012, AIAA 2012-1773.

Chandra and Hubble Space Telescope detection of a WHIM filament towards PG 1116+215

Massimiliano Bonamente[1]

Department of Physics, University of Alabama in Huntsville, Huntsville, Al

Nomenclature

WHIM = warm-hot intergalactic medium
z = redshift
Chandra = the Chandra X-ray telescope
LETG = Low Energy Transmission Grating
XMM = The X-ray Multi-Mirror telescope
RGS = Reflection Grating Spectrometer
HST = Hubble Space Telescope
CIA = collisional ionization equilibrium
BLA = broad Lyman-α absorption

Abstract

We analyze *Chandra* LETG and *XMM* RGS spectra towards the $z = 0.177$ quasar PG 1116+215, a sightline that is rendered particularly interesting by the *HST* detection of several O VI and H I broad Lyman-α absorption (BLA) lines that may be associated with the Warm–Hot Intergalactic Medium.

We perform a search for resonance Kα absorption lines from O VII and O VIII at the redshift of the detected FUV lines. We detect an absorption line in the *Chandra* spectra that is consistent with O VIII Kα at $z \simeq 0.091$, with a nominal significance of detection of 5.2σ. We have also analyzed the available *XMM* RGS data towards PG 1116+215. Unfortunately, the *XMM* data are not suitable to investigate this line because of instrumental features at the wavelenghts of interest. The absorption line detected by *Chandra* is associated with a BLA of exceptionally large Doppler parameter ($b \simeq 130$ km/s) at $z = 0.0927$, consistent with the redshift of the *Chandra* line within the measurement errors. The combination of H I BLA and the O VIII Kα absorption lines indicates that we may have detected a WHIM filament at high temperature, $\log T(K) \geq 6$, with a total column density of order $\log N_H(\mathrm{cm}^2) \simeq 20$. This detection highlights the importance of BLA absorption lines as possible signposts of high–temperature WHIM filaments.

1. The search for missing baryons at low redshift

The intergalactic medium (IGM) contains the vast majority of the universe's bayons at all redshifts (Shull et al. 2012, and references therein). At high redshift, the bulk of this mass is in the photoionized phase that gives rise to the Lyman-α forest, but at lower redshifts a diffuse warm–hot intergalactic medium (WHIM) at temperatures $10^5 - 10^7$ K is predicted to contain approximately 50% of the baryons in the universe (e.g. Davé et al. 2001; Cen & Ostriker 1999). Absorption–line spectroscopy in the ultraviolet (UV) has proven a successful means for studying the IGM at low redshift, and a number of surveys have used space–based observations to place constraints on the baryonic content of its different phases (e.g., Danforth & Shull 2008; Tripp et al. 2008; Tilton et al. 2012; Shull et al. 2012). Nonetheless, these surveys have detected only a fraction of the expected baryons. The detection of WHIM gas remaining particularly incomplete owing to the difficulty associated with detecting the broad H I lines and highly ionized metal species characteristic of diffuse gas at WHIM temperatures, such as O VII and O VIII lines at soft X–ray energies.

The main challenge with the detection of X–ray absorption lines from the WHIM is the limited resolution and effective area of the current generation X–ray grating spectrometers. To date, there have been only a handful of reported detections of X–ray lines from the WHIM, typically from O VII and O VIII. They include H 2356-309 (Fang et al. 2010), PKS 2155-304 (Fang et al. 2002, 2007; Yao et al. 2009), Mkn 421 (Nicastro et al. 2005; Rasmussen et al. 2007; Yao et al. 2012), Mkn 501 (Ren et al. 2014) and 1ES 1553+113 (Nicastro et al. 2013). Given the limited statistical significance of all X–ray lines detected to date, it is important to investigate additional sightlines, and understand the correlation between UV and X–ray absorption lines.

In this paper we investigate the presence of X–ray absorption lines from the WHIM towards the source PG 1116+215, a quasar at $z = 0.177$. This sightline is quite well studied in the FUV (e.g., Tilton et al. 2012; Danforth et al. 2010; Lehner et al. 2007; Sembach et al. 2004) and it is rendered particularly interesting by the presence of several H I broad Lyman–α absorption (BLA) lines and O VI absorption line systems at $z > 0$ reported by Tilton et al. (2012) from *HST* STIS and COS data. In particular, the BLA at $z = 0.0927$ detected from *HST* data is one of the broadest H I lines in the Tilton et al. (2012) sample ($b = 130$ km/s), and it is indicative of gas at $T \simeq 10^6$ K.

The *Chandra* data analyzed in this paper provides the tentative detection of an O VIII K α absorption line at $z \simeq 0.091$, likely related to an H I BLA detected by Tilton et al. (2012). We have also analyzed several *XMM* observations towards PG 1116+215. Unfortunately, the RGS2 camera has no effective area in the spectral region of interest (20-24 Å), and the RGS1 camera has likewise a sharp drop in its efficiency in correspondence of the O VIII K α absorption line at $z \simeq 0.091$. We therefore cannot use the *XMM* data to address the presence of this absorption line. Throughout this paper we assume a standard ΛCDM cosmology with $h = 0.7$ and $\Omega_\Lambda = 0.7$.

2. The sightline towards PG 1116+215

PG 1116+215 is a quasar at redshift $z = 0.177$. *FUSE* and *HST* FUV data were analyzed by Tilton et al. (2012), who detected several absorption lines from intervening gas towards the source. Among the absorption lines detected in the FUV, we are especially interested in following up those absorption–line systems that have the potential for associated X–ray lines, in particular the two Kα resonant lines from oxygen, O VII ($\lambda = 21.602$ Å) and O VIII (doublet at a center wavelength of $\lambda = 19.969$ Å). The atomic data relevant to this paper are presented in Table 2, where we also list the two intercombination and forbidden O VII lines that are at small wavelength distance from the resonance line of interest. Oxygen is expected to be the most

Table 1: Atomic data from Verner et al. (1996)

Ion	Line Transition	Line type	Name	Wavelength (Å)	X–ray Energy (eV)	Osc. frequency
H I	$1s-2p$	Resonance	Lyman-α	1215.67*	—	0.416
O VI	$1s^2 2s - 1s^2 2p$	Resonance		1037.6,1031.9	—	0.199
O VII	$1s^2 - 1s2p$	Resonance	K-α	21.602	574.02	0.696
	$1s^2 - 1s2p$	Intercomb.	—	21.80	568.74	—
	$1s^2 - 1s2s$	Forbidden	—	22.10	561.02	—
O VIII	$1s-2p$	Resonance	K-α	18.969**	653.66	0.416

$\star$ The H I Lyman-α is a doublet of $\lambda\lambda 1215.6736, 1215.6682$.

$\star\star$ The O VIII K-α is a doublet of $\lambda\lambda 18.9725, 18.9671$.

abundant element at $Z > 2$ in the interstellar medium, and O VII and O VIII are the most abundant oxygen ions in collisional ionization equilibrium at $\log T(K) \geq 6$ (i.e., the high–temperature end of the WHIM range, Mazzotta et al. 1998).

For this purpose, we select two classes of absorption–line systems towards PG 1116+215 among those detected by Tilton et al. (2012): O VI systems that have both lines in the doublet detected, and broad H I Lyman-α absorption lines (BLA) with $b \geq 80$ km/s. O VI systems are traditional signposts for the WHIM, since O VI is the most abundant ion with strong resonance lines in the FUV (e.g. Shull et al. 2012). It is clear that, for a single–temperature WHIM cloud in collisional ionization equilibrium, O VI and O VII will coexist in significant amounts only in a very narrow range of temperatures, and one does not expect virtually any O VIII at temperatures where O VI is present. Nonetheless, it is possible that WHIM clouds are multi–temperature, as speculated by Shull et al. (2003), and therefore O VI is a useful indicator of WHIM at higher temperatures. BLA's are also potential indicators of hot gas, with a thermal broadening of $b \geq 80$ km/s indicating a temperature of $\log T(K) \geq 5.6$. In this temperature range, we may in fact expect to find significant column densities of the O VII and O VIII ions. The FUV absorption lines that meet these criteria are listed in Table 2.

In particular, we note that the $z = 0.0927$ BLA has the highest Doppler b parameter of the entire sample studied by Tilton et al. (2012). For this paper we have re–analyzed the STIS and COS data at the redshift of the $z = 0.0927$ BLA absorption line using the latest version of the pipeline used in the original detection (Tilton et al. 2012). Fitting a single Voigt component to the COS data we obtain $z = 0.0926814$ (with an uncertain by about 20 km/s), $b = 153 \pm 17$ and $\log N_{HI} = 13.26 \pm 0.06$. Fitting a single Voigt component to the STIS/E140M data we measure $z = 0.0927801$ (with an uncertain by about 12 km/s), $b = 126 \pm 14$ and $\log N_{HI} = 13.43 \pm 0.05$. n Tilton et al. (2012) we reported an equivalent width of $W_\lambda = 0.11$ A, which corresponds to an H I column density of $N_{HI} = 2.0 \pm 0.3 \times 10^{13}$ cm^{-2} (or $\log N = 13.30 \pm 0.06$). It is also worth noting that there is a possible contribution from foreground Galactic C I in this line. The STIS data shows a narrow feature that could be CI or could be noise. It is not apparent in the COS data, but that could just be a resolution effect. If we assume that there is a Galactic C I line at the expected position and fit that as a separate component, the STIS fit changes slightly tp $z = 0.0927143$ (uncertain by about 15 km/s), $b = 139 \pm 17$ km/s and $\log N = 13.38 \pm 0.05$. The COS data don't have sufficient resolution to perform a similar experiment there. The re–analysis therefore finds similar results as the original detection by Tilton et al. (2012). In this paper we make use of those values, as listed in Table 2.

The X–ray spectra towards PG 1116+215 have been previously used to search for absorption lines. Fang

et al. (2015) studied $z = 0$ absorption lines from warm–hot gas in the Galaxy, and did not investigate the $z > 0$ systems that arise from the extragalactic WHIM. Yao et al. (2009) focused on selected O VI systems detected with earlier FUV data, including two systems at $z = 0.059$ and $z = 0.1358$ we also investigate in this paper, and Yao et al. (2010) performed a blind search; both papers did not report any positive identification of absorption lines from the extragalactic WHIM towards PG 1116+215. The prior knowledge on the redshift of potential O VII and O VIII systems that we have from the FUV data (Table 2) is essential to search for fain X–ray absorption lines. Given that we only seek to study lines at a known redshift, the statistical significance of detection can be simply defined as the ratio of the line flux K and its 1-σ uncertainty, as discussed for example by Nicastro et al. (2013). In the case of blind searches, i.e., without a prior knowledge on the redshift, one needs to account for the number of redshift trials available for a given transition, leading to a reduction in the significance of detection relative to the case of lines with a redshift prior (Nicastro et al. 2013).

3. Spectral analysis of the Chandra and XMM data

In this paper we analyze the *Chandra* and *XMM* X–ray grating spectra of PG 1116+215. The *Chandra* HRC/LETG data provides a uniform coverage at all wavelengths of possible O VII and O VIII absorption lines of interest to this study. The *XMM* data can be used to study only some of these absorption lines, given a number of instrumental features that make several wavelength intervals of interest unavailable with the RGS spectrometer.

3.1. Analysis of the Chandra data

Chandra observed PG 1116+215 for a total of 88 ks of clean exposure time with the HRC/LETG spectrometer, observation ID was 3145. Data reduction was performed in CIAO 4.7, using the standard processing pipeline (*chandra_repro*) that generates source spectra, background spectra and response files. The +1 and -1 order spectra were kept separate to better address the presence of spectral features in each order spectrum. The spectra were rebinned to a bin size of 0.05 Å that approximately matches the spectral resolution of the instrument.

Spectral analysis was perfomed in XSPEC in the wavelength range 18–26 Å where all relevant O VII and O VIII lines from the systems listed in Table 2 are expected. For completeness, we also investigate $z = 0$ absorption lines from the same ions. At the redshift of $z = 0.1358$, the redshifted O VIII line position coincides with the $z = 0$ O VII line. We therefore set the flux of the redshifted $z = 0.1358$ O VIII line to zero, and let the flux of the $z = 0$ O VII line be free in the fit. The continuum was modelled with a power law model in wich both the normalization and the spectral index was allowed to vary to find the best–fit parameters of the lines and when determining the significance of detection of the lines. Each line was parameterized with a Gaussian model that uses as parameter the total line flux (K, in units of photons s^{-1} cm^{-2}), redshift, line energy and line width (parameter σ_K of the Gaussian, in units of eV; we use this notation to avoid confusion with the value of σ used for the significance of detection).

The redshifts of the lines were fixed at the position of the expected lines using the redshifts shown in Table 2; in the case of the detected $z = 0.0927$ feature, we allowed the redshift to be free in the final analysis to allow for small adjustments around the expected value, as discussed in Section 3.4. Given the limited spectral resolution of the data, we fixed the line width parameter σ_K of all lines to a fiducial value

Table 2: FUV absorption lines from Tilton et al. (2012) investigated in this paper.

Redshift	Line ID	Doppler b (km/s)	W_λ (mÅ)
0.1337	HI Lyman-α (BLA)	81 ± 6	82 ± 6
0.0928	HI Lyman-α (BLA)	133 ± 17	111 ± 14
0.0412	HI Lyman-α (BLA)	89 ± 10	73 ± 9
0.1734	OVI 1032,1038	$47 \pm 7, 24 \pm 13$	$60 \pm 10, 28 \pm 18$
0.1385	OVI 1032,1038	$24 \pm 8, 41$	$65 \pm 8, 43 \pm 10$
0.0593	OVI 1032,1038	$10 \pm 6, 17 \pm 12$	$25 \pm 5, 22 \pm 11$

that corresponds to a width of 100 km/s, or $\sigma_K = 0.2$ eV, which is a characteristic values for the thermal broadening of lines from ions in the temperature range $\log T(K) = 6 - 6.5$. The line width is significantly smaller than the intrinsic resolution of the LETG spectrometer, which is of order 1 eV for the wavelength range of interest. Small changes from the nominal value used of 0.2 eV have therefore negligible effect on the fit results. We address the source of systematic error associated with this assumption in our assessment of the significance of detection of the lines in Section 3.4.

We use the Cash statistic $\mathcal{C}$ as the fit statistic, which is appropriate for a data set of independent Poisson data points that may have bins with a low number of counts. We prefer this over rebinning the spectra, in order to retain a fixed bin width that matches the resolution of the *Chandra* data. The $\mathcal{C}$ statistic is approximately distributed like a χ^2 distribution with $N - m$ degrees of freedom, where N is the number of datapoints and m is the number of (interesting) fit parameters (Bonamente 2013). To determine the 1-σ uncertainty in the flux K of the lines, σ_K, and in the other free parameters we therefore vary each interesting parameter until $\Delta\mathcal{C} = 1$, and use $1/2$ of this range as the 1-σ uncertainty, following the same procedure that applies to Gaussia datasets with χ^2 as the fit statistic. In Section 3.4 we further discuss the effects of fitting the *Chandra* data using a variable bin size with a minimum of 25 counts per bin.

The *Chandra* spectra and the best–fit models are shown in Figure 1. The error bars shown in the spectrum are based on the Geherels approximation of the Poisson errors (Gehrels 1986). The results of our fit are shown in Table 3. The best–fit statistic is $\mathcal{C}_{min} = 338.1$ for 302 degrees of freedom.

3.2. Analysis of the XMM data

XMM observed PG 1116+215 in four separate visits (observations 0201940101, 0554380101, 0554380201 and 0554380301) for a total of 372 ks of clean exposure. Reduction of the data was performed with the *SAS* software, using the *rgsproc* pipeline and the calibration data current as of June 2015. The products of the reduction are ±1 order averaged spectra for each observation and the matching background spectra and response matrices.

Each spectrum was rebinned to a bin size of 0.05Å, approximately matching the RGS resolution in the wavelength range of interest (18-26 Å). The bin size is therefore the same as for the *Chandra* spectra. We followed the same method of analysis of the spectra as for the *Chandra* data. The only difference in the analysis is the fact that several spectral regions corresponding to the lines of Table 2 are unavailable with RGS. Figure 2 shows the *Chandra* HRC/LETG and the *XMM* RGS effective areas. The main instrumental feature is the lack of effective area of RGS2 between 20–24 Å, due to the failure of one of the CCD's in the focal plane of RGS2. RGS1 has also a number of instrumental edges that prevent an accurate determination

Table 3: Results of the fit to the *Chandra* spectra

Line ID	Redshift	Flux K (10^{-6} phot cm^{-2} s^{-1})	K/σ_K
O VII	0.0	-14.5 ± 6.8	-2.1
O VII	0.041	-7.7 ± 7.2	-1.1
O VII	0.059	7.4 ± 8.9	+0.8
O VII	0.0911 ± 0.0004	-11.0 ± 7.5	-1.5
O VII	0.1337	-3.1 ± 8.6	-0.4
O VII	0.1385	39.1 ± 11.1	+3.6
O VII	0.1734	8.4 ± 10.1	+0.8
O VIII	0.0	-8.9 ± 4.6	-1.9
O VIII	0.041	-6.8 ± 6.8	-1.0
O VIII	0.059	-2.5 ± 7.3	-0.3
O VIII	$0.0911 \pm 0.0004^{\star}$	-31.4 ± 6.0	-5.2
O VIII	0.1337	-2.2 ± 8.3	-0.3
O VIII	0.1385	0.0	—
O VIII	0.1734	1.4 ± 8.9	+0.2

* The redshifts of the two $z \simeq 0.091$ lines were linked in the fit.

of those lines that follow near sharp gradients in the effective areas. In particular, the $z \simeq 0.091$ O VIII absorption line detected with *Chandra* near at $\lambda = 20.7$ Å falls at the edge of a sharp intrumental feature of RGS1, and therefore we cannot reliably address the presence of such line using the RGS data.

Results of our RGS spectral analysis are summarized in Table 4, where we have used a dash in correspondence of those lines that cannot be probed because of these instrumental features. The four ± 1 order RGS1 spectra were fit simultaneously to the same model used for the *Chandra* data, and so were the four ± 1 order RGS2 spectra; normalizations of the continua was left free among the observations to allow for an overall flux variation among the different spectra. The goodness of fit was measured using the Cash statistic as $\mathcal{C}_{min} = 619.6$ for 574 degrees of freedom for the RGS1 spectra, and $\mathcal{C}_{min} = 339.7$ for 288 degrees of freedom for the RGS2 spectra.

3.3. Results of the spectral analysis

The strongest feature detected in the *Chandra* data is an absorption line at $\lambda \simeq 20.7 \AA$ that corresponds to a Kα absorption from O VIII at $z \simeq 0.091$. The nominal significance of detection for this line is 5.2 σ, and the feature is clearly visible in each of the ± 1 order *Chandra* grating spectra (Figure 1). As we discussed in Section 3.2, this feature cannot be measured accurately by *XMM*. The redshift of this feature is approximately coincident with that of the H I BLA absorption dentified a priory by Tilton et al. (2012), therefore we need not account for redshift trials for the determination of its significance of detection (e.g. Nicastro et al. 2013). In Section 3.4 we address the robustness of this detection with respect to background variations and other aspects of the data analysis.

The only other spectral feature detected at a significance $\geq 3\sigma$ is an emission line near $\lambda = 24.6$ Å in the *Chandra* data (nominal significance of 3.6σ). This line would correspond to an O VII Kα line from O VII at $z = 0.1385$, the same redshift where Tilton et al. (2012) detected both components of an O VI

Table 4: Results of the fit to the *XMM* spectra. Units are the same as in Table 3. There is no spectral feature detected at a confidence greater than 2σ.

Line ID	Redshift	RGS1		RGS2	
		Flux K	K/σ_K	Flux K	K/σ_K
O VII	0.0	-3.1 ± 2.1	-1.5	—	—
O VII	0.041	-1.0 ± 2.5	-0.4	—	—
O VII	0.059	—	—	—	—
O VII	0.0927	-2.1 ± 2.5	-0.8	—	—
O VII	0.1337	-3.1 ± 3.0	-1.0	—	—
O VII	0.1385	—	—	$-1.0 \pm^{8.6}_{3.3}$	$\pm^{0.3}_{0.1}$
O VII	0.1734	-1.3 ± 3.2	-0.4	-0.9 ± 3.2	-0.3
O VIII	0.0	—	—	-0.3 ± 2.0	-0.2
O VIII	0.041	—	—	-2.0 ± 2.6	-0.8
O VIII	0.059	-0.5 ± 2.1	-0.2	—	—
O VIII	0.0927	—	—	—	—
O VIII	0.1337	0.4 ± 2.7	-0.2	—	—
O VIII	0.1385	0.0	—	—	—
O VIII	0.1734	-2.5 ± 2.7		—	—

doublet (Table 2). The *Chandra* detection, however, is not confirmed by the *XMM* data. RGS2 is the only detector that can accurately probe this line, and the RGS2 does not require the presence of an emission line at that redshift (see Table 4). To address the consistency between the two spectra, we calculated the change in fit statistic in the *XMM* data assuming an emission line of respectively 4,2 or 1×10^{-5} phot cm^{-2} s^{-1} (respectively the best–fit *Chandra* value, and approximately a -2σ and -3σ deviation). The changes in fit statistic are respectively $\Delta\mathcal{C} = +187, +57$ and $+24$, indicating that any additional component to the RGS2 data leads to a significantly worse fit. We conclude that the *Chandra* and *XMM* data provide inconsistent results for this spectral feature. The *Chandra* feature is therefore either a spurious detection due to an unlikely Poisson fluctuation, or a transient feature. Such putative transient emission line would have to be associated with a region of very small size, such that its high density can produce the narrow emission line and have sufficiently low O VII column density as to be unable to produce absorption in the PG 1116+215 spectrum. Given the limited significance of detection and the inconsistency between *Chandra* and *XMM*, additional data at this redshift are needed before providing a conclusive statement as to its origin.

3.4. Statistical analysis of the significance of detection of the putative O VIII Kα $z \simeq 0.091$ absorption line

The putative O VIII Kα absorption line at $z \simeq 0.0911$ is the strongest spectral feature detected in our spectra. To address the robustness of this detection, we performed a set of tests on the data and the method of analysis used to obtain this result. They consist of the following: (1) re–analysis of the data using binned data with a minimum of 25 counts, following a more traditional method of analysis that uses χ^2 as the fit statistic (e.g. Yao et al. 2010; Fang et al. 2015); (2) re–analysis using different background levels, to assess the dependence of the significance of detection on the background; (3) use of different values of the line width parameter σ_K to study its effect of the line detection; and (4) use of a fixed redshift of $z = 0.0927$ for the putative O VIII Kα line.

3.4.1. Fit with spectra rebinned to ≥25 counts

For the analysis with a minimum of 25 counts per bin, we grouped the *Chandra* data with the *grppha* FTOOL, and re–fitted the data in *XSPEC* using χ^2 as the fit statistic. The best–fit statistic was $\chi^2_{min} = 217.1$ for 214 degrees of freedom ($\chi^2_{red} = 1.01$), which corresponds to a null hypothesis probability of 42.7%. The best–fit parameters of the continuum in the 18-26 Å band are $\alpha = 2.74 \pm 0.17$ (power–law index) and $norm = 3.35 \pm 0.32 \times 10^{-3}$ (normalization, in *XSPEC* units), which are indistinguishable from those obtained from the $\mathcal{C}$ fit statistic method ($\alpha = 2.79 \pm 0.16$ and $norm = 3.45 \pm 0.31 \times 10^{-3}$). For the significance of detection of the line, we find a redshift of $z = 0.0898 \pm 0.0014$ and $K = -23.6 \pm 7.0 \times 10^{-6}$, for a significance of detection 3.4 σ.

The difference in the significance of detection between the two methods of analysis can be explained with the differences in the spectral binning. Each of the 0.05 Å width bins contain significantly less than 25 counts, and therefore the two fitting methods ($\mathcal{C}$ fit statistic with fixed bin width and χ^2 statistic with a minimum of 25 counts) are not equivalent. A comparison of the spectral bins used in the two analysis is shown in Figure 5. The effect of rebinning to achieve a minimum of 25 counts is clear, with the bins being significantly wider than in the fixed–width Poisson fit method. Some of the wider bins are an average of region of continuum and regions where the absorption line is, and this limits both the ability to identify the line position (or redshift), and its depth. Even with these limitations, the O VIII line is detected at $\geq 3\sigma$ confidence level. We conclude that the fixed bin–width method of Table 3 provides a more accurate method of measuring the absorption line, while the 25–count bin method is still able to confirm the detection. The lower significance of detection with the latter method is clearly attributed to limitations in the ability to measure the absorption line parameters due to the width of the bins.

3.4.2. Background analysis

We address the effect of the background on the detection of the line by rescaling the nominal background by ±10 %, to account for possible systematics of the HRC detector. We perform this test by increasing and decreasing the background spectra by 10%, and re–fit the data to the same model as described in the previous section. The effect of a background change by ±10 % is negligible: the best–fit $\mathcal{C}$ statistic is virtually unchanged ($\Delta\mathcal{C} \leq 2$ for both cases), the best–fit redshift value remains the same as that in Table 3, and the best–fit normalization becomes $K = -30.6 \pm 6.0 \times 10^{-6}$ (for -10% background level) and $K = -31.9 \pm 6.0 \times 10^{-6}$ (for +10% background level), both negligible changes (≤ 1 %) relative to the nominal background. We conclude that the background has a negligible effect on the significance of detection of the O VIII absorption line.

3.4.3. Effect of the line width parameter σ_K

The significance of detection of the line is likewise insensitive to the parameter σ_K. We changed the fixed value of the width parameter to $\sigma_K = 0.4$ eV and $\sigma_K = 0.1$ eV (corresponding to a change of ±100 % relative to the nominal value of $\sigma_K = 0.2$), and re–fitted the spectra. The best–fit statistic was unaffected ($\Delta\mathcal{C} \leq 1$ for both cases), the best–fit redshift value remains the same as that in Table 3, the best–fit normalization became $K = -31.6 \pm 6.1 \times 10^{-6}$ ($\sigma_K = 0.4$ eV) and $K = -31.3 \pm 6.1 \times 10^{-6}$ ($\sigma_K = 0.1$ eV), both virtually identical to the values of Table 3. We conclude that the *Chandra* data are insensitive to changes in the Doppler b parameter of the line in the range $b = 100 \pm^{100}_{50}$ km s^{-1}, and the significance of detection of the

O VIII absorption line is unaffected.

3.4.4. Use of a fixed redshift of $z = 0.0927$ and systematic error on redshift due to the LETG spectral resolution

The Tilton et al. (2012) BLA absorption line has a measured redshift of $z = 0.0927$, which is confirmed by the re–analysis of the *HST* data presented in Section 2. By fixing the redshift of the *Chandra* absorption line at this value we obtain a line flux of $K = -21.1 \pm 5.8 \times 10^{-6}$ phot cm^{-2} s^{-1}, and a best–fit statistic of $\mathcal{C}_{min} = 348.6$ ($\Delta\mathcal{C} = +8.9$ for one additional d.o.f. relative to the fit with variable redshift). In this case, the absorption line is detected at a confidence level corresponding to 3.7σ, instead of 5.2σ for a variable redshift. In the case of the variable fit presented in Section 3.1, the best–fit redshift was found to be $z = 0.0911 \pm 0.0004$, where the statistical 1σ error bar only accounts for the uncertainties due to Poisson statistics.

As illustrated in Figure 5, the centroid of the redshifted $z = 0.0927$ O VIII line ($\lambda = 20.73\mathring{A}$, green arrow) is well within the wavelength range of the absorption feature, approximately half bin–length from the midpoint of the absorption feature. At a wavelength of 20.73 Å, the adopted bin size of $\Delta\lambda = 0.05\mathring{A}$, which is also the approximate resolution of the *Chandra* LETG detector, corresponds to redshift uncertainty of $\Delta z = 0.0024$. Using this value as an estimate for the systematic error in the determination of the redshift due to resolution of the instrument brings the *HST* value for the BLA in accord with the best–fit value of the Kα absorption line. We conclude that the redshift of the two absorption lines are consistent when systematic errors due to the limited resolution of *Chandra* are accounted.

4. Interpretation

In this section we discuss possible interpretations for the absorption line at $\lambda = 20.7$ Å, tentatively identified as Kα from O VIII at $z \simeq 0.091$. The spectral fits of Table 3 can be used to calculate the equivalent width and the column density of the line. The flux of PG 1116+215 at the wavelength of the line is measured as $F_\lambda = 4 \times 10^{-4}$ photons cm^{-2} s^{-1} Å in the *Chandra* observation, and the equivalent with W_λ (measured in Å) is obtained from the relationship $W_\lambda F_\lambda = K$, where K is the total line flux from Table 3. From this relationship, which assumes a Gaussian profile for the line, we obtain $W_\lambda = 0.079 \pm 0.015$ Å.

For an optically thin absorber, the rest–frame equivalent width W_λ and the column density N (in cm^{-2}) are related by

$$N = 1.13 \times 10^{20} \frac{W_\lambda}{\lambda^2 f} \text{ cm}^{-2} \quad (1)$$

where $f = 0.416$ is the oscillator strength of the O VIII Kα line and $\lambda = 18.97\mathring{A}$ is the rest–frame wavelength (e.g. Morton 2003). We therefore obtain a column density of $N_{OVIII} = 6.0 \pm 1.1 \times 10^{16}$ cm^{-2}.

It is in principle possible that both the H I BLA and the O VIII Kα lines originate from the same isothermal medium. In this simple scenario, the relationship between the column densities N_{HI} and N_{OVIII}, the temperature of the WHIM and the chemical abundance A (relative to Solar) is provided by

$$\frac{N_{HI}}{f_{HI}} = \frac{N_{OVIII}}{f_{OVIII}} \frac{1}{A \cdot n_O/n_H} = N_H \quad (2)$$

where f_{HI} and f_{OVIII} are the temperature–dependent ion fractions, which can be calculated assuming

CIE, n_O/n_H is the relative number density of oxygen and hydrogen ($\log n_O/n_H = -3.17$, e.g. Grevesse & Sauval 1998). The equation also lets us estimate the total hydrogen column density N_H. It is not possible to estimate simultaneously, from the available data, the unknown chemical abundance A of the gas and its temperature. If we assume a temperature near the peak of the O VIII ionization curve in CIE, i.e., $\log T(K) = 6.4$ (Mazzotta et al. 1998), we can then calculate the ionization fractions of H I and O VIII, to obtain $f_{HI} \simeq 10^{-7}$ and $f_{OVIII} = 0.45$ (Gnat & Sternberg 2007). Notice that at this temperature there are only trace amount of neutral hydrogen in CIE, with the last datapoint in the Gnat & Sternberg (2007) tables for f_{HI} corresponding to a temperature of approximately $\log T(K) = 6.3$; our estimate should therefore be scaled downward somewhat. With these values, we estimate a value of $\log A \simeq 0.07 \pm 0.14$, consistent with a range of chemical abundances near the Solar value. In this case, the total hydrogen column density would be $N_H \simeq 2 \times 10^{20}$ cm^{-2}.

This calculation should only be regarded as an order–of–magnitude check of a simple scenario to test whether H I and O VIII may coexist in thermal equilibrium. There are reasons to suspect that the real physical state of the absorbing plasma at $z \sim 0.091$ towards PG 1116+215 is more complicated. For example, the Doppler b parameter of the H I BLA corresponds to a thermal broadening for a plasma at $\log T(K) = 6.0$ or so, i.e., somewhat off the peak of the O VIII ionization curve. At that temperature and in CIE, O VII is the dominant ion, although O VIII can still be found in significant amounts. If we use the Doppler b parameter of the BLA as a temperature indicator, we would expect a stronger O VII absorption line than that from O VIII. Our analysis of the *Chandra* and *XMM* data (Tables 3 and 4) do not detect significant absorption from O VII at that redshift, only a 1.5σ absorption line from *Chandra* and $< 1\sigma$ feature from *XMM*. It is clear that, before investigating any further the physical state of the WHIM towards PG 1116+215, we need a confirmation of the putative O VIII Kα absorption line reported in this paper, and better constraints on any O VII at the same redshift. Should both O VII and O VIII lines be present, the temperature would be easily calculated without any assumptions on the overall chemical abundance of the plasma.

An alternative origin for the O VIII and the FUV lines is from the halo of an intervening galaxy. Tripp et al. (1998) find that there are three galaxies along the sightline towards PG 1116+215 in the redshift range $z = 0.091 - 0.093$. All galaxies, however, lie at a projected distance of > 1 Mpc. It is therefore unlikely that there is a significant amount of gas associated with any of these galaxies at such a large projected distance. A more in–depth analysis of the sightline towards PG 1116+215 will be provided in a separate paper, including identification of all possible filaments towards PG 1116+215 from the analysis of galaxy redshift data.

5. Conclusions

In this paper we have analyzed the *Chandra* and *XMM* X–ray grating spectra towards PG 1116+215, a quasar at $z = 0.177$ with several intervening FUV absorption lines detected in the *HST* data (Tilton et al. 2012) that may be related to the WHIM. We use the redshift of the FUV detections as priors for the search of O VII and O VIII Kα lines. This method of analysis ensures that any detection has a statistical significance that simply corresponds to the ratio of the equivalent width of the line and its $1 - \sigma$ error (Nicastro et al. 2013).

The strongest feature we detect is an absorption line at $\lambda \simeq 20.7$ Å in the *Chandra* spectra that we tentatively identify as a Kα resonance line from O VIII at $z \simeq 0.091$. This absorption line has a nominal statistical significance of 5.2σ, and corresponds (within the uncertainties of the *Chandra* redshift measurements) to a very broad H I Lyman-α (BLA) absorption line at $z = 0.0927$ present in the *HST* STIS

and COS data. We have investigated several sources of possible systematic uncertainties in the measurement of this line, and concluded that they do not affect significantly the detection. The parameters of the two lines (Doppler broadening for the BLA and the two column densities N_{OVIII} and N_{HI}) are in principle consistent with a scenario in which both lines originate from plasma in CIE at $\log T(K) \sim 6.3$, although it is likely that the absorbing plasma is in a multi–temperature phase. We therefore conclude that we have detected a WHIM system towards PG 1116+215 at $z \simeq 0.091 - 0.093$ that features H I BLA and O VIII Kα absorption.

The limited significance of detection of this putative O VIII absorption line requires a confirmation with independent data before its presence and physical state of the absorbing plasma can be established unambiguously. Unfortunately, the available *XMM* data towards PG 1116+215 cannot be used effectively to address the presence of this O VIII absorption line, since at the wavelengths of this line RGS2 has no effective area, and RGS1 has a significant drop in its efficiency due to an instrumental feature. The most effective means for a confirmation of this line would be additional *Chandra* data, which can also further address the presence of O VII at the same redshift.

The detection of this putative O VIII Kα absorption line in the *Chandra* spectra of PG 1116+215 underscore the importance of H I BLA absorption lines as signposts of the elusive high–temperature WHIM plasma (e.g. Danforth et al. 2011; Prause et al. 2007). If this line is confirmed, the detected H I column density of order $\log N_{HI} \sim 13$ would correspond to a total hydrogen column density of order $\log N_H \sim 20$, thanks to the temperature constraints provided by the X-ray data. The combination of BLA's and X–ray data for large samples has therefore the potential to identify large reservoirs of warm–hot baryons, and possibly close the missing–baryons gap (Shull et al. 2012).

REFERENCES

Bonamente M., 2013, Statistics and Analysis of Scientific Data. Springer, Graduate Texts in Physics

Cen R., Ostriker J. P., 1999, ApJ, 514, 1

Danforth C. W., Keeney B. A., Stocke J. T., Shull J. M., Yao Y., 2010, ApJ, 720, 976

Danforth C. W., Shull J. M., 2008, ApJ, 679, 194

Danforth C. W., Stocke J. T., Keeney B. A., Penton S. V., Shull J. M., Yao Y., Green J. C., 2011, ApJ, 743, 18

Davé R. et al., 2001, ApJ, 552, 473

Fang T., Buote D., Bullock J., Ma R., 2015, ApJS, 217, 21

Fang T., Buote D. A., Humphrey P. J., Canizares C. R., Zappacosta L., Maiolino R., Tagliaferri G., Gastaldello F., 2010, ApJ, 714, 1715

Fang T., Canizares C. R., Yao Y., 2007, ApJ, 670, 992

Fang T., Marshall H. L., Lee J. C., Davis D. S., Canizares C. R., 2002, ApJ, 572, L127

Gehrels N., 1986, ApJ, 303, 336

Gnat O., Sternberg A., 2007, ApJS, 168, 213

Grevesse N., Sauval A. J., 1998, Space Sci. Rev., 85, 161

Lehner N., Savage B. D., Richter P., Sembach K. R., Tripp T. M., Wakker B. P., 2007, ApJ, 658, 680

Mazzotta P., Mazzitelli G., Colafrancesco S., Vittorio N., 1998, A&AS, 133, 403

Morton D. C., 2003, ApJS, 149, 205

Nicastro F. et al., 2013, ApJ, 769, 90

Nicastro F. et al., 2005, ApJ, 629, 700

Prause N., Reimers D., Fechner C., Janknecht E., 2007, A&A, 470, 67

Rasmussen A. P., Kahn S. M., Paerels F., Herder J. W. d., Kaastra J., de Vries C., 2007, ApJ, 656, 129

Ren B., Fang T., Buote D. A., 2014, ApJ, 782, L6

Sembach K. R., Tripp T. M., Savage B. D., Richter P., 2004, ApJS, 155, 351

Shull J. M., Smith B. D., Danforth C. W., 2012, ApJ, 759, 23

Shull J. M., Tumlinson J., Giroux M. L., 2003, ApJ, 594, L107

Tilton E. M., Danforth C. W., Shull J. M., Ross T. L., 2012, ApJ, 759, 112

Tripp T. M., Lu L., Savage B. D., 1998, ApJ, 508, 200

Tripp T. M., Sembach K. R., Bowen D. V., Savage B. D., Jenkins E. B., Lehner N., Richter P., 2008, ApJS, 177, 39

Verner D. A., Verner E. M., Ferland G. J., 1996, Atomic Data and Nuclear Data Tables, 64, 1

Yao Y., Shull J. M., Wang Q. D., Cash W., 2012, ApJ, 746, 166

Yao Y., Tripp T. M., Wang Q. D., Danforth C. W., Canizares C. R., Shull J. M., Marshall H. L., Song L., 2009, ApJ, 697, 1784

Yao Y., Wang Q. D., Penton S. V., Tripp T. M., Shull J. M., Stocke J. T., 2010, ApJ, 716, 1514

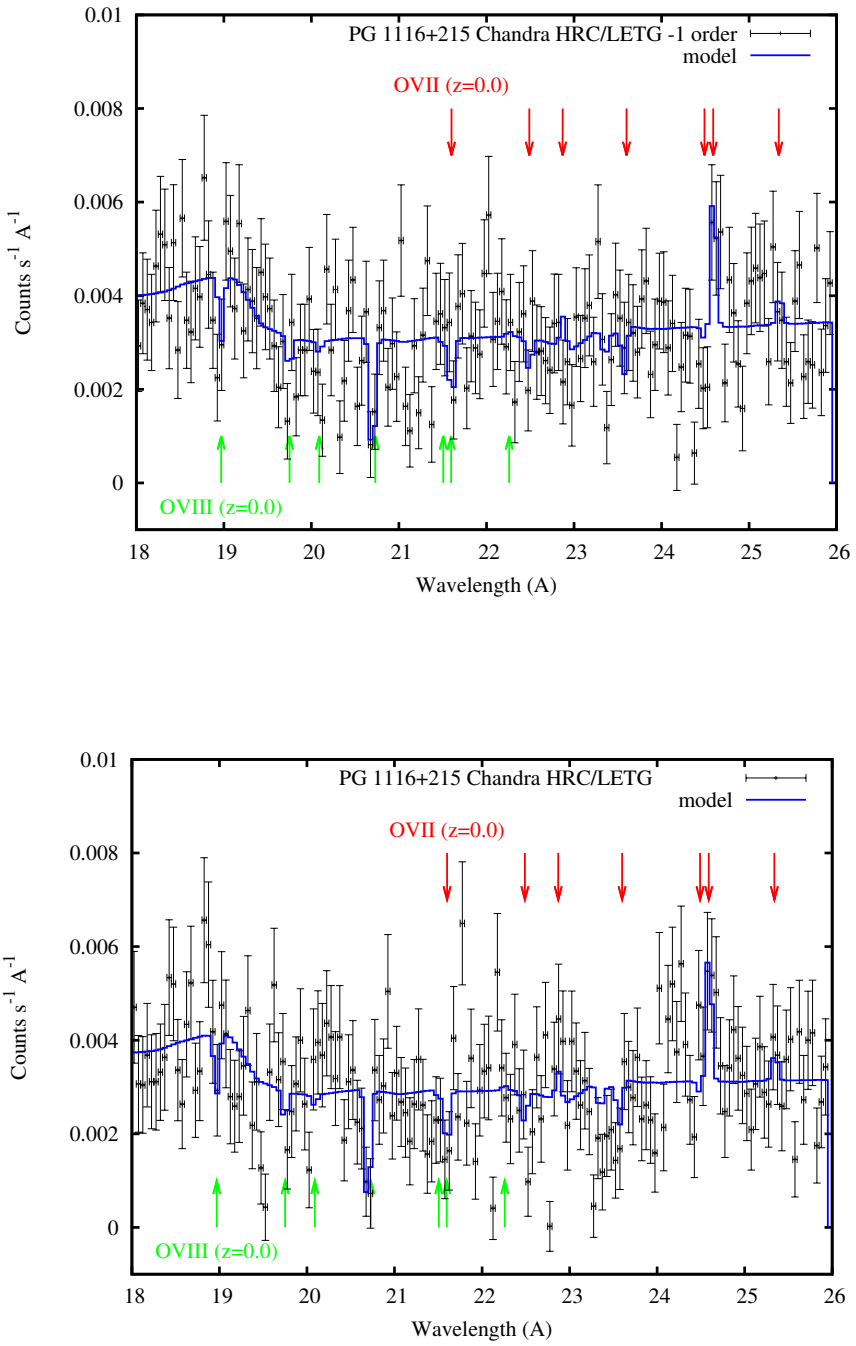

Fig. 1.— LETG spectrum of PG 1116+215. The spectra were binned to a 0.05 Å resolution, and the error bars correspond to the Poisson errors accoding to the Gehrels (1986) approximation. Several datapoints in both spectra correspond to a small number of counts ($\leq$ 10), where the Gaussian approximation of the Poisson distribution would not be accurate. Arrows mark the expected positions of the two O VII and O VIII Kα lines respectively at redshift 0, 0.041,0.059,0.0927,0.1337 and 0.1385.

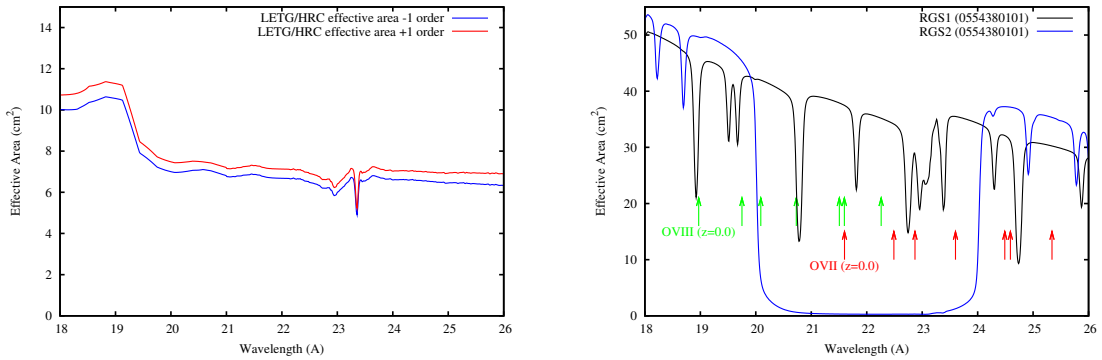

Fig. 2.— Effective areas of the HRC/LETG instrument (left, ±1 order shown separately) and of the RGS1 and RGS2 instruments (right, ±1 order averaged for each instrument). Several instrumental edges and the lack of effective area between 20-24 Å for RGS2 limit the use of the *XMM* data for this study of PG 1116+215. Arrows mark the expected positions of the two O VII and O VIII Kα lines respectively at redshift 0, 0.041,0.059,0.0927,0.1337 and 0.1385.

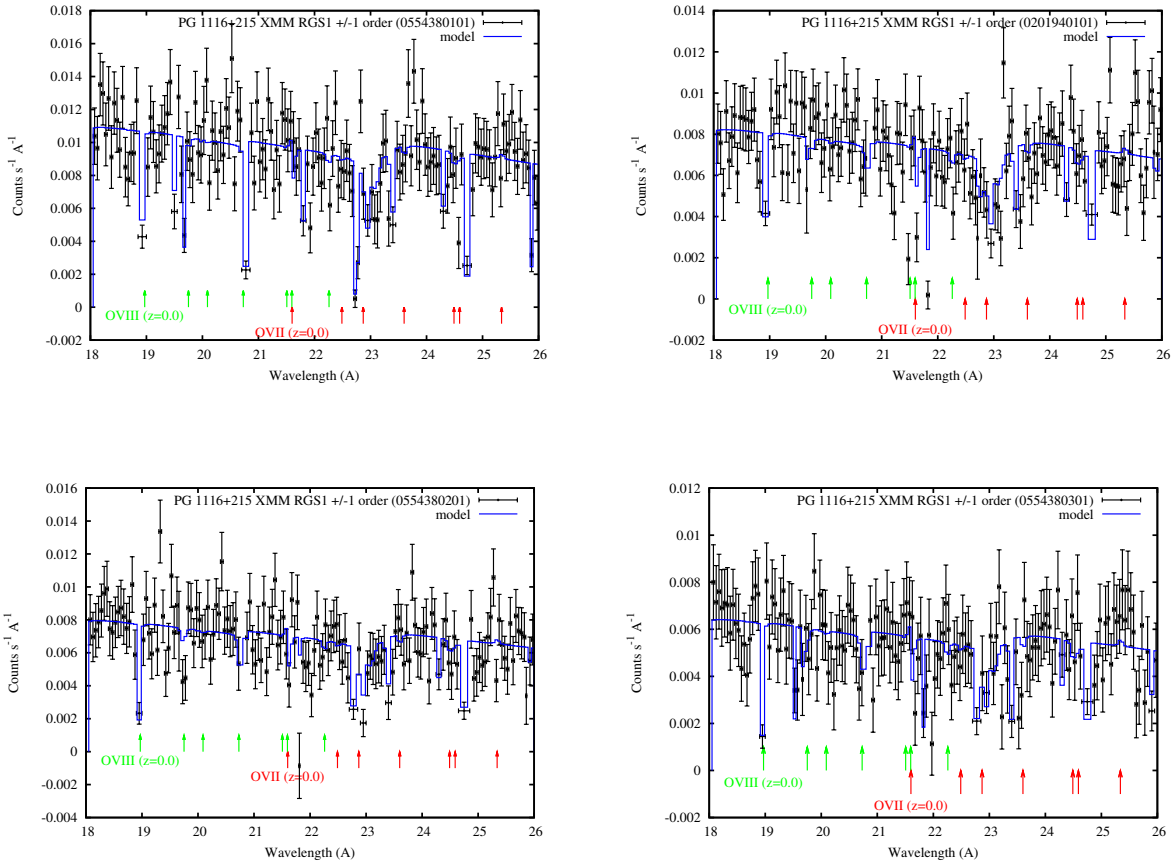

Fig. 3.— RGS1 spectra of PG 1116+215. The spectra were binned to a 0.05 Å resolution, same as for the *Chandra* LETG spectra. All apparent features in these spectra are due to instrumental effects, as illustrated by the effective area curves of Figure 2. Arrows mark the expected positions of the two O VII and O VIII Kα lines respectively at redshift 0, 0.041,0.059,0.0927,0.1337 and 0.1385.

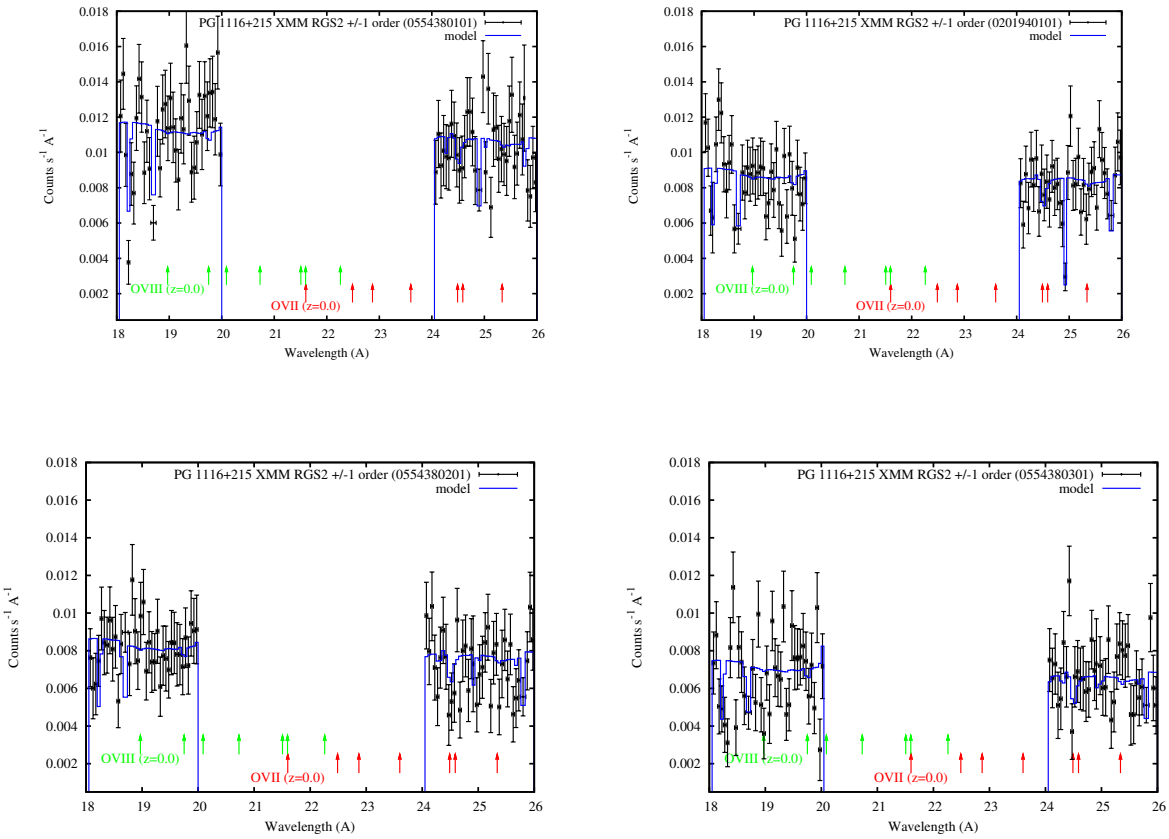

Fig. 4.— RGS2 spectra of PG 1116+215. As in the case of the RGS1 spectra, all apparent features are instrumental. Notice the broad gap in the data between 20-24 Å, due to failure of RGS2 CCD4. Arrows mark the expected positions of the two O VII and O VIII Kα lines respectively at redshift 0, 0.041,0.059,0.0927,0.1337 and 0.1385.

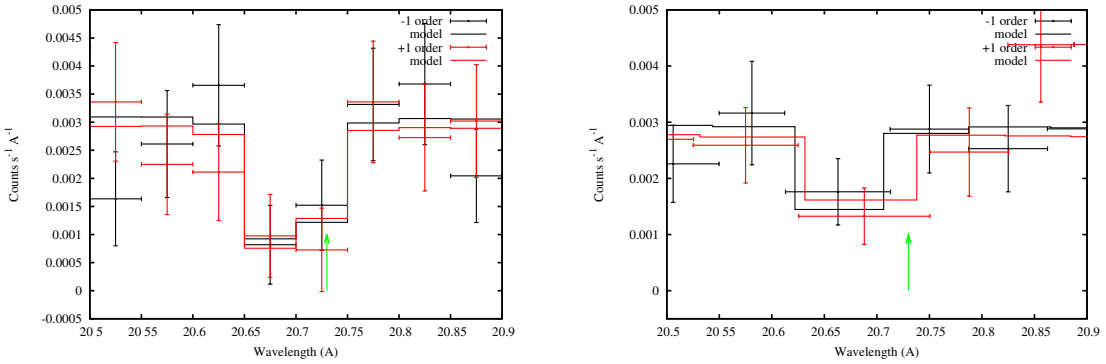

Fig. 5.— Left: Zoom–in of Figure 1 in the region of interest for the $z \simeq 0.091$ O VIII spectral region. Right: Same spectral region as in the top panel, using the same *Chandra* spectra except for a re–binning to have at least 25 total counts per bin (before background subtraction). Green arrows mark the position of the $z = 0.0927$ O VIII Kα line.

Classification and observation of interpersonal space needs for close proximity team activities.

Anthony O. Carton[1]
South Dakota State University, Brookings, SD, 57006

Hugh C. Dischinger
NASA Marshall Space Flight Center, Huntsville, AL 35812

Teamwork and social cohesion are important factors for the success of long-duration missions. Though these factors are well accepted and understood from the perspectives of cognitive and organizational psychology, there has been less work attending to the physical human factors of team activity and the spatial needs of close proximity team activity. Through an analysis of astronaut work procedures and interview of payload operations personnel, seven classifications of team activity have been identified. To identify preliminary spatial characteristics, participants performed a generic close proximity team activity during a pilot observational study.

Nomenclature

BHP = Behavioral Health and Performance
ISS = International Space Station
NHV = Net Habitable Volume
MELFI = Minus Eighty-Degree Laboratory Freezer for ISS

I. Introduction

Teamwork and social cohesion are important factors for mission success during long-duration space exploration and are emphasized during training. However, equipment design requirements do not address close proximity work and payload procedures are not often written for team activity. When combined with the strain on interpersonal relationships due to communication delays these factors have the potential to increase failure risk on future missions. Therefore, a need to facilitate social interaction through team activity that potentially outweighs productivity losses commonly associated with teamwork may exist. This report provides initial taxonomic classification of team tasks based on interviews with payload operations personnel and content analysis of procedural documents. In addressing the first research question, "what do astronauts do together on the International Space Station (ISS)?" current evidence suggests that team activities can be divided into seven (7) activity types: *Leak Pinpoint and Repair*, *Large Object Relocation and Manipulation*, *Quality Control and Documentation*, *System Assembly and Installation*, *Stowage*, *Spotting*, and *Medical Tasks.* This report also provides observational data from characterization/pilot research of the spatial requirements of close-proximity team activity. Preliminarily, evidence of acceptable operational envelop overlap is emergent.

[1] Assistant Professor, School of Design, South Dakota State University.

II. Background

The importance of teamwork is recognized and well represented in the training of astronauts.[1] Anecdotally, it has been suggested that one benefit of T38 flight training is teamwork, ensuring team bonding. Training to enhance team performance and cohesion are addressed through requirements for teamwork skills, techniques for coping with interpersonal stressors, communication, multicultural teamwork and conflict resolution. In their review of evidence for the Risk of Performance Errors due to Poor Team Cohesion and Performance, Inadequate Selection/Team Composition, Inadequate Training, and Poor Psychosocial Adaptation, Behavioral Health and Performance (BHP) element members Schmidt, Keeton, Slack, Leveton and Shea note that the evidence of training effectiveness from space flight studies is limited and comprised of opinion and anecdote, but see general support in ground studies.[2] They outline several issues that are overcome through team training such as interpersonal, emotional and group-interaction support,[3] interactive techniques[4] and interpersonal training to enhance cohesion and performance.

Social cohesion is one of several factors that contribute to the success of long duration missions in space exploration. As missions continue to grow in duration, astronauts will encounter strained interpersonal relationships due to both time delays in communication with loved ones and monotony of social interaction due to the small crew size. As we extend the scope of space exploration to include Mars, the element of time may introduce a need to assign team activity to address social cohesion that outweighs the loss of overall performance often associated with team activity, i.e. overall performance being better than the average performance of any member but not better than the best performer.[5, 6] The BHP element also identify breakdowns of social cohesion as being a potential issue during long-duration missions even when space flight crews have been screened for personality or mood disorders and cite evidence that these breakdowns can cost crews accuracy, efficiency and coordination.[7, 8, 9]

Evidenced by the lack of standards for equipment, systems and procedures[1, 10] for close proximity use by crew teams, habitat equipment is not currently designed for teamwork. Design requirements also do not address close proximity work. Even though the advantages of teamwork during both training and crew missions are acknowledged and accepted, analysis of procedures on ISS reveal a surprising few tasks in which two crew work in close proximity on a coordinated activity. While team activity is discussed in the context of crew coordination and collaboration, physical objects and environments are designed to anthropometric requirements and there are currently no anthropometric requirements for close-proximity tasks.

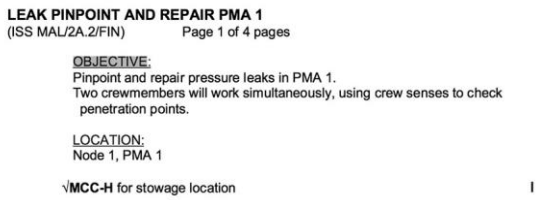

LEAK PINPOINT AND REPAIR PMA 1
(ISS MAL/2A.2/FIN) Page 1 of 4 pages

OBJECTIVE:
Pinpoint and repair pressure leaks in PMA 1.
Two crewmembers will work simultaneously, using crew senses to check penetration points.

LOCATION:
Node 1, PMA 1

√**MCC-H** for stowage location

Figure 1. Crew specification example: "Objective".

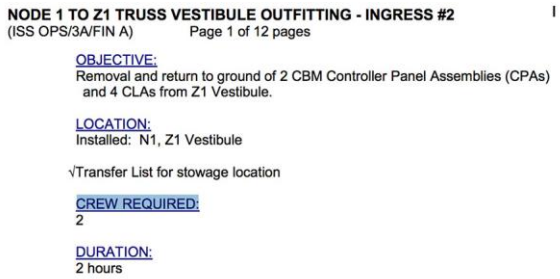

NODE 1 TO Z1 TRUSS VESTIBULE OUTFITTING - INGRESS #2
(ISS OPS/3A/FIN A) Page 1 of 12 pages

OBJECTIVE:
Removal and return to ground of 2 CBM Controller Panel Assemblies (CPAs) and 4 CLAs from Z1 Vestibule.

LOCATION:
Installed: N1, Z1 Vestibule

√Transfer List for stowage location

CREW REQUIRED:
2

DURATION:
2 hours

Figure 2. Crew specification example: "Crew Required".

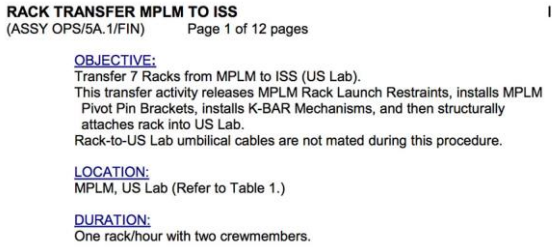

RACK TRANSFER MPLM TO ISS
(ASSY OPS/5A.1/FIN) Page 1 of 12 pages

OBJECTIVE:
Transfer 7 Racks from MPLM to ISS (US Lab).
This transfer activity releases MPLM Rack Launch Restraints, installs MPLM Pivot Pin Brackets, installs K-BAR Mechanisms, and then structurally attaches rack into US Lab.
Rack-to-US Lab umbilical cables are not mated during this procedure.

LOCATION:
MPLM, US Lab (Refer to Table 1.)

DURATION:
One rack/hour with two crewmembers.

Figure 3. Crew specification example: "Duration".

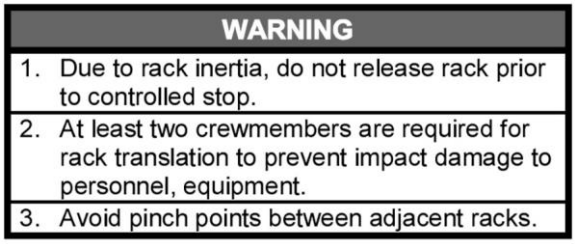

WARNING
1. Due to rack inertia, do not release rack prior to controlled stop.
2. At least two crewmembers are required for rack translation to prevent impact damage to personnel, equipment.
3. Avoid pinch points between adjacent racks.

Figure 4. Crew specification example: "Warning".

By failing to understand the interpersonal space requirements of these close proximity tasks, systems are not designed for team use in an environment where space is highly leveraged and at a premium. The ultimate goal of this research is to develop standards and requirements for proposal and adoption by NASA. In light of this aim, two research questions are currently proposed. First, what are the team activities taking place on ISS currently? Finding out what team tasks exist will help researchers identify crucial aspects and variables of team work. Classification and identification of tasks allow for the prioritization of work and the ability to identify team tasks for analysis and characterization. Second, pilot observation of generic team tasks allows for the identification of variables that influence the way people structure interpersonal space when engaged in team activity. A need to characterize the volumes necessary for close proximity activity exists. A practical application of this observation is the development of guidelines for evaluation of NHV.

Image 1. Mission specialist Sandra Magnus and Expedition 5 Science Officer Peggy Whitson are photographed in the International Space Station (ISS) Node 1/Unity module working with the Interim Resistive Exercise Device (IRED) and Hand crank Assembly - Fore.
NASA Image: S112E05165

Image 2. Participants A & B completing generic close proximity team activity.

III. Method

A. Content Analysis of Procedures

To identify close proximity team activity, 14 procedural collections with a total of 378 procedures were surveyed. Procedures in this context are defined as a procedural entry consisting of multiple discrete tasks or steps with a defined objective section. Identification of team activities proceeded through systematic search of each document for the keywords *crew, crewmember,* and *crew required*. As crew specification is located in any of the following sections: *Objective, Crew Required, Duration,* or *Warning,* see fig. 1, 2, 3, and 4; each document was searched for these headings and then surveyed for crew requirements, see table 1.

Procedural Document	Date	Team Tasks	Total Tasks
ISS Operations Checklist, ISS-2A.2A & 2A.2B	8/15/2000	0	9
ISS Ground Handbook Specific ISS-2A.2B	6/9/2000	0	3
ISS Malfunction Checklist ISS-2A.2A & 2A.2B	8/17/2000	4	17
ISS/Shuttle Joint Operations Book, ISS-3A	9/20/2000	0	0
ISS Assembly Operations Book ISS-3A	9/21/2000	0	0
ISS Malfunction Checklist ISS-3A	9/20/2000	5	52
ISS Operations Checklist ISS-3A	9/19/2000	2	25
ISS Assembly Operations Book ISS-4A	11/14/2000	0	7
ISS/Shuttle Joint Operations Book ISS-4A	11/10/2000	0	4
ISS In-Flight Maintenance Book ISS-4A	11/20/2000	6	54
ISS Assembly Operations Book ISS-5A	8/16/2000	2	32
ISS Assembly Operations Book ISS-5A1	8/24/2000	3	33
ISS/Shuttle Joint Operations Book	6/28/2005	0	39
ISS EVA Systems Checklist	8/15/2000	5	103
Total		**27**	**378**

Table 1. Procedures documents.

B. Interviews of payloads operations personnel

In addition to the content analysis of ISS procedures, personnel from EO20, Payload Operations were interviewed and asked if they could think of any tasks or types of tasks that would require the assignment of multiple crew to accomplish. From these interviews, 19 tasks or relevant activities were identified and assigned to seven (7) categories, confirming one (1) from the content analysis, see table 2.

C. Observation of generic team activity

Eight (n=8) participants from a convenience sample of NASA civil servants, contractors and interns were asked to perform a generic close proximity team task during observation and intermittent motion capture. The generic task observed was the assembly of a *LEGO® Technic Compact Tracked Loader* children's construction toy. The toy was selected based on the number of pieces (252) and online reviews of the time it would take to complete (~45 minutes) as well as the similarity to the types of tasks an astronaut might complete, i.e. manipulation of multiple components, assembly or repair of a small system etc., see images 1 and 2. Finally, LEGO® instructions are a close generic analog to the payload procedures that astronauts use to complete tasks on ISS.

Each participant pair was given an informed consent document that included this brief description of the purpose of the study:

> The purpose of the study is to investigate the spatial aspects and postures associated with team activities. Basically, I'm interested in how people use space when they are doing something with someone else. I've asked you to come here and complete a simple, and hopefully fun task.

Participants were notified of their voluntary participant status, audio and video recording, still photography and intermittent motion capture. Each participant then donned a skintight suit with motion capture markers, see image 5. Participants were handed the printed instruction booklet as well as a bag containing all of the parts needed to complete the model and were then asked to walk to the testing area with the only requirement that they both stand on the same side of the counter. They were not given any instructions as to arrangement or placement of objects in the testing area.

The testing area is comprised of a standing height work surface with an array of light pointers aimed at spatial markers on the table, positioned laterally at 3" increments. A camcorder is mounted above the table to record participant hand position in conjunction with the light pointers throughout the task, see images 3 and 4. During the second, third, and fourth sessions, a motion capture system is also used to record and calculate three dimensional positions of participants, see image 5.

Image 3. Camcorder field of view.

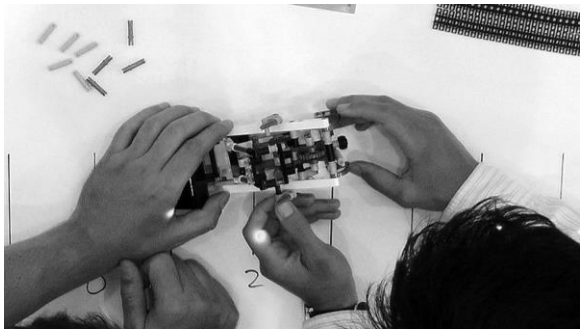

Image 4. Light markers to aid hand position recognition.

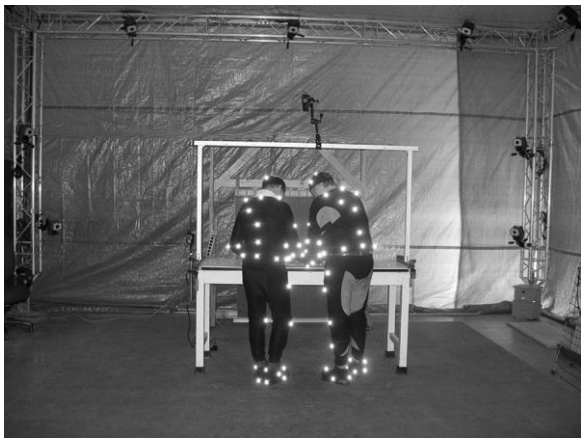

Image 5. Participants C & D in motion capture environment.

IV. Results

A. Team Activity Classes

A total of seven (7) team activity classes are identified through analysis of International Space Station procedural documents and through interviews with payload operations personnel, see table 2. These classes are: *Leak Pinpoint and Repair, Large Object Relocation and Manipulation, Quality Control and documentation, System Assembly and Installation, Stowage, Spotting,* and *Medical Tasks.*

The survey of 378 in-flight assembly procedures reveals two classes of team activity on ISS. Procedures, as noted in the method section, are defined as step-by-step task sets with specified objectives. In the set of 378 tasks, 27 tasks required two or more crewmembers to complete as specified in one of the following areas: objective, duration, crew required, or special warnings. Of these 27 tasks, 14 are involved in the rapid identification and repair of leaks and are categorized as *Leak Pinpoint and Repair*, and the remaining 13 are involved in the coordinated relocation and manipulation of large objects and are categorized as *Large Object Relocation and Manipulation*.

Five additional activity classes were identified and one class from the survey of procedures was verified through interviews with six payload operations personnel. These activity classes were either proposed by personnel who could think of examples of the tasks, such as VEGGIE-HW ASSMB-INST being an example of *System Assembly and Installation*, or speculated as being something they had managed in the past but could think of no examples. The activity that one interviewee gives as an example of team stowage is the cold stowage transfer between MELFI and Glacier/Polar requiring two crew members, see image 8, however this team activity requirement could not be verified by examination of MELFI procedures at this time. A logical next step is the planned verification of these activity types

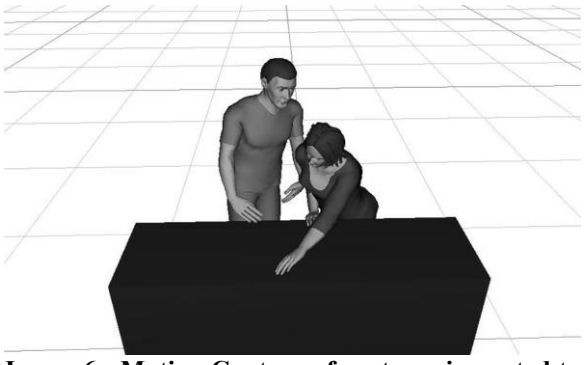

Image 6. Motion Capture of postures imported to JACK of Participants E & F.

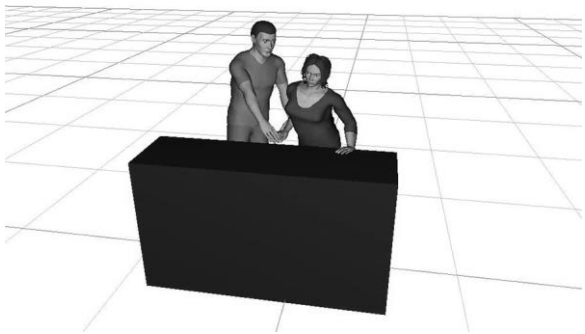

Image 7. Motion Capture of postures imported to JACK of Participants E & F.

Class	Source	Collocation	Coordination
Leak Pinpoint and Repair	ISS Procedures	No	Yes
Large Object Relocation and Manipulation	ISS Procedures & Payload Ops Interviews	Yes	Yes
Quality Control and Documentation	Payload Ops Interviews	Yes	Yes
System Assembly and Installation	Payload Ops Interviews	Yes	Yes
Stowage	Payload Ops Interviews	Yes	Yes
Spotting	Payload Ops Interviews	No	Yes
Medical Tasks	Payload Ops Interviews	Yes	No

Table 2. Team Activity Classes.
*** In some instances, there are plausible scenarios in which the answer could be no.**

with a representative sampling of International Space Station timeline logs.

B. Observation of generic close proximity team activity

Four participant pairs completed a generic task similar to what we would see during a *System Assembly and Installation* task. The overhead camcorder has been effective in capturing approximately one hour of video per each participant pair. One interesting finding so far is that participants seem to stay in close proximity even when performing individual subtasks. The array of light pointers has also aided in determining hand position during tasks. Future variables of interest are foot position, team envelop, net habitable volume, and acceptable range of reach envelope overlap.

Two-person motion capture, done for the first time at MSFC, is also yielding usable postures that we have imported to JACK for analysis. The number of participants is too small to yield a distribution of NHV, but this is a future goal. See images 6 and 7. Once specific task are identified, evaluation of NHV can proceed.

V. Discussion

A. Activity Classes

The result of the survey of procedures documents and interviews with payload operations personnel, these classes represent team activity currently taking place on ISS. As a result, the only evidence of some classes is anecdotal, for instance, though there are examples of *Quality Control and Documentation* tasks, verification with either task timelines or procedures is still required. In another example, payload ops personnel recommended the Minus Eighty-Degree Laboratory Freezer for ISS (MELFI) *Stowage* task as being a team task and imagery of team use is available, see image 8, however examination of MELFI procedures has not confirmed team use. Next steps include identification of team tasks through examination of ISS timeline logs, and request of identified task procedures.

1. Leak Pinpoint and Repair

Leak pinpoint and repair were the most common team activities found in the procedures surveyed from 2000 during the assembly of ISS. These tasks are characterized by rapid search and repair of leaks by pairs of crew for leak. Typically, procedures stipulate that crew members go to opposite ends of the module, and search back towards the center, assisting each other once a leak is found. These tasks are not collocated as a result of this search.

2. Large Object Relocation and Manipulation

Large object relocation and manipulation is a close second for most common team activity found in procedures surveyed from ISS assembly. These tasks were also verified by interviews with payload operations personnel. Though weightless, large objects such as racks are cumbersome and require two or more crew members to move. These tasks are collocated, but require little coordination beyond spatial orientation, direction and body position. In 2002, Boeing conducting a thorough study of rack translation, incorporating JACK simulation of body position to verify adequate clearance from both rack and crew, making recommendations for hand hold position and mechanical aids.[11]

3. Quality Control and Documentation

Interviews with payload operations personnel provide evidence for *Quality Control and Documentation* activities. These activities could not be verified through survey of task procedures. Activities are characterized by tasks in which a second crew member is available to visually confirm correct placement, installation or connection, or to capture historical documentation, although these tasks do not seem to require close proximity. Payload Ops examples include the MICRO-8 experiments and Rodent Research as well as the historic photography session for Capillary Beverage. Task procedures are not available at this time.

4. *System Assembly and Installation*

Interviews with payload operations personnel provide evidence for *System Assembly and Installation* tasks. Though not verified through the initial survey of procedures, a procedure for system assembly of the VEGGIE, Vegetable Production System has been located. Examination of 1.001 Veggie Hardware Assembly, Installation and Checkout procedure shows that "two people are required to perform steps 1.4 - 1.13" as specified in the Note under Assembly Hardware and Installation in Express Rack. Activities are characterized by coordinated assembly of hardware in close proximity. These activities would likely present appropriate opportunities for ground study of close proximity team activity, and a better understanding of net habitable volume.

5. *Stowage*

Interviews with payload operations personnel provide evidence for *Stowage* tasks, citing MELFI as an example. This class has not been verified through initial survey of procedures. Procedures 1.001 through 2.611 for MELFI do not specify a requirement for two crew to accomplish. Several images do exist of two person teams loading or unloading MELFI, so further investigation is necessary, see image 8.

Image 8. Team Stowage Task. *NASA astronauts Tracy Caldwell Dyson (right) and Shannon Walker, both Expedition 24 flight engineers, prepare to insert biological samples in a dewar tray in the Minus Eighty Laboratory Freezer for ISS (MELFI-1) in the Kibo laboratory of the International Space Station.*
NASA Image: ISS024-E-007352

6. *Spotting*

Interviews with payload operations personnel provide evidence for *Spotting* tasks, citing Rodent Research as an example task. This has not currently been verified as a team task. Additionally, operation of the robot arms is understood to require a second crew member to communicate visual position of the arm to the operator, though this also has not been confirmed through procedures, interviews with payloads or timelines as of yet.

Image 9. Team Medical Task. *Astronaut Satoshi Furukawa prepares for an in-flight echocardiogram for the Integrated Cardiovascular experiment using the Ultrasound 2.*
NASA Image: ISS028E036079

7. *Medical Tasks*

Interviews with payload operations personnel provide evidence for *Medical Tasks*, citing ultrasounds and lower body negative pressure experiments as examples. Again, though images of two person medical tasks are readily available, verification through procedure surveys and requests was not successful.

Though two crew are required for the completion of many medical tasks, one of the crew is often the subject of the task. Comparing images of close proximity team activity such as *Large Object Relocation and Manipulation* or *System Assembly and Installation*, see image 7, to those of medical tasks requiring two people, see image 9, we can quickly see a difference in the interaction of operational envelopes and reach requirements that may have an impact on NHV or other variables related to the interpersonal space requirements for team activity. It would be difficult to characterize medical tasks as being coordinated, as the subject may not actually need to complete any tasks. Further characterization is required.

VI. Conclusion

Classification of team activity currently taking place on ISS is an important first step towards characterizing the interpersonal space needs of astronaut teams during long-duration missions. By identifying tasks taking place, we can begin to analyze and measure team tasks. One conclusion to emerge during this investigation is this, where are the team tasks? It is possible that team activity could facilitate social interaction that offsets the loss of productivity associated with teamwork.[5, 6] A practical application of this understanding would be design requirements for systems and equipment that require team operation based on comprehensive understanding of these tasks. Future verification

of the activity classes and a taxonomy could be developed with attention to orthogonally and span of classes as well as precision and usability of the system of classification overall. A preliminary literature points to evidence documenting the benefit of team activity on social cohesion, a next logical research question might address how these types of close proximity team activities contribute to the maintenance of social cohesion, and in what cases does the detriment to performance override the benefit for social cohesion. In addition, full scale ground studies of generic team activity and simulated ISS team activity will build the case for design guidelines and standards addressing the net habitable volumes associated with close proximity team activity.

Acknowledgments

This work is supported by the Faculty Fellowship program at NASA Marshall Space Flight Center. The author would like to thank Frank Six, Rachael Damiani, and Gerald Karr for organizing and administering the program. A thank you is also in order for my collaborator, Charles Dischinger, and an enormous debt is owed to the entire EV74 team, especially to Vicky Garcia for her assistance with the use of the virtual environments lab.

References

[1]NASA. (2010). *Human Integration Design Handbook (HIDH)* (NASA Handbook No. NASA/SP-2010-3407).

[2]McPhee, J. C., & Charles, J. B. (2009). *Human Health and Performance Risks of Space Exploration Missions*. Houston, TX: National Aeronautics and Space Administration, Johnson Space Center.

[3]Nicholas, J. (1989). Interpersonal and group-behavior skills training for crews on space station. *Aviation, Space, Environmental Medicine*, *60*(6), 603–608.

[4] National Research Council. (1998). *Space studies board annual report 1998.* Washington, D.C.

[5] Hare, A. P. (1992). *Groups, teams, and social interaction: theories and applications*. New York, NY: Praeger.

[6] Hill, G. W. (1982). Group versus individual performance: are N + 1 heads better than one? *Psychological Bulletin*, *91*, 517–539.

[7]Hackman, R. (1996). *Team performance in aeronautical and space environments.* (No. NASA-CR-200947). Moffett Field, CA: NASA Ames Research Center.

[8]NASA. (1987). *Effects of confinement, social isolation, and diurnal disruption of crew adjustment and performance in long duration space missions.* (No. NASA order T-1082-K: NASA/JSC-CR-188280). Houston, TX: NASA Johnson Space Center.

[9]Vinograd, S. (1974). *Studies of social group dynamics under isolated conditions. Objective summary of the literature as it relates to potential problems of long duration space flight.* (No. NASA/JSC-CR-2496). Houston, TX: NASA Johnson Space Center.

[10]NASA. (2015). *NASA Space Flight Human-System Standard Volume 2: Human Factors, Habitability, and Environmental Health* (NASA Technical Standard).

[11]Boeing. (1999). *Rack Translation Task.*

Weather Modification Via Earth Orbital Constellation

Victoria Coverstone[1]
University of Illinois, Urbana, IL, 61801

Charles Johnson[2]
NASA Marshall Space Flight Center, Huntsville, AL, 35816

An array of rotating sunshades based on emerging solar sail technology will be deployed in a novel Earth orbit to provide near-continuous partial shading of the Earth, reducing the heat input to the atmosphere by blocking a small percentage of the incoming sunlight, and mitigating local weather effects of anticipated climate change over the next century. The technology will provide local cooling relief during extreme heat events (and heating relief during extreme cold events) thereby saving human lives, agriculture, livestock, water and energy needs. A synthesis of the solar sail design, the sails' operational modes, and the selected orbit combine to provide local weather modification.

Nomenclature

A_s	=	Sun's apparent area
A_{sh}	=	area of individual shade, km^2
B	=	percentage of blocked solar energy globally
CO_2	=	carbon dioxide
GE	=	geo-engineering
K	=	non-dimensional distance from earth $=x/R_e$
L_1	=	Sun-Earth libration point $1.5x10^6$ km away from Earth
R_e	=	Earth's average radius = 6378 km
SRM	=	Solar Radiation Management
b	=	percentage of blocked solar energy locally
$ppmv$	=	parts per million by volume
x	=	distance between sub-solar point and shade centroid

I. Introduction

Global climate change is a hotly debated topic amongst the American public but many leading scientists believe that the data substantiates the claims that weather patterns are changing. Several National Academy of Science studies correlate global temperature change with the build-up of greenhouse gases, carbon dioxide (CO_2) in particular, in the atmosphere.[1-3] The Earth's principal greenhouse gases are water vapor, CO_2, nitrous oxide, methane, ozone and chlorofluorocarbons. These greenhouse gases are responsible for regulating the Earth's average temperature by absorbing and emitting radiation within the thermal infrared spectrum. One key difference between these various gases is their lifetime in the Earth's atmosphere. Reference 1 claims that the climate change resulting from increases in CO_2 is essentially irreversible for 1,000 years after the emissions cease.

Figure 1 shows the predicted CO_2 emission and associated global temperature increase.[1] Climate system responses are taken from Ref. 1 and assume a ramp of CO_2 emissions at a rate of 2%/year to peak CO_2 values of 450, 550, 650, 750, 850, and 1200 ppmv, followed by zero emissions. The rate of global fossil fuel CO_2 emission grew at ≈1%/year from 1980 to 2000 and >3%/year in the period from 2000 to 2005.[1] Warming over land is expected to be larger than the global averaged values. Also shown is the sea level rise (meters) from thermal expansion only (not including loss of glaciers, ice caps, or ice sheets).

Attempts to regulate the human production of greenhouse gases have been proposed but country participation is optional.[4] With CO_2 emissions continuing to increase and no uniform global policy being enforced, deliberate human actions to mitigate the warming of the planet have been considered. One class of solutions that have been proposed is geo-engineering (GE). Geo-engineering is the application of technologically-based approaches that result in changes to planet properties. Although some oppose GE on the basis that these types of solutions take the

[1] Professor, Aerospace Engineering Department, AIAA fellow.
[2] Insert Job Title, Department Name, Address/Mail Stop, and Center for second author.

pressure off changing the underlying problem of the world's overdependence on fossil fuels for energy production, GE solutions should not be dismissed without consideration.

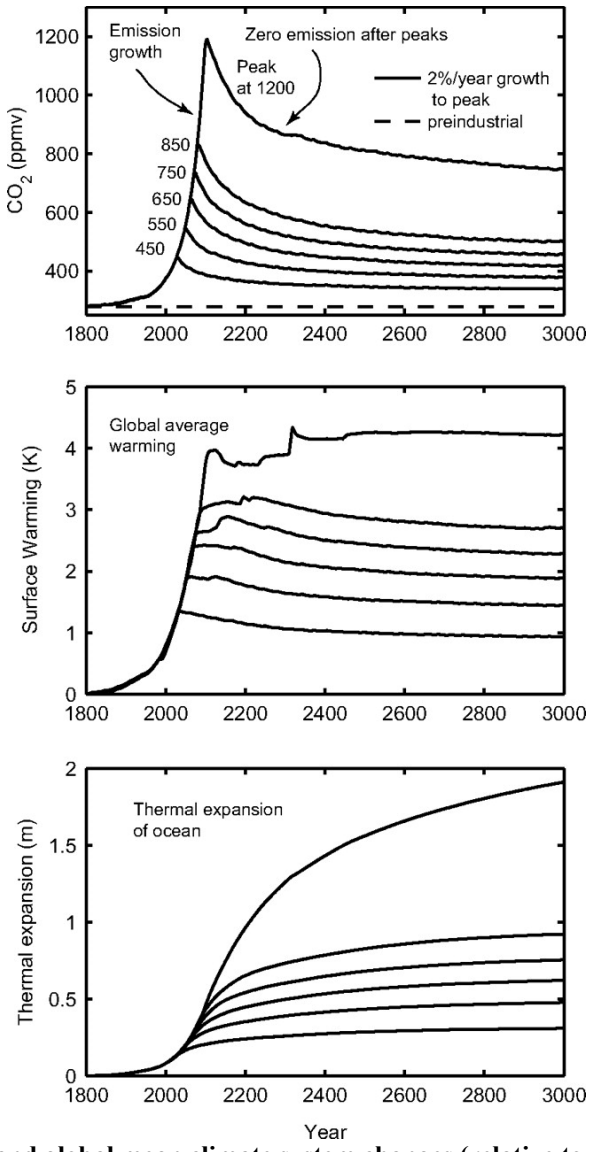

Figure 1. Carbon dioxide and global mean climate system changes (relative to preindustrial conditions in 1765.) [1]

II. Solar Radiation Management of the Earth

Two main themes exist in GE research. The first is CO_2 removal and typically involves the seeding of clouds with chemicals that react with CO_2. The seeding can cause irreversible side-effects and damage (acid rain.) The second GE approach to climate change is to influence the energy balance equation of the Earth by reducing the amount of incoming solar radiation (SRM) and is the approach used here. SRM tactics use solar sunshades or parasols in space to redirect a portion of the incoming sunlight.

Reference 5 provides conceptual design on a sun shade near the Sun-Earth L_1 point that provides global shading. The solution presented requires a 700,000 km^2 reflective surface levitated in a non-Keplerian orbit with a radial distance inside the L_1 Sun-Earth location. The purpose of the shade is dual. Firstly, a reduction in the solar radiation by 3.4 W/m^2 is desired in an attempt to lower the Earth's average temperature. Secondly, the reflective

shade would produce power to beam to Earth. This GE solution does address two very important issues but requires an enormous financial investment. The physical location and energy beaming requirements placed on the design increase launch costs and risk. A simpler GE solution is to design an earth-orbiting flotilla of shades with a single goal of solar radiation management.

Simulations indicate that geoengineering methods could markedly diminish regional and seasonal climate change from increased atmospheric CO_2, despite differences in radiative forcing patterns.[6] Based on numerical modeling, the reduction of 4.17 W/m^2 of incident solar radiation would compensate the effect of a CO_2 doubling.[6]

Various earth orbiting SRM GE systems are presented with the objective to move the shade closer than the L_1 location thereby reducing costs and risks.

III. Global Shading Coverage

To predict the shade patterns cast upon the Earth, the physical dimensions of the sun must be modelled. An opaque body blocking light from a finite emitter produces three distinct regions- umbra, penumbra and antumbra. Figure 2 depicts these regions. The umbra is the darkest part of a shadow where the light source is completely blocked by the occluding body. The penumbra is the region in which only a portion of the light source is covered by the occluding body. The antumbra is the zone where the occluding body appears entirely contained within the sun's image.

The Earth's orbit about the sun defines the ecliptic plane. For global shading, it is optimal to locate the sunshade also in the ecliptic so that its shade with respect to the Earth is consistent. At a given moment, a horizontal axis along the Sun-Earth line can be defined. This axis is rotating about the sun with a period of one Earth year. The location of the shade with respect to this axis determines the shadow conditions on the Earth. In the GE solution proposed in Ref. 5, the height of the shade about the ecliptic is negligible (100s of Km) with respect to the sun's radius (7x10^5 Km) and the distance the shade is from the sun (1.49x10^8 Km) and the entire global is shadowed in antumbra and the shade would appear as a dot on the sun, similar to an interior planet during transit.

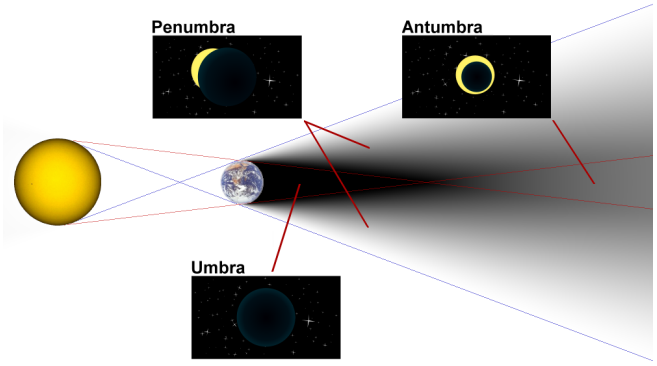

Figure 2: Umbra, Penumbra and Antumbra Definitions[7]

If the shadow cone originates on the Sun-Earth line approximately 1.43 million kilometers from the Earth, it will grow to one earth radii when it intersects the Earth. As the shade is moved farther away from the Earth, the shadow cone encompasses space outside of the earth's radius and the shade is lost. As the shade moves closer to the Earth, the shade cone does not encompass the globe. In addition, this distance is within the Earth's gravity well and will not remain on the Sun-Earth line without constant radial acceleration. The magnitude of the required acceleration at 11 Earth radii is 0.08 m/s^2 in a radial direction away from the Earth. Several current technologies were investigated. Electrodynamic tethers can provide acceleration away from the Earth but are most efficient closer to the Earth's surface. The required acceleration mandated excessive amounts of current and tether lengths. Solar Electric Thruster could also provide the acceleration but the propellant usage limited any useful mission lifetimes.

IV. Localized Shading Coverage

A shade located within 1.43 million kilometers from the Earth will provide sub-global, regional shading. The shade's size and location depends on the desired percentage of blocked local energy, b and realized global blocked energy B. Consider the moon and a total solar eclipse as a natural inspiration. In a total solar eclipse, the disk of the

Sun is fully obscured by the Moon and b=1 but B<1. If the Moon were in a perfectly circular orbit, a little closer to the Earth, and orbited the Earth in the ecliptic plane, then there would be a total solar eclipse each orbit or once a month. However, the Moon's orbit is inclined at more than 5 degrees to the ecliptic, so the shadow cast when passing through the Sun-Earth plane usually misses the Earth.

To develop a relationship between the B and the shade area A_{sh}, the distance between the sun's subsolar point and the shade centroid must be defined using the variable x. To block b of sun's area, as the shade is brought closer to the earth the shade area decreases as x^2. The antumbra shade on the earth is equal to A_{sh} surrounding the subsolar point resulting in Eq (1) where $B < b \leq 1$.

$$x = 224R_e * \sqrt{\frac{B}{b}} \tag{1}$$

For B=0.25 (3.4 W/m^2) and b=1 (total local blocking), x=11.18 R_e. Shade area is 320,000 km^2 which is less than the L1 solution but due to orbital mechanics, the shade will move away from the ideal position. Therefore, a constellation of satellites are required to maintain constant shading on the Earth.

V. Ring-World Regional Shade

An artist's rendering of a ring of shades that circles the Earth is shown in Figure 3. The ring-world concept will constantly maintain a shade on the Earth and Sun line. To size the shade area, the sun's image will be modeled as a circle as shown in Figure 4. Define the sun's area, A_S, and the rectangular area of the shade A_{sh} as seen by an observer on Earth assuming that the shield is always on the sun and earth line. To satisfy this assumption, orbital maintenance is required and is performed by the shade. If the shade is stationary with respect to the sun, a small reduction in the total irradiance of the sun by b W/m^2 can be represented by Eq. (2).

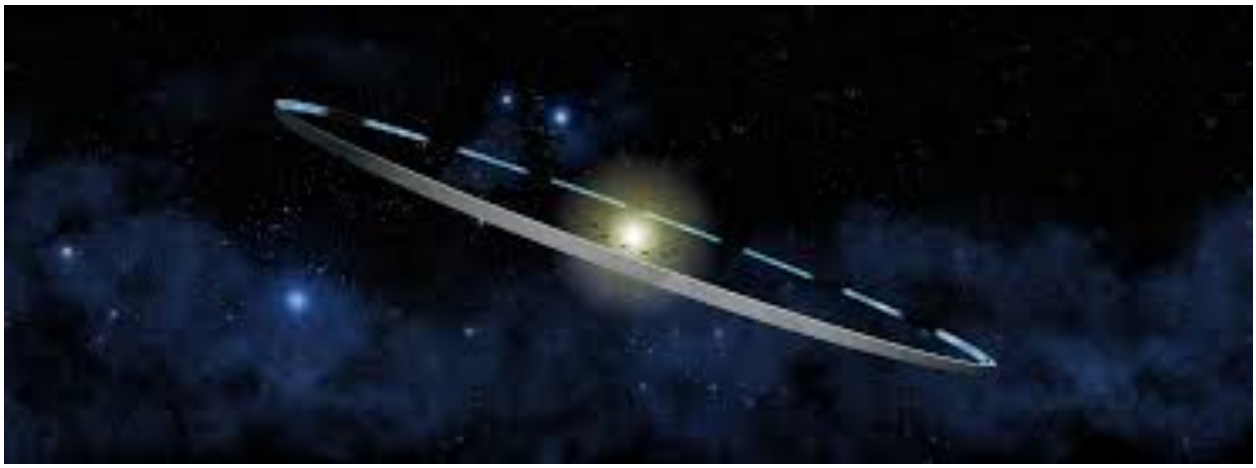

Figure 3. A ring of sun shades.

$$\frac{A_{SH}}{A_S} = b \tag{2}$$

The average solar irradiance of the sun is 1367 W/m^2. The sun's radius appears to fill a local radius of 0.276 degrees of the sky leading to the apparent area in degrees of $A_S=\pi(0.276^o)^2$
To cover the sun, the rectangular area of the shade is given as;

$$A_{SH}=4* R_s * \Delta z_{SH}^{\ o} = b*A_S=b\pi R_s^{\ 2} \tag{3}$$

Substituting values yields an angle in degrees.

$$\Delta z_{SH}^{\ o} = 0.2*b \tag{4}$$

In radians,

$$\Delta z_{SH}^{\ rad}=b*3.5*10^{-4} \tag{5}$$

The shade's height above the ecliptic plane in kilometers depends on the distance from the observer on Earth. In kilometers the shade height is then

$$\Delta z_{SH}^{km} = x * \Delta z_{SH}^{rad} \quad (6)$$

Next, define a non-dimensional variable K.

$$K = x/R_{earth} \quad (7)$$

For a sun shield to always be in between the sun and earth, a flotilla of discrete shades must form a ring in the ecliptic plane. This protective fleet of shades will be rotating faster or slower than the earth depending on the value of K. To form a ring around the earth, the required total number of shades is given by the integer round-off of 360/0.523 = 688. Therefore the total area of the ring,

$$A_r = 688 * A_{sh} \quad (8)$$

R_s^{km} is the sun's apparent radius to the observer in kilometers.

$$A_{sh} = 2.6x10^3 bK^2 \quad (9)$$

Substituting equation (9) into equation (9) yields an expression for the total area of the ring.

$$A_r = 1.8x10^6 * b * K^2 \ km^2 \quad (10)$$

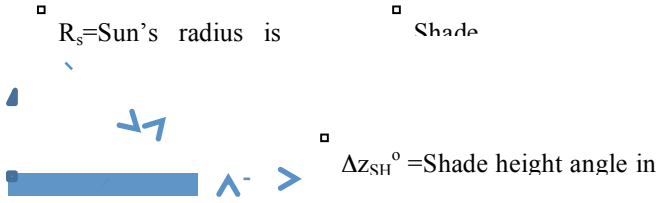

Figure 4: Simplified Geometry of Sun and Shade.

VI. Elliptical Orbit Regional Shades

Elliptic orbits were investigated as candidates for the regional shades. A unique orbit that provides consistent daily shading of the Earth's surface was discovered. The orbital characteristics include a 24-hour period with 16 hours in sunlight. The orbit is retrograde with perigee at local mid-night provides at substantial hang-time around the Sun-Earth line. Sixteen shades provide 24-hours shading of the sub-solar point. Figure 5 captures constellation. In this figure the sun is located along the apogee line.

The slowly rotating sail is used to distribute the shade about the ecliptic plane. The reflecting sails provide thrust to maintain the proper orbital alignment. Each individual shade is sized via Eq. (9). For equivalent regional shading b, the required sail area is an order of magnitude less than that of the orbital ring presented above.

VII. In-Space Mean Solar Irradiance Measurements

A typical value for the solar constant is 1367 W/m^2 but the solar energy output is not constant. In-space radiation measurements fluctuate on the order 0.1%.[8] Sun shades must be capable of blocking more radiation than 0.1% in order to have any meaningful control of the energy input into the Earth's system. Figure 6 displays data of solar radiation measured by spacecraft between the years 1979-1999.[8] The data is measured in a plane normal to the incident rays. The solid line shows the filtered trend. The sun's energy production is dynamic and is not completely understood. The output follows the well-known 11-year cycle and energy output has been correlated with the presence or absence of sun spots.

VIII. Elliptical Orbit GE Shade Design

Geosynchronous orbits have a period of 24 hours and in two-body dynamics return to the original state after completing one revolution about the Earth. A value of K=6.61 defines the orbit size. The perigee radius is between $1.2 \leq K \leq 2$ to avoid orbital debris. Apogee occurs between $11 \leq K \leq 12$. Orbital inclination aligns with the ecliptic plane and oscillates between $\pm 23.4°$ depending on the time of year. A reduction of 0.25% or 3.4 W/m^2 is desired. Each shade has an area A_{sh}=940 Km^2. The total ring area at K=6.61 is A_r=644,000 Km^2 while the 16 satellite constellation is 15,000 km^2, an order of magnitude reduction for regional shading. Global reduction of 3.4

W/m^2 is achieved by using 50 different orbital inclinations each with 16 satellites. Total blocking area is increased by 50 fold to 750,000 km^2. The individual shade areas most likely will be groups of smaller sails working as a group to redirect the sun's energy.

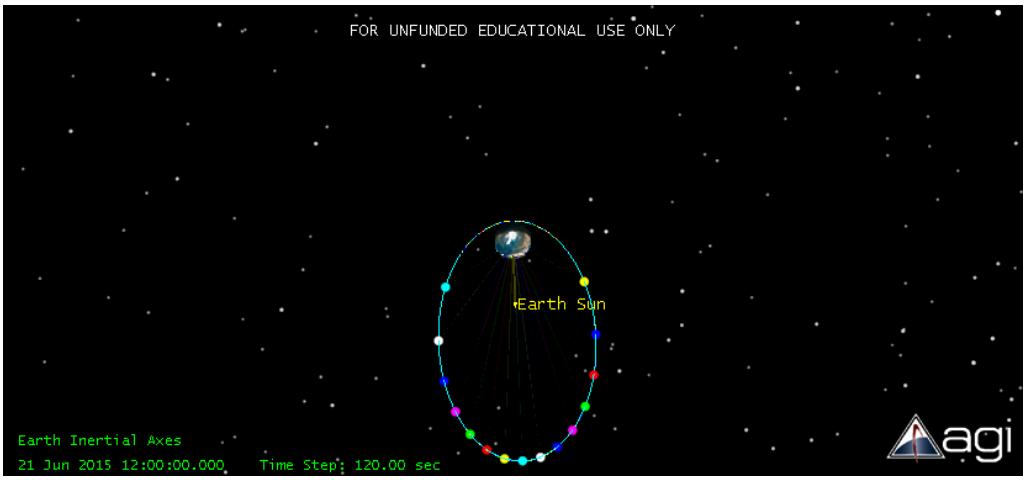

Figure 5. Constellation of 16 Shades in Elliptic Orbit.

IX. Advanced Metamaterials

The cost of launching a system of shades is linearly proportional to the total system launch mass. The shades large reflective surface dominates the shade design so any reduction in reflective material areal density is magnified. Recent advances in nanosheet technology have produced areal densities of 2.6x10^{-2} g/m^2 of transparent material.[9] Silver nanoparticles have been combined with various composites into nanosheets that produce reflective characteristics. [10,11] In Ref. 11, the thickness of a 2D silver nanosheet is stated to be 1.9x10^{-9}m. Assuming that the thickness is entirely Silver (an approximation), the areal density of this particular 2D silver nanosheet is estimated to be the material density of silver multiplied by the sheet thickness or 0.02 g/m^2. Reference 11 also graphs absorptive and reflective properties versus optical wavelengths for 1-5 layers of 2D nanosheets. For wavelengths greater than 750 nm, 5 layers provides approximately 100% reflectivity. However, as the wavelength decreases so does reflectivity. From the graph it appears that the reflectivity is about 40% for 500nm and drops to near zero at 300nm. By combining multiple layers of silver nanosheets with different percentages of silver versus composite materials, a resulting reflective surface tailored to redirect a given range of wavelengths can be engineering. In the near future, a full spectrum reflector can be produced by fusing 10 layers of metamaterials. If each layer is approximated by the density of the 2D silver nanosheet, then the resulting areal density is 0.2 g/m^2 thereby greatly reducing the total launch mass of the shade system.

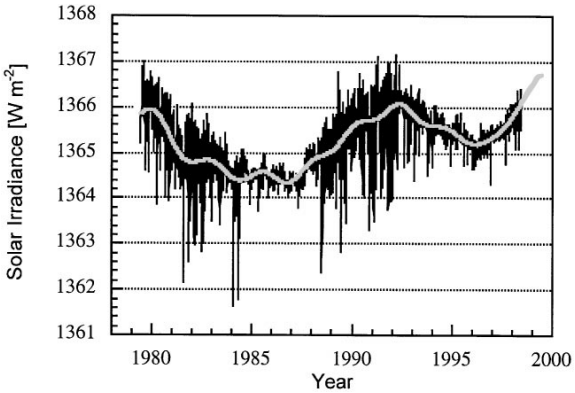

Figure 6. Measurement of Solar Irradiance.

X. Demonstrator Mission

One noteworthy aspect to the earth orbiting regional sunshade is that it is scalable. As shown in Eq. (9), the sail area scales linearly with b, the local blocked energy percentage. A demonstrator mission with b=0.001 could be flown as an experiment in LEO. Using equation (9), a single shade area is approximately 4 km^2. Using a near term value for the reflective material areal density of 1g/m^2 yields a shade mass of 4,000 kg. Adding the deployment system and spacecraft mass yield a launch mass of approximately 5,000kg. Assume an optimistic negotiation with the launch company results in a contract of $5000/kg. A demonstrator mission could be launched for $25 M. Total estimated design, development, test, and evaluation for delivery to launch pad is estimated as$25M leading to a total cost for a demonstrator mission of approximately $50M, well within the constraints of many government and commercial industry financial budgets.

Figure 7 depicts the concentration of human population by latitude. The population distribution centers around 30 N latitude. The first demonstration mission may want to target this region.

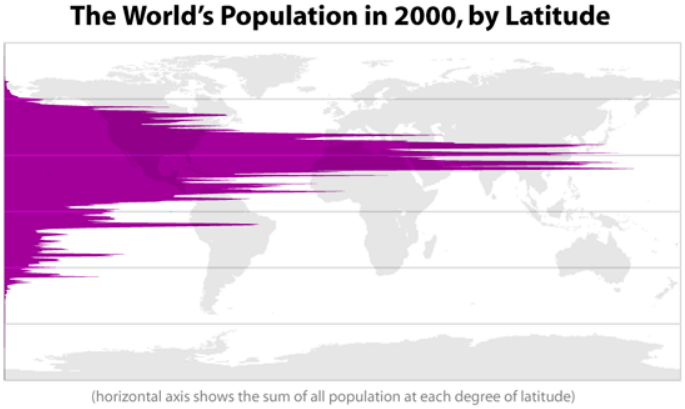

Figure 7. Concentration of Human Population

XI. Conclusion

Earth orbiting sunshades designed to reduce the amount of solar energy that is transmitted to the Earth's surface is presented. The approach outlined is scalable in terms of redirected energy and distance from the earth. Although global shading requires tremendous financial investment, a regional shading solution that would provide weather modification is feasible. A demonstrator mission that would serve as an experiment of the concept is well within many organization's financial budgets.

Acknowledgments

The authors thank the NASA Marshall Space Flight Center's Summer Faculty Fellow programs that allowed them the opportunity to collaborate.

References

[1] Solomon, S. et al., "Irreversible Climate Change Due to Carbon Dioxide Emissions," *Proceedings of the National Academy of Sciences*, Vol. 106, No. 6, 2009, pp. 1704-1709, doi: 10.1073/pnas.0812721106: available online July 8, 2015 at http://www.pnas.org/content/106/6/1704 full?wptouch_preview_theme=enabled

[2] Canadell, J., et al., "Contributions to Accelerating Atmospheric CO2 Growth from Economic Activity, Carbon Intensity, and Efficiency of Natural Sinks," *Proceedings of the National Academy of Sciences*, Vol 104, No. 47, pp. 18866-18870, doi:10.1073/pnas.0702737104; available online July 8, 2015 at http://www.pnas.org/content/104/47/18866.full.pdf+html-pmid=17962418-pmc=2141868

[3] Raupach, M., et al., "Global and Regional Drivers of Accelerating CO2 Emissions," *Proceeding of the National Academy of Sciences*, Vol. 104, No. 24, pp. 10288-10293: doi:10.1073/pnas0700609104. Available online July 8, 2015 at http://www.pnas.org/content/104/24/10288.full?hits=10

[4] Oberthur, S. and H. Ott, "The Kyoto Protocol: International Climate Policy for the 21st Century," Springer Science and Business Media, 1999.

[5] Kennedy, R. G. III, et al., "Dyson Dots and Geoengineering: The Killer App", *Journal of the British Interplanetary Society*, Vol. 66, No. 10/11, 2013.

[6] Govindasamy, B. and K. Caldeira, "Geoengineering Earth's Radiation Balance To Mitigate CO_2-Induced Climate Change," *Geophysical Research Letters*, Vol. 27, No. 14, 2000, pp. 2141-2144.

[7] "Diagram of umbra, penumbra & antumbra" by Qarnos - Own work. Licensed under Public Domain via Wikimedia Commons - https://commons.wikimedia.org/wiki/File:Diagram_of_umbra,_penumbra_%26_antumbra.png#/media/File:Diagram_of_umbra,_penumbra_%26_antumbra.png

[8] Beer, J, W. Mende and R. Stellmacher, "The Role of the Sun in Climate Forcing," Quaternary Science Reviews, Vol. 19, pp. 403-415, 2000.

[9] Zhang, M., et al., "Strong Transparent Multifunctional Carbon Nanotube Sheets," *Science*, Vol 309, No. 5738, 2005, pp. 1215-1219: doi:10.1126/science.1115311. Available online July 8 2015 at http://www-eng.lbl.gov/~shuman/NEXT/MATERIALS%26COMPONENTS/CNTsheets.pdf

[10] Kharlampieva, E., et al., "Flexible Silk-Inorganic Nanocomposites: From Transparent to Highly Reflective," *Advanced Functional Materials*, No. 20, 2010, pp. 840-846. Available online on July 8, 2015 at http://www.dtic mil/dtic/tr/fulltext/u2/a577957.pdf

[11] Okamoto, K., et al., "Tuning Colors of Silver Nanoparticle Sheets By Multilayered Crystalline Structure on Metal Substrates," *Plasmonic*s, No. 8, 2013, pp. 581-590. Doi:10/1007/s11468-9437-2. Available online July 8, 2015 at http://www.plasmonic net/Documents/Plasmonics_8_581-2013.pdf

Modeling and Characterization of Gas Bubble Dynamics in Propellant Simulant

Z.T. Deng[1]
Mechanical Engineering, Alabama A&M University, Huntsville, AL 35762

Heath Martin[2], Alicia Turpin[3] and Stanley Tieman[4]
NASA Marshall Space Flight Center, Huntsville, Alabama

Abstract: A new thixotropic and shear thinning two-phase fluid viscosity sub-model was developed and implemented into ANSYS Fluent simulation tool to model gas bubble dynamics in propellant simulant. This model was developed to simulate the characteristics of bubble dynamics though out the length of the propellant casting/curing pot-life. It combines the requirements of gas bubble dynamics computation in Fluent Volume of Fluid (VOF) with the viscosity measurement data. The propellant simulant viscosity was treated as a function of the curing time, shear rate, relaxation/recovering time, and shear time. A propellant simulant viscosity measurement plan was developed to characterize the effects of thixotropic and shear thinning property. Preliminary measurements of the viscosity was obtained for various shear rate and shear time. The measurement clearly demonstrated the thixotropic and shear thinning characteristics of the propellant simulant. Preliminary comparison of bubbled dynamics simulation between the Newtonian and Non-Newtonian viscosity sub-modeling was presented.

Nomenclature

E = internal energy
$\vec{f}$ = body force
h = enthalpy
$\vec{J_J}$ = diffusion flux
k_{eff} = conduction coefficient
P = pressure
S_h = heat source
T = temperature
$\bar{\bar{\mathbb{T}}}$ = stress tensor
$\vec{V}$ = fluid velocity vector, $\vec{V} = (u, v, w)$ in Cartesian Coordinates
ρ = fluid density
μ = fluid viscosity
σ = stress tensor component in Cartesian coordinates

I. Introduction

During the casting and curing of propellant into solid rocket motors, the casting voids or cracks in propellant may be generated through the gas bubble. The voids and cracks in the propellant presents adverse effects to the

[1] Professor, Marshal Space Flight Center Faculty Fellow, Mechanical Engineering, Alabama A&M University.
[2] Thermal Analyst, Jacob Engineering, Collaborator, ER 43, NASA Marshall Space Flight Center.
[3] Branch Chief, Collaborator, ER 43, NASA Marshall Space Flight Center.
[4] Division Chief, Collaborator, ER 40, NASA Marshall Space Flight Center.

combustion process. Solid fuel rockets are intolerant to cracks and voids because the combustion process is dependent on the surface area of the fuel and voids and cracks represent local increases in burning surface area. This increases the local temperature, system pressure and radiative heat flux to the surface and can easily lead to catastrophic failure [1]. Understanding of the Propellant Liner Insulation (PLI) Unbound (Void in Propellant) and the relationship between gas bubble formed on the wall in casting/curing environment and PLI can provide crucial information to eliminate the cracks and voids during the propellant casting and curing process. However, the rheological properties of the propellant, meaning its flow properties in terms of shear rate, stress and time, usually change substantially though out the length of the processing line [2] and presented a significant challenges to the modeling efforts and the manufacturing process. The mechanism producing the PLI unbounds is not well understood. The relationship between casting/curing environment and dynamics of a gas bubble being formed on the wall is still unknown [3]. In order to identify process controls that may be implemented to mitigate occurrence of PLI unbounds, it is important to determine the relationship between propellant bubble dynamics and the propellant casting/curing variables.

The objective of the current research is to determine the relationship between gas bubble dynamics and the propellant casting/curing environment. A suitable constitutive viscosity model for bubble dynamics in the thixotropic and shear thinning propellant simulant will be developed through experiment. The viscosity sub-model will then be implemented for the subsequent process calculations of bubble dynamics to analyze the bubble growth, detachment, and transport.

II. Modeling of Bubble Dynamics in Thixotropic and Shear Thinning Fluid

A. Modeling of Bubble Dynamics in Non-Newtonian Fluid

Based on the conservation of mass, momentum and energy, the general governing equations for the continuum single phase fluid flow can be written as

$$\frac{\partial \rho}{\partial t} + \nabla \cdot \left(\rho \vec{V}\right) = 0$$

$$\frac{\partial \left(\rho \vec{V}\right)}{\partial t} + \nabla \cdot \left(\rho \vec{V}\vec{V}\right) = -\nabla P + \nabla \cdot \bar{\bar{\mathbb{T}}} + \rho \vec{f}$$

$$\frac{\partial (\rho E)}{\partial t} + \nabla \cdot \left(\vec{V}(\rho E + P)\right) = \nabla \cdot \left(k_{eff} \nabla T - \sum_j h_j \vec{J_j} + \bar{\bar{\mathbb{T}}} \cdot \vec{V} \right) + S_h$$

where $\sum_j h_j \vec{J_j}$ is the Diffusion Heat Flux, h_j include Latent Heat. This equation is incomplete. To close this set of conservational system of equations, one must make hypotheses on the constitutive law for the stress tensor $\bar{\bar{\mathbb{T}}}$. Based on the assumptions of the stress tensor constitutive relations, the fluid can be classified as Newtonian and Non-Newtonian.

For a Newtonian fluid, the viscosity depends only on temperature and pressure, $\mu(P,T)$, not on the forces acting upon it. It remains constant at all shear rates at a given temperature and pressure. The continuum governing equations can be closed based on three fundamental assumptions: 1) The stress tensor is a linear function of the strain rates, 2) The fluid is isotropic and 3) for a fluid at rest, the divergence of shear stress tensor, $\nabla \cdot \bar{\bar{\mathbb{T}}}$ must be zero. In the widely used Navier-Stokes equations, the shear stress tensor component $\bar{\bar{\mathbb{T}}}_{ij}$, for Newtonian fluid can be written as

$$\bar{\bar{\mathbb{T}}}_{ij} = \mu(P,T)\left(\frac{\partial V_i}{\partial x_j} + \frac{\partial V_j}{\partial x_i}\right) + \delta_{ij}\lambda \nabla \cdot \vec{V}\,, \quad \left(\text{where } \lambda \approx \frac{2}{3}\mu(P,T)\right)$$

$\delta_{ij}=1$ when $i=j$. Therefore, the divergence of the shear stress tensor becomes

$$\nabla \cdot \bar{\bar{\mathbb{T}}} = \nabla \cdot \left(\mu(P,T)\overline{\overline{\left(\nabla \vec{V} + \nabla \vec{V}'\right)}}\right) + \nabla\left(\frac{2}{3}\mu \nabla \cdot \vec{V}\right)$$

For incompressible fluid flow, this divergence of shear stress tensor reduces to

$$\nabla \cdot \overline{\overline{\mathbb{T}}} = \nabla \cdot \left(\mu(P,T)\overline{\overline{\left(\nabla\vec{V} + \nabla\vec{V}'\right)}}\right)$$

In three-dimensional (x, y, z) Cartesian Coordinates, the Newtonian Shear Stress can be represented by three components of shear stress acting on the $x-$face (oriented normal to the $x-$axis),

$$\sigma_{xx} = -2\mu\frac{\partial V_x}{\partial x}$$
$$\sigma_{xy} = -\mu\left(\frac{\partial V_x}{\partial y} + \frac{\partial V_y}{\partial x}\right)$$
$$\sigma_{xz} = -\mu\left(\frac{\partial V_x}{\partial z} + \frac{\partial V_z}{\partial x}\right)$$

During the casting and curing process of solid rocket propellant, the "fluid" does not behave like the traditional Newtonian fluid. The viscosity does depend on the forces acting upon and in short time it varies with the shear rate and shear time. This is a typical characteristics of "Non-Newtonian" fluid. In a study conducted to evaluate flow parameters of uncured solid composite propellants during motor casting, Non-Newtonian pseudoplastic flow is observed [4], and the viscosity of the propellant is dependent upon applied shear stress and the age of the uncured propellant. The rheological behavior of concentrated suspension for a uncured solid rocket fuel simulant indicated that the suspension of the fluid exhibited shear thinning characteristics [5, 6].

The modeling of the gas bubble moving inside complex two-phase propellant liquid involves the tracking of bubble growth, deformation, breakup, detachment, and transport. Most importantly, the propellant liquid is behaved as an extremely high viscosity, time-dependent Shear-thinning and shear thinning Non-Newtonian fluid.

Any Non-Newtonian fluid constitutive equation must obey two cornerstone principles: 1) the material frame indifference principle (objectivity principle) which stated that all constitutive equations are independent of the observer; and 2) the entropy principle which stated that any solution of the full system of differential equations must satisfy the entropy balance law with a non-negative entropy production. The typical constitutive relations for viscosity assumes that the viscosity of non-Newtonian fluids is a function of shear rate, pressure, temperature and shear time t, $\mu(\dot{\gamma}, P, T, t)$. The fluid is also assumed to be isotropic. Therefore, the stress tensor $\overline{\overline{\mathbb{T}}}$ can be defined as

$$\overline{\overline{\mathbb{T}}}_{ij} = \mu(\dot{\gamma}, P, T, t)\left(\frac{\partial V_i}{\partial x_j} + \frac{\partial V_j}{\partial x_i}\right) + \delta_{ij}\lambda\nabla\cdot\vec{V}\,, \quad \left(\lambda \approx \frac{2}{3}\mu\right)$$

where the shear rate $\dot{\gamma}$ can be determined by

$$\dot{\gamma} = \sqrt{\tfrac{1}{2}\overline{\overline{D}}:\overline{\overline{D}},} \qquad \overline{\overline{D}} = \overline{\overline{\left(\nabla\vec{V} + \nabla\vec{V}'\right)}}$$

In three-dimensional Cartesian Coordinates, the shear rate becomes

$$\dot{\gamma} = \sqrt{\frac{1}{2}(D_{11}D_{11} + D_{12}D_{21} + D_{13}D_{31} + D_{21}D_{12} + D_{22}D_{22} + D_{23}D_{32} + D_{31}D_{13} + D_{32}D_{23} + D_{33}D_{33})}$$

$$\overline{\overline{D}} = \begin{pmatrix} 2\frac{\partial u}{\partial x} & \left(\frac{\partial u}{\partial y} + \frac{\partial v}{\partial x}\right) & \left(\frac{\partial u}{\partial z} + \frac{\partial w}{\partial x}\right) \\ \left(\frac{\partial u}{\partial y} + \frac{\partial v}{\partial x}\right) & 2\frac{\partial v}{\partial y} & \left(\frac{\partial v}{\partial z} + \frac{\partial w}{\partial y}\right) \\ \left(\frac{\partial u}{\partial z} + \frac{\partial w}{\partial x}\right) & \left(\frac{\partial w}{\partial y} + \frac{\partial v}{\partial z}\right) & 2\frac{\partial w}{\partial z} \end{pmatrix} = \begin{pmatrix} D_{11} & D_{12} & D_{13} \\ D_{21} & D_{22} & D_{23} \\ D_{31} & D_{32} & D_{33} \end{pmatrix}$$

For incompressible fluid,

$$\nabla \cdot \bar{\bar{\mathbb{T}}} = \nabla \cdot \left(\mu(\dot{\gamma}, P, T, t)\overline{\overline{(\nabla\vec{V} + \nabla\vec{V}')}}\right).$$

It is critical to understand the characteristics of Non-Newtonian fluid viscosity before any theoretical model or experimental plan can be developed. There are many ways to describe the characteristics of Non-Newtonian fluid. In general, the Non-Newtonian fluid can be grouped into time-dependent or time-independent fluid in terms of shear time [7]. Note that the shear time may not be the same as physical time the fluid is moving. If the fluid viscosity memorize its time history and changes according to its shear time, then the fluid is "Time-Dependent." If the fluid property do not depend on its time history, then the fluid is "Time-Independent." However, in both cases, the viscosity may also change depending on the shear rate. Therefore, it is more convenient to classify the Non-Newtonian fluid into four categories: 1) Time dependent shear thinning fluid (Thixotropic), 2) time dependent shear thickening fluid (Rheopectic), 3) time independent shear thinning fluid (Pseudoplastics), and 4) time independent shear thickening fluid (Dilatant). The Rheopectic fluid gets more viscous as they are stressed over a period of time. The Thixotropic fluid decreases its viscosity when a constant shear is applied over a period of time [8]. The Dilatant fluid increases its viscosity with increasing applied force on it. Its viscosity dependent on how much force applied, not how long for. The Pseudoplastics fluid decreases its viscosity when harder force applied. The viscoelastic fluid has the ability to store and recover shear energy in the absence of thixotropy and rheopexy effects. Perfectly viscous flow and perfectly elastic deformation denote the two limiting cases of viscoelastic behavior [9]. Experimental observation of the propellant simulant behavior as shown in Fig. 1, recently measured by the authors, indicated that a gap existed between the ramp up and down viscosity curves. At any given time of propellant curing pot-life, the propellant simulant behaves as a Thixotropic and shear thinning Non-Newtonian fluid. Therefore, the modeling of bubble dynamics in propellant simulant faces great challenges for viscosity model. It must consider the viscosity change with thixotropic time history and shear thinning as a function of shear rate.

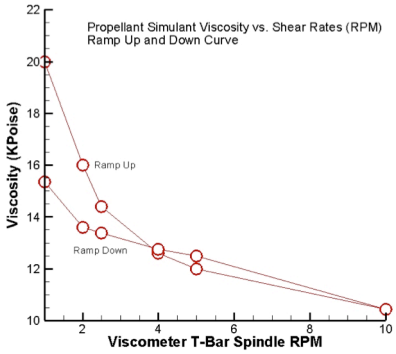

Figure 1. Sample Propellant Simulant Viscosity ramp up and down curve.

B. Thixotropic and Shear Thinning Viscosity Sub-Model

The thixotropic and shear thinning fluid presents great challenges to the theory of viscosity constitutive relation. It is also difficult to implement thixotropic viscosity model to the computational fluid dynamics (CFD) tool. As shown in Fig. 2, the key challenges can be described as in [8], "if we place a thixotropic material into a viscometer and apply a constant shear rate, the measured viscosity will decrease with time, but it will eventually steady out to a constant value. If we then switch off the shear and allow the material to rest for a long time (without drying or any other artifacts such as sedimentation or separation occurring), and switch the shear on again, the measured viscosity will be initially higher, but it will then again decrease and end up at the same value as that which was seen after the original long-term shearing. However, the level for the original value will not necessarily be the same, because that will depend on how carefully or vigorously the material was initially loaded into the viscometer and how long it was left to rest before shearing." This phenomenon is directly related to the microstructural changes in the fluid.

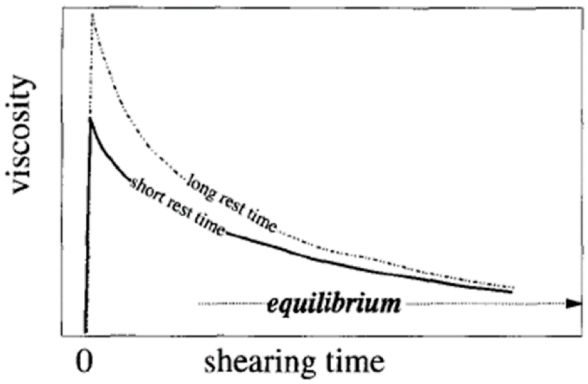

Figure 2. Shearing a thixotropic liquid after a short and long rest times. Courtesy of Barnes, H.A. [8], page 8.

The viscosity modeling of Non-Newtonian fluid can be grouped in 1) empirical constitutive relations for time independent Non-Newtonian fluid [10,11,12,13,14,15] and 2) theoretical models for time dependent Non-Newtonian fluid, such as thixotropic fluid [8,16,17,18,19,20,21]. It was observed that the empirical models can be applied to model viscosity behavior for time independent Non-Newtonian fluid. However, most of the models cannot be applied to thixotropic fluid modeling because it simply did not memorize the history of the fluid. In ANSYS Fluent [14], as shown in Table 1, four types of empirical viscosity models for time-independent fluid were adopted: the Power law model, the Carreau model for pseudo-plastics, the Cross model, and the Herschel-Bulkley model for Bingham plastics.

Table 1. Widely Used Viscosity Model for Time-Independent Non-Newtonian Fluid as in [15].

Power Law	$\mu(\dot{\gamma},T) = \mu_0\dot{\gamma}^{n-1}H(T),$ $or\ \ \mu(\dot{\gamma},T) = \mu_0\dot{\gamma}^{n-1}e^{T_0/T}$	μ_0: Average Viscosity *n=1* Newtonian *n<1* Shear Thinning *n>1* Shear Thickening T_0 Reference temperature
Carreau Model	$\mu(\dot{\gamma}) = \mu_\infty + (\mu_0 - \mu_\infty)\cdot(1+(\lambda\dot{\gamma})^2)^{\frac{n-1}{2}}$. At low shear rate ($\dot{\gamma} \ll 1/\lambda$) Carreau fluid behaves as a Newtonian fluid and at high shear rate ($\dot{\gamma} \gg 1/\lambda$) as a power-law fluid.	$\mu_0\ and\ \mu_\infty$ are zero and infinite viscosities respectively, λ is the time constant for the fluid which determines the shear rate at which the transition takes place from the zero-shear rate plateau to the power law portion and also the transition from power law region to $\mu_0 = \mu_\infty$ and *n* is power law index which depends on the slope of the rapidly decreasing portion of the curve.
Cross Model	$\mu(\dot{\gamma}) = \mu_\infty + \frac{\mu_0 - \mu_\infty}{1 + (K\dot{\gamma})^{1-n}}$	$\mu_0\ and\ \mu_\infty$ are the zero and infinite shear viscosities. K is the consistency index
Herschel-Bulkley Model	$\mu(\dot{\gamma}) = \mu_\infty + \frac{\tau_0 + K(\dot{\gamma}^n - (\frac{\tau_0}{\mu_0})^n)}{\dot{\gamma}}$	$\mu_0\ and\ \mu_\infty$ are zero and infinite shear viscosities respecti, μ_0 vely and λ is the consistency index.

These four models can be applied to Non-Newtonian fluid modeling at equilibrium or steady-State conditions, however, it cannot be directly applied to thixotropic fluid modeling. In order to model a non-Newtonian fluid without using any of the available models, one can specify a user-defined viscosity model.

A typical mathematical model for thixotropy is normally consists of two equations: 1) a constitutive equation for relating the instantaneous shear stress to the instantaneous fluid structure, 2) a kinetic equation for representing the time evolution of the fluid structure. However, most of the indirect microstructural mathematical models depend on the scalar numerical value which describes the microstructure of the fluids. Thixotropic fluid viscosity measurement also presents a great challenge because the interpretation of the non-repeatable experimental data is difficult.

As observed in [22], the propellant simulant will encounter thixotropy and shear thinning, as indicated in Fig. 3. Therefore, the viscosity sub-modeling for propellant simulant requires accurate accounting of the two characteristics: 1) Thixotropic behavior of the propellant when shearing at a constant shear rate with a short period of time and 2) Shear thinning behavior when shearing at different shear rates.

To model a gas bubble dynamics inside a Non-Newtonian propellant fluid, we developed a new viscosity sub-modeling technique based on the combination of viscosity measurement, experimental correlation and thixotropic fluid theory. This viscosity model has the following components:

1) At any given time (For example Point A on the curve) within the pot-life of the propellant casting/curing process, the propellant viscosity is provided by experimental measurement as indicated in Fig. 4.

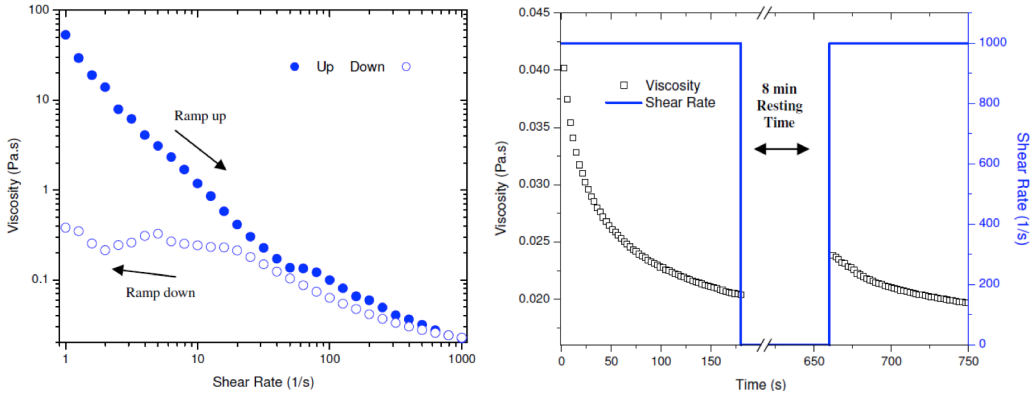

Figure 3. Similar behavior of propellant simulant as in the hydrocarbon gelled fluid. Ramp up and page 8.down viscosity Hysteresis Loop and viscosity as function of shear time. Courtesy of Santos, et. al [22].

2) The thixotropic behavior of fluid is modeled based on a series of measurements according to the developed viscosity measurement plan. This measurement provides viscosity change with *shear time* at constant shear rates. The viscosity changes with various shear rates were obtained from experiment. For each measurement, the pressure and temperature of the propellant simulant is held constant. The relaxation time, equilibrium time, maximum and minimum viscosity will be recorded. It is very important to note that the equilibrium viscosity does not have information about the shear history.

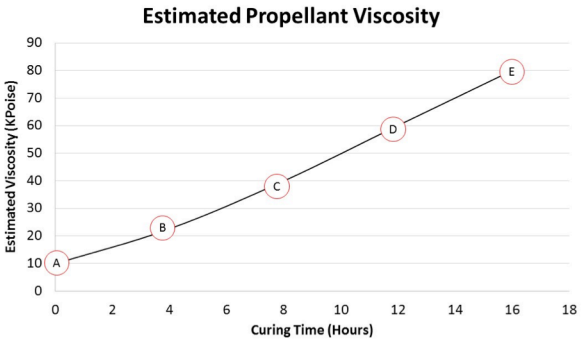

Figure 4. Viscosity measurement at curing time A, B, C, D, and E.

3) The shear thinning behavior of the fluid is modeled based on a time average of three individually measured repeated ramp up and down viscosity curves.

4) A fourth-order polynomial curve is obtained to describe the thixotropic behavior of the fluid viscosity vs. time at each measured shear rate,

$$\mu(\dot{\gamma}_1,t) = \mu_{10}(\dot{\gamma}_1) + \mu_{11}(\dot{\gamma}_1)t + \mu_{12}(\dot{\gamma}_1)t^2 + \mu_{13}(\dot{\gamma}_1)t^3 + \mu_{14}(\dot{\gamma}_1)t^4$$
$$\mu(\dot{\gamma}_2,t) = \mu_{20}(\dot{\gamma}_2) + \mu_{21}(\dot{\gamma}_2)t + \mu_{22}(\dot{\gamma}_2)t^2 + \mu_{23}(\dot{\gamma}_2)t^3 + \mu_{24}(\dot{\gamma}_2)t^4$$
$$\cdots\cdots$$
$$\mu(\dot{\gamma}_i,t) = \mu_{i0}(\dot{\gamma}_i) + \mu_{i1}(\dot{\gamma}_i)t + \mu_{i2}(\dot{\gamma}_i)t^2 + \mu_{i3}(\dot{\gamma}_i)t^3 + \mu_{i4}(\dot{\gamma}_i)t^4$$
$$\cdots\cdots$$
$$\mu(\dot{\gamma}_6,t) = \mu_{60}(\dot{\gamma}_6) + \mu_{61}(\dot{\gamma}_6)t + \mu_{62}(\dot{\gamma}_6)t^2 + \mu_{63}(\dot{\gamma}_6)t^3 + \mu_{64}(\dot{\gamma}_6)t^4$$

where the μ_{ij} $(i = 1,2,3,\ldots,6,\ \ j = 0,1,2,3,4)$ are the curve fitting coefficients at shear rate $\dot{\gamma}_i$. The corresponding time derivative of viscosity with respect to time is obtained

$$\frac{\partial\mu(\dot{\gamma}_i,t)}{\partial t} = \mu_{i1}(\dot{\gamma}_i) + 2\mu_{i2}(\dot{\gamma}_i)t + 3\mu_{i3}(\dot{\gamma}_i)t^2 + 4\mu_{i4}(\dot{\gamma}_i)t^3 \quad (i = 1,2,\ldots,6)$$

5) Based on the obtained 6 shear rate viscosity equilibrium viscosity curves, the equilibrium viscosity as function of shear rates can be obtained through curve fitting, as

$$\mu_{Ae}(\dot{\gamma}) = \mu_{A\infty} + (\mu_{A0} - \mu_{A\infty}) \cdot (1+(\lambda\dot{\gamma})^2)^{\frac{n_A-1}{2}}$$

Note that it is assumed that the equilibrium viscosity follows the shear thinning trend and can be described through Carreau model. In this formula, $\mu_{A\infty}$ is the equilibrium viscosity at infinity large shear rate, μ_{A0} is the equilibrium viscosity at zero shear rate, $\mu_{Ae}(\dot{\gamma})$ is the equilibrium viscosity as a function of shear rate $\dot{\gamma}$ for curing point A. λ and n_A are determined by curve fitting.

6) In order to determine the shear thinning effects, a time averaged ramp up down viscosity measurement plan is developed. The ramp up and down viscosity will be measured three times independently for un-disturbed propellant. Time average of the three curves will be used to conduct curve fitting for ramp-up and down data. A fourth-order polynomial curve is then used to fit the experimental data to describe the ramp up and down section of viscosity, $\mu_{up}(\dot{\gamma},t)$ and $\mu_{dn}(\dot{\gamma},t)$,

$$\mu_{up}(\dot{\gamma},t) = \mu_{up0} + \mu_{up1}\dot{\gamma} + \mu_{up2}\dot{\gamma}^2 + \mu_{up3}\dot{\gamma}^3 + \mu_{up4}\dot{\gamma}^4$$
$$\mu_{dn}(\dot{\gamma},t) = \mu_{dn0} + \mu_{dn1}\dot{\gamma} + \mu_{dn2}\dot{\gamma}^2 + \mu_{dn3}\dot{\gamma}^3 + \mu_{dn4}\dot{\gamma}^4$$

It is noted that the general Hysteresis viscosity curve shows the thixotropic fluid behavior. The ramp up and ramp down shearing process will produce difference in absolute viscosity. It is directional. To model the viscosity change with respect to the shear rate, we should use the ramp up curve for increasing shear rate and ramp down curve for decreasing shear rate. This creates significant challenges to the modeling since the Hysteresis curve is obtained between maximum and equilibrium viscosity. However, the good news is that the current model does not need information about the absolute viscosity value, it only relies on the slope of the viscosity curve with shear rates. If multiple ramp up and down viscosity measurement were obtained, then it is possible to compute the averaged ramp up and down slopes of the viscosity vs. shear rates,

$$\frac{\partial\mu(\dot{\gamma},t)}{\partial\dot{\gamma}} = \begin{Bmatrix} \frac{\partial\mu_{up}(\dot{\gamma},t)}{\partial\dot{\gamma}} = \mu_{up1} + 2\mu_{up2}\dot{\gamma}^1 + 3\mu_{up3}\dot{\gamma}^2 + 4\mu_{up4}\dot{\gamma}^3 \\ \frac{\partial\mu_{dn}(\dot{\gamma},t)}{\partial\dot{\gamma}} = \mu_{dn1} + 2\mu_{dn2}\dot{\gamma}^1 + 3\mu_{dn3}\dot{\gamma}^2 + 4\mu_{dn4}\dot{\gamma}^3 \end{Bmatrix}$$

7) To implement the thixotropic and shear thinning viscosity model into any of the transient CFD model such as ANSYS Fluent, it is critical to know that the physical time is not the same as the shear time! The CFD tool should have an ability to memorize the viscosity and shear rate history for each computational element (cell). We assume that the viscosity and shear rate history for each computational node, cell, volume or element, are all memorized at current physical and computational time, *t*. To advance the transient calculation to time, $t+\Delta t$, we assumed that within this very small computational time step Δt, the fluid is undergoing shear at the shear rate at time *t,* and the shear time is the same as the computational time step, Δt. Of course, if the shear rate is zero, there will be no shear force acted on the fluid cell in this small time increment. Then, for each cell, the viscosity of the fluid cell will be updated using

$$\frac{d\mu(\dot{\gamma},t)}{dt} = \frac{\partial\mu(\dot{\gamma},t)}{\partial\dot{\gamma}} * \frac{\partial\dot{\gamma}}{\partial t} + \frac{\partial\mu(\dot{\gamma},t)}{\partial t}$$

and

$$\mu(\dot{\gamma}_i,\ t+\Delta t) = \mu(\dot{\gamma}_i,t) + \frac{d\mu(\dot{\gamma}_i,\ t)}{dt}\Delta t_{computation\ time\ step}\ ,$$

with the restriction that the viscosity should be within the equilibrium $\mu_e(\dot{\gamma}_i)$ and maximum viscosity $\mu_{max}\ (\dot{\gamma}_i)$ value.

$$\mu_e(\dot{\gamma}_i) \le \mu\left(\dot{\gamma}_i\ ,\ t_{previous}\right) \le \mu_{max}\ (\dot{\gamma}_i)$$

8) Condition of the cell viscosity. In order to avoid non-physical shear strain rates and the possibility of divide-by-zero error, the current model conditioned the viscosity based on the shear rate, equilibrium viscosity and maximum viscosity at each computational time.

$$\text{If } \mu(\dot{\gamma},t)_{cell} \le \mu(\dot{\gamma})_e, \text{ then } \mu(\dot{\gamma},t)_{cell} = \mu(\dot{\gamma})_e;$$

If $\mu(\dot{\gamma})_e \leq \mu(\dot{\gamma},t)_{cell} \leq \mu(\dot{\gamma})_{max}$, then use the above developed algorithm to compute viscosity;
If $\mu(\dot{\gamma},t)_{cell} \geq \mu(\dot{\gamma})_{max}$, then $\mu(\dot{\gamma},t)_{cell} = \mu(\dot{\gamma})_{max}$.

9) Repeat steps 1 through 8 for curing points B, C, D, and E on Fig. 4, the thixotropic and shear thinning viscosity model will be completely developed.

Once the establishment of the thixotropic shear thinning viscosity sub-model, the modeling of gas bubble dynamics in the propellant simulant can be conducted using ANSY Fluent VOF. The Carreau model for equilibrium viscosity change with shear rates is a build-in feature of the developed thixotropic viscosity model. A User-Defined-Function is required to link the developed viscosity model to ANSYS Fluent solver.

C. Viscosity Measurement Plan and Measurement Data Map

The most direct method is to shear a material with a rotational viscometer using a spindle that runs at a fixed speed. Observing the change in viscosity as a function of time is a measure of the thixotropic nature of the fluid. A standard characterization test used to quantify the amount of thixotropy in a material is the so-called "up/down" test. The material is sheared at variable speeds, going from low to high (say 10 to 100rpm), then from high to low (100 to 10rpm), and the viscosity curve for the up ramp is compared to the viscosity curve for the down ramp. The spatial separation between the 2 curves is a measure of the thixotropy in the material and can be quantified by calculating the area. The recovery of the material after shearing is another piece of information that can be useful. How quickly does the material return to its original viscosity? This can be measured by first rotating a spindle in the material, then stopping the spindle and observing the decay in the torque signal. Start the spindle back up at the original speed and observe whether the viscosity returns to the original value.

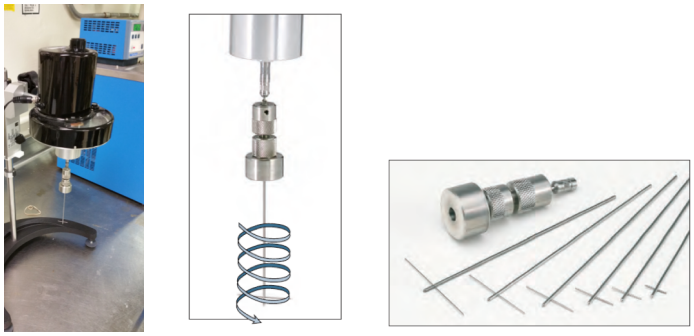

Figure 5. Brookfield viscometer HBT, T-bar spindle and sketch of the Helipath spindle motion.

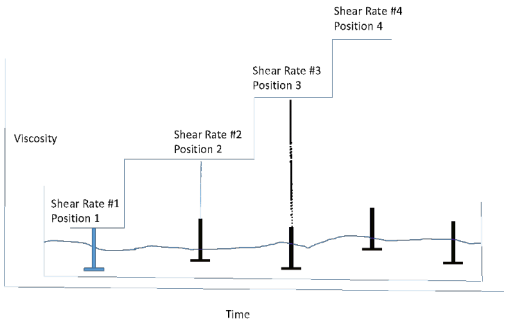

Figure 6. Viscosity measurement location distribution.

In general, the viscometers measure the viscosity and flow properties of a fluid and the Rheometers measure the way a fluid responds to applied shear or stress. In this proposed measurement plan, the viscosity of the propellant simulant will be measured using the Brookfield Viscometer HBT with the Helipath T-bar as spindle, as shown in Fig. 5. Many substances, because of the nature of their yield values, have been considered unsuitable for viscosity or consistency measurements with rotational viscometers. Any rotating spindle, be it cylinder, disc, or paddle, will create a channel in such substances and after a very short time exert a negligible and meaningless torque on any sensing device. This effect also occurs with materials that have a gel structure. The Brookfield Helipath™ Stand is designed to slowly lower or raise a Brookfield Viscometer/Rheometer so that its rotating T-bar spindle will describe a helical path through the test sample. By always cutting into fresh material, the problem of channeling or separating is eliminated and meaningful viscosity/consistency measurements can be made. The automatic reversing feature of the Helipath™ Stand allows measurements to be made over a variable period of time.

As indicated in Fig. 6, at each shear rate a fresh sample will be used and the pre-shearing of the propellant simulant was avoided. The sample loading procedure was kept the same for all the experiments. Since Propellant

curing time (Potlife) is about 12-14 hours, if shearing measurement takes short time to reach equilibrium (seconds), then location 1,2, 3, 4,5 and 6 are considered "Same" propellant or considered "Undisturbed" or "Original Fluid".

To characterize the thixotropic and shear thinning feature of the propellant viscosity, the following measurement plan has to be followed. To measure thixotropic viscosity behavior at curing time A, Viscosity vs. time @Shear Rate 1,2,3,4,5,6), will be recorded, including viscosity vs. time, equilibrium viscosity and breakdown time at the given shear rate (RPM). The measurement procedure includes the following six steps.

1) Position T-bar Spindle into propellant Simulant fresh sample (or fresh location)
2) Set the time counter to zero, Apply constant Shear Rate 1 (RPM) at time zero
3) Record Viscosity vs Time (Watch for time to take to Equilibrium)
4) Keep the T-bar spindle in the propellant simulant, stop spinning and Rest for 30 seconds, keep recording of the viscosity, then apply the same Shear Rate 1, continue to record viscosity vs Time (till equilibrium), stop the spinning, stop recording, remove spindle T-bar from propellant simulant (or keep the T-bar in propellant, prepare next shear rate test.
5) Repeat steps 1, 2, 3, and 4 for various Shear Rates 2, 3, 4, 5, and 6. Minimum of 6 shear rates curve are required for curve fitting purpose.
6) Obtain a hysteresis shearing curve according to Viscometer default plan. Repeat this step for three times to get time averaged Hysteresis curve.

Repeat for Potlife Points B, C, D, and E to get a complete viscosity data map.

III. Results: Fluent VOF Simulation of Bubble Dynamics in Propellant Simulant

A. Characterization of Propellant Simulant Viscosity

The developed viscosity measurement plan was used to measure propellant viscosity. The experimental setup of the viscometer and propellant sample is shown in Figure 7. Immediately after the propellant was mixed, it was put into the sample container and positioned at a 145 degree water bath, in order to keep the constant propellant temperature during the measurement.

Figure 7. Setup of Viscometer, T-bar Spindle and propellant simulant test sample.

Since the measurement is conducted at the very end of the project phase and in a very short time, only the preliminary results of viscosity measurement is discussed here. Three independent measurement were conducted to obtain the ramp up and down curves for viscosity change with shear rates. Figure 8 shows the time averaged viscosity change and the relative error (the ratio of standard deviation to the average value) as shear rates varies. The viscosity ranges from 10 to 20 KPoise, and the maximum relative error is 5.36%. The measurement was carried out by applying an up and down ramp of spindle RPMs. The viscosity was measured at each revolution for each RPM. Minimum two revolutions at each shear rate (RPM) is performed. The varying of RPMs represents varying shear rates. Viscosity difference was observed at the lower RPM or relatively smaller shear rates, based on the ramp up and down curve. The maximum relative error also appeared at lower shear rates. Notice that at lower RPM, the spindle T-bar rotate at very low speed. At 2-RPM, it takes 30 seconds for the spindle T-bar to complete one revolution. The viscosity is recorded at the time interval of 30 seconds. Hat 10-RPM shear rate, the spindle T-bar will spin faster and it takes only 6 seconds to complete one revolution. The viscosity is then recorded at the time interval of 6 seconds. The longer shear time at low RPM may cause the viscosity to change so that the relative measurement data discrepancy will appear at the lower RPMs. This

can be found in Figure 8 when shear rate is below 2.5 -RPM. Figure 9 shows the viscosity time history at shearing rate of 10-RPM. It is apparent that the thixotropic characteristics of the propellant simulant was captured. The equilibrium viscosity is higher than the 2-RPM compared to that at 10 RPM. This clearly demonstrated the shear thinning characteristics of the propellant simulant.

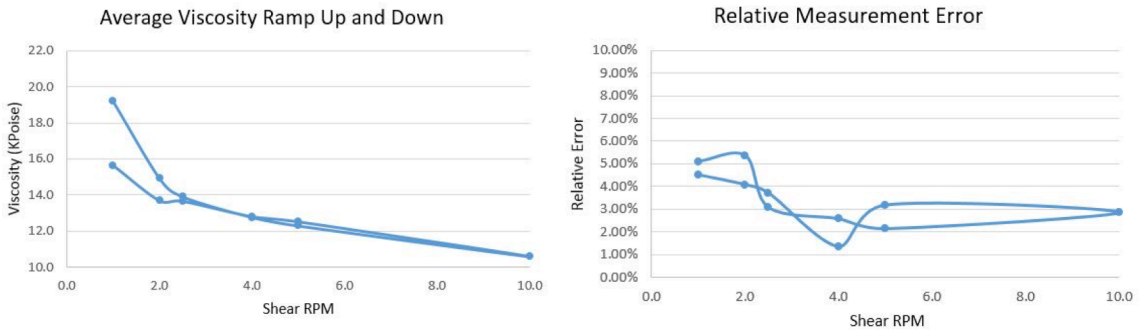

Figure 8. Time averaged and standard deviation of Ramp up and down viscosity versus shear rates.

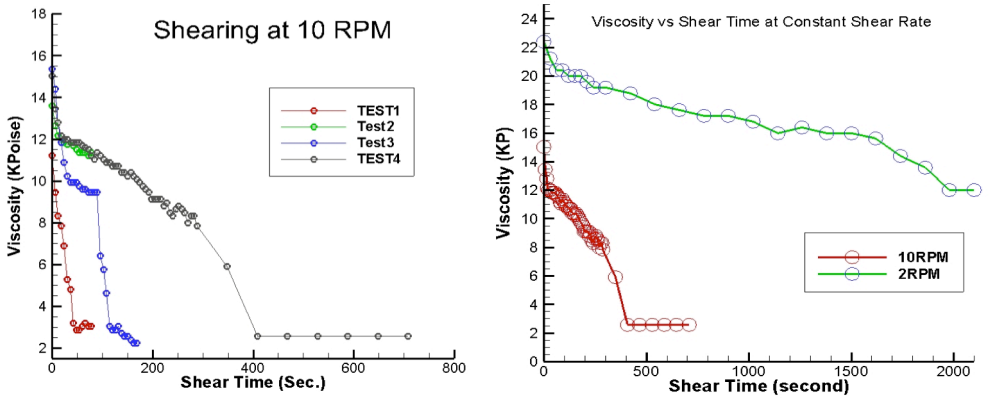

Figure 9. Thixotropic history of viscosity vs. shear time at 10 and 2 RPM shear rate.

B. Modeling of Bubble Dynamics

The developed viscosity model was implemented through a User-Defined Function (UDF) to ANSYS Fluent two-phase VOF model. Table 2 shows the key features of the viscosity sub-model UDF. Note that like source term UDFs, property UDFs (defined using DEFINE_PROPERTY) are called by ANSYS FLUENT from within a loop on cell threads. The solver passes all of the variables needed to allow a DEFINE_PROPERTY UDF to define a custom material, since properties are assigned on a cell basis. Consequently, the developed UDF will not need to loop over cells in a zone since ANSYS FLUENT is already doing it.

Table 2 Key features of the sample Thixotropic Shear Thinning Viscosity UDF

```
#include "udf h"
#include "unsteady.h"
DEFINE_INIT(Initial_Strain,d)
    { Thread *t;  cell_t c; thread_loop_c (t, d)
          { begin_c_loop(c, t)
              {C_UDMI(c, t, 0)= 0;}
           end_c_loop (c, t);}}
DEFINE_PROPERTY(Propellant_Thixotropic_
viscosity,c,t)
{delta_t = CURRENT_TIMESTEP;
strain = C_STRAIN_RATE_MAG(c,t);
    strainm1=C_UDMI(c,t,0);
        lambda = 10.0;n = 0.2;power= (n - 1.0)/2.0;
mu_lam_e = mu_inf + (mu_0 - mu_inf) * pow(1.0 +
pow(strain * lambda,2), power)
dmu_lam = + 0.0112*4*pow(delta_t,3) -
0.2656*3*pow(delta_t,2)+ 2.1519*2*pow(delta_t,1) -
6.8535;
mu_lam = C_MU_L(c,t) + (dmu_dgama * (strain -
strainm1)/delta_t +dmu_lam )  * delta_t *100;
if(mu_lam >= mu_max1)     {mu_lam = mu_max1;};
if(mu_lam <= mu_lam_e)    {mu_lam = mu_lam_e;} }
else
{ mu_max2 = 2000; mu_inf = 1000.0;mu_0 = 2000.0;
```

```
    mu_up_0=0;mu_up_1=0;mu_up_2=0;mu_up_3=0;
    mu_up_4=0;mu_dn_0=0;mu_dn_1=0;mu_dn_2=0;
    mu_dn_3=0;mu_dn_4=0;
if(strain >= strainm1) {dmu_dgama=mu_up_1
+2*mu_up_2*strain+3*mu_up_3*pow(strain,2)
+4*mu_up_4*pow(strain,3);};
    if(strain < strainm1)
    {dmu_dgama = mu_dn_1 + 2*mu_dn_2*strain +
3*mu_dn_3*pow(strain,2)+4*mu_dn_4*pow(strain,3);
}; mu_lam = 3000;
    if(strain <= 0.05)
    {    mu_max1=3000;mu_inf = 1000.0;mu_0 =
3000.0;
lambda = 10.0;n = 0.2;power= (n - 1.0)/2.0;
mu_lam_e = mu_inf + (mu_0 - mu_inf) * pow(1.0 +
pow(strain * lambda,2), power) ;
dmu_lam = + 0.0230*4*pow(delta_t,3) -
0.5557*3*pow(delta_t,2)
                + 4.6157*2*pow(delta_t,1) - 15.647;
 mu_lam = C_MU_L(c,t) + (dmu_dgama * (strain -
strainm1)/delta_t +dmu_lam )  * delta_t *100;
if(mu_lam >= mu_max2)     {mu_lam = mu_max2;};
if(mu_lam <= mu_lam_e)    {mu_lam = mu_lam_e;};}
if(strain <= 1.0E-05) {mu_lam = C_MU_L(c,t);};
C_UDMI(c, t, 0)= strain;return mu_lam;
}
```

When bubble is created, detached and moving inside the propellant simulant, different phases are treated as interpenetrating continua. Volume fraction is tracked for each fluid and each computational cell throughout. We use the Eulerian fixed-grid Interface tracking scheme. It solves only one set of momentum equation, shared by all fluids and volume fraction of each of the fluid in each computational cell is tracked. The VOF method utilizes a single energy equation for the entire system. No heat transfer between phases are considered for this comparison.

For demonstration purpose, two simple viscosity thixotropic curves are used for the simulation. It is assumed that at shear rate of *0.10* s^{-1}, the propellant simulant viscosity is ranged between 10 and 30 Kpoise with the fourth-order polynomial distribution of

$$\mu(\dot{\gamma}_1, t) = 29.871 - 15.647t + 4.6157t^2 - 0.5557t^3 + 0.023t^4 \quad when\ \dot{\gamma}_1 = 0.10.$$

At the shear rate of *0.05* s^{-1}, the propellant simulant viscosity is ranged between 10 kPoise and 20 KPoise with the fourth-order polynomial distribution of

$$\mu(\dot{\gamma}_2, t) = 16.974 - 6.8535t + 2.1519t^2 - 0.2656t^3 + 0.0112t^4 \quad when\ \dot{\gamma}_2 = 0.05.$$

It was also assumed that slope of the Hysteresis ramp up and down curves has a slope *-0.2* and *-0.1* respectively. The Carreau viscosity model is assumed to be

$$\mu(\dot{\gamma}) = \mu_\infty + (\mu_0 - \mu_\infty) \cdot (1+(\lambda\dot{\gamma})^2)^{\frac{n-1}{2}}$$

where $\mu_\infty = 10\ Kpoise,\ \mu_0 = 30\ Kpoise,\ \lambda = 10\ s,$ and $n = -1$. The bubble dynamics was simulated within physical time of 10 seconds. Fig. 10 shows the comparison of transient history of the gas bubble dynamics between Carreau Model and the newly developed viscosity sub-model. The viscosity at 5 seconds from the start shows difference between the Carreau model and thixotropic shear thinning model, however, small difference was found in the bubble shape.

IV. Conclusion

A new thixotropic and shear thinning two-phase fluid viscosity sub-modeling technique was developed and implemented into ANSYS Fluent to model gas bubble dynamics in propellant simulant. This viscosity sub-model considers the thixotropic and shear thinning characteristics of the Non-Newtonian propellant simulant characteristics though out the length of the propellant casting/curing pot-life. It combines the ANSYS Fluent two-phase VOF modeling requirements and experimental measurement of propellant simulant viscosity. Preliminary measurement of propellant simulant viscosity demonstrated the thixotropic and shear thinning characteristics. This viscosity model is considered new and was approved working for the bubble dynamics simulation. Preliminary comparison of bubbled dynamics between the Newtonian and Non-Newtonian viscosity sub-modeling was conducted. It is anticipated that with a comprehensive viscosity data map, this viscosity sub-model will be greatly enhanced and can be applied for modeling of complex fluid flows with thixotropic and shear thinning characteristics.

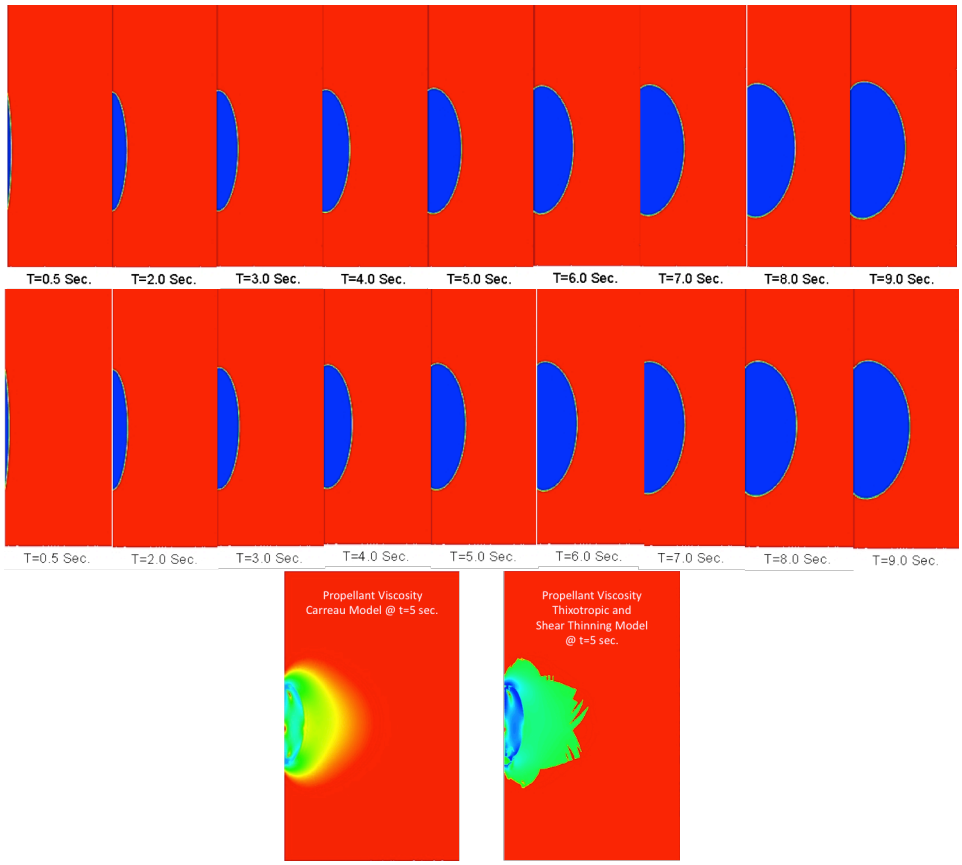

Figure 10. Comparison of time history of bubble generation and viscosity between Carreau model, n=-1 and thixotropic shear thinning viscosity model.

Acknowledgments

The author Dr. Z.T. Deng greatly thanks the support of NASA Marshall Faculty Fellowship Program for this research. Dr. Deng also greatly thanks the excellent guidance and support of Dr. Heath Martin, Dr. Alicia Turpin, Dr. Stanley Tieman of ER 43 at NASA MSFC, Dr. Frank Six, the Director of NASA Marshall Faculty Fellowship Program, and Dr. Gerald Karr, Professor of the University of Alabama in Huntsville.

References

[1]Remakanthan, S., Moideenkutty, KK, Gunasekaran, R., Thomas C., and Thomas, C.R., "Analysis of Defects In Solid Rocket Motors Using X-Ray Radiography," National Seminar & Exhibition on Non-Destructive Evaluation, NDE 2014, Pune, December 4-6, 2014 (NDE-India 2014), Vol.20 No.6 (June 2015) - *The e-Journal of Nondestructive Testing* - ISSN 1435-4934.

[2]Sutton, George P., Biblarz Oscar, *Rocket Propulsion Elements*, 8th ed., John Wiley & Sons, New Jersey, 2010, pp. 529.

[3]Martin, H., Bradley, D., "MSFC Propellant Void Study," JACOBS ESSSA Group presentation, 2014.

[4]Rogers, C. J., Smith, P. L. Klager, K., "Rheology of composite solid propellants during motor casting," Internationale Jahrestagung ueber Analysenmethoden fuer Treib- und Explosivstoffe; 19th; June 14-16, 1978; Karlsruhe; Germany

[5]Dilhan M. Kalyon, Piraye Yaras, Birnur Aral, and Ulku Yilmazer, "Rheological behavior of a concentrated suspension: A solid rocket fuel simulant," *Journal of Rheology* 37(1), pp. 35-53. 1993.

[6]Ivanchenko, A.M., Bondarenko, Sergiy G., Protsan, Yulian, Wilson, Shaun A., "Deep Regulation and Reusable Rocket Propulsion Using Premixed Slurry Propellant," *Journal of Propulsion and Power*, Vol. 28, No. 5 (2012), pp. 869-875.

[7]Chhabra, R.P., "Non-Newtonian Fluids: An Introduction," http://www.physics.iitm.ac.in/~compflu/Lect-notes/chhabra.pdf.

[8]Barnes, Howard A., "Thixotropic – a Review," *Journal of Non-Newtonian Fluid Mechanics*, Vol. 70, (10997). Pp. 1-33.

[9]Boger D.V. and Halmos, A.L., "Non-Newtonian Flow 1- Characterization of Fluid Behavior," Modular Series, American Institute of Chemical Engineers, 1981. ISBN 0270-7632/81/1123-0001.

[10]Rao, M.A., "Rheology of Fluid, Semisolid, and Solid Foods," Food Engineering Series, DOI 10.1007/978-1-4614-9230-6_2, © Springer Science & Business Media New York 2014.

[11]Carreau, PJ, De Kee DCR, Chhabra RP., *Rheology of Polymeric Systems*, Cincinatti: Hanser/Gardner Publications, Inc., 1997.

[12]Jonasova, A., and Vimmr, J., "Numerical simulation of non-Newtonian blood flow in bypass models," PAMM · Proc. Appl. Math. Mech. 8, 10179 – 10180 (2008) / DOI 10.1002/pamm.200810179.

[13]Kanakamedalan, A., "Numerical Simulation of the Flow of a Power Law Fluid in an Elbow Bend," Master Thesis, Texas A&M University, December 20-09.

[14]ANSYS Fluent User Guide, ANSYS, Inc. Release 14.5. Canonsburg, PA 15317, October 2012.

[15]Rupak K Banerje, Koustubh D Ashteka, Tarek A Helmy, Mohamed A Effat, Lloyd H Back and Saeb F Khoury, "Hemodynamic diagnostics of epicardial coronary stenoses: in-vitro experimental and computational study," BioMedical Engineering OnLine 2008, 7:24 doi:10.1186/1475-925X-7-24.

[16]Ebrahimi, B., Taghavi, S-M., and Sadeghy, K., "Two-phase viscous fingering of immiscible thixotropic fluids: A numerical study," *Journal of Non-Newtonian Fluid Mechanics, 218 (2015) 40–52.*

[17]Antosev, S.N., Diaz, J.I., and Oliveira, H.B., "Mathematical Models in Dynamics of Non-Newtonian Fluids and in Glaciology," CMNE/CILAMCE 2007, Porto, 13 a 15 de Junho, 2007.

[18]Derksen, J.J., and Prashant, "Simulations of complex flow of thixotropic liquids," *Journal of Non-Newtonian Fluid Mechanics, 160 (2009) 65–75.*

[19]Dullaert, K., and Mewis, J., "A structural kinetics model for thixotropy," *Journal of Non-Newtonian Fluid Mechanics*, Volume 139, Issues 1–2, 15 November 2006, pp. 21–30.

[20]Barkhudarov, M.R., Bronisz, C.L., and Hirt, C.W., "Three-Dimensional Thixotropic Flow Model," FSI-96-00-1, Presented at 4th International Conferences on Semi-Solid Processing of Alloys and Composites, June 19-21, 1996, England.

[21]Mujumdar, A., Beris, A.N., and Metzner, A.B., "Transiet Phenomena in Thixotropic Systems," *Journal of Non-Newtonian Fluic Mechanics,* 102 (2002), pp. 157-178.

[22]Santos, P.H.S., Carignano, M.A., and Campanella, O.H., "Qualitative Study of Thixotropy in Gelled Hydrocarbon Fuels," Engineering Letters, 19:1, EL-19-1-3., 2011.

Concepts for In-Space Additive Manufacturing of Thermal-Curing Thermosets and Embedded Wireless Sensors

Aaron D. Mazzeo[1],
Rutgers University, Piscataway, NJ 08812, USA
Marshall Space Flight Center, Huntsville, AL 35811, USA

Patrick V. Hull[2], Alexander C. Few[3], and Jason D. Waggoner[4]
Marshall Space Flight Center, Huntsville, AL 35811, USA

This paper describes two advanced concepts for earth- and space-based additive manufacturing (AM): (i) thermal-curing thermosets and composites for in-space additive manufacturing (ISAM) and (ii) embedded wireless sensors for measuring mechanical strain. Thermal-curing thermosets and composites for ISAM have the potential to overcome the limited mechanical performance of thermoplastics currently deposited through fused deposition modeling. For the AM of these materials, two particular advantages of low-gravity environments include limited lateral spreading of extruded droplets and reduced loss of heat surrounding extruded droplets with a lack of buoyancy-driven convection. With respect to embedded wireless sensors, AM has the potential to facilitate the inclusion of recessed channels filled with conductive material for patterned traces. These patterned conductive traces will then be essential components for embedded wireless sensors, which will aid in intermittent structural health monitoring.

I. Introduction

Additive manufacturing (AM) has the potential to serve as a new tool for construction of aerospace structures, sensors, and hardware built both in space and on earth. With respect to AM itself, there are opportunities to improve the strength-to-weight ratio and thermal properties of printed materials. Research for earth-based additive manufacturing is just beginning to scratch the potential of producing composites with improved mechanical strength. Evaluating, adapting, or inventing processes for in-space additive manufacturing (ISAM) of composites will involve designing systems that work within constrained environments, which either manage or take advantage of varied-gravity environments. Exploring physics that might take advantage of low-gravity environments for high-resolution printing of composites (i.e., thermal-curing thermosets with embedded fibers) will help guide the design and development of future machines for ISAM.

In addition to improving capabilities for ISAM, efforts toward improving the capabilities of earth-based AM will lead to higher resolution, faster rates of production, and wider ranges of printable materials than currently available. With these improvements, printing conductive materials within AM-based components will lead to new opportunities for embedding sensors. Once embedded, these sensors may be difficult to access or function in hard-to-reach locations, so the design and fabrication of passive wireless sensors compatible with AM will eliminate the need for onboard batteries, which could discharge and degrade over time.

II. Overview of In-space Additive Manufacturing

Current in-space additive manufacturing (ISAM) relies on fused deposition modeling (FDM) of thermoplastics, such as acrylonitrile butadiene styrene (ABS), which have limited mechanical performance (e.g., thermal stability up to ~100°C[1]). To overcome the operating temperature limits of currently employed thermoplastic materials, this

[1] Assistant Professor, Department of Mechanical and Aerospace Engineering, Rutgers University
Marshall Space Flight Center Faculty Fellow, ES21, Building 4487, Marshall Space Flight Center
[2] Technical Assistant, ES21, Building 4487, Marshall Space Flight Center
[3] Designer, ES21, Building 4487, Marshall Space Flight Center
[4] Supervisory Assistant, ES21, Building 4487, Marshall Space Flight Center

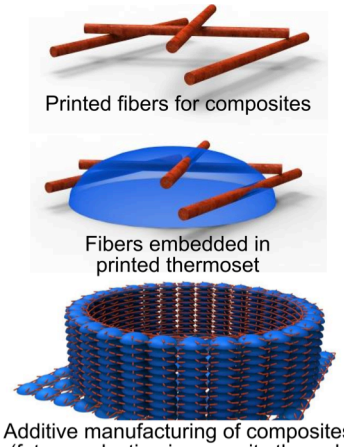

Figure 1. Vision for future additive manufacturing with thermosets and embedded fibers.

report proposes the extruded printing of thermoset materials with embedded fibers (i.e., composites), as depicted in Figures 1 and 2. Further development of ISAM with the extruded printing of thermal-curing, high-performance polymers in low gravity will enable functional tools and actuators made of hard epoxies and soft elastomers. The target outcome is an experimental and theoretical platform with an AM-based machine on earth and accompanying numerical simulations, which will then be capable of predicting performance in low or high-gravity environments. Once created, this platform will enable the design and fabrication of new machines for ISAM with high-performance thermosets with embedded fibers. In the future, we envision this work in design and predictive modeling will be useful for AM and deposition of new materials beyond thermal-curing thermosets with embedded fibers, such as recycled feedstock, concrete, high-temperature thermoplastics, and even regolith, because we will be able to enter new material properties into multi-physics-based simulations.

The resulting technology will provide new materials for ISAM and go further in providing marketable capabilities of test and simulation to companies working to evaluate the feasibility of printing or depositing advanced materials that spread and cure on surfaces. Additionally, this technology will serve as a test system for the embedding of composite fibers within an additively manufactured thermoset matrix. The testing of fiber wetting within these AM thermoset matrices is critical to the material and application developments of composite additive manufacturing (CAM). A study of the commercial market shows that there are no AM-based techniques suitable for printing thermal-curing thermosets with embedded fibers and possessing high-performance properties, and there is likewise very little academic research, which is indicative of the technical hurdles we will overcome by taking advantage of low gravity (see next section).

To create new technologies for ISAM and CAM with thermal-curing thermosets with embedded fibers and move it toward commercial feasibility, one might pursue the following technical tasks/objectives: (i) Modify existing 3D printers for the extrusion of thermosets; (ii) Build analytical model to predict the behavior of extrusion and thermal curing of viscous materials; (iii) Extrude droplets, puddles, and linear beads of thermal-curing thermosets on heated surfaces; (iv) Compare extruded features to simulated predictions; (v) Use calibrated models to predict performance in varied-gravity environments; and (vi) Embed composite fibers into extruded thermosets using a modified 3D printer. This project is an opportunity to combine NASA's extensive experience with mechanical design, optimization, ISAM, and small-scale AM with new university-based expertise in processing of thermosets, high-gravity spreading of liquid coatings, and modeling. The innovation comes from realizing that low-gravity environments will aid ISAM of thermal-curing thermosets by (i) limiting the lateral spread of extruded droplets and (ii) reducing the loss of heat surrounding an extruded droplet with a lack of buoyancy-driven convection.

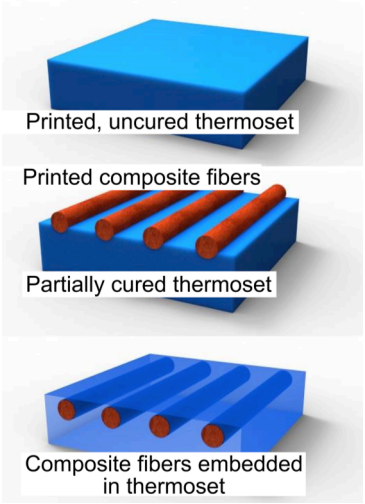

Figure 2. Alternative method of additive manufacturing with a primary thermoset layer, followed by fibers, which sink into the liquid.

III. Potential Approach to In-space Additive Manufacturing

A. Motivation

To produce parts in space for repairs, instrumentation, or convenience (e.g., an astronaut recently requested a 3D-printed back scratcher), FDM is the current choice for the extrusion of thermoplastics through a nozzle from reels of ribbon-like feedstock. This process is adequate as a proof of concept, helps us understand the economic and physical requirements for ISAM, and will lead to useful applications for spacecraft. However, FDM with thermoplastics will always be limited by the fundamental physical issue that a material formed through melting will deform again if exposed to temperatures similar to those used during forming. In other words, improvements in high-temperature properties of thermoplastics require materials with high glass transition temperatures and high processing temperatures, which can result in a cycle of continual development of processing machines that require

operation at higher and higher temperatures. For ISAM, we will quickly run into a limit on resources for processing high-performance thermoplastics, just as selective metal sintering (SLM), while effective on earth for processing Inconel, would similarly be cost prohibitive in space. Outside of ISAM, the physical understanding to be developed will also aid efforts in earth-based additive manufacturing, which will have an estimated market value ranging from a few billion dollars to more than $20 billion in 2020[2].

B. State of the Art

There are two main deficiencies in existing AM-based technologies that limit their use in space. First, conventional ISAM uses FDM of thermoplastics, which currently have limited thermal performance as previously described. Second, common stereolithographic processes on earth that use a laser to form geometries require UV-sensitive thermosets in open liquid baths[3], and these liquid baths would be prohibitive in space[4]. To overcome these limitations for ISAM, an ideal solution would be to extrude thermosets in a controllable fashion with fast thermal curing before the extruded thermoset has a chance to spread laterally and limit the resolution of printable features[5,6]. This process will eliminate the potential need for a liquid bath while also being compatible with a host of thermoset materials with superior mechanical properties to thermoplastics currently employed in ISAM. While thermal-curing thermosets have received academic attention in composites, reaction injection molding, potting, and molding ranging from the nano to meso scales, they have received minimal attention[5,6] in AM because of the technical issue of undesirable spreading/smearing during general extrusion. This proposal will mark an effort to overcome this issue in ISAM by exploring the potential benefits of low-gravity for innovative control of liquid spreading during extrusion and quantifying the proper conditions for embedding composite fibers in the additively manufactured thermosets.

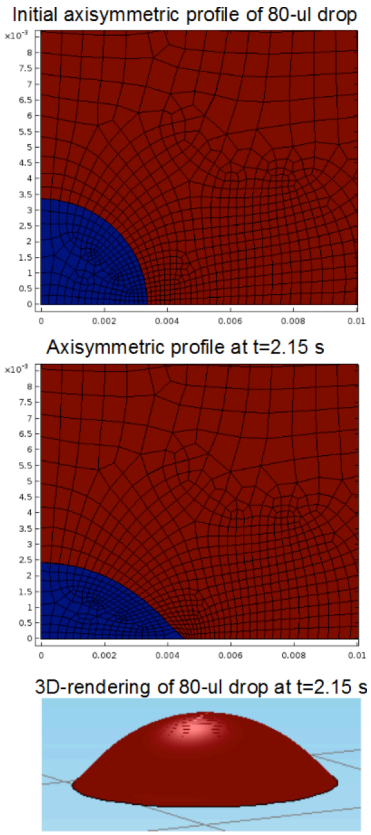

Figure 3. Simulated spreading of a liquid drop.

C. "Innovativeness"

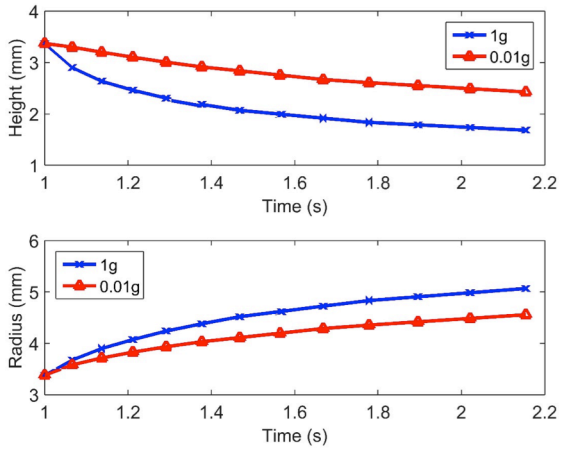

Figure 4. Under low gravity, liquid drops spread more slowly on wetting substrates. These plots show the height and radius of simulated spreading drops (Figure 3) under 1 g and 0.01 g.

The innovation in this concept comes through the synergistic combination of thermal-curing thermosets, low-gravity extrusion for ISAM and embedded fibers. The hypothesis is that low gravity will permit high-resolution AM of thermal-curing thermosets because the low-gravity environment will limit lateral spreading of flowing liquids and convection of surrounding heat involved with curing extruded droplets/puddles. On earth, droplets/puddles have a capillary length on the order of a millimeter, which means droplets of this size resting on wetting surfaces (e.g., liquid polymers on untreated metallic surfaces) will spread laterally with surface tension and gravity working together to drive the lateral spreading. With the elimination of gravity, the capillary length essentially becomes infinite, which means there will be a reduction in the lateral spreading of a liquid on a solid surface, as surface tension will be the only driver for liquid flow (Figures 3 and 4). For ISAM, this reduced lateral spreading suggests that low-gravity environments might improve the resolution of printable features. In addition to low gravity affecting the liquid flow of the thermoset, it will also minimize heat transfer associated with buoyancy-driven or natural convection. This reduction in heat transfer will insulate the extruding nozzle from the heated substrate, which means the thermal gradient between the thermoset leaving the nozzle and the extruded bead/puddle will be sharper than it would be on earth. The elimination of natural convection will also allow extruded beads/puddles resting on heated surfaces to cure more quickly than they would on earth for a given amount of heat flux.

D. Technical Merit and Anticipated Benefits

While there is an interesting DIY project[5], some academic work[6], and a polymer chemistry-based exploration of AM with thermosets by Glenn Research Center (potential collaborators)[7,8], there are no commercially available machines or simulation-based models in current existence for AM-based deposition of thermosets. While significant effort will be necessary to create a commercially ready machine and/or a complete understanding of the physics, there is merit in starting an experimental and theoretical platform to serve as a springboard for further development of ISAM and CAM with thermal-curing thermosets. Such a platform would permit exploration of the physical tradeoffs between gravity, curing kinetics, surface tension, viscosity, size of the extruding nozzle, rate of deposition, motion of the nozzle, and composite fiber properties.

IV. Overview of Embedded Wireless Sensing for Structural Health Monitoring

Characterization of structural health with wired, surface-mounted strain sensors is expensive and time consuming. To reduce costs and enable rapid characterization of mechanical strain of composites with additive manufacturing-based, polymeric components for space systems, we suggest there is an opportunity to design and fabricate a new class of wireless strain sensors. The target outcome would be an embeddable sensing technology for structural health monitoring that gets incorporated during fabrication, layup of composites, or ISAM-based printing. This project would combine NASA's extensive experience with instrumentation for measuring mechanical strain on space structures, fabrication of composite structures, and testing of low-power wireless antennas with new university-based technologies involving electronic paper and liquid conductors. The resulting technology with passive devices and capabilities for direct incorporation into components during manufacture will provide a marketable alternative to current commercial wireless sensors/components. An analysis of the market in this domain shows that current commercially available sensors require onboard power (e.g., a battery), are bulky (not directly embeddable within structures during fabrication), or have limited ranges of operating temperatures. To overcome these limitations of the current market, the objectives might be to (i) perform the engineering development of the wireless sensors, (ii) develop methods for embedding sensors, (iii) evaluate the technical limits of the sensors, (iv) leverage existing internal and external relationships to build strong collaborating efforts for future external funding opportunities, and (v) assess the return on investment associated with simple, cost-saving, *in situ* measurements that will enable marketable, wireless sensing technology. The products would be prototypes of strain-sensitive antennas and coils, along with simulations describing their physical behavior.

V. Potential Approach to Embedded Wireless Sensing for Structural Health Monitoring

A. Motivation

To ensure the safety of space and transportation systems, it is common to instrument and test loaded structures with hundreds of wired strain sensors to detect cracks and mechanically yielding regions. This process is laborious and time consuming with the manual attachment of sensors and wired connections running from the sensors to data logging systems. This tedious technique is also not unique to aerospace structures, as researchers and agencies desire structural health monitoring with wireless strain sensors that might be embedded in roads, bridges, and buildings[9–12]. Embedded sensors will aid in preventing failures of the nation's ailing infrastructure, which received a D+ on its last report card[13]. The report cited needs for more than $21 billion to repair aging, high-hazard dams and $76 billion for structurally deficient bridges ($1/9^{th}$ of the nation's more than 600,000 bridges). As assessments and repairs of existing infrastructure go forth, incorporating new sensors to monitor their structural health will provide long-term savings in cost.

B. State of the Art

There are a number of deficiencies in existing wireless strain sensing technologies for potential use by NASA and those designed for general structural health monitoring. First, conventional wireless sensors often require a battery that limits the lifetime of the devices. Second, passive sensors without onboard batteries (e.g., passive wireless sensors offered by Phase IV Engineering, Inc.) are currently bulky and not suitable for simple integration during fabrication. Third, new passive surface acoustic waves (SAW) with piezoelectric materials and integrated circuits appear well-suited for applications in mild environments, but their operating temperatures are limited (e.g., -20 °C to 85 °C from French company SENSeOR).

C. Functional Requirements for a Successful Outcome

With these deficiencies in the state of the art, an ideal system would have wireless sensors with the following functional requirements (FR):

FR 1: A compact size for simple integration during fabrication
FR 2: No battery for power on the embeddable unit (passive strain gauge)
FR 3: Wireless range of detection greater than 6 inches
FR 4: Simple geometries/materials without semiconductor-based integrated circuits and temperature-sensitive components

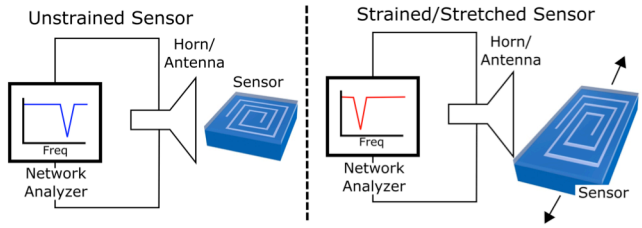

Figure 5: The resonance of the antenna/coil changes when exposed to mechanical strain.

To meet these requirements, we propose the design and fabrication of a wireless strain sensor that will work in conjunction with a wireless transmitter/receiving unit that makes analog-based measurements of strain experienced by the sensor (see Figure 5). The wireless sensor itself will be made of liquid metal (e.g., eutectic gallium indium or Galinstan) or electronic paper patterned into the form of a strain-sensitive antenna or inductive coil as shown in Figure 6. Using conductors of only liquid metal (liquid at room temperature during fabrication but solid at colder temperatures) or electronic paper (aluminum will be the initial prototyping material of choice from AR Metallizing and Rutgers University) will facilitate compact size and ease of fabrication (FR 1). The embeddable sensor will be a passive antenna or coil with calibrated resonance, which will not require a battery (FR 1) and permit ranges of detection greater than 6 inches (FR 3). As the number of materials to be integrated in the sensing unit will be few and the sensors will not have semiconductor-based integrated circuits, the sensing units with liquid metal will be capable of enduring larger ranges of temperature than the SAW-based device from SENSeOR and should be suitable for space, although further testing (Task 6) will be necessary (FR 4).

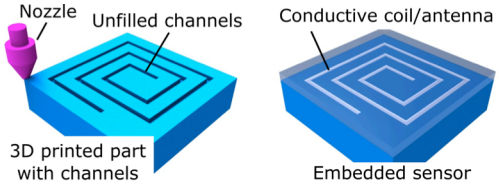

Figure 6: Steps for additive manufacture of a wireless strain sensor.

D. Suggestions for Design

After reviewing the literature, performing initial experiments with RF-based antennas, and running calculations and simulations (not included in this report), the first designs should probably use inductive coupling with frequencies less than 100 MHz. These initial designs would be similar to configurations and sensing performed with low-frequency RFID, but they would not require an integrated circuit or semiconductor-based processing. Furthermore, AM would enable the ability to tune the resonant frequencies of individual embedded sensors with slight variations in the printed geometries. In so doing, these designs would provide an analog-based approach to designing passive wireless strain gauges.

VI. Conclusions

To conclude, this report presents concepts for the future development of ISAM for improved mechanical properties and AM of embedded wireless sensors for structural health monitoring. As the costs continue to decline and the quality and resolution of AM-based technologies improve, it will be possible to build structures in space and monitor their structural health. These advances will improve the reliability and capabilities of components produced in low volumes to enable advances in near-earth orbit, lunar habitation, and deep-space exploration to Mars and beyond.

Acknowledgments

A. D. Mazzeo thanks Frank Six and the NASA MSFC Summer Faculty Program for a summer fellowship at MSFC. The authors also thank Bill Hopkins, Leon Bell, DeLisa Wilkerson, Kosta Varnavas, Chuck Wilkerson, Rex Graves, and Niki Werkheiser for helpful discussions, assistance with experiments, and/or future potential collaborations in ISAM and passive wireless sensing.

References

[1] MatWeb, "Heat Deflection Temperature Testing of Plastics" Available: http://www matweb.com/reference/deflection-temperature.aspx.

[2] Columbus, Louis, "2015 Roundup Of 3D Printing Market Forecasts And Estimates," *Forbes* Available: http://www forbes.com/sites/louiscolumbus/2015/03/31/2015-roundup-of-3d-printing-market-forecasts-and-estimates/.

[3] Jacobs, P. F., *Rapid Prototyping & Manufacturing: Fundamentals of Stereolithography*, Society of Manufacturing Engineers, 1992.

[4] "3D Printing in Space Is Really Hard (Interview with Quincy Bean)," *Motherboard* Available: http://motherboard.vice.com/read/3d-printing-in-space-is-really-hard.

[5] "DIY 3D Printing: Mataerial thermosetting polymers 3d printing."

[6] Compton, B. G., and Lewis, J. A., "3D-Printing of Lightweight Cellular Composites," *Advanced Materials*, vol. 26, Sep. 2014, pp. 5930–5935.

[7] Chuang, K., Hughes, T. W., Avakian, R., and Hu, L., *Reactive Extrusion of High Temperature Resins for Additive Manufacturing*, 2013.

[8] Chuang, K. C., Grady, J. E., Arnold, S. M., Draper, R. D., Shin, E., Patterson, C., Santelle, T., Lao, C., Rhein, M., and Mehl, J., *A Fully Nonmetallic Gas Turbine Engine Enabled by Additive Manufacturing, Part II: Additive Manufacturing and Characterization of Polymer Composites*, 2015.

[9] Jia, Y., Sun, K., Agosto, F. J., and Quiñones, M. T., "Design and characterization of a passive wireless strain sensor," *Measurement Science and Technology*, vol. 17, Nov. 2006, p. 2869.

[10] Tata, U., Huang, H., Carter, R. L., and Chiao, J. C., "Exploiting a patch antenna for strain measurements," *Measurement Science and Technology*, vol. 20, Jan. 2009, p. 015201.

[11] Yi, X., Wu, T., Wang, Y., Leon, R. T., Tentzeris, M. M., and Lantz, G., "Passive wireless smart-skin sensor using RFID-based folded patch antennas," *International Journal of Smart and Nano Materials*, vol. 2, Feb. 2011, pp. 22–38.

[12] Zhang, Y., and Bai, L., "Rapid structural condition assessment using radio frequency identification (RFID) based wireless strain sensor," *Automation in Construction*, vol. 54, Jun. 2015, pp. 1–11.

[13] *Report Card for America's Infrastructure*, American Society of Civil Engineers, 2013.

Slow-Light-Enhanced Spectral Interferometry

Jamiu A. Odutola[1] and David D. Smith[2]
NASA Marshall Space Flight Center, Space Systems Department, Optics and Imaging Branch, ES34 Huntsville AL 35812

I. Introduction

Interferometry is an important metrology tool in the physical sciences. Interferometer can measure length changes. It can measure distances in the range of nanometers and smaller. In spectral interferometers the fringes produced by the length changes are different for different wavelengths resulting in the beating of fringes. By taking the Fourier transform these frequency changes can be resolved. In this way an interferometer can provide a sensitive means of resolving closely spaced frequencies. Such spectral interferometers find uses in diverse area such as Fourier Transform infra-red (FTIR) spectroscopy used in chemistry to interpret the organic functional groups and to discriminate the samples from impurities.

There are many academic, industrial, and government applications of spectroscopic interferometers. Many of the early NASA exploratory missions[1] employed different versions of the Infrared Interferometer Spectrometer and Radiometer (IRIS). Among these missions are: the first planetary orbiter in 1962 - Mariner-9, the twin spacecraft launched in 1977 - Voyager-1 and Voyeger-2, and the 1964 NOAA satellites Nimbus-3 and Nimbus-4. A later variant, the Thermal Emission Spectrometer (TES) was used in the Mars Global Surveyor mission in 1996. Closer to home, NASA monitors our lowest atmospheric activities by using the Far-Infrared Spectroscopy of the Troposphere (FIRST) and In-situ Net FLux within the AtMosphere of the Earth (INFLAME). The incessant climatic activities on earth prompted NASA to propose a mission for continuous long term close monitoring of our planet through the CLimate Absolute Radiance and REflectivity Observatory (CLARREO) project both from earth and from the international space station, which involves infrared spectrometers and infrared reflected solar spectrometers. CLARREO impacts many sectors namely: civil and military governments, industrial and human activities. There is also the ObseRvations of Aerosols above CLouds and their intEractionS (ORACLES) mission with several instruments which include a cavity-enhanced absorption spectrometer to measure aerosol extinction. Optical properties, such as cavity transmission, are strongly affected by small changes in additional loss and these changes can be used to quantitatively determine the extinction of an aerosol sample contained within the cavity.[2,3] The Aura satellite, launched in 2004, also carried infrared instruments designed to study troposphere's chemistry by monitoring the air pollution on a daily basis.

The spectral sensitivity of an interferometer depends on the length difference ΔL between the arms. Therefore the usual method for enhancing resolution is to make the interferometer larger, but this obviously has its drawbacks in space missions where weight and volume are at a premium. Here we discuss an alternative method that does not require increasing ΔL or instrument size by introducing a slow-light element into the interferometer.

Slow-light is the case where the group velocity is less than the phase velocity of light and this occurs when $dn/d\omega > 0$, where n is the refractive index of the medium and ω is the frequency. The quantity $dn/d\omega$ is proportional to the group index; n_g which in some materials can be extremely large.[4,5,7] As we will demonstrate, by incorporating slow-light medium we can increase the resolving power of spectral interferometers without increasing their size, resulting in high resolution compact instrument.

This project employs a Mack-Zehnder (M-Z) interferometer where a light beam is first split into two by a beam splitter (BS1), and each beam is subsequently sent through the two arms of the interferometer and recombined by the second beam splitter (BS2). The objective is to determine the phase difference between the two paths. We can introduce a slow-light material or cavity, or a sequence of such elements, into one of the interferometer arms to vary

[1] Associate Professor of Chemistry, Department Physics, Chemistry and Mathematics, College of Engineering, Technology and Physical Sciences, Alabama A&M University Normal AL 35762.
[2] David D. Smith, PhD, (Physicist), NASA Marshall Space Flight Center, Optics and Imaging Branch, Huntsville AL 35812.

the path length and therefore effect a phase difference. The total phase difference is then determined by sum of the path length difference and the phase shift introduced by the additional element. The phase difference between the two arms can be adjusted, either by physically changing the length of one of the arms with respect to the other, or by varying the phase shift of the slow-light element, and this produces fringes which can be recorded on a photo-detector placed after the second beam splitter. Usually spectral interferometers utilize the first method, which necessitates the use of a very large instrument to accommodate the large path length difference between the beams. The IRIS instruments, therefore, have been large and heavy instruments. Our aim is to use the latter method, i.e, produce fringes by changing the phase of the slow-light medium, thereby eliminating the need for a large instrument.

II. Mach-Zehnder Interferometer

A schematic diagram of the M-Z interferometer is presented in figure 1. The light source passes through BS1 taking two distinct paths. The lower path passes through a slow-light element of length *L*. In figure 1 this element is a Fabry-Perot cavity having mirror reflection coefficients r1 and r2. The two beams are recombined at BS2 and each interference pattern can be detected by a photodiode at A or B. Alternatively, the signals at A and B can be subtracted to yield the homodyne (AC) signal.

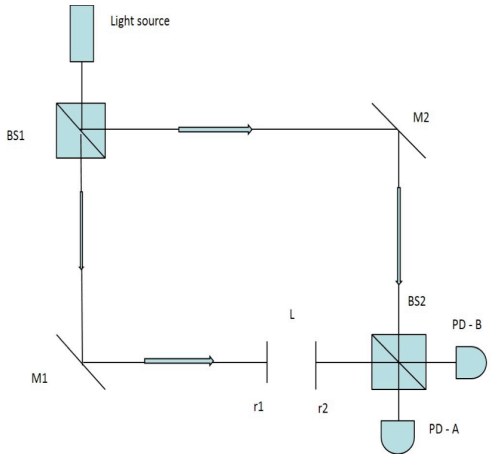

Figure 1. A schematic diagram of Mach-Zehnder Interferometer. *BS1 and BS2 are the beam splitters, M1 and M2 the mirrors, PD-A and PD-B are the photo-detectors. r1 and r2 are the mirror reflection coefficients of the Fabry-Perot cavity*

III. Theory

For the case of one cavity in the interferometer and considering the case of an input with multiple frequencies we must integrate over the frequencies. The output intensity, $I_{out}^{\pm}$, that is recorded after the BS2 is

$$I_{out}^{\pm} = \frac{1}{4}\int I_{in}(\nu)\left|1 \pm t(\nu)e^{\quad}\right| d\nu \,, \tag{1}$$

where $\tau(\omega)$ and $\Phi(\omega)$ take into account the transmittance and phase shift introduced by the slow-light element, $\Delta L = L_1 - L_2 - L$ is the path difference between the two beams subtracting off the length of the slow-light element, and the superscript + or – refers to the bright (A) at the photo-detector PD-A or dark (B) at photo-detector PD-B interferometer outputs. The total difference between the arms can be defined as $\Delta f = \Phi + k_0 \Delta L$. Then, Eq. (1) can be rewritten as

$$I_{out}^{\pm} = \frac{1}{4}\int I_{in}(\omega)\left(1 + \tau^2(\omega) \pm 2\tau(\omega)\cos\quad \phi(\omega)\right) d\omega \,. \tag{2}$$

The homodyne signal can be obtained by subtracting the bright and dark signals,

$$I_{out}^{+} - I_{out}^{-} = \int I_{in}(\nu)\cdot t(\nu)\cdot \cos\Delta f\ (\nu)\, d\nu \,. \tag{3}$$

The advantage of the homodyne signal is that it eliminates the DC signal as well as some of the changes in the intensity due to $\tau(\omega)$.

We refer to the interferometer as being balanced when $\Delta L = 0$. Changing the path length difference ΔL will cause the two paths to be unbalanced and will produce fringes which is equivalent to what is observed in the traditional Fourier Transform Infra-Red (FTIR) spectrometer. On the other hand, note that we can also produce fringes by varying $\Phi(\omega)$. The consequence of this is a change in the group index, n_g. This is a key point for the research undertaken here.

The M-Z interferometer in figure 1 has a slow-light element in the lower arm which we can associate with the refractive index *n* and the path length *L* across the medium therefore the phase difference between the two arms of the interferometer is $\Delta\Phi_{medium}$ according to Zhimin, Shi et. Al.[6]

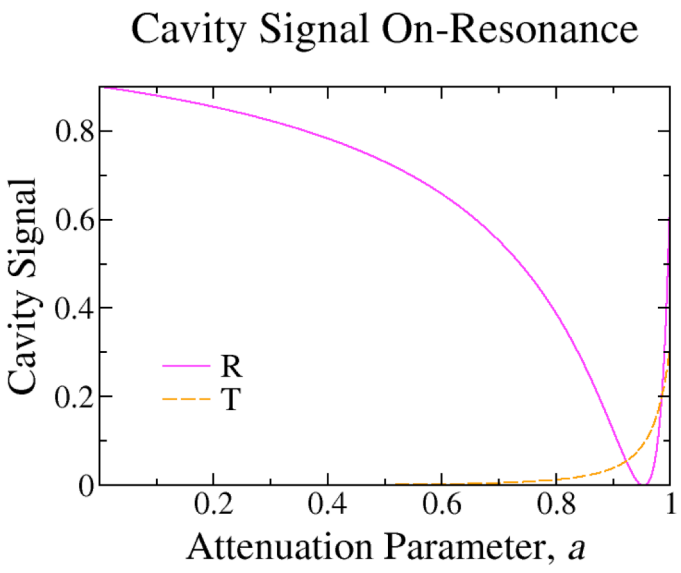

Figure 2: Cavity reflection and transmission versus the attenuation parameter *a*. *Parameters used for these calculations include path length L = 0.3m, r1 and r2 are the mirror reflection coefficients r1= √0.9, r2 = √0.99 and the mirror absorptions b1 =*

$$\frac{d\Delta\Phi_{medium}}{d\omega} = \frac{(L/c)d[n(\omega)]}{d\omega} = (L/c)[n(\omega) + \omega\frac{dn}{d\omega}] = n_g(L/c) \quad \textbf{(4)}$$

We implement the slow light interferometer by keeping the path length *L* constant and vary the group index. The expression $d\Delta\Phi_{medium}/d\omega$ represents the variation of phase difference with respect to the change in frequency and this quantity is used to describe the sensitivity of the interferometer. A large value of this quantity indicates a very sensitive interferometer. The group index is in turn proportional to the sensitivity of the interferometer.

It is important to note that transmission of a cavity always displays slow-light irrespective of whether the cavity is over-coupled or under-coupled. On the other hand reflection of a cavity can show both slow-light or fast-light depending on the coupling; ($r_1 > r_2.a$, is the case of under-coupling implying a fast-light). For the case when $r_1 = r_2.a$, this is the critical-coupling and it occurs at the transition from slow and fast light.

We may compare the relative sensitivity of an M-Z interferometer for the case where there is a cavity in the lower arm to the one without a cavity. The result is presented in equation (5). This equation predicts that the relative sensitivity approaches unity when there is large difference in path length, *ΔL*. However when the path length is balanced then the relative sensitivity approaches the group index.

$$\frac{d\Delta\Phi/d\omega}{d\Delta\Phi^{(empty)}/d\omega} = \frac{n_g + \Delta L/L}{1 + \Delta L/L} \quad \textbf{(5)}$$

For the interferometer using a slow-light medium and involving a large group index, the sensitivity can be enhanced tremendously.

It is expected that the interferometer will have equal intensity when there is no slow-light element. For any interferometer the minimum detectable angular frequency shift, $\Delta\omega_{min}$ is given by the ratio of the fringe width to the signal-to-noise ratio (S/R). There is reduction in S/R due to the presence of slow-light element compared to the empty cavity. The consequence of this is that the ratio of $\Delta\omega^{sl}{}_{min}$ (for the slow light element) to $\Delta\omega^{empty}{}_{min}$ (for

the empty cavity) produces a reduction in the minimum detectable shift in frequency. The inverse of the expression $\Delta\omega^{sl}{}_{min} / \Delta\omega^{empty}{}_{min}$ is referred to as the Resolution Enhancement and may be defined as the ratio of $\Delta\omega^{(empty)}{}_{min} / \Delta\omega^{sl}{}_{min}$. This Resolution Enhancement is given in equation (6).

$$\frac{\Delta\omega_{\min}^{(empty)}}{\Delta\omega_{\min}^{sl}} = n_g \cdot \sqrt{\frac{2R}{(1+R)}} \qquad (6)$$

IV. Discussion

A plot of the calculated[8] reflection and transmission versus the attenuation parameter *a,* is presented in figure 2. The parameters used for the plots are: cavity path length, L is 0.3 m, the reflection coefficients r_1 and r_2, are $\sqrt{0.9}$ and $\sqrt{0.99}$ respectively and the mirror absorption b_1 and b_2 are each zero. The critical coupling of the cavity occurs at $a = 0.9535$. This corresponds to $r_1 = r_2.a$. Notice also that Reflectance drops to zero at this point.

Figure 3 is a plot of group index versus the attenuation parameter *a*, for both the case of reflection and transmission. The plot for reflection displays cavity over-coupling $r_1 < r_2.a$ to the right of the critical coupling and under-coupling $r_1 > r_2.a$ to the left. Importantly, a pole in the group index occurs at the critical coupling where $r_1 = r_2.a$. This pole is indicative of higher sensitivity.

In figure 4 we calculated large enhancement values for the slow-light in reflection. The reflection shows a much larger enhancement than the transmission. As a result of the pole occurring in reflection for the plot of group index in figure 3 there is a higher sensitivity enhancement for reflection.

V. Conclusion

Our analysis shows that: (i) the slow-light interferometer has no better spectral sensitivity than the slow-light medium itself. This can be seen by comparing equation (5) and (7)

$$\frac{d\Delta\phi / d\omega}{d\Phi / d\omega} = \frac{n_g + \Delta L / L}{n_g}, \qquad (7)$$

in the limit of ΔL approaching zero. (ii) At the resonance frequency, although the group index changes with the attenuation parameter, the phase shift does not. Hence fringes do not result. Therefore, the function $d\Phi / d\omega$ (or group index) does not provide the only figure of merit for slow light interferometers. The change in the phase shift with changes in attenuation parameter *a*, $d\Phi / da$ (or alternatively the change in phase shift with changes in the group index, ($d\Phi / dn_g$) should also be considered.

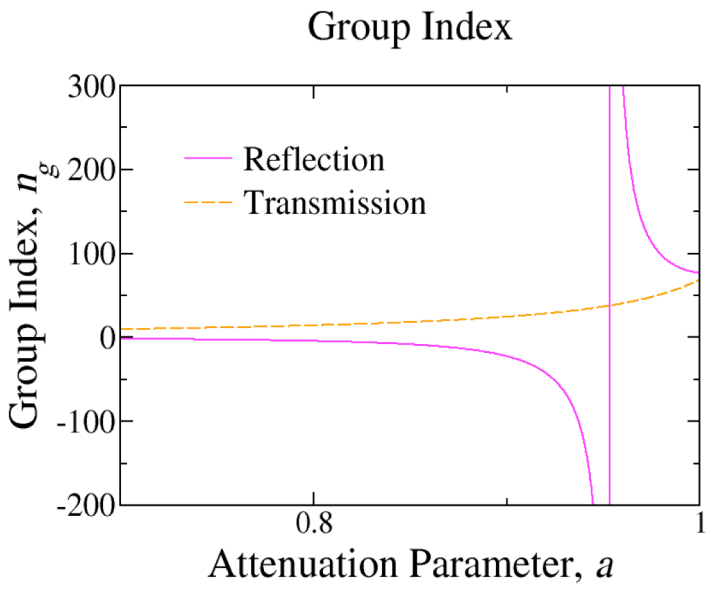

Figure 3: Cavity group index versus the attenuation parameter *a*

(iii) Even in cases where $d\Phi/da$ is large, fringes were not produced for a single cavity because the plot of $d\Phi/da$ vs. a showed a sharp peak. This is indicative of the use of only one cavity. It may be possible to use multiple cavities to produce a broader feature to produce such fringes.

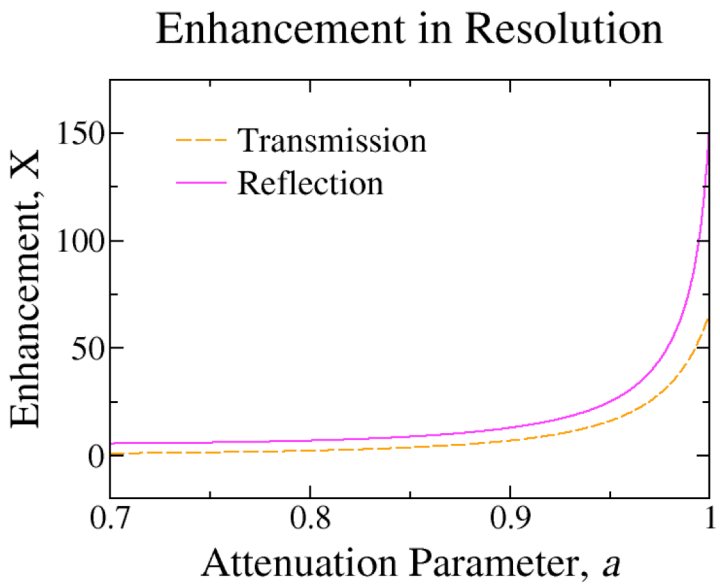

Figure 4: Cavity enhancement versus the attenuation parameter *a*

Acknowledgments

I would like to express my profound gratitude to Dr. David D. Smith, my NASA colleague for the invaluable time spent with me on this project. I am also very grateful to the optics and imaging branch in building 4487 for their hospitality. My gratitude extends to Dr. Frank Six (of the NASA MSFC Education office) and the Summer Faculty Fellowship program committee members for giving me opportunity to work at the NASA MSFC this summer. I would like to thank Dr. Gerald Karr the summer Faculty Fellowship program Manager/coordinator and the supporting NASA MSFC Education Office staff for organizing the educative and inspiring seminars and for planning the after hour activities particularly for faculty members from out town. Finally my gratitude goes to the Fellow faculty members for their fellowship and making my summer 2015 a memorable and productive one.

References

Periodicals

[2]Berden G., Peeters, R., Meijer, G., "Cavity Ring-Down Spectroscopy, Experimental Schemes and Applications", *Int. Rev. Phys. Chem*., Vol. *4*, 2000, pp 565-607.

[3]Anthony O'Keefe; T. Kan, D. Deacon; "High sensitivity atmospheric transmission measurements using a cavity ring-down technique", *Appl. Opt.*, Vol. 27, 1988, pp 4606-4608.

[4]Myneni, K., Smith, D.D., Odutola, J.A., Schambeau, C.A., "Tuning the scale factor and sensitivity of a passive cavity with optical pumping", *Phys. Rev. A* Vol. 85, 2012 pp 063813.

[5]Smith, D.D., Myneni, K., Odutola, J.A., Diels J.C., "Enhanced sensitivity of a passive optical cavity by an intracavity dispersive medium", *Phys. Rev. A* Vol. 80, 2009, pp 011809

[6]Zhimin Shi, Robert W. Boyd, Daniel J. Gauthier and c. C. Dudley, "Enhancing the spectral sensitivity of interferometers using slow-light media", *Optics Lett*. Vol. 32, 2007 pp 915.

Proceedings

[7]D. D. Smith, K. Myneni, H. Chang, A. Toftul, C. Schambeau, J. A. Odutola, and J. C. Diels, "Tuning the sensitivity of an optical cavity with slow and fast Light," *Proc. SPIE 8273, 82730T in Advances in Slow and Fast Light* V; S. M. Shahriar and F. A. Narducci; Eds., (2012).

Electronic Publications

[1]URL: http://www nasa.gov/missions [cited 14 August 2015].

Computer Software

[8]R version 3.2.1 (2015-06-18) -- "World-Famous Astronaut" Copyright (C) 2015 The R Foundation for Statistical Computing Platform: x86_64-w64-mingw32/x64 (64-bit)

Adaptive Time Stepping Scheme For Enhancing Transient Simulation Capability of GFSSP

S.S. Ravindran [1]
The University of Alabama in Huntsville, Huntsville, AL 35899

An adaptive time stepping algorithm is presented for enhancing GFSSP's capability for simulating fluid and thermal transients in rocket propulsion systems. The algorithm uses linear feedback control theory to design a new automatic time step size selection algorithm. In order to show feasibility and applicability of the algorithm, it is used to predict pressure surges in a pipeline that has entrapped air at one end of the pipe. A network flow simulation software (Generalized Fluid System Simulation Program) based on the finite volume method has been employed for spatial discretization. Numerical predictions are compared with available experimental data and are found to be in good agreement. It is found that the use of the time adaptivity can not only resolve the steady-state solutions but also the dynamical changes of the solution accurately and efficiently. Numerical experiments show significant savings in CPU time in long time simulations. These experiments also show that adaptive time step selection can also improve the convergence behavior of the nonlinear iterative solver leading to further reduction in CPU time.

I. Introduction

In dynamic analysis of rocket propulsion systems, fast and accurate simulations of fluid and thermal transients is crucial for their design and operation. For instance, in propellant feed-line system accurate prediction of pressure surges due to sudden opening and closing of valves is very important from the structural point of view. It is therefore essential that the fluid transients are predicted accurately for satisfactory performance of rocket propulsion system.

In spite of great advances in computational methodologies for solving complex fluid transient problems, there has been an increasing need for improved algorithms such as automatic (adaptive) time stepping algorithms that allow one to choose the largest possible step size while maintaining a prescribed accuracy. Adaptive time stepping has been well studied for solving initial value problems in ordinary differential equations. For explicit schemes, the time step size is primarily determined by the stability condition considerations. In [1], a step size selection has been proposed in which the step size is selected based on the "apparent highest frequency", see [2] for additional references for adaptive time step selection for explicit time stepping schemes. For implicit time stepping schemes, adaptive time step selection has been proposed using the concept of "apparent current frequency" in [3]. Such a concept is limited only to vibration problems and even if it can be defined it may be close to zero. In [4], two adaptive time stepping schemes have been compared with fixed time stepping schemes for coupled flow and deformation models. In their work, the schemes use a so called pore pressure method to adjust the time step. In unconditionally stable implicit schemes like the one used in this work, the time step size selection is entirely based on accuracy considerations. In single step algorithms, an "error per step" method is used for the step size control [5,6,7,8] in which one chooses the time step size in such a way that the local error of each step is roughly equal to a prescribed tolerance. The local error is normally estimated by comparing the numerical results when different step sizes are used [5] or by comparing the computed solutions when two different order methods are used [7]. However, the computational cost for the error estimate is high for both methods.

[1] Professor, Department of Mathematical Sciences and Propulsion Research Center; ravinds@uah.edu, Member SIAM and ASME.

Signal processing mechanisms and digital filters have been applied to adaptive time stepping design in [9].

In this work, we investigate the feasibility of applying adaptive time stepping for semi-discrete systems arising in network fluid flow models. In particular, we will consider finite volume based network flow modeling computer program called the Generalized Fluid System Simulation Program (GFSSP) [10]. GFSSP has been developed at NASA Marshall Space Flight Center (MSFC) to calculate network flow distribution in propulsion systems applications. The GFSSP has been extensively validated by comparing its predictions with test data and other numerical methods [11] for applications such as internal flow of the turbopump, propellant tank pressurization, and chill down of a cryogenic transfer line [12]. However, no attempt has been made in GFSSP to monitor the adequacy of the time step size for the particular solution behavior. We therefore study a proportional-integral-derivative feedback control algorithm based on controlling accuracy for semi-discrete systems arising in network fluid flow model applications and integration of this procedure into GFSSP. The control utilizes normalized changes in the unknown variables in the systems such as flow rate, pressure and temperature to compute the local errors. The proposed adaptive scheme is effective for highly oscillatory transients and long time simulations. The efficiency of the adaptive time stepping algorithm is compared with the fixed time stepping already included in the GFSSP code. We show that, with the adaptive scheme, we obtain solutions with a smaller number of time steps without any loss of accuracy. Feasibility and applicability of PID adaptive time stepping scheme is demonstrated in an example problem in which it is used to predict pressure surges in a pipeline that has entrapped air at one end. Numerical predictions by the proposed approach are validated by comparing the results with experimental data available in the literature.

II. Network Fluid Flow Modeling

A network fluid flow simulation software based on finite volume method (GFSSP [10]) has been used to model the example application problem in Section IV. The GFSSP is a general-purpose finite volume-based network flow analysis code. A fluid system is discretized into nodes and branches. Mass-conservation and energy-conservation are solved at the fluid nodes, whereas momentum-conservation equations are solved at the flow branches in conjunction with the thermodynamic equation of state. Fluid enters into the flow network through inlet boundary nodes. The mass and energy conservation equations are solved at the flow nodes, whereas momentum conservation equations are solved at the flow branches. The fluid exits the flow network through the outlet boundary node.

The GFSSP employs a pressure-based algorithm; therefore, pressure is calculated from the mass-conservation equation. It also uses a hybrid solution scheme that consists of a simultaneous and successive substitution method of solving nonlinear conservation equations. The mass and the momentum conservation equations and the equation of state are strongly coupled and solved simultaneously by the Newton–Raphson method, whereas the energy equation is solved by a fixed point iteration method. The GFSSP is integrated with the thermodynamic property programs GASP and WASP, which provide required thermodynamic and thermophysical properties in all conservation equations during iterative calculation.

III. Adaptive Time Stepping Strategies

In the adaptive time stepping scheme described below the time step selection is cast as a feedback control problem. In this approach, one estimates the change in the computed solution and compares it with a given tolerances, and the result is fed back to find the proportional integral derivative feedback control, we may define the new time step as

$$\Delta t_{n+1} = \left(\frac{e_{n-1}}{e_n}\right)^{k_p}\left(\frac{tol}{e_n}\right)^{k_I}\left(\frac{e_{n-1}^{\,2}}{e_n e_{n-2}}\right)^{k_D}\Delta t_n$$

where k_p, k_I and k_D are the feedback gain parameters. Moreover, $e_n = \max(e^{\dot{m}}, e^{p}, e^{H})$, where $e^{\dot{m}}$, e^{p}, e^{H} are normalized changes in flow rate, pressure and enthalpy, respectively. For example, $e^{p}=\|p_n - p_{n-1}\|/\|p_n\|$, where $\|p\|$is the maximum norm defined by $\|p\|=\max_i p_i$. The computational cost in computing the new time-step Δt_{n+1} as above in (6) is negligible as it involves storing a few extra vectors and computation of norms. We employ time-step limiters Δt_{min} and Δt_{max} to prevent too small and too large time step sizes. These limiters reduce both overshoot and control effort in the feedback system. In the examples studied in this paper, we fix the feedback gain parameters to be $k_p=0.1125$, $k_I=0.2625$, $k_D=0.015$ for all the simulations.

IV. Numerical Results

In this example, we consider the water-hammer (pressure surge) problem in a straight pipe with entrapped air due to sudden valve opening. This problem has been experimentally studied in [13] and [14], for example. Recently, this problem has been studied numerically using GFSSP in [15] and the numerical results were compared with experimental data. In the experimental work, a liquid water tank is attached to a long pipe that is closed at the other end, as shown in Figure 1. The water and air are separated by a valve. The valve is slowly

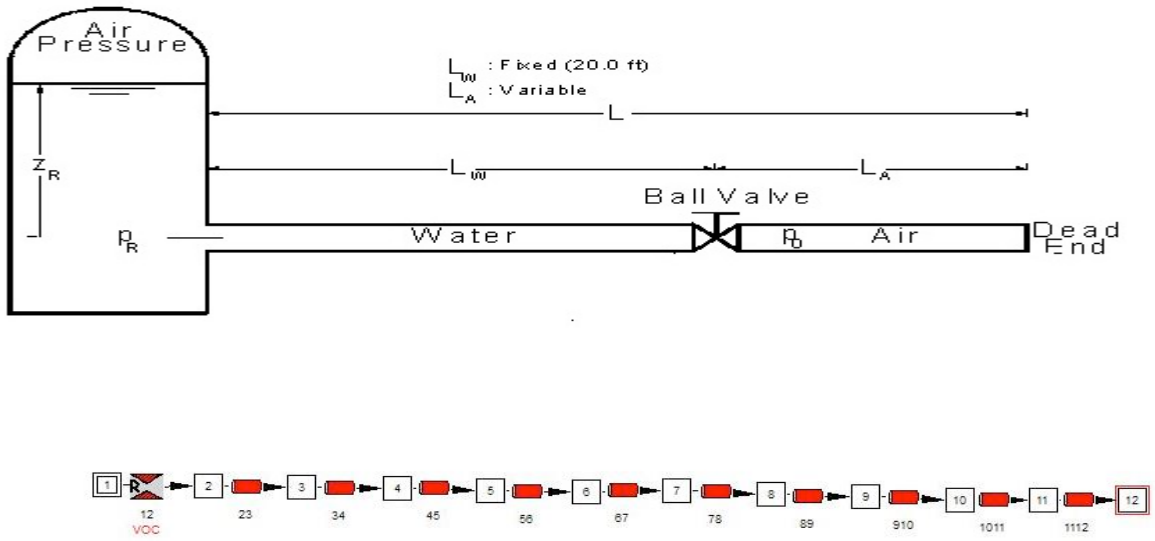

Figure.1 Schematic of waterhammer experimental setup [15] (top) and a ten-branch GFSSP model (bottom).

opened from 0% opening to 100% opening. The two controlling parameters are the ratio of the tank pressure to the initial pressure P_R and the ratio of air column length L_A to the total length of the pipe α ($=L_A/L_w$). The initial water column length L_w is fixed at 20ft and the air column length is varied. The pipe diameter is 1.025 inches and the initial pressure and temperature of air and water are at 14.7 psia and 60^0F, respectively. All the numerical experiments reported in this paper were carried out for about 45% initial air volume (α=0.4491).

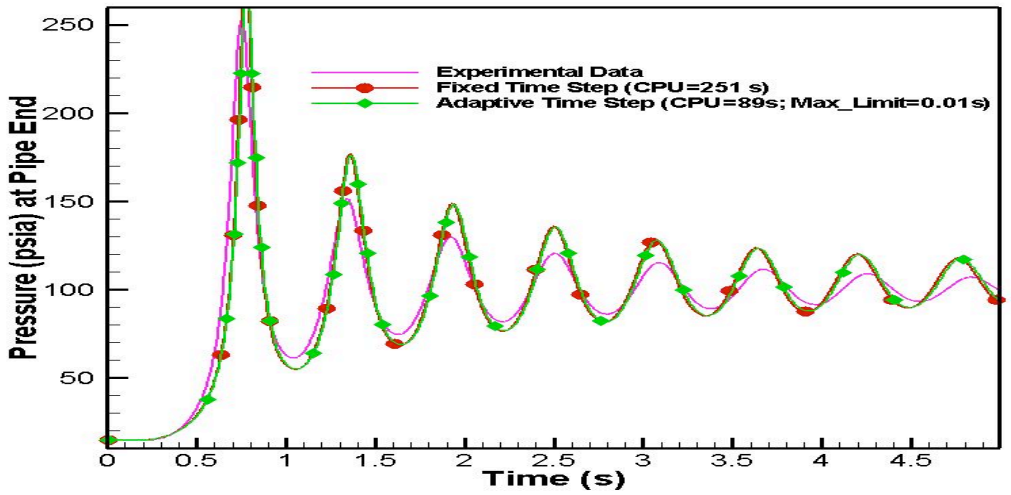

Figure 2. Predicted air pressure using adaptive time-stepping scheme for P_R =7 at about 45% initial air volume (α=0.4491). Also shown are the predicted air pressure using fixed time step and experimental data.

For this model problem, we compare the numerical results obtained from the adapted time stepping scheme with fixed time stepping scheme and experimental data. Figure 2 shows the transient pressure at the end of the pipe with α=0.449. As observed from this plot, numerical results using the adaptive time stepping scheme matches quite well with that of the fixed time stepping scheme results and experimental data.

It also shows the CPU time needed to compute this problem using fixed time step and adaptive time step. As we can see, we obtain solutions with significantly less computational time. The computational time reduction is about one tenth even when the spatial grid is refined. For each case we also calculate the number of Newton/fixed point iterations from nonlinear solver and the number of time steps. We start with a time step-size of 0.005, and we set a minimum and maximum time steps of 0.001 and 0.01, respectively. Figure 3 shows the time-step size against time (left) and the number of nonlinear iterations against time (right) with adaptive time-stepping strategy and with fixed time step. In our experiments, if the time step size is bigger than the maximum time step allowed, then the step size is set to a fixed value of $\Delta t_{max} = 0.01$. Moreover, if the number of nonlinear iterations obtained is larger than the maximum number of nonlinear iterations allowed, the maximum number of iterations is set at $ITER_{max} = 2000$. As a consequence, we can observe that at the end of the process, the timestep sizes are kept equal to the maximum size allowed. Moreover, the adaptive time stepping strategy produces larger time steps and decrease in nonlinear (Newton/Fixed point) iterations. In order to verify the robustness of the adaptive algorithm with respect to controlling parameters, we used it to compute the problem for several different values of P_R (ratio of the tank pressure to the initial pressure). Figures 4-9 show the computational results with fixed and adaptive time step for P_R=6,5, and 4, respectively. The results seem to confirm our conclusions about the accuracy, efficiency and applicability of the adaptive algorithm proposed in this paper.

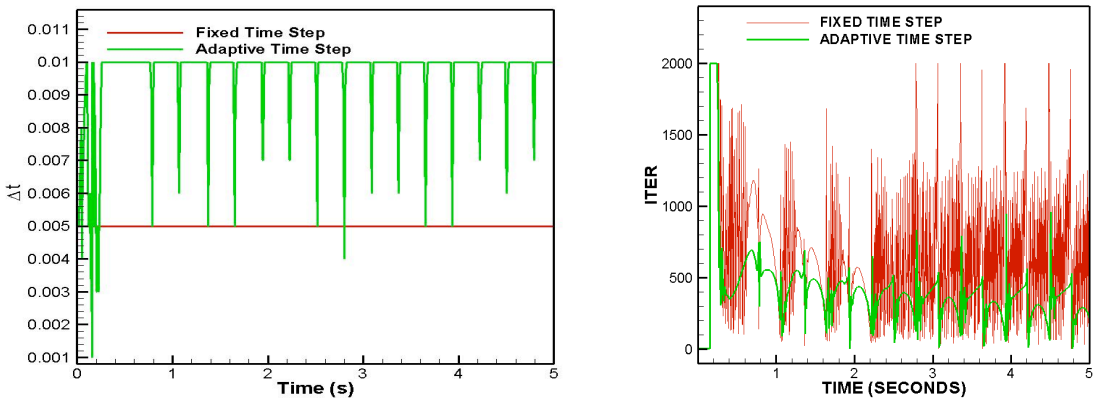

Figure 3. Timestep variation (left) and nonlinear iterations (right) as a function of time with adaptive time-stepping and with fixed time stepping (P_R=7).

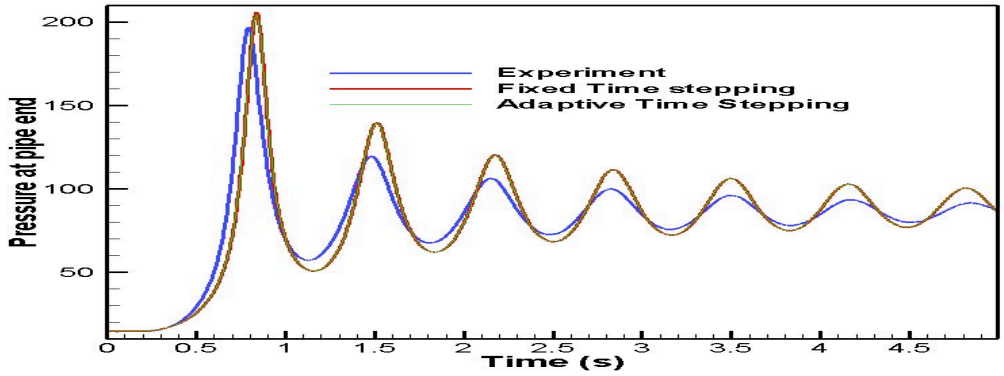

Figure 4. Predicted air pressure using adaptive time-stepping scheme for P_R =6 at about 45% initial air volume (α=0.4491). Also shown are the predicted air pressure using fixed time step and experimental data.

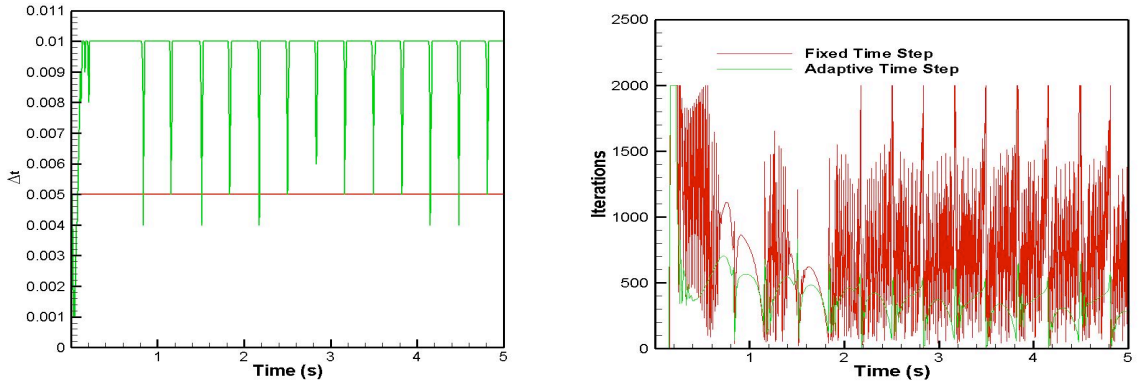

Figure 5. Timestep variation (left) and nonlinear iterations (right) as a function of time with adaptive time-stepping and with fixed time stepping (P_R=6).

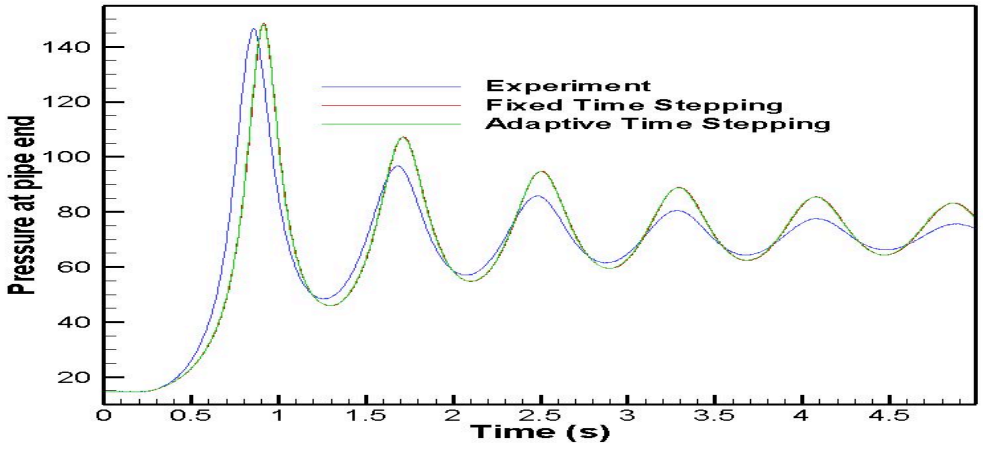

Figure 6. Predicted air pressure using adaptive time-stepping scheme for P_R =5 at about 45% initial air volume (α=0.4491). Also shown are the predicted air pressure using fixed time step and experimental data.

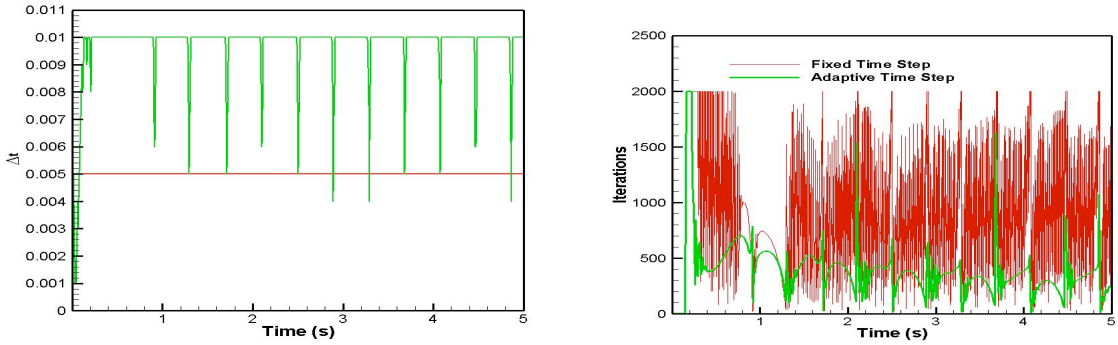

Figure 7. Timestep variation (left) and nonlinear iterations (right) as a function of time with adaptive time-stepping and with fixed time stepping (P_R=5).

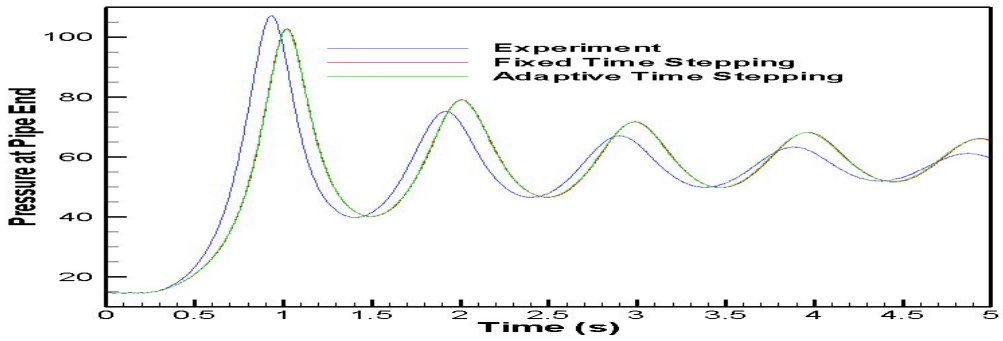

Figure 8. Predicted air pressure using adaptive time-stepping scheme for P_R =4 at about 45% initial air volume (α=0.4491). Also shown are the predicted air pressure using fixed time step and experimental data.

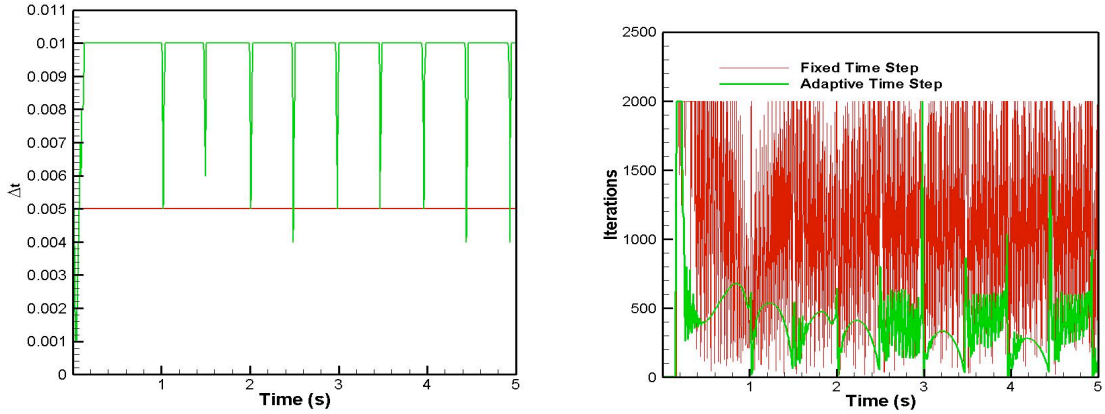

Figure 9. Timestep variation (left) and nonlinear iterations (right) as a function of time with adaptive time-stepping and with fixed time stepping (P_R=4).

V. Conclusion

This paper presents an adaptive time stepping algorithm for network flow simulation of fluid and thermal transients in rocket propulsion systems. The algorithm uses linear feedback control theory to design the automatic timestep size selection. The algorithm was tested for predicting pressure surges in a pipeline that has entrapped air at one end of the pipe. A network flow simulation software (Generalized Fluid System Simulation Program) based on the finite volume method has been employed for spatial discretization. Numerical experiments show significant savings in CPU time in long time simulations. These experiments also show that adaptive time step selection can also improve the convergence behavior of the nonlinear iterative solver leading to further reduction in CPU time.

Acknowledgments

This work was supported by a fellowship awarded to S. S. Ravindran under the NASA Summer Faculty program. The author was also supported in part by a grant from NASA Tech Excellence Program. The work was conducted at Marshall Space Flight Center, Huntsville, Alabama, in the ER43/Thermal Analysis Branch. The author would like to thank Alok Majumdar of the Thermal Analysis Branch for useful discussion and help with GFSSP.

References

[1] Park, K.C. and Underwood, P.G., *A variable-step central difference method for structural dynamics analysis-Part I: Theoretical aspects,* Computer Methods in Applied Mechanics and Engineering, 22(1980), pp. 241-258.

[2] Underwood, P.G. and Park, K.C., *A variable-step central difference method for* structural dynamics analysis-Part I: *Implementation and Performance Evaluation***,** Computer Methods in Applied Mechanics and Engineering, 23(1980), pp. 259-279.

[3] Bergan, P.G. and Mollestad, E., *An automatic time stepping algorithm for dynamic problems*, Computer Methods in Applied Mechanics and Engineering, 49 (1985), pp. 299-318.

[4] Minkoff, S. E. and Kridler, N. M., *A comparison of adaptive time stepping methods for coupled flow and deformation modeling*, Appl. Math. Modelling, 30 (2006), pp. 993–1009.

[5] Gear, C.W., *Numerical Initial Value Problems in Ordinary Differential Equations*, Prentice Hall, Englewood Cliff, N.J., 1971.

[6] Johnson, C., *Error estimates and adaptive time step control for a class of one step methods for stiff ODEs*, SIAM Journal of Numerical Analysis, 25 (1988), pp. 908-926.

[7] Thomas, R.M. and Gladwell, I., *Variable-order variable-step algorithms for second order systems-Part I: The method*, International Journal of Numerical Methods in Engineering, 26 (1988), pp. 39-53.

[8] Zienkiewicz, O.C., Wood, W.L., Hine, N.W. and Taylor, R.L., *A unified one-step algorithms-Part I: General formulations and Applications,* International Journal of Numerical Methods in Engineering, 20(1984), pp. 1529-1552.

[9] Soderlind G., *Digital filters in adaptive time-stepping*, ACM Transactions on Mathematical Software, 29(1) (2003), pp. 1-26.

[10] Majumdar, A. K., LeClair, A. C., Moore, R., and Schallhorn, P. A., *Generalized Fluid System Simulation Program*, Version 6.0, NASA TM-2013-217492, Oct. 2013.

[11] Majumdar, A. and Ravindran, S.S, *Numerical Prediction of Conjugate Heat Transfer in Fluid Network***,** AIAA Journal of Propulsion and Power**,** Volume 27 (3), pp.620-630, 2011.

[12] Alok Majumdar and S.S. Ravindran, *Fast, Nonlinear Network Flow Solvers for Fluid and Thermal Transient Analysis*, International Journal of Numerical Methods for Heat and Fluid Flow, Volume 20(6), pp. 617-637, 2010

[13] Lee, N. H., and Martin, C. S., *Experimental and Analytical Investigation of Entrapped Air in a Horizontal Pipe*, Proceedings of the 3rd ASME/JSME Joint Fluids Engineering Conference, American Soc. Of Mechanical Engineers, Fairfield, NJ, July 1999, pp. 1–8.

[14] Lee, N. H., *Effect of Pressurization and Expulsion of Entrapped Air in Pipelines*, Ph.D. Thesis, Georgia Inst. of Technology, Atlanta, Aug. 2005.

[15] Bandyopadhyay, A and Majumdar, A.K., *Network Flow Simulation of Fluid Transients in Rocket Propulsion System*, Journal of Propulsion and Power, Vol. 30, No. 6 (2014), pp. 1646-1653.

The Ultra-HiTEMS Instrument: Impact of Temperature Matching of Sample and Blackbody Reference

Patrick J. Reardon, PhD[1]
The University of Alabama in Huntsville, Huntsville, AL 35899

Trudy L. Allen, David J. Vermilion, and Jan R. Rogers
NASA Marshall Space Flight Center, Huntsville, AL 35812

The Ultra-HITEMS instrument at NASA/MSFC measures emissivity of samples at high temperature (up to 2000C). The system consists of five independent devices coupled through optics, software and/or operation. Emissivity measurements are made by comparing the spectral radiant emittance of a sample to a calibrated blackbody source at the same temperature. This paper discusses the impact of a temperature mismatch between the sample and blackbody on the emissivity measurements.

I. Introduction

The Ultra-HITEMS (High Temperature Emissivity) instrument at NASA/MSFC is a multi-component system for measuring the emissivity of high temperature samples. Originally completed in 2007, the instrument was shown to measure the emissivity of some specific, known samples. A detailed review of the operation of this system, at a component-by-component level, was performed. This paper presents a discussion of one aspect of the instrument, temperature matching between the sample under test and the blackbody reference, and how that affects the measurements made by the system. The rest of this paper is organized as follows. Section 2 briefly describes the operation of the system, with a description of the individual components and how they interact. Section 3 discusses temperature matching error and its impact on measurements.

II. Ultra-HITEMS Operation

This section presents both the fundamental basis for, and step-by-step operation of the Ultra-HITEMS system. Created to measure the emissivity of samples at high temperature, Ultra-HITEMS requires a number of precision instruments operating correctly, independently and in concert with all the other components.

A. Fundamental Overview

Emissivity is a fundamental property of a material[1]. It is a measure of how efficiently a material radiates energy compared to a theoretically perfect blackbody. For a given sample, it is temperature dependent. It can be presented as a spectrally dependent function, or integrated over all (or specific) spectral bands and presented as a single value, always less than or equal to 1.0. The emissivity can be defined as hemispherical, or normal (or any other angle) depending on the direction(s) from which the radiant energy leaves the surface.

In an absolutely calibrated system, one could measure the spectral or total radiance of a sample at some temperature and compare it to a theoretical curve for a blackbody to determine its emissivity. However, measured samples and measurement systems are complicated. Samples are seldom perfectly homogeneous and isotropic. Sample surfaces are rarely perfectly smooth. Absolute calibration of any system is challenging, especially one which requires broad spectral measurements into the IR region and beyond since everything radiates (and absorbs) energy following the Plank spectral radiation curve. Thus, Ultra-HITEMS is a relative measurement system, measuring samples against a well-known high-quality blackbody source. And the measured value may also be more appropriately called "emittance" to indicate that the sample surface quality (roughness) is contributing to the measurement. The rest of this report details how this relative measurement system is (or should be) able to make accurate relative (traceable) measurements. And throughout this paper, "emissivity" is used whether or not "emittance" is a more appropriate term.

---

[1] Asst. Prof. & Assoc. Dir., Electrical & Computer Eng., Center for Applied Optics, U. of Alabama in Huntsville.

B. Component by Component Operational Description

HITEMS consists of five instrumental components, plus relay optics, linked together physically, through software, and/or interconnected operation, which measures radiant emittance for computing the emissivity of heated samples. Fig.1. These components are:

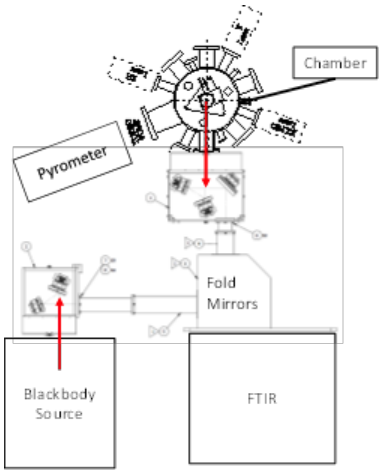

Figure 1 The Ultra-HITEMS system, major components

a. Evacuated sample compartment with multiple viewing ports
b. 50W fiber laser (1.064um wavelength, fiber)
c. A calibrated blackbody source (Mikron 390)[2]
d. Pyrometer (FAR FMP 2/2X)[3]
e. A Fourier Transform Infrared Spectrometer (FTIR, Nicolet 6700)[4]
f. Relay optics (two paths, COTS powered elements and fold mirrors)

To make a measurement on a sample requires the following steps.

1. The sample is heated in the sample chamber to some elevated temperature by illuminating it with the 50W laser source.
2. The FAR pyrometer is used to remotely (outside of the evacuated chamber) determine the sample temperature.
3. The blackbody source is then set to the same temperature as the sample.

The FTIR measures the radiant spectra from the sample and the blackbody that is relayed by reflective optics near the sample and blackbody, respectively, with the selection of sources set by actuating fold mirrors just outside of the FTIR.

The atmosphere in the FTIR and the optical path traversed by the blackbody or sample beams is dry and CO2 scrubbed. The optical interfaces seen along the two paths are identical, as is the path length so that any spectral absorption or reflection losses will be identical. Once the two spectra are acquired, the sample spectral radiant energy is divided by the blackbody spectral radiant energy to calculate the spectral emissivity. To compute a single emissivity value, the integrated radiant energy from the sample is divided by the integrated radiant energy from the blackbody.

III. Temperature Matching

Given the components and operational steps to compute a measurement, this section further discusses the impact temperature mismatches between the sample and the blackbody reference have on the results. This section again starts with further discussion of the theoretical form of blackbody radiators, and then shows how mismatches will affect the measured output.

A. Spectral bands

The radiant energy from a perfect theoretical blackbody follows the Plank blackbody curve[5]. The peak of the radiant energy is inversely proportional to the temperature, and the total radiant energy depends on the temperature to the 4th power. Additionally, at all wavelengths, the radiant energy increases with increased temperature, Fig. 2.

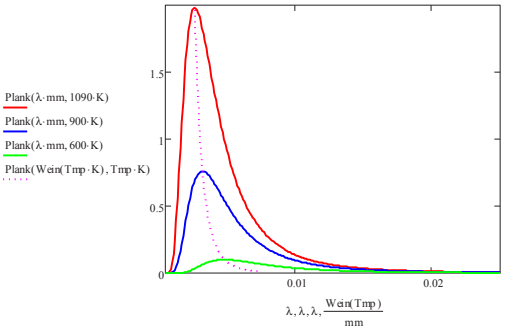

Figure 2 Plank spectral emission curves for black bodies at 3 temperatures. Dotted curve shows temperature dependent location of peak spectral emission.

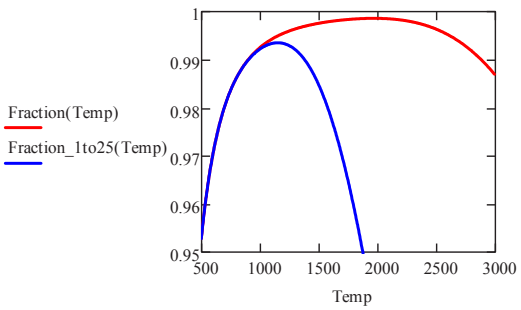

Figure 3 Fraction of total radiated energy captured vs temperature (K) over spectral bands of 0.5-25um and 1-25um.

is temperature matching. Depending on the temperature of the object being measured, the fraction of energy radiated from the sample that is contained within this spectral band will vary – and it will never be 100% since the Plank curve theoretically extends in wavelength from zero to infinity. Thus, the single value emissivity calculated by integrating over different spectral ranges could yield different values. This will occur if the measured spectral range does not include regions which the material exhibits unusual, non-blackbody (or non-gray body) behavior. A calculation showing the fraction of energy contained within a 0.5-25um spectral band and a 1-25um spectral band is plotted in Fig. 3 as a function of object temperature. As expected, integrating the data over the spectral bandwidth starting at 1um misses far more energy as the sample temperature increases. The spectral emissivity computed by Ultra-HITEMS will be accurate over any spectral range, since it is compared to a blackbody. The integrated emissivity value, however, could be missing spectral radiant variations that would affect the calculation. Thus, all presented measured data should include the spectral bandwidth over which the measurement is made as well as the temperature of the sample.

B. Temperature matching

To compute the spectral emissivity of the sample, the measured spectral radiance of the sample is divided by the spectral radiance of the blackbody. In order for this simple calculation to be correct, several properties of the sample and blackbody paths must match.

a. The path length through the controlled atmosphere environment must be the same for the sample path as for the blackbody path. This eliminates any atmospheric differential absorption effects between the sample and blackbody paths in the FTIR measured spectral signatures. This condition is met.

b. The number, and kinds of optical surface and material interactions must be the same between the sample and blackbody paths. Simply put, the same and same number of transmitting and reflecting surfaces are required. This condition is met.

c. The etendue (throughput, or flux gathering capacity) of the sample path must be identical to the etendue of the blackbody path. If they are not identical, but the imaging paths are unaberrating and the difference is not large, a simple multiplicative constant will correct the difference. This system currently is highly aberrated which affects the measurement, but is a separate topic for another paper.

d. The sample must be the same temperature as the blackbody. How well this condition is met is uncertain. Contributions to the uncertainty include temperature gradients across the sample, accuracy of the FAR pyrometer, and complexity of the sample emissivity.

The simplest example of how (d) impacts the measurements is to assume the sample is also a perfect blackbody.

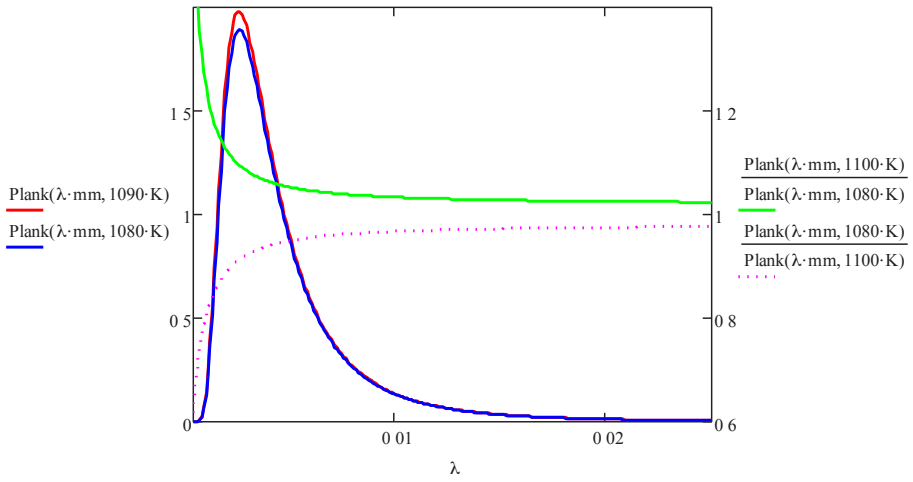

Figure 4 Plank curves for hotter (red), cooler (blue) blackbodies. Calculated blackbody sample spectral emissivity if sample is hotter (green), cooler (dotted purple) vs blackbody reference. Both emissivity's are wrong, green curve is not physical.

If it is at a different temperature, Plank's law describes a different spectral radiant energy curve, so the emissivity will not be calculated as 1.0, which it should be, Fig. 4. Thus, the spectral emissivity calculation will exhibit errors if the temperatures are not well matched.

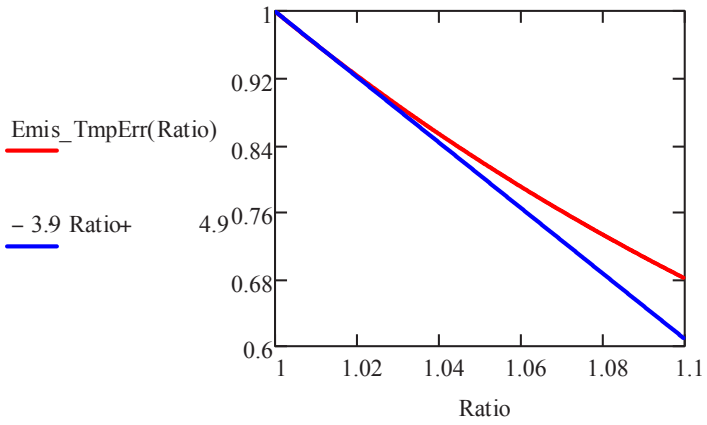

Figure 5 Error in calculated emissivity vs Ratio of sample and blackbody temperature. Assumes sample is also a blackbody.

In Fig. 5, the integrated emissivity is calculated versus the ratio of the blackbody temperature to the sample temperature, with the temperature ratio ranging from 1 to 1.1 (a 9% lower sample temperature). Since the sample is assumed to be a perfect blackbody, its emissivity should be 1.0, but because the sample temperature differs from the blackbody reference, the ratio is less than 1, and the error grows with temperature mismatch. The results show that the error in emissivity is roughly linear, with a 3.9X multiplier for small errors going from temperature error to calculated emissivity error. Thus, if the blackbody is 1% lower in temperature than the sample, the error in calculated emissivity will be ~3.9%. This error is independent of the temperature of the blackbody and sample; it only depends on the temperature ratio. This error is also independent of sample emissivity if sample is assumed to be a graybody. Thus, it is critical that the sample temperature and blackbody temperatures be matched, or that the uncertainty in their matching is known so that the appropriate uncertainty can be applied to the emissivity measurement.

IV. Conclusion

The Ultra-HITEMS instrument is a unique and highly capable system for measuring emissivity of samples at high temperature. A thorough understanding of its operation shows how systematic errors induced by temperature mismatches can be understood. Once understood, these potential errors can be addressed and reduced, resulting in more accurate data.

References

[1] Boyd,R.W., "*Radiometry and the Detection of Optical Radiation*", John Wiley and Sons, New York, 1982, pp. 28-68.
[2] Lumasense Technologies, Inc., Santa Clara, CA, www.lumasenseinc.com
[3] FAR Associates, Macedonia, OH, www.pyrometry.com
[4] Thermo Fisher Scientific, Inc, Waltham, MA, http://www.thermofisher.com
[5] Hudson, R.D., "*Infrared System Engineering,*", John Wiley and Sons, New York, 1969, pp. 20-84.

Material flow modification in a friction stir weld through introduction of flats

Judy Schneider[1] and Arthur C. Nunes, Jr.[2]

University of Alabama in Huntsville [1], Huntsville, Al 35899

NASA[2], Marshall Space Flight Center, Al 35811

Nomenclature

FSW = Friction Stir Weld

RPM = rotation per minute

mmpm = millimeters per minute

VWT2 = vertical weld tool 2

I. Abstract

FSW is a solid-state process in which a non-consumable weld tool is used to stir metal together to obtain a fully consolidated weld seam. There is controversy regarding the contributions of various attributes of the pin design, especially with regards to flats and flutes. In this study similar FSWs made with threaded cylindrical pin-tools having 0, 1, 2, 3, 4, and 5 flats were compared. Slight increases in torque were noted with increasing flats. Significant changes in the FSW structure with varying numbers of flats were observed, but without significant changes in tensile strength for the FSW coupons. Changes in the textural banding shape, the addition of sub-bands and a new set of bands from coalescence of band kinks constitute the structural changes observed. Explanations of these structural changes in terms of tool interactions with the FSW metal are offered.

II. Introduction

Most FSW tool studies in the literature focus on the resulting structural integrity of the FSW joint since that ultimately affects the cost and robustness of the process. Recent reviews of tool design have been published by Rai, et al. [1] with special regard to material selection and wear. A tool design is considered good if it improves the quality of the FSW within an acceptable parameter processing window [2]. Usually the acceptable processing window is determined by the capability of the FSW machine being used. Generally the tool is made from a material that retains sufficient strength at the FSW temperature and does not chemically react with the work pieces. The tool dimensions are ultimately designed to resist breakage during the FSW process. Specific design features of the FSW tool are often based on intuitive concepts [3], details of which can often be closely guarded. Different FSW tools, especially those with flats or flutes have been compared on the basis of the ratio of swept to static volume with a higher swept volume reported to promote better mixing [4, 5].

While various studies in the literature target tool design, the main published focus is on the overall geometric relationships. A typical tool is comprised of a shoulder and a pin. The pin shape can range from tapered and smooth, to cylindrical and threaded. In low melting temperature alloys, such as Al and Mg, the ratio of the shoulder diameter to the pin diameter is nominally 2:1 [2], whereas in higher melting temperature alloys with low thermal conductivity, such as Ti [6, 7], the ratio may decrease to 1.2 :1. The interaction of the tool motion with the work piece generates the temperature needed to plasticize the material so that it can flow around the tool in the solid state. The heating has been attributed to friction between the shoulder [8-10] and the workpiece and to deformation around the weld tool [11-16] as the movement of the pin shears the material in thin layers forming a banded structure referred to as “onion rings [17]”.

---

[1] Professor, Department of Mechanical and Aerospace Engineering, University of Alabama in Huntsville.

[2] Welding Process Analyst, EM32, Marshall Space Flight Center

Schemes to optimize shoulder dimensions relate to containing the material within the flow zone [18-20]. Most studies concur that shoulder contact is needed to contain the plasticized material to prevent wormhole formation [11]. Whether this is simply a geometrical constraint or a source of heat input is difficult to separate [11, 21, 22]. The interaction with the shoulder has been referred to as "shoulder driven" flow which describes the flow of material from the crown to the root surface or the through material thickness flow [11]. Whereas the taper and/or threads affect the local flow around the pin, affecting the layered deposition of material related to the onion ring structure [11, 17, 23-26]. It has been proposed that the proper amount of shoulder driven and pin driven flow are needed to provide adequate pressure to prevent volumetric defects [11, 27].

A recent review by Zhang, et al. [28] provides an overview of the various pin geometries. Studies continue to back up the initial claim [29] of the pin providing heat to the material, disrupting the faying surfaces, shearing material in front of the pin, and depositing it in the wake. Threads on the pin are noted to improve the through material thickness flow from crown to root [2, 5], although tapered tools are also reported to provide a similar benefit [30]. Variation in pin shape, whether cylindrical or tapered, has been found to correlate with material thickness [2, 31] and workpiece conductivity [32]. Typically tapered tools are used in thicker material as well as in material with lower conductivity.

The pin surface, whether threaded or smooth, may have features called flats or flutes [2, 28]. Thomas patented the incorporation of flats into the tool features to change the material movement around the pin [4, 33-35]. The flats are reported to act as a paddle in moving material whereas the flutes were considered to move material downward toward the root surface [36, 37]. Both features change the overall pin shape from cylindrical to either a rectangle with 2 flats, a triangular with 3 flats, a square with 4 flats, or a hexagon with 5 flats.

Understanding of the material flow during a FSW as influenced by the tool design and weld parameters, has relied on various marker studies. Studies by Colligan [38] using steel shot embedded in the faying surface of a FSW, illuminated the orderly flow of material in response to the FSW tool movement. Later AA5454 inserts identified differences in the advancing versus retreating side of the FSW [39]. Capture of material moving multiple times around the tool was traced using an Al-SiC composite material insert [40]. The influence of shoulder contact on material flow in a FSW was highlighted using lead markers [41]. These past marker studies have facilitated the understanding of the influence of the FSW tool and weld parameters on material flow. Guided by the marker studies, a kinematic model was developed to explain the material flow as streamlines around the tool influenced by the threads on the FSW pin [42]. The tracer results have linked the velocity field components of the model with various macro and microstructural features in a FSW [42], allowing now for interpretation of material flow variations directly from the microstructural features observed.

Marzbanrad, et al. [43], conducted a study comparing a square tool with a cylindrical tool. Both tools had smooth surfaces, with the square tool formed by 4 flats. They concluded that the square pin generated more swept volume and also provided a pulsing action that is missing in cylindrical tools [30, 43-45]. This pulsing action has also been associated with eccentrically mounted tools which can also lead to increased forces on the tool [24, 46]. It is interesting to note that off centered tools are finding increased usage in friction stir spot welding (FSSW) due to increased swept volume [47] which induces a pulsating motion.

Studies with flats or flutes have generally compared tools with and without flats [18, 19, 48, 49]. While these studies have been beneficial in identifying benefits, exact nature of the change in material flow is not well understood. In these studies, some pin profiles used threads while others were smooth. Understanding of variations in material flow from the changing geometry was difficult to correlate with the FSW quality since volumetric defects were reported in many of the FSWs. Other studies in which the effect of tool parameters was found to change the strength and hardness, correlated these variations with the resulting precipitate structure [50-54]. Thus fine textural variations alone would not be expected to produce significant strength or hardness variations. This study compares the sequential addition of flats ranging from 1 to 5 on a threaded cylindrical tool. The process parameters were held constant and lack of volumetric defects was verified. As the number of flats was increased, a slight increase was observed in the torque, which suggested more material movement. No significant change was found in either the forces or the tensile strength.

III. Experimental Procedure

Conventional FSWs were made in 8.306 + 0.178 mm thickness and 610 mm length panels of AA2219-T87. All FSWs were bead on plate to eliminate any fit-up issues. A 7^0 concave shoulder was used with all weld tool designs

and the FSW was made with a tool tilt of 2.5^0. The pin position was set with a ligament length of 0.381 mm and a heel plunge of 0.330 mm to ensure adequate engagement. The number of flats on the threaded tools, shown in Figure 1, was varied from 1 to 5. To incorporate 5 flats while retaining the threads, a shallower depth was used as noted in Table I. The FSWs were made using the VWT2 machine at the NASA-Marshall Space Flight Center operated in load control. All FSWs were made at a tool rotation rate of 200 RPM, travel speed of 203 mm/min and a plunge force of 47 kN. These parameters were previously established on the basis of adequate tool engagement to produce void free FSWs.

Figure 1. The sets of tool geometries evaluated in this study using a threaded pin with varying number of flats.

Table I. Test matrix of FSW parameters.

	Panel thickness (mm)	Pin diameter (mm)	Pin length (mm)	Thread pitch	Flats - number and depth (mm)	Shoulder Dia (mm)
0	8.3	12.7	8.1	20 UNC	0	30.5
1	8.3	12.7	8.1	20 UNC	1 - 0.89 deep	30.5
2	8.3	12.7	8.1	20 UNC	2 - 0.89 deep	30.5
3	8.3	12.7	8.1	20 UNC	3 - 0.89 deep	30.5
4	8.3	12.7	8.1	20 UNC	4 - 0.89 deep	30.5
5	8.3	12.7	8.1	20 UNC	5 - 0.76 deep	30.5

After the FSWs, metallographic specimens and tensile bars were prepared from the weld panel. Metallographs were prepared by mounting longitudinal and transverse sections of the FSW nugget. Standard metallurgical procedures were used to grind and polish the specimen prior to a Keller's etch to reveal the macrostructure which was recorded using a Nikon D1 camera. Measurements of the grain area were made from the metallographs using NIH image analysis software, ImageJ.

Three each tensile specimens, 6 mm wide were cut transverse to the FSW direction. Testing was conducted using an Instron Model 5869 electro-mechanical load frame with a 50 kN load cell. For each tool design, 6 specimens were tension tested in extension control with no preload at a constant crosshead velocity of 13 mm/m. Corresponding hardness measurements were made using a Rockwell Model 574 machine.

IV. Results

Variations in the onion ring pattern can be observed in the transverse macros shown in Figure 2. Figure 2a, which used a standard threaded pin without flats, shows a very distinct, typical "onion ring" pattern. When 3 flats are included on this tool, Figure 2b shows a distortion in the former distinct onion rings. Figure 2c and 2d show a progressive distortion between the 1 flat and 5 flats, respectively.

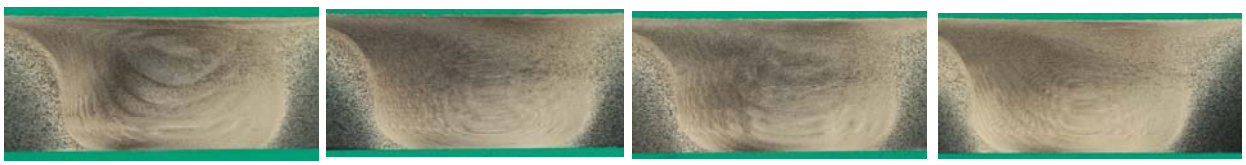

(a) (b) (c) (d)

Figure 2. Transverse FSWs comparing with a threaded pin with no flats (a), 3 flats (b), 1 flat (c) and 5 flats (d).

Figure 3 presents a montage of longitudinal macrographs of the FSWs progressing from no flats to 5 flats. As the number of flats increases, new sets of bands can be observed to emerge.

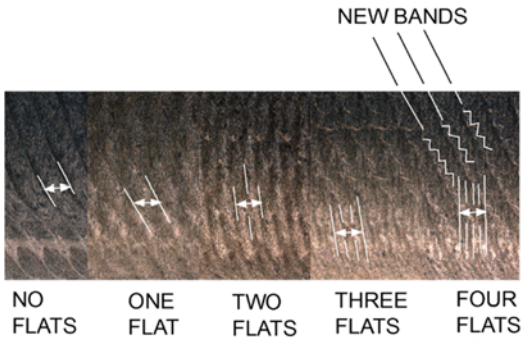

Figure 3. Montage of longitudinal macros showing changes in angle of internal textural bands and band subdivisions with numbers of flats. A second set of bands emerges out of successive axial interruption of the original bands as the number of flats increases.

Figure 4 shows the average torque slightly increasing with the number of flats with no corresponding trend in either longitudinal x or transverse y forces.

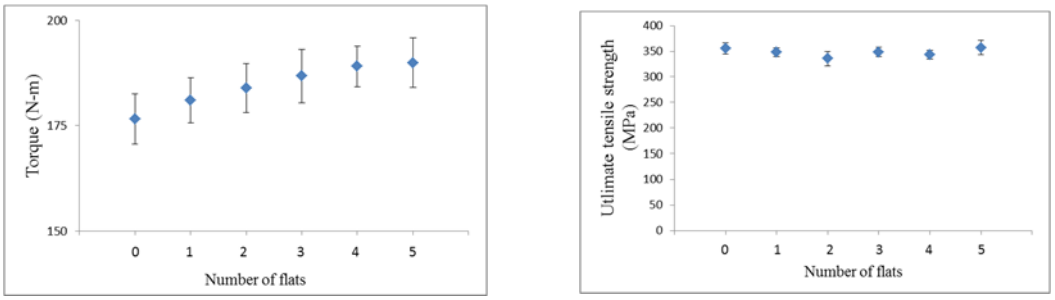

Figure 4. Slight increased noted in torque requirements as flats are incorporated on a threaded pin (a) with no apparent change in ultimate tensile strength (b).

Grain areas measured for transverse and longitudinal macrographs are shown in Figure 5. Measurements were made from the top, middle, and bottom portions of the FSW nugget. Larger grain areas were measured from the transverse images as compared to the longitudinal images indicating grain elongation.

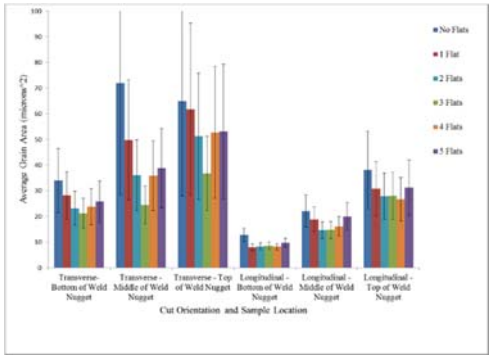

Figure 5. Grain area analysis for the welds with varying number of flats.

V. Discussion

The largest variation observed in the data was in the grain area shown in Figure 5. Grain area was used as the grains differed in the longitudinal vs transverse orientations. Similar to other studies, the grain size was larger near the top of the FSW nugget with the finest grains observed near the root side. The decrease in grain size with the number of flats can result from either a difference in the amount of strain the material experiences or a lower temperature. Estimation of FSW temperature variation due to the increasing torque showed a negligible variation in FSW temperature of 7° C per flat. Thus the addition of flats, and the resulting increase in torque suggests that there was additional strain input due to the creation of additional flow paths. As the flats are seen as either embedded in the FSW metal revolving with the tool or as encountering the moving FSW metal, they necessitate a locally adjusted longer flow path or additional strain input. The adjustment is only needed toward the root end of the pin, where the shear surface separating moving metal from the pin is close to the pin and the flats are close enough to the moving metal to cause some flow [23, 42].

Figures 6 through 8 shows that the surface ripples in the wake of a FSW and the underlying interior textural band structure are parts of the same phenomenon: an up-and-down axial flow of metal around the FSW pin driven by eccentricity of the rotating pin. Variations in axial flow produce variations in texture. At the surface they produce up-and-down displacements, i.e. ripples.

Krishnan's initial study [17] showed that the bands or onion rings form as the material is sheared, swept around the tool, and deposited in the wake with each newly sheared segment of material depositing in an orderly fashion corresponding to the tool travel divided by the tool rotation. Various studies have shown a fiber type texture associated with the banded structure [42, 59-61]. More detailed analysis by Prangnall and Heason [61] revealed slight textural variations within a band that give rise to the light and dark regions observed in light microscopy. Although no explanation was given, their work also reported a textural weakening in the banded structure in FSWs with a 3 flat tool.

The band structure originally conforms to a flared cylinder enclosing pin and shoulder. The refined grain structure of the FSW nugget exhibits a flared cylinder shape. The pin threads push the metal axially down, setting up a ring vortex circulation around the pin. This circulation contracts the bands in the flared region toward the shoulder and expands them into a bulge further down the pin. The bulge appears as an "onion ring" in transverse sections in Figure 2.

How, then, would a flat be expected to affect the flow around the pin? First, a flat cuts away some of the threads on the pin. Since the threads drive the ring vortex circulation, one would expect a flat to reduce the ring vortex circulation, which in turn would reduce the bulge in the band structure. Figure 3 shows just such a reduced bulge with one and two flats. With higher numbers of flats, however, a new set of bands emerges with more than two flats (Figure 2b, 2d, and 3) apparently a coalescence of periodic axial disturbances in the bands induced by flats.

The band structure takes the form of a flared cylinder. A transverse section of a series of flared cylinders would look like loops sagging down from the FSW shoulder morphing into vertical legs at the bottom of the pin. A faint sagging loop is seen in Figure 2a, but the legs are not visible, possibly too broad to be distinct with low cylinder curvature. In Figure 2b additional banding due to flats brings out some band structure toward the edges of the nugget where the band is seen intersected more obliquely. The bands appear more vertical like legs than rounded like part of an onion ring at the edges, but onion ring rounding is seen at the center, perhaps an effect of the lead angle.

Second, a flat shortens and then extends the pin radius locally so as to induce a pulse of radial flow; it superposes on the fundamental eccentric back-and-forth radial surface oscillation a local suction-and-compression stroke. The local suction-and-compression stroke introduced by the flat alters the axial flow sequence that generates the textural banding so as to introduce a sequence of textural bands within the bands produced by pin eccentricity alone. A set of disturbances at different axial levels is also generated and from these periodic disturbances a new set of bands emerges (Figure 3). It is not clear how these disturbances form at successive axial levels; this is a subject for further study.

Figure 2a shows a very distinct onion ring pattern for a tool with threads, but no flats. Figure 2b shows a fainter, but still distinguishable onion ring pattern as three flats are added; the rings have been distorted, presumably due to a reduced ring vortex flow, and reduced in width, presumably due to the imposition of extra bands by the flats.

Figure 2c shows the effect of a single flat. The basic onion ring pattern looks much like that of Figure 2a, but the pattern is less distinct and the rings appear irregular and interrupted by disturbances. The corresponding longitudinal

sections also show axial band perturbations. With 5 flats the transverse effects shown in Figure 2d and the longitudinal effects shown in Figure 3 become more regular.

One might at first expect that the shear surface would simply jump over the flat as if it did not exist and as if the FSW metal in the flat were a part of the tool and so cause no effect on the torque. But Figure 4a does show a small increase in torque, perhaps 2% per flat for the threaded pins up to three flats, with smaller increases thereafter.

Empirically and theoretically, the flats produce only a small increase in torque. The flat is taken to impart a local rocking motion that rotates around the tool, generating an additional torque, but it has little effect upon the overall geometry of the cylindrical boundary of the tool where the heat is being lost. The rocking motion can be interpreted as a "bump", illustrated in Figure 6, being developed in the boundary as the tool rotations. As the rotating plug of metal sticking to the tool flares out toward the shoulder, the flats are buried deeper and deeper and cease to disturb the flow of metal outside the rotating plug. As the metal would form an eddy or recirculation within this area, the bump does not leave a void when examining the removed tool.

The kinds of structural alterations produced by the flats, primarily alterations of internal textural details made visible in band structures, would be expected to have little or no effect upon strength. The strengths of the FSWs made with from 0 to 5 flats shown in Figure 4b showed negligible change as expected.

The reduction in grain size with the addition of flats is expected from the increased strain input. As the threads drive a downward flow of material through the material thickness, the presence of a flat interrupts this flow by adding planar movement. The best balance appears to be with 3 flats as further addition of flats reduces the threaded portion of the pin. With 5 flats, very little of the thread remains.

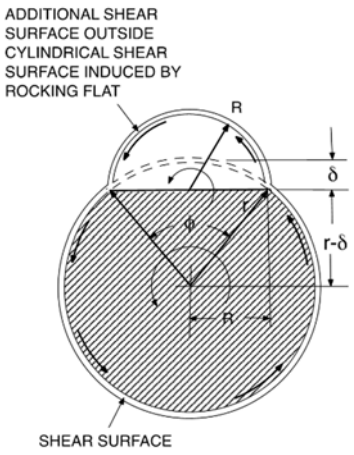

Figure 6. Hypothetical perturbation of a cylindrical shear surface by a flat.

VI. Conclusion

A flat-caused perturbation in the eccentric pumping effect that produces the band structure appears to break up the internal structure in the bands. Reductions in the ring- vortex circulation that bulges out the bands are also seen with increasing numbers of flats. A new set of jagged bands appears with 3 to 5 flats; the mechanism by which these new bands form is not yet understood. The analysis of the effect of flats on the pin-tools should continue on to address the effect of flats on the strength of the FSWs. There are not many studies in this area and unanticipated results could emerge. Although the material flow increases, as evidenced by the macrographs and increased torque,

there was no change observed in either the tool forces or the resulting FSW quality as determined by tensile strength.

Further details regarding the material flow are being documented in a technical manuscript which will be sent to either Metallurgical and Materials Transactions or the Journal of Materials Processing Technology.

Acknowledgments

J.A. Schneider wishes to thank the Welding Group at the NASA-Marshall Space Flight Center for conducting the experiments and the funding provided by the NASA MSFC Summer Faculty Program under the direction of Dr. Frank Six and Dr. Gerald Karr.

References

1) Rai, R., De, A., Bhadeshia, H. K. D. H. and DebRoy, T. 2011. Review: friction stir welding tools. Sci. & Tech. Welding & Joining, 16 (4): 325-342.

2) Mishra, R. S. and Mahoney, M. W. 2007. Friction stir welding and processing, Materials Park, OH, ASM International Pub.

3) Mishra, R. S. and Ma, Z. Y. 2005. Friction stir welding and processing. Mater. Sci. Eng. R, 50: 1–78.

4) Thomas, W. M., Nicholas, E. D. and Smith, S. D. 2001. Proc. 2001 TMS Annual Meeting Automotive Alloys and Joining Aluminum Symp. eds. G. Kaufman, J. Green, S. K. Das, pp. 213-224. TMS pub.

5) Nandan, R., Debroy, T. and Bhadeshia, H. K. D. H. 2008. Recent advances in friction stir welding—Process, weldment structure and properties. Progress in Materials Science 53: 980–1023.

6) Fonda, R. W., Knipling, K. E., Feng, C. R. and Moon, D. W. 2007. Microstructural Evolution in Ti 5-1-1-1 Friction Stir Welds. Friction Stir Welding & Processing IV, eds. R. S. Mishra, M.W. Mahoney, E. J. Lienert, K. V. Jata, pp. 295-301. Wiley Pub.

7) Pilchak, A. L., Li, Z. T., Fisher, J. J., Reynolds, A. P., Juhas, M. and Williams, J. 2007. The Relationship Between Friction Stir Process (FSP) Parameters and Microstructure in Investment Cast Ti-6Al-4V. Friction Stir Welding & Processing IV, eds. R. S. Mishra, M.W. Mahoney, E. J. Lienert, K. V. Jata, pp. 419-428. Wiley Pub.

8) McClure, J. C., Tang, W., Murr, L. E. and Guo, X. 1998. A Thermal Model of Friction Stir Welding. Proc. 5th Int. Conf. Trends in Welding Res. pp. 590-595, ASM International Pub.

9) Chao, Y. J., Qi, X. and Tang, W. 2003. Heat Transfer in Friction Stir

Welding—Experimental and Numerical Studies. Trans. ASME 125: 138–145.

10) Frigaard, O., Grong, O. and Midling, O. T. 2011. A process model for friction stir welding of age hardening aluminum alloys. Metall. Mater. Trans. 32A: 1189–1200.

11) Kumar, K. and Kailas, S. V. 2008. The role of friction stir welding tool on material flow and weld formation. Mater. Sci. Eng. A 485(1–2): 367–374.

12) Schmidt, H., Hattel, J. and Wert, J. 2004. An analytical model for the heat generation in friction stir welding Model," Simul. Mater. Sci. Eng. 12: 143–57.

13) Khandkar, M. Z. H., Khan, J. A. and Reynolds, A. P. 2003. Prediction of temperature distribution and thermal history during friction stir welding: input torque based model. Sci. Technol. Weld. Join. 8 (3): 165–174.

14) Chen, C. M. and Kovacevic, R. 2003. Finite element modeling of friction stir welding thermal and thermomechanical analysis. Int. J. Mach. Tools Manuf. 43: 1319–1326.

15) Schmidt, H. and Hattel, J. 2008. Thermal modelling of friction stir welding. Scripta Mater. 58: 332–337.

16) Chen, Z. W., Pasang, T. and Qi, Y. 2008. Shear flow and formation of nugget zone during friction stir welding of aluminium alloy 5083-O. Mater. Sci. Eng. A 474: 312-316.

17) Krishnan, K. N. 2002. On the formation of onion rings in friction stir welds. Mater. Sci. Eng. A 327: 246–251.

18) Elangovan, K. and Balasubramanian, V. 2008. Influences of tool pin profile and tool shoulder diameter on the formation of friction stir processing zone in AA6061 aluminium alloy. Material Design 29(2): 362–373.

19) Elangovan, K. and Balasubramanian. V. 2007. Influences of pin profile and rotational speed of the tool on the formation of friction stir processing zone in AA2219 aluminum alloy. Mater. Sci. Eng. A 459: 7–18.

20) Arora, A., De, A. and DebRoy, T. 2011. Toward optimum friction stir welding tool shoulder diameter. Scripta Mater. 4(1): 9–12.

21) Buffa, G., Hua, J., Shivpuri, R. and Fratini, L. 2006. A continuum based fem model for friction stir welding—model evelopment. Mater. Sci. Eng. A 419: 381–388.

22) Colegrove, P. A. and Shercliff, H. R. 2005. 3-Dimensional CFD modelling of flow round a threaded friction stir welding ol profile. J. Mater. Process. Technol. 169: 320–327.

23) Nunes, A.C., Jr. 2001. Wiping metal model of friction stir welding. Proc. 2001 TMS Annual Meeting Automotive Alloys ıd Joining Aluminum Symp. eds. G. Kaufman, J. Green, S. K. Das, pp. 235–248. TMS pub.

24) Gratecap, F., Girard, M., Marya, S. and Racineux, G. 2011. Exploring material flow in friction stir welding: Tool :centricity and formation of banded structures. Int. J. Material Forming 5: 99–107.

25) Leal, R. M., Leitaoa, C., Loureiroa, A., Rodriguesa, D. M. and Vilac, P. 2008. Material flow in heterogeneous friction stir elding of thin aluminium sheets: Effect of shoulder geometry. Mater. Sci. Eng. A 498: 384–391.

26) Mendez, P. F., Tello, K. E. and Lienert, T. J. 2010. Scaling of coupled heat transfer and plastic deformation around the n in friction stir welding. Acta Mater. 58: 6012–6026.

27) Kumar, K., Kailas, S. V. and Srivatsan, T. S. 2008. Influence of tool geometry in friction stir welding. Matls & Mfgt Proc. 3: 189-195.

28) Zhang, Y. N., Cao, Z., Larose, S. and Wanjara, P. 2012. Review of tools for friction stir welding and processing. Canadian et. Quarterly 51(3): 250-261.

29) Thomas, W. M., Nicholas, E. D., Needham, J. C., Murch, M. G., Temple-Smith, P. and Dawes, C.J. 1991. International ıtent Application No. PCT/GB92/02203 and GP Patent#9125978.9, Friction Stir Butt Welding.

30) Lorrain, O., Favier, V., Zahrouni, H. and Lawrjaniec, D. 2010. Understanding the material flow path of friction stir welding ocess using unthreaded tools. J. Matl. Proc. Tech. 210(4): 603-609.

31) Vaze, S. P., Xu, J., Ritter, R. J., Colligan, K. J., Fisher, J. J., Jr. and Pickens, J. R. 2003. Friction stir processing of aluminum loy 5083 plate for cold bending. Mat. Sci. Forum 426-432: 2979-2986.

32) Loftus, Z., Takeshita, J., Reynolds, A. and Tang, W. 2003. An overview of friction stir welding beta 21S titanium. Proc. h Intl. Conf. FSW. TWI Pub.

33) Thomas, W. M., Nicholas, E. D., Needham, J. C., Temple-Smith, P., Kallee, S. W. K. W. and Dawes, C. J. 1996. UK ıtent Application 2306366, Friction stir welding.

34) Thomas, W. M., Johnson, K. I. and Wiesner, C. S. 2003. Friction stir welding – recent developments in tool and process chnologies. Adv. Eng. Mater. 5(7): 485–490.

35) Thomas, W. M. and Dolby, R. E. 2003. Friction Stir Welding Developments. Proc. 6th Int. Conf. Trends in Welding Res.). 203–211. ASM International Pub.

36) Burford, D. A. 2008. US Patent 2008/0251571A1, Friction stir welding tool having a counterflow pin configuration.

37) Rowe, D. and Thomas, W. M. 2006. Advances in Tooling Materials for Friction Stir Welding. Materials Congress – isruptive Technologies for Light Metals, Cedar Metals Ltd. TWI Pub.

38) Colligan, K. 1999. Material Flow Behavior during Friction Stir Welding of Aluminum. Welding Research. 229s-237s.

39) Seidel, T.U. and Reynolds, A.P. 2001. Visualization of Material Flow in AA2195 Friction Stir Welds Using a Marker sert Technique. Met. & Mat. Trans. 32A: 2879-2884.

40) London, B., Mahoney, M., Bingel, W., Calabrese, M., Bossi, R.H. and Waldron, D. 2003. Material flow in friction stir elding monitored with Al-SiC and Al-W composite markers. Friction Stir Welding and Processing II, ed. K.V. Jata, M. Mahoney, . Mishra, S.L. Semiatin, T. Lienert, TMS Pub. pp. 3-12.

41) Doude, H.R. Schneider, J.A. and Nunes, A.C., Jr. 2014. Influence of the Tool Shoulder Contact Conditions on the Material ow During Friction Stir Welding. Met. Trans. 45A:4411- 4422.

42) Schneider, J.A. and Nunes, A.C., Jr. 2004. Characterization of plastic flow and resulting micro textures in a friction stir eld. Met. Trans. B. 35:777-783.

43) Marzbanrad, J., Akbari, M., Asadi, P. and Safaee, S. 2014. Characterization of the influence of tool pin profile on icrostructural and mechanical properties of friction stir welding. Met. Trans. B 45: 1887-1894.

44) Vijay, S. J. and Murugan, N. 2010. Influence of tool pin profile on the metallurgical and mechanical properties of friction stir welded Al–10 wt.% TiB2 metal matrix composite. Mater. Des. 31(7): 3585–3589.

45) Chen, Z. W. and Cui, S. 2008. On the forming mechanism of banded structures in aluminium alloy friction stir welds. Scripta Mat. 58: 417-420.

46) Brendel, M. and Schneider, J. A. 2012. Influence of Friction Stir Weld Tool Geometry and Runout on Magnitude and Form of In-process Weld Forces. 9th Intl Friction Stir Welding Symp. TWI Pub.

47) Mishra, R. S., Freeney, T. A., Webb, S., Chen, Y. L., Herling, D. R. and Grant, G. H. 2007. Friction stir spot welding of 6016 aluminum alloy. Friction Stir Welding and Processing IV. eds. R. S. Mishra, M.W. Mahoney, E. J. Lienert, K. V. Jata, pp.341-348. Wiley Pub.

48) Colligan, K. J., Xu, J. and Pickens, J. R. 2003. Welding tool and process parameter effects in friction stir welding of aluminum alloys. Friction stir welding and processing II. eds. K. V. Jata, M. W. Mahoney, R. S. Mishra, S. L. Semiatin, T. Lienert, pp. 181–190. TMS Pub.

49) Boz, M. and Kurt, A. 2004. The influence of stirrer geometry on bonding and mechanical properties in friction stir welding process. Mats. & Design 25: 343-347.

50) Sato, Y.S., Park, S.H.C. and Kokawa, H. 2001. Microstructural Factors Governing Hardness in Friction-Stir Welds of Solid-Solution-Hardened Al Alloys. Met. Trans. A. 32A(12):3032-3042.

51) Sato, Y.S., Urata, M. and Kokawa, H., 2002. Parameters controlling microstructure and hardness during friction-stir welding of precipitation-hardenable aluminum alloy 6063. Met. Trans. A, 33A:625-623.

52) Sato, Y.S., Kokawa, H., Enomoto, M., Jogan, S. and Hashimoto, T., 1999. Precipitation sequence in friction stir weld of 6063 aluminum during aging. Met. Trans. A., 20A:3125-3130.

53) Sato, Y.S. and Kokawa, H., 2001. Distribution of tensile property and microstructure of a friction stir weld of 6063 aluminum. Met. Trans. A., 32A:3023-3031.

54) Schneider, J.A., Stromberg, R., Schilling, P., Cao, B., Zhou, W., Morfa, J. and Myers, O. 2013. Processing effects on the friction stir weld stir zone. Welding Journal, January pp. 11s-19s.

55) Pew, J.W., Nelson, T.W. and Sorensen, C.D. 2007. Torque based weld power model for friction stir welding. Sci. Tech. Weld. Join., 12:341–347.

56) Jonckheere, C., de Meester, B., Denquin, A. and Simara, A. 2013. Torque, temperature and hardening precipitation evolution in dissimilar friction stir welds between 6061-T6 and 2014-T6 aluminum alloys. J. Matls Proc. Tech., 213:826– 837.

57) Querin, J.A. and Schneider, J.A. 2012. Developing an Alternative Heat Indexing Equation for FSW. Welding Journal. 91:76s-82s.

58) ASM Metals Handbook Vol. 2. 1990. ASM International Pub. Materials Park, OH.

59) Field, D.P., Nelson, T.W, Hovanski, Y. and Jata, K.V. 2001. Heterogeneity of crystallographic texture in friction stir welds of aluminum. Met. Trans. A. 32A:2869-2877.

60) Jata, K.V. and Semiatin, S.L. 2000. Continuous dynamic recrystallization during friction stir welding of high strength aluminum alloys. Scripta Mater. 43:743-749.

61) Prangnell, P.B. and Heason, C.P. 2005. Grain structure formation during friction stir welding observed by the stop action technique. Acta Mater. 53:3179–3192.

Experimental Investigation on Acousto-ultrosonic Sensing Using Polarization-maintaining Fiber Bragg Gratings

Gang Wang[1]
University of Alabama in Huntsville, Huntsville, AL, 35899

Curtis E. Banks[2]
NASA Marshall Space Flight Test Center, Huntsville, AL, 35811

This report discusses the guided Lamb wave sensing using polarization-maintaining (PM) fiber Bragg grating (PM-FBG) sensor. The goal is to apply the PM-FBG sensor system to composite structural health monitoring (SHM) applications in order to realize directivity and multi-axis strain sensing capabilities while using reduced number of sensors. Comprehensive experiments were conducted to evaluate the performance of the PM-FBG sensor in a composite panel structure under different actuation frequencies and locations. Three Macro-Fiber-Composite (MFC) piezoelectric actuators were used to generate guided Lamb waves and they are oriented at 0, 45, and 90 degrees with respect to PM-FBG axial direction, respectively. The actuation frequency was varied from 20kHz to 200kHz. It is shown that the PM-FBG sensor system is able to detect high-speed ultrasound waves and capture the characteristics under different actuation conditions. Both longitudinal and lateral strain components in the order of nano-strain were determined based on the reflective intensity measurement data from fast and slow axis of the PM fiber. It must be emphasized that this is the first attempt to investigate acouto-ultrosonic sensing using PM-FBG sensor. This could lead to a new sensing approach in the SHM applications.

Nomenclature

n_0	=	Nominal index of refraction of the fiber core (n_0=1.46)
p_{11},p_{12}	=	Strain-optic coefficients (p_{11}=1.21;p_{12}=0.27)
υ	=	Poisson's ratio of fiber
ε_{xx}	=	Normal strain along fiber axial direction
ε_{yy}	=	Normal strain along slow axis (i.e., lateral)
ε_{zz}	=	Normal strain along fast axis (i.e., transverse)
λ_f	=	Initial unstrained wavelength of fast axis (λ_f=1549.563nm)
λ_s	=	Initial unstrained wavelength of slow axis (λ_s=1550.120nm)
λ_B	=	Bragg wavelength
Δ	=	Grating pitch
$\Delta\lambda_f$	=	Wavelength shift along fast axis when strained
$\Delta\lambda_s$	=	Wavelength shift along slow axis when strained

I. Introduction

Composites structures are increasingly being used in the construction of aerospace, mechanical, civil, marine, automotive, and other high performance structures due to their high specific stiffness and strength, excellent fatigue resistance, longer durability as compared to their metallic counterparts, and due to their ability to be easily tailored

[1] Ph.D., Assistant Professor, Department of Mechanical and Aerospace Engineering, gang.wang@uah.edu
[2] Ph.D., MSFC-E35, BLD 4487/B102

for specific applications. One example is the composite over-wrapped pressure vessels (COPVs)[1],which are currently used at NASA to contain high-pressure fluids in propulsion, science experiments and life support applications, as shown in Figure 1. These COPVs have a significant weight advantage over all-metal vessels; but, as compared to all-metal vessels, COPVs require unique design, manufacturing, and test requirements. COPVs are in general subjected to significant multi-axial, dynamic state of stress and can be of significant risk to structural damages. Damage analysis, diagnostics, and life predictions are key factors in the structural health monitoring (SHM) of COPVs.

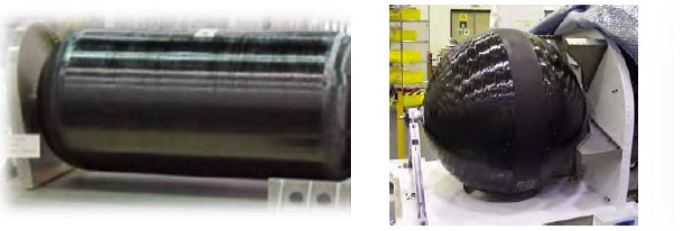

a). Nitrogen Tank **b). Oxygen Tank**

Figure 1: Carbon-epoxy COPVs

The Acousto-ultrasonic (AU) approach has been used to identify damages in engineering structures[2-7]. Worlton proposed an AU type approach for damage detection in structures[3]. Rose has presented a literature review of the most salient work with regard to AU research[4]. Dalton conducted studies of Lamb wave propagation through aircraft structures and noted that long range inspection is possible[5]. Cawley and Alleyne discussed the different Lamb modes present in thin plates and their applicability toward damage detection. It is mentioned that dispersion, the change in the shape of the waveform as the wave propagates through the structure, is an important factor in choosing a wave mode for AU damage detection[6]. Wilcox *et al.* extends Cawley's thoughts about factors critical for AU inspection of structures[7]. Recent advancements in this area including applications of guided ultrasonic Lamb waves for identification of damage in composite structures are discussed in Ref. 8.

Effective and efficient sensors play a major role in order to achieve the in-situ AU damage detection for composite structures. Piezoelectric based sensors have proven to be suitable to this application because of superior electro-mechanical coupling property and high frequency sensing capability. Lead Zirconate Titanate (PZT) is a typical piezoelectric transducer that is extensively used in guided Lamb wave studies[9-10]. PZT transducers are advantageous as they have wide frequency responses, excellent mechanical strength, low power consumption and acoustic impedance. They are light weight and low cost as well. As the counterparts of piezoelectric sensors, fiber Bragg grating (FBG) sensors also offer many benefits including small size, light weight, immunity to electro-magnetic-interference, amenability to multiplexing, and high sensitivity[11-13]. The FBG strain sensor consists of a traditional silicon glass fiber upon which a Bragg grating is created. When the Bragg grating is strained, the wavelength reflected by the grating changes linearly[14]. Abroad range of static and dynamic strains can be accurately measured with fiber optic Bragg grating sensors capable of measuring strains as small as 1 $\mu\varepsilon$[15]. A true distributed sensor with multiple (4 to 16) Bragg gratings can be serially multiplexed on one single cable. The capability of Lamb wave sensing using FBGs was demonstrated by testing a Perspex plate under PZT actuation as discussed by Betz *et al*.[16].

The multiplexing feature of FBGs allows us collect strain data at multiple locations simultaneously. However, due to directional dependent properties in composites, multi-axis strain measurements are needed in order to comprehensively evaluate the health of a composite structure. Therefore, a multi-parameter fiber optic strain sensor is required. Two-parameter FBG strain sensors were developed by writing a single fiber Bragg grating onto a polarization-maintaining (PM) optical fiber[17-20]. The birefringence results in a slight change in the index of refraction along two mutually perpendicular directions[20], termed the polarization axes (i.e., fast and slow axis). By measuring different reflective intensity in both polarization axes, one can determine the corresponding wavelength shifts of Bragg peaks and derive the biaxial strain field. A tri-axial strain can be realized by writing two distinct gratings into one polarization fiber[20-21]. Mawatari and Nelson developed a model to predict longitudinal and two orthogonal transverse strain components from measured wavelength shifts and experimentally validate the model prediction by conducting combined loading test on the fiber[21].

This study focuses on the application of the PM-FBG sensor to conduct guided Lamb wave sensing in a composite panel structure. The goal is to advance the state-of-the-art of multi-axis sensing in composite SHM applications. We expect to measure in-plane 2D strain fields using a single PM-FBG sensor. To authors' best knowledge, such approach has not been reported in the literature. The PM-FBG sensor performance in terms of frequency bandwidth, directivity, sensitivity, accuracy, is expected to be characterized. Macro Fiber Composite (MFC) piezoelectric actuators were used to excite the composite plate by applying a 5-cycled Hanning windowed sinusoidal signal under various excitation frequencies. Based on the collected reflective intensity measurements in

both fast and slow axis, the 2-D strain field can be determined by relating the strain components to the wavelength shifts.

The report is organized as follows. In section 2, a brief introduction to FBG and PM-FBG is presented. Section 3 will discuss the acousto-ultrasonic experimental setup and procedure to determine the wavelength shifts. Results will be included in Section 4 and conclusion remarks are given in Section 5.

II. Polarization-maintaining Fiber Bragg Grating

A. Fiber Bragg Grating

As shown in Figure 2, a fiber Bragg grating[12] operates by acting as a wavelength selective filter that reflects a narrow band of light centered on the grating's characteristic wavelength referred to as the Bragg wavelength, λ_B. The Bragg wavelength is related to the grating pitch,Λ, and the mean refractive index of the core, n_0, by $\lambda_B = 2\Lambda n_0$. Both the fiber refractive index and the grating pitch vary when strain is applied to the FBG and/or the temperature is changed. Wavelength change measurement then provides a basis for strain and temperature sensing.

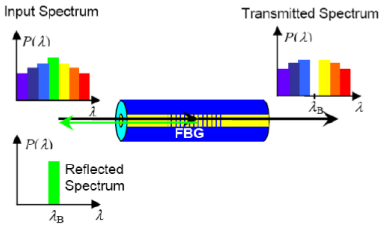

Figure 2: Operational principle of a FBG sensor

B. Polarization-Maintaining FBG

There are three main types of polarization-maintaining (PM) fiber, i.e., elliptical, bow-tie, and panda type. The polarization axes are setup by applying stress-inducing claddings[20]. Then, the birefringence in the fiber is created with this built-in residual stress introduced during the fiber draw. Figure 3 shows the schematic of the acousto-ultrasonic sensing using a PM-FBG sensor on a plate structure, in which a bow-tie PM fiber is employed. The ultimate goal is to derive the in-plane strain components along axial and lateral directions. First, a calibration is required to relate the wavelength to reflective intensity using an optical spectrum analyzer. Then, we need to collect corresponding reflective intensity responses in both polarization axes when the plate is strained. Finally, the in-plane strain components can be calculated. The strain applied to the grating will result in a shift in the wavelength of two peaks from both fast and slow axis, which is given by

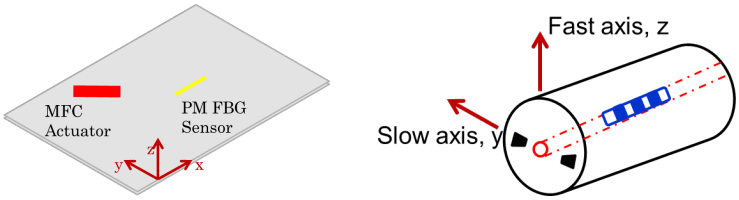

(a). actuator and sensor **(b) bow-tie PM-FBG**

Figure 3: Schematic of Lamb wave sensing using PM-FBG

$$\frac{\Delta\lambda_f}{\lambda_f} = \left(1 - \frac{n_0^2}{2} p_{12}\right)\varepsilon_{xx} - \frac{n_0^2}{2} p_{12}\varepsilon_{yy} - \frac{n_0^2}{2} p_{11}\varepsilon_{zz} \qquad (1)$$

$$\frac{\Delta\lambda_s}{\lambda_s} = \left(1 - \frac{n_0^2}{2} p_{12}\right)\varepsilon_{xx} - \frac{n_0^2}{2} p_{11}\varepsilon_{yy} - \frac{n_0^2}{2} p_{12}\varepsilon_{zz}$$

Recall that the out-of-plane stress (σ_{zz}) is zero. Corresponding out-of-plane strain (ε_{zz}) can be expressed in terms of in-plane strain components as shown below

$$\varepsilon_{zz} = \frac{-\nu}{1-\nu}\left(\varepsilon_{xx} + \varepsilon_{yy}\right) \qquad (2)$$

Note that the optical fiber is assumed to be isotropic. The final expression between in-plane strain components and the shifts in the wavelength is given by

$$\begin{bmatrix}\varepsilon_{xx}\\ \varepsilon_{yy}\end{bmatrix} = \begin{bmatrix}k_{11} & k_{12}\\ k_{21} & k_{22}\end{bmatrix}^{-1}\begin{bmatrix}\frac{\Delta\lambda_f}{\lambda_f}\\ \frac{\Delta\lambda_s}{\lambda_s}\end{bmatrix} \qquad (3)$$

where

$$k_{11} = 1 - p_{12}\frac{n_0^2}{2} + p_{11}\frac{n_0^2\nu}{2(1-\nu)} \quad k_{12} = -p_{12}\frac{n_0^2}{2} + p_{11}\frac{n_0^2\nu}{2(1-\nu)} \quad k_{21} = 1 - p_{12}\frac{n_0^2}{2} + p_{12}\frac{n_0^2\nu}{2(1-\nu)} \quad k_{12} = -p_{11}\frac{n_0^2}{2} + p_{12}\frac{n_0^2\nu}{2(1-\nu)}$$

III. Experimental Test

A. Setup

Figure 4a shows a composite plate with surfaced bonded MFC actuators (M2503-P1 from Smart Material Corp.) and a PM-FBG sensor (TimberCon FBG PM Bowtie, 1550nm). The composite plate is made of IM7 material with 18 cross-ply layup. The plate is 24 in. long and 11 in. wide. It was hung in the air to create the free edge boundary conditions. Three MFC actuators were oriented at 0, 45, and 90 degrees with respect to the axial direction of the PM-FBG sensor in order to investigate the directional sensing capability, which are labeled as MFC 1, MFC 2, and MFC 3. The active size of each MFC is 25mm long and 3mm wide. Majority strain will be induced along its length direction. Figure 4b shows the schematic of the demodulation system to collect the reflective intensity responses from both fast and slow axis. In all tests, the temperature effect on the PM-FBG sensor is neglected because the temperature fluctuation in the laboratory environment is very small.

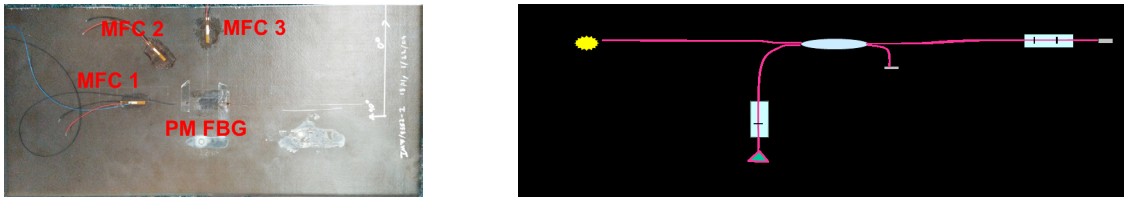

(a). (b)

Figure 4: Experimental setup: (a). composite plate with in-situ actuators and PM-FBG; b). schematic of demodulation system

B. Procedure

As aforementioned, there are three key steps to derive in-plane strain field as outlined below.

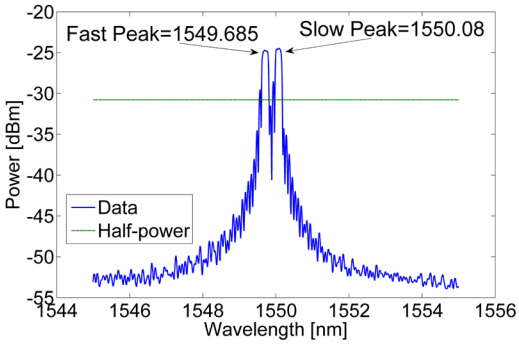

Figure 5: Spectrum of PM grating

Step 1: Determine the grating spectrum

The goal is to obtain the wavelength peaks in polarization axes and calibrate the response curve between the wavelength and reflective intensity. Figure 5 shows the PM-FBG spectrum responses. Clearly, we can identify two peaks which separate the fast axis and slow axis. Ideally, the laser should be set to the wavelength at full width at half-maximum (FWHM) as for the regular FBG sensing[16]. Accordingly, the driving wavelength for the fast axis was set at 1549.563 nm and the wavelength of 1550.120 nm was applied to the slow axis.

Step 2: Collect the reflective intensity

Five-cycled Hanning windowed sine burst was applied to the MFC actuator in order to reduce the side lobes[22-23]. The peak amplitude was 175 volts. Comprehensive tests were performed to collect the reflective intensity responses at different actuating frequencies, ranging from 20 kHz to 200 kHz and repeated the testing for each MFC actuator.

Step 3: Conduct post-processing to calculate strain

Based on the results from step 1 and 2, we can calculate the strain responses using Eq. 1-3.

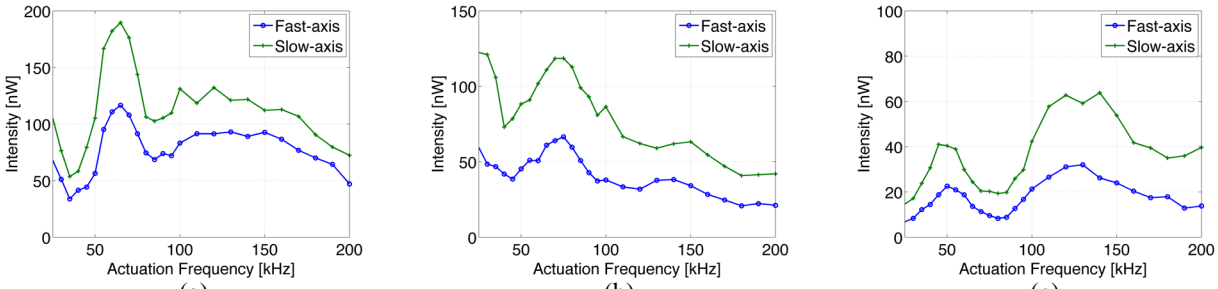

(a) (b) (c)

Figure 6: Reflective intensity responses: (a). 0 degree MFC; (b). 45 degree MFC; and (c) 90 degree MFC

IV. Results

Figure 6 shows the frequency responses of the reflective intensity in both fast and slow axis for each actuation case. Clearly, the intensity responses vary with the excitation frequency and reach peak values at certain frequencies, i.e., impedance matching frequencies. As illustrated in Figure 6, the PM-FBG shows directivity because the grating is more sensitive to the induced strain along the fiber axis. The reflective intensity magnitude reduces as the angle of between the MFC actuator and PM-FBG sensor increases from 0 to 90 degrees. A unimorph actuation scheme was employed. Therefore, both antisymmetric modes (i.e., A0, A1, A2, etc.) and symmetric modes (i.e., S0, S1, S2, etc.) were excited[2,8,24]. The wave speed of the first symmetric mode (S0) is much higher than antisymmetric mode (A0). Also, the S0 wave is less dispersive. In the following sections, we apply these basic understandings of Lamb wave to interpret the measurement data.

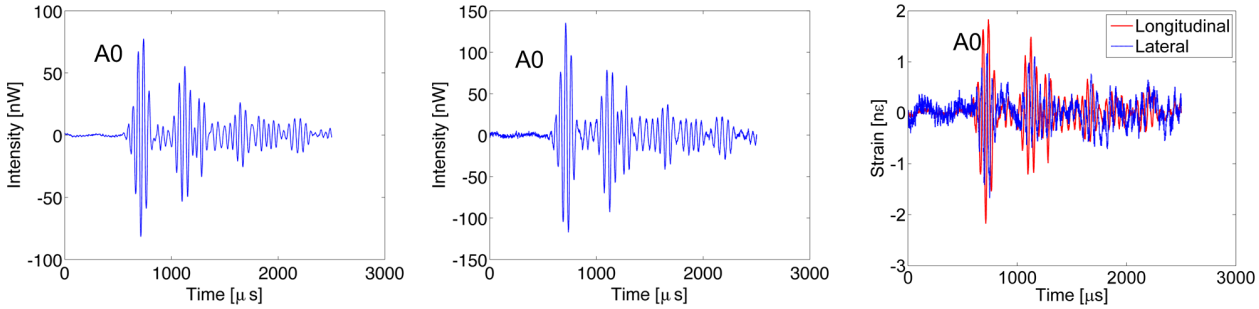

(a) **(b)** **(c)**

Figure 7: Reflective intensity and strain responses under 20 kHz actuation using 0 degree MFC: (a). fast axis; (b). slow; and (c) in-plane strain field

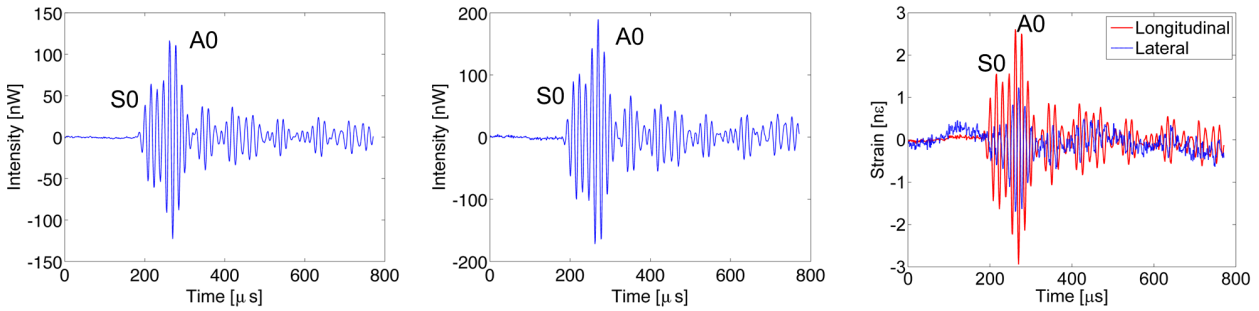

(a) **(b)** **(c)**

Figure 8: Reflective intensity and strain responses under 65 kHz actuation using 0 degree MFC: (a). fast axis; (b). slow; and (c) in-plane strain field

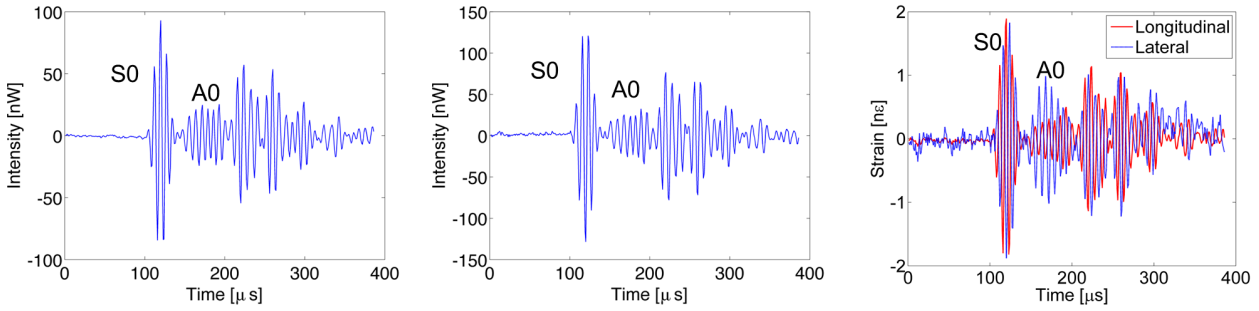

(a) **(b)** **(c)**

Figure 9: Reflective intensity and strain responses under 130 kHz actuation using 0 degree MFC: (a). fast axis; (b). slow; and (c) in-plane strain field

Figure 7-9 show reflective intensity and strain time responses of 20 kHz, 65 kHz, and 130 kHz, respectively, in which the Lamb wave was generated by MFC 1 (shown in Figure 4a). For the 20 kHz case (Figure 7), the A0 mode was dominant and it decays as it reflects from the edges of the composite plate. The longitudinal strain responses are slightly higher than the lateral responses. As we increase the actuation frequency to 65 kHz (Figure 8), we observe both A0 and S0 wave responses. The amplitude of A0 wave is larger than the amplitude of S0 wave. But, the A0

wave is more dispersive as it propagates. There are some interactions between two wave modes. Clearly, both wave modes separate at 130 kHz (Figure 9). Again, the S0 wave is less dispersive compared to the A0 wave mode. The strain responses under 65 kHz frequency actuation show higher amplitudes compared to the cases of 20 kHz and 130 kHz, which is consistent to the reflective intensity frequency responses as shown in Figure 6.

The 70 kHz results actuated by MFC 2 are shown in Figure 10. Similar trends are observed as shown in Figure 8, in which both A0 and S0 wave modes are excited. The 140 kHz results actuated by MFC 3 are shown in Figure 11. The S0 wave is dominant. However, the reflective amplitudes are larger than the instantaneous wave response due to the intensification after the reflection from boundaries. In this case, the MFC actuator is perpendicular to the PM fiber axis. The reflective intensity responses in both fast and slow axis are substantially reduced compared to the cases actuated by MFC 1 and 2. The lateral strain responses are slightly larger than the longitudinal strains as shown in Figure 11c to illustrate the directivity of the PM-FBG sensor.

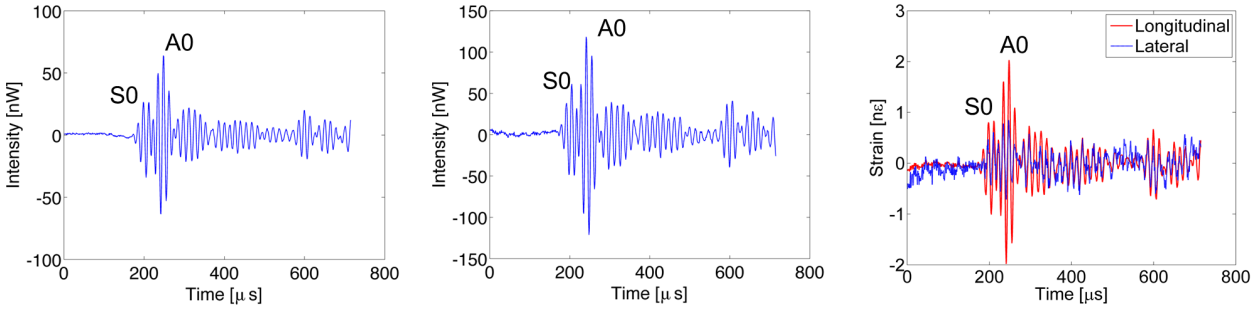

(a) **(b)** **(c)**

Figure 10: Reflective intensity and strain responses under 70 kHz actuation using 45 degree MFC: (a). fast axis; (b). slow; and (c) in-plane strain field

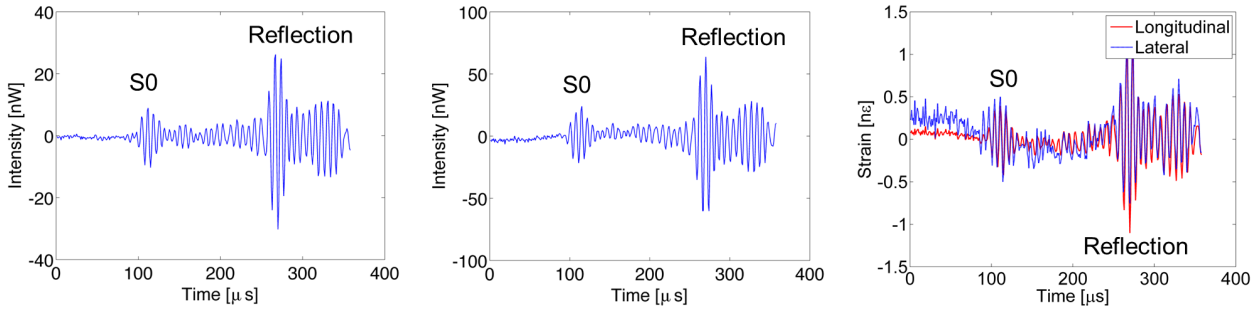

(a) **(b)** **(c)**

Figure 11: Reflective intensity and strain responses under 140 kHz actuation using 90 degree MFC: (a). fast axis; (b). slow; and (c) in-plane strain field

V. Conclusion

This is the first attempt to demonstrate the acousto-ultrasonic sensing using a PM-FBG sensor in a composite plate. The PM-FBG senor is able to capture both Lamb wave propagation characteristics and derive associated 2-D strain field based on measured reflective intensity responses in both fast and slow axis. The PM-FBG sensor can collect reflective intensity data up to 200 kHz using the proposed demodulation system. The detectable strain is in the range of nano-strain. It is clearly demonstrated that one PM-FBG sensor is able to characterize two-axis strain responses. Therefore, at least 50% reduction on the sensor number can be achieved, which is substantial in the SHM applications.

Acknowledgments

Authors would like to thank Claude Chris Conn and Rush Elkins for their assistance to bond actuators and PM-FBG.

References

[1] Smart COPV" Composite Overwrapped Pressure Vessels (COPVs) Integrated with Structural Health Monitoring (SHM) Systems That Target Space Exploration and ISS Needs, NASA Technical Report, JSC-CN-26776, August 13, 2012.
[2] Viktorov, I. A., *Rayleigh and Lamb Waves—Physical Theory and Applications*, Plenum Press, New York, NY, 1967.
[3] Worlton, D. C., "Ultrasonic testing with Lamb waves," *Nondestructive Testing*, Vol.15, pp. 218–222, 1957.
[4] Rose, J. L., "A baseline and vision of ultrasonic guided wave inspection potential," *Journal of Pressure Vessel Technology,* Vol. 124, pp. 273–282, 2002.
[5] Dalton, R. P., Cawley, P., and Lowe, M. J. S. "The potential of guided waves for monitoring large areas of metallic aircraft fuselage structure," *Journal of Nondestructive Evaluation,* 20(1), pp. 29–46, 2001.
[6] Cawley, P. and Alleyne, D., "The use of Lamb waves for the long range inspection of large structures," *Ultrasonics,* Vol. 34, pp. 287–290, 1996.
[7] Wilcox, P. D., Lowe, M. J. S., and Cawley, P., "Mode and transducer selection for long range Lamb wave inspection," Journal of Intelligent Material Systems and Structures 12, pp. 553–565, 2001.
[8] Su, Z. and Ye, L. *Identification of Damage Using Lamb Waves: From Fundamentals to Applications*, Springer Verlag, London, UK, 2009.
[9] Chang, Fu-Kuo eds, *Structural Health Monitoring: Current Status and Perspectives*, CRC Press, April 1998.
[10] Giurgiutiu, V. *Structural Health Monitoring with Piezoelectric Wafer Active Sensors*; Academic Press: Burlington, MA, USA, 2007.
[11] Davis, M. A. and Kersey, A.D., "All-fiber Bragg grating strain-sensor demodulation technique using a wavelength division coupler," *Electronics Letters*, **30**, pp. 75-77, 1994.
[12] Udd, E., ed., *Fiber Optic Sensors, An Introduction for Engineers and Scientists*, John Wiley & Sons Ltd, New York, New York, 1991.
[13] Udd, E., ed., *Fiber Optic Smart Structures,* John Wiley & Sons Ltd, New York, New York, 1995.
[14] Al-Chalabi, S., Culshaw, B., and Davies, D., "Partially Coherent Sources in Interferometric Sensors," *Proceedings of the 1st International Conference on Optical Fiber Sensors (IEEE Conf. Publ. No. 221)*, IEEE, London, United Kingdom, pp. 1332-1335, 1983.
[15] Inaudi, D., "State of the art in fiber optic sensing technology and EU structural health monitoring projects." *Proceedings of Structural Health Monitoring and Intelligent Infrastructure (SHMII)*, Tokyo, Japan, pp.191-198, 2003.
[16] Beta, D.C., Thursby, G., Culshaw, B., and Staszewski, W.J., "Acousto-ultrasonic sensing using fiber Bragg gratings." *Smart Materials and Structures,* VOl. 12, pp. 122-128, 2003.
[17] Nelson, D.V., Makino, A., Lawrence, C., Seim, J.M., Schulz, W., and Udd, E., "Determination of the K-Matrix for the Multi-parameter fiber grating sensor in AD072 fibercore fiber," *Proc. SPIE,* 3489, 79, 1998.
[18] Udd, E., Schulz, W.L., Seim, J.M., Haugse, E., Trego, A., Johnson, P.E., Bennett, T.E., Nelson, D.V., and Makino, A. "Multidimensional strain field measurements using fiber optic grating sensors," *Proc. SPIE,* 3986, 254, 2000.
[19] Schulz, W.L., Udd, E., Seim, J.M., Trego, A., and Perez, I.M., "Progress on monitoring of adhesive joints using multi-axis fiber grating densors," *Proc. SPIE* 3991, 52, 2000.
[20] Udd, E., "Review of multi-parameter fiber grating sensors," *Proc. SPIE*, 6706, 2007.
[21] Mawatari, T. and Nelson, D., "A multi-parameter Bragg grating fiber optic sensor and triaxial strain measurement," Smart Materials and Structures, Vol. 17, 035033, 2008.
[22]Lin, X and Yuan, F.G., "Diagnostic Lamb waves in an integrated piezoelectric sensor/actuator plate: analytical and experimental studies," *Smart Materials and Structures* 10: 907-913, 2010.
[23] Giurgiutiu V, Bao J and Zhao W., "Piezoelectric wafer active sensor embedded ultrasonics in beams and plates," *Experimental Mechanics* 43: 428-449, 2003.
[24]Roh Y-S, Chang F-K, "Effect of impact damage on Lamb wave propagation in laminated composites," In: Sun C (ed.) *Proceedings of the ASME International Mechanical Engineering Congress and Exposition (Dynamic Responses and Behavior of Composites)*, San Francisco, CA, USA, November 12–17, pp. 127–138, 1995.

Performance Analysis of a 22 Newton High Performance Green Propellant Thruster

Stephen A. Whitmore[1]
Utah State University, Logan, Utah, 84322

and

Christopher G. Burnside[2]
NASA (MSFC) Marshall Space Flight Center
Huntsville, Alabama, 35812

In late April 2015 the Spacecraft Propulsion Branch (ER23) at the NASA Marshall Space Flight Center (MSFC) completed ground tests of two small spacecraft thrusters with nominal thrust levels of 5 and 22 Newtons. These thrusters were designed to operate with the new high performance green propellant developed by the *ECological Advanced Propulsion Systems* (ECAPS) Group, a subsidiary of the Swedish Space Corporation. The tested heavy-weight ground test articles were not flight units, but were generally representative of flight hardware designs. The 5-N thruster was used to perform checkouts of the NASA Center's Component Development Area altitude test stand. Only a small data set was generated by the 5-N tests. The 22-N thruster was comprehensively tested, and generated a significant volume of data. This database allows independent comparison and assessment of data sets previously generated by ECAPS and its commercial affiliate, Orbital/ATK. This series of tests marked the first time he 22-N thruster had been tested outside of the ECAPS facility. This paper details the signal processing techniques used to reconstruct the 22-N thruster performance parameters from the measured database. Results of these calculations are compared against theoretical expectations and data previously published by ECAPS.

I. Nomenclature

A^*	=	nozzle throat area, cm^2
A_e	=	nozzle exit area, cm^2
A_p	=	effective pulse train amplitude, N
C_F	=	thrust coefficient
C_p	=	specific heat at constant pressure, $J/kg\text{-}K$
c^*	=	thruster characteristic velocity, m/sec
c^*_{eff}	=	effective value of characteristic velocity, m/sec
c^*_{max}	=	theoretical maximum value of characteristic velocity, m/sec
Dia	=	thruster diameter, cm
F_{vac}	=	vacuum thrust, N
f_n	=	frequency at harmonic order n, Hz
f_{low}	=	low pass frequency, Hz
I_{max}	=	total impulse, $kN\text{-}s$
I_{min}	=	minimum impulse bit, $N\text{-}s$
I_{sp}	=	specific impulse, s
$I_{sp\ eff}$	=	effective specific impulse, sec
j	=	imaginary number, $(-1)^{1/2}$
k	=	sample time index
g_0	=	mean acceleration of gravity at sea level, $9.8067\ m/sec^2$

[1] Professor, Mechanical and Aerospace Engineering Department, Propulsion Research Laboratory, Utah State University.
[2] Aerospace Engineer, Spacecraft Propulsion Branch (ER23), NASA MSFC.

L = thruster length, *cm*
m_{tot} = thruster mass, *g*
m_{prop} = consumed propellant mass, *g*
$\dot{m}_{prop}$ = propellant mass flow rate, *g/s*
M_e = exit plane mach number
M_w = molecular weight of exhaust products, *kg/kg-mol*
N = number of data points in the record
n = harmonic order
R_g = gas-specific constant (per unit molecular weight) of exhaust products, *J/kg-K*
P_c = chamber pressure, *kPa*
p_{alt} = vacuum chamber altitude pressure, *kpa*
p_e = exit plane pressure, *kPa*
P_{0e} = exit plane stagnation pressure, *kPa*
$\hat{P}_0$ = exit plane stagnation pressure reconstructed using thrust measurement, *kPa*
P_{prop} = thruster inlet propellant feed pressure, *kPa*
T = sampled record length or pulse period, *s*
T_{prop} = thruster inlet propellant feed temperature, ^oC
T_0 = ideal flame temperature, ^oC
t = time, *s*
t_{burn} = burn time, *s*
t_p = thruster pulse "on" time during active duty cycle, *s*.
Y_n = complex Fourier coefficient of harmonic order *n*
Y^*_n = complex conjugate of Fourier coefficient of harmonic order *n*
y_k = data sample at time index *k*
$||S/\eta||$ = ultimate signal-to-noise ratio
ΔT = sample interval, *s*
ε = nozzle expansion ratio
γ = ratio of specific heats of exhaust products
η^* = thruster combustion efficiency
ω = radian frequency, *rad/s*

II. Introduction

Volumetric efficiency is a primary consideration for small-spacecraft systems and compactness and simplicity are key system design elements. Although usually offering lower performing than bipropellant systems, monopropellant systems are inherently lighter and less complex because only a single propellant storage and feed system is required. Hydrazine is by far the most commonly used monopropellant for primary spacecraft propulsion and attitude control thrusters. Hydrazine thrusters are extremely simple and consist of an electric solenoid valve, a pressurant tank, and a catalyst bed of alumina pellets impregnated with iridium (Shell 405®[i]). The catalyst initiates an exothermic decomposition of the hydrazine to produce ammonia, nitrogen, and hydrogen gases with approximately 1600 kJ of heat for each kilogram of decomposed propellant. Hydrazine decomposition using the Shell 405 catalyst requires no additional heat input at room temperature.

Unfortunately, hydrazine is a powerful reducing agent that poses serious environmental concerns. Hydrazine is extremely destructive to living tissues, and is a probable human carcinogen. Exposure produces a variety of adverse systemic effects including damage to liver, kidneys, nervous system, and red blood cells.[ii] In addition to these biological and toxicological impacts, hydrazine presents significant environmental dangers for the spacecraft and launch vehicle. As a chemical prone to rapidly decompose or explode when struck, vibrated, or otherwise agitated, hydrazine is listed among the most sensitive shock-sensitive chemicals by the US Department of transportation.[iii,iv]

Although procedures are in place to allow hydrazine to be managed safely on tightly controlled military and NASA-owned flight experiments; the toxicity and explosion potential of hydrazine requires extreme handling precautions. Increasingly, with a growing regulatory burden, infrastructure requirements associated with hydrazine transport, storage, servicing, and clean up of accidental releases are becoming cost prohibitive. As space flight operations continue to shift from government–run organizations to private companies and universities operating away from government-owned test reservations, servicing payloads requiring hydrazine as a propellant becomes

operationally infeasible. Extreme handling precautions generally do not favor hydrazine as a propellant for secondary payloads. In 2003 a study performed by the (EADS ST) for the European Space Agency (ESA) showed the potential for considerable operational cost savings by simplifying propellant ground handing procedures.[v] A non-toxic, stable propellant alternative for hydrazine is clearly desirable.

A. Ammonium Dinitramide (ADN) as a "Green" Oxidizer

Recently, the *ECological Advanced Propulsion Systems* (ECAPS), a subsidiary of the Swedish Space Corporation (SSC) has developed a High performance Green Propellant (HPGP) as a potential alternative to Hydrazine. The primary component of the HPGP is the ammonium salt of dinitraminic acid, Ammonium DiNitramide (ADN, $NH_4(NO_2)_2N$) [vi,vii]. ADN decomposes under heat to leave only nitrogen, oxygen, and water. ADN is a strong oxidizing agent, and was developed in the former Soviet Union as a potential replacement for ammonium perchlorate (AP). The manufacturing process for ADN was classified until 1989 when Bottaro, et al, at the Stanford Research Institute (SRI)[viii] independently synthesized ADN.[ix] Currently ADN is manufactured and marketed commercially by EURENCO Bofors, Karlskoga, Sweden and Alexandria VA, USA.

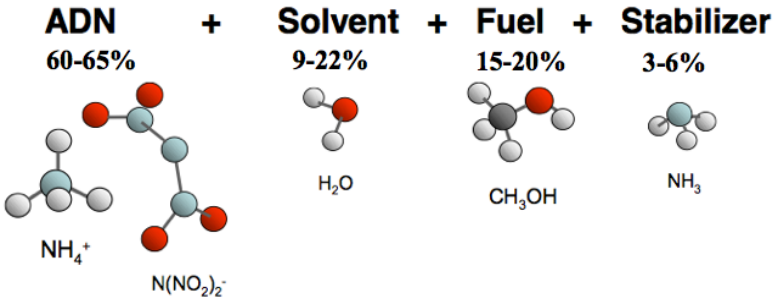

Figure 1. HPGP LMP -103S Propellant Blend Constituents.

B. Physical Properties of LMP-103S

As shown in Figure 1 the ECAPS HPGP propellant blend -- known by the commercial product number LMP-103S - by weight consists of 60-65% ADN, 15-20% methanol (C_4HO), 3-6% Ammonia (NH_3), and 9-22% water. The water acts as the solvent for ADN oxidizing agent and methanol fuel component, and the ammonia component acts as a solution stabilizer and balances the pH level of the solution. The water also helps to moderate the reaction temperature, and as the water component is reduced, the more propellant becomes more energetic. The nominal mix concentration of LMP-103S is approximately 25% denser than hydrazine, and this feature increases the volumetric efficiency advantage of the propellant. The "green" LMP-103S propellant blend is catalytically decomposed to produce water vapor and approximately 2000 kJ/kg of heat. Together with its American partner, Orbital/ATK, ECAPS is currently developing a suite of space thrusters with thrust levels varying from 0.5 N (0.11 lbf) to 220 N (49.4 lbf).

Extensive safety-related testing has been performed since 1998, as *LMP-103S* essentially is a premixed bi-propellant (fuel mixed with oxidizer) with high energy content. In its pure form, ADN is a highly energetic material and is extremely flammable and is classified as a secondary explosive by the US Department of Transportation (DOT) – in the same category as TNT or RDX. ADN is significantly more prone to detonation than ammonium perchlorate. ADN is classified as a UN/DOT 1.1 explosive. Pure ADN salts cannot be transported by air. In the LMP-103s mixture, the material heat and shock stability is significantly increased. *LMP-103S* propellant is *transport classified* according to UN/DOT Class 1.4S, allowing air *transportation* in passenger and cargo carriers when packaged in the recommended shipping container.

In support of the analysis to be presented later in this paper, the thermodynamic and transport properties of the decomposition products LMP-103S were calculated using the NASA Equilibrium Chemistry program "Chemical Equilibrium with Applications," (CEA).x Fir this analysis the formulation was assumed consist of 65% ADN, 20% Methanol, 56% Ammonia, and 10% Water by mass. For this analysis the exhaust products were assumed to be exclusively {H2O, N2, H2, CO, and CO2}, and the "ONLY" feature of CEA was used. Exhaust properties for catalyst bed pressures varying from 1000 kPa (145 psia) to 5000 kPa (725 psia) were calculated. The decomposition products were frozen at the throat conditions. Because the "ONLY" feature was used, the output properties showed little variation with pressure. The following mean properties were calculated, and will be used where appropriate throughout the remainder of this paper. Table 1 summarizes the physical properties of the LMP-103S propellant blend.[xi,xii] Results for the exhaust product properties presented by Table 1 agree well with data previously published by ECAPS.[xiii]

Table 1. Physical Properties of ECAPS LMP-103s (HPGP) Propellant Blend.

(65% ADN, 20% Methanol, 56% Ammonia, 10% Water @1 ATMs)

Propellant Property	**Value**
Density	1.24 g/cm^3
Mean Molecular Weight	89.7 kg/kg-mol
Freezing Point	-6.0 C
Boiling Point	120 C
Operating Temperature Range	10-50 C
Vapor Pressure *(15 C)*	0.24 kPa
Specific Heat Capacity	2.4 kJ/kg-K
Heat of Vaporization	1328.9 kJ/kg
Decomposition Species Concentrations (mole fraction)	**Value**
H_2O	*0.4554*
N_2	*0.2386*
H_2	*0.1854*
CO	*0.0772*
CO_2	*0.0434*
Exhaust Product Thermodynamic Properties	**Value**
Specific heat ratio	$\gamma = 1.2318$
Specific heat at constant pressure	$C_p = 2285.3$ *J/kg-K*
Molecular weight	$M_w = 19.335$ *kg/kg-mol*
Gas constant per unit molecular weight	$R_g = 430.0$ *J/kg-K*
Ideal combustion temperature	$T_0 = 1895.0\ ^oC$
Characteristic velocity	$c^* = 1475.6$ *m/sec*

C. ECAPS Prisma HPGP 1-N Thruster Flight Experiment

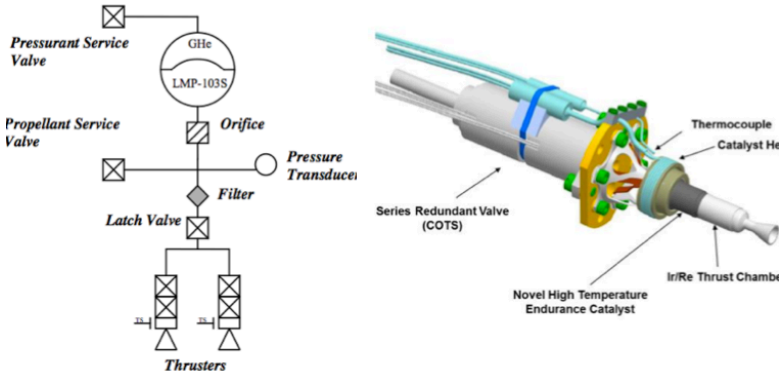

a) P&ID Diagram b) Thruster Schematic

Figure 2. 1-N HPGP Thruster Layout.

In August 2011, ECAPS announced the results of a year-long series of in-space tests of a 1-N thruster, as implemented on the Prisma spacecraft platform, comparing their High Performance Green Propellant (HPGP) to hydrazine. The comparisons claimed that HPGP delivered equivalent–to-superior performance. ECAPS has claimed that their 1-N thruster has achieved a TRL level of 7.0 following this spaceflight demonstration.[xiv,xv] Specific impulse (I_{sp}) levels exceeding 230 seconds were reported from these tests.

Figure 2 the design of the 1-N HPGP thruster flown on the Prisma mission. The Prisma HPGP system consists of one diaphragm-type propellant tank with a capacity of 5.5 kg of propellant, two service valves, one pressure transducer, one system filter, one isolation latch valve, a pipework and two 1 N thrusters. The propellant and the helium pressurant gas are stored in the tank and are separated by means of a flexible diaphragm. The design and function of Figure 1the thrusters developed for ADN-based monopropellant blends have several similarities with hydrazine thrusters. The HPGP thruster operates at a combustion temperature of 1600℃, which is significantly higher than for a hydrazine thruster. The thrust chamber assembly is therefore made of high temperature resistant materials. ECAPS has also developed and patented a proprietary, high

temperature catalyst for HPGP dissociation. Table 2 summarizes the achieved performance of the 1-N HPGP thrusters during the Prisma Mission.[xvi]

III. High Performance Green Propellant Testing at NASA MSFC

The development of practical "green" propellants to replace hydrazine for in-space propulsion has been a goal of NASA for quite some time, and is an essential element of NASA's In-Space Propulsion Systems Roadmap (ISPSR).[xvii] A key element of ISPSR, identifies difficulties associated with hydrazine as a spacecraft propellant and recommends development of "*less hazardous, less toxic*" alternatives -- Specifically, NASA itemizes *TA02.2.1.1, In-Space Propulsion Technologies, Liquid Storable Propellants: "Evaluate alternate green propellants that allow thrusters to operate in pulse and continuous modes with these new propellants."*

Table 2. Performance Characteristics of HPGP Thrusters Delivered for Prisma Mission.

Item	Typical Values
Thrust – steady state	1.05 N – 0.30 N (22 – 5.5 bar)
Thrust Spread – thruster to thruster	± 3% at 22 bar BOL ± 7% at 5.5 bar BOL
Thrust Change During Life – same thruster	± 5%
Specific Impulse – steady state	2281 Ns/kg (233 s) at 22 bar 2008 Ns/kg (205 s) at 5.5 bar
Specific Impulse Degradation Over Life – steady state	- 0.7%
Thrust Rise Time to 90% (after on command)	25 ms at 22 bar BOL 25 ms at 5.5 bar BOL 50 ms at 5.5 bar EOL
Thrust Decay to 10% (after off command)	110 ms at 22 bar BOL 50 ms at 5.5 bar BOL 60 ms at 5.5 bar EOL
Specific Impulse – pulse mode, on 300ms, off 900ms	2184 Ns/kg (223 s) at 22 bar 1870 Ns/kg (191 s) at 5.5 bar
Minimum Impulse Bit – 50 ms on time	0.05 Ns at 22 bar 0.015 Ns at 5.5 bar
Preheating Power	10 W @ 28 VDC
Valve Power	8.25 W @ 28 VDC
Valve Heater Power	Mission Specific
Overall Length	176 mm
Mass	0.34 kg
Demonstrated Life – Demonstrated Qualification	
Total Impulse	50 kNs
Pulses	> 60 000
Propellant Throughput	> 25 kg
Accumulated Firing Time	25.1 hours
Longest Continues Firing	1.5 hours
Thermal Cycles	> 1500
Status	
TRL 7, 2 units delivered for the PRISMA mission	

In response to this directive, NASA recently awarded a $40M contract to a team lead by Ball Aerospace Corporation for a Green Propellant Infusion mission (GPIM)[xviii] to space-test a green-propellant thruster system based on AF-M315E.[xix] AF-M315E is a USAF-proprietary Hydroxylammonium Nitrate (HAN)-based IL propellant blend. Aerojet Corporation was selected to build the green propellant thruster.[xx]

With the GPIM award to Ball Aerospace NASA has committed near-term to AF-M315E as the "go-forward" green propellant option. However, in order to expand future propulsion options, NASA is also very interested in the suite of LMP-103S thrusters developed by ECAPS. Prior to the testing campaign to be described in this paper, had no experience with the LMP-103S propellant. In an effort to gain experience with their suite of green-propellant thruster systems, and to also provide an independent assessment of the thruster system performance. For this test campaign NASA MSFC recently procured two HPGP thrusters with nominal 5-N (1.12 lbf) and 22-N (5 lbf) thrust capabilities. These units were laboratory-weight, but possessed overall similarity to the flight-weight hardware being built by ECAPS. In order to reduce setup time required for hot-fire testing of HPGP thrusters. Orbital ATK -- the US distributor of HPGP technologies -- provided the 5-N thruster thrust stand, propellant cart, and controller hardware for use by NASA under a non-reimbursable space act agreement (SAA). NASA purchased the 22-N thruster from ECAPS.

These systems were tested in the Component Development Area (CDA) altitude test stand in late April 2015. The testing campaign had two primary objectives, 1) CDA perform facility check-outs using the 5-N thruster, and 2) perform comprehensive testing of the 22-N thruster. At the time of the testing campaign the CDA altitude simulation facility had not had a thorough check-out of the recently-installed mechanical and electrical systems, and the 5-N thruster -- previously tested and well characterized by ECAPS and Orbital-ATK -- was used to perform the facility

"calibration." Following the initial system evaluations performed using the 5-N thruster, the 22-N testing was perform with minimal modifications to the test setup. The second objective was quite important to NASA as it marked the first time that a 22-N or larger HPGP thruster had been tested outside of the ECAPS facility.

D. 22-N HPGP Thruster Description

The 22-N thruster is a scaled up version of the original Prisma 1-N thruster, and was delivered to MSFC pre-assembled at ECAPS along with 10L of LMP-103S propellant for eventual hot-fire test campaign. Figure 3 shows the 22-N thruster as integrated onto the CDA test stand. This figure shows the catalyst bed, catbed heater, thrust chamber and nozzle. The oxidation on the surface of the thrust chamber is a result of oxygen in the altitude chamber during pre-heating and hot-fire testing. The oxidization not cause a measurable change in the performance of the thruster except the need to increase the power into the reactor heater to reach the 400 ^{o}C temperature requirement for hot-fire operations.

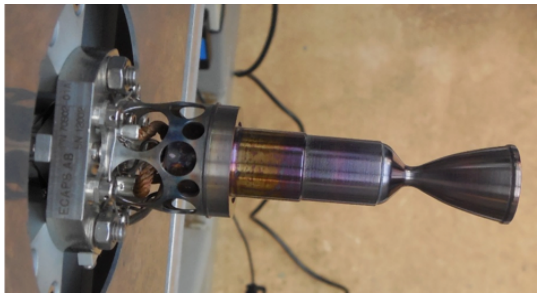

Figure 3. 22-N As Integrated onto the CDA Test Stand.

E. CDA Test Facility Description

As mentioned previously the 22-N hot-fire tests were conducted in the altitude simulation facility located at the Component Development Area (CDA) on the MSFC campus. This test activity was the first time LMP-103S had been introduced to the facility and some modifications were required prior to hot-fire testing. Previous work at the CDA facility had focused on AF-M315E and did not use the altitude capabilities of the test stand. The CDA has a control and data acquisition system for the altitude simulation facility that is independent from the thruster test stand and is not covered in this paper.

The CDA facility uses a combination of vacuum pumps and a two-stage gaseous nitrogen ejector system for altitude simulation. The ejector system is run only during hot-fire tests and is easily disabled between tests by closure of a large gate valve to keep the altitude chamber isolated. A vacuum pump is operated continuously throughout the test day to maintain altitude when only small gas loads are used. During operation of the vacuum pump altitude was maintained at approximately *14 torr (1.87 kPa, 0.27 psia)* continuously. The ejector system is designed to handle gas loads of larger thrusters than output by the 22-N thruster and exhibited only small changes in altitude pressure during operation. The ejector maintained pressure between approximately *14 and 23 torr (3.1 kPa, 0.23 psia)* for the entire set of tests.

Table 3. 22-N HPGP Thruster Design Geometry and Expected Performance Parameters

Parameter	22-NN HPGP Thruster
Thrust, F_{vac}	5.5 – 20 N
Specific Impulse, I_{sp}	224 – 241 s
Total Impulse, I_{max}	15,000 N-s
Min Impulse Bit, I_{MIN}	1 N-s @ 50 ms
Prop Flowrate, $\dot{m}_{prop}$	2.5 – 9 g/s
Inlet Temp, T_{prop}	10 – 50 °C
Inlet Pressure, P_{prop}	5.5 – 24 *x* 10^2 kPa
Chamber Pressure, P_c	3.4 – 15 *x* 10^2 kPa
Nozzle Throat Area, A_t	0.08 cm^2
Nozzle Exit Area, A_e	5.51 cm^2
Expansion Ratio, ε	68.6:1
Thruster Mass, m_{tot}	850 g +/- 20 g

F. HPGP Thruster Test System Description

As mentioned in the previous section the HPGP test stand instrumentation, data acquisition system, and control system is independent of the altitude simulation facility. Figure 4 shows the piping and instrumentation diagram (P&ID) of the systems employed for the 22-N thruster tests. The propellant delivery system consisted of a pressurization system, propellant storage assembly, propellant feed system, and the thrust stand. The propellant feed cart was modified from the original Orbital ATK propellant cart to accommodate the available space in the CDA bunker.

The pressurization system is responsible for containing the high-pressure helium gas and reducing it to the working pressure of the propellant feed system. A remotely variable dome-loaded pressure-reducing regulator set the delivery pressure of the LMP-103S propellant. Downstream of the pressure reducing regulator a relief valve

protects the feed system from high pressures in the event of a regulator failure. Redundant check valves preclude liquid propellant from entering the pressurant system in the unplanned event of overfilling the propellant tank. Remote isolation valves control pressurization of the propellant feed system from the CDA control room. A normally open vent valve is also included to allow a safe return to an unpressurized state in the event of a power failure or an intentional shutdown of the control system.

The propellant delivery system stores the desired quantity of LMP-103S in a pre-loaded run tank and distributes that propellant to the thruster inlet. For this set of tests, the propellant flow rate was measured with three different flowmeters; 1) Two coriolis meters located on the Orbital ATK propellant cart, and a turbine flow meter located on the downstream feed system just upstream of the altitude chamber inlet. Various hand-operated valves are used to prime the feed system up to the thruster to remove gas from the feed line. A piezoresistive bridge-type pressure transducer and type E thermocouple provide propellant properties upstream of the thruster inlet. No direct chamber pressure measurement was available for this system. A 4-arm bridge-type load cell provided direct thrust measurements. The Orbital/ATK propellant cart also provided direct propellant mass measurement in real-time by suspending the run-tank from a load cell. For the 22-N thruster tests, the low-mass flow Coriolis flow meter was bypassed, and only the high-mass flow measurement was available for analysis.

The thruster test stand and propellant feed system were controlled by three DAQ/control system components. First, a Dewetron® (Dewe-800) DAQ system provided primary data acquisition and data storage. Second, a LABView®-based control system was used to remotely-operate the required fill and run-sequence control valves necessary to prepare the system for firing. Finally, component is an Arduino®-based microcontroller operated the real time valve sequences necessary to fire the motor. The three systems communicated using discrete TTL-level commands. Table 4 shows the measurements that were archived by the Dewetron System.

G. 22-N Thruster Test Matrix.

Table 5 shows the test matrix for the 22-N thruster. The first series of tests consisted of single discrete pulses with multiple pulses were performed for some test conditions. The thruster was allowed to cool down naturally without any mechanical or forced gas cooling between pulses. Prior to hot-firing, various hand-operated valves were used to prime the feed system up to the thruster to remove vapor or pressurant gas from the feed line. Priming the system prior to firing allows for more accurate thrust characterization. The single-pulse firings allow the quasi-steady performence of the system to be characterized. The multiple pulse firings cycled the system rapidly with different pulse duty cycles. This series of tests was intended to examine the response fidelity of the system and to allow parameters such as the minimum impulse bit and thrust and impulse-bit consistency.

Table 4. Available Measurements for HPGP 22-N Thruster Test System.

Sensor #	Measurement ID	Description	Model #	Expected Range		Units
				Min	Max	
1	FM-124	Low Flow FM	Bronkhorst M14-ABD-88-O, S/N B9200563A	0	10	kg/h H2O
2	FM-125	High Flow FM	Bronkhorst M54-AAD-99-O-S, S/N 12200260A	0	100	kg/h H2O
3	FM-129	High Flow FM	FTI Meters FTO-3AINW-LHC-YS/N 120601M13128	0.025	0.25	GPM
4	V1_Voltage	SV-134 Voltage	Included in Valve Driver	0	32	Volts
5	V2_Voltage	SV-135 Voltage	Included in Valve Driver	0	32	Volts
6	V1_Current	SV-134 Current	Included in Valve Driver	0	1	Amps
7	V2_Current	SV-135 Current	Included in Valve Driver	0	1	Amps
8	ACC-139	Thruster Accelerometer	PCB Electronics Model 352C22, S/N LW159791	-500 (pk)	500 (pk)	g's
9	FS-141	Thrust	Kistler Model 9207, S/N 3196046	-50	50	N
10	PT-115	Pressurization Panel Pressure	Stellar ST120-500G-135, S/N 1403282	0	500	psig
11	PT-131	Propellant Pressure @ chamber inlet	Stellar ST120-500G-135, S/N 1413369	0	500	psig
12	PT-146	Altitude Pressure	Stellar ST120-15A-135, S/N 1414373	0	15	psia
13	LC-118	Propellant Tank Weight	Delta Metrics P/N 99-3998-0001, S/N 122346	-25	25	lbm
14	TC-132	Propellant Temperature @ chamber inlet	Type E	– 328	1652	deg F
15	TC-147	Chamber Ambient Temperature	Type K	– 328	2282	deg F
16	TC-137	Heater #1 Temperature	Type K, (or Type R)*	– 328 32	2282 2642	deg F
17	TC-149	Heater #2 Temperature	Type K	– 328 32	2282 2642	deg F
18	TC-136	Thruster Valve Surface Temperature	Type K**	– 328 32	2282 2642	deg F
19	TC-150	Thruster Inlet Tube Surface Temperature	Type K	– 328 33	2282 2643	deg F
21	ACC-140	Thruster Accelerometer	PCB Electronics Model 352C22, S/N LW159792	-500 (pk)	500 (pk)	g's

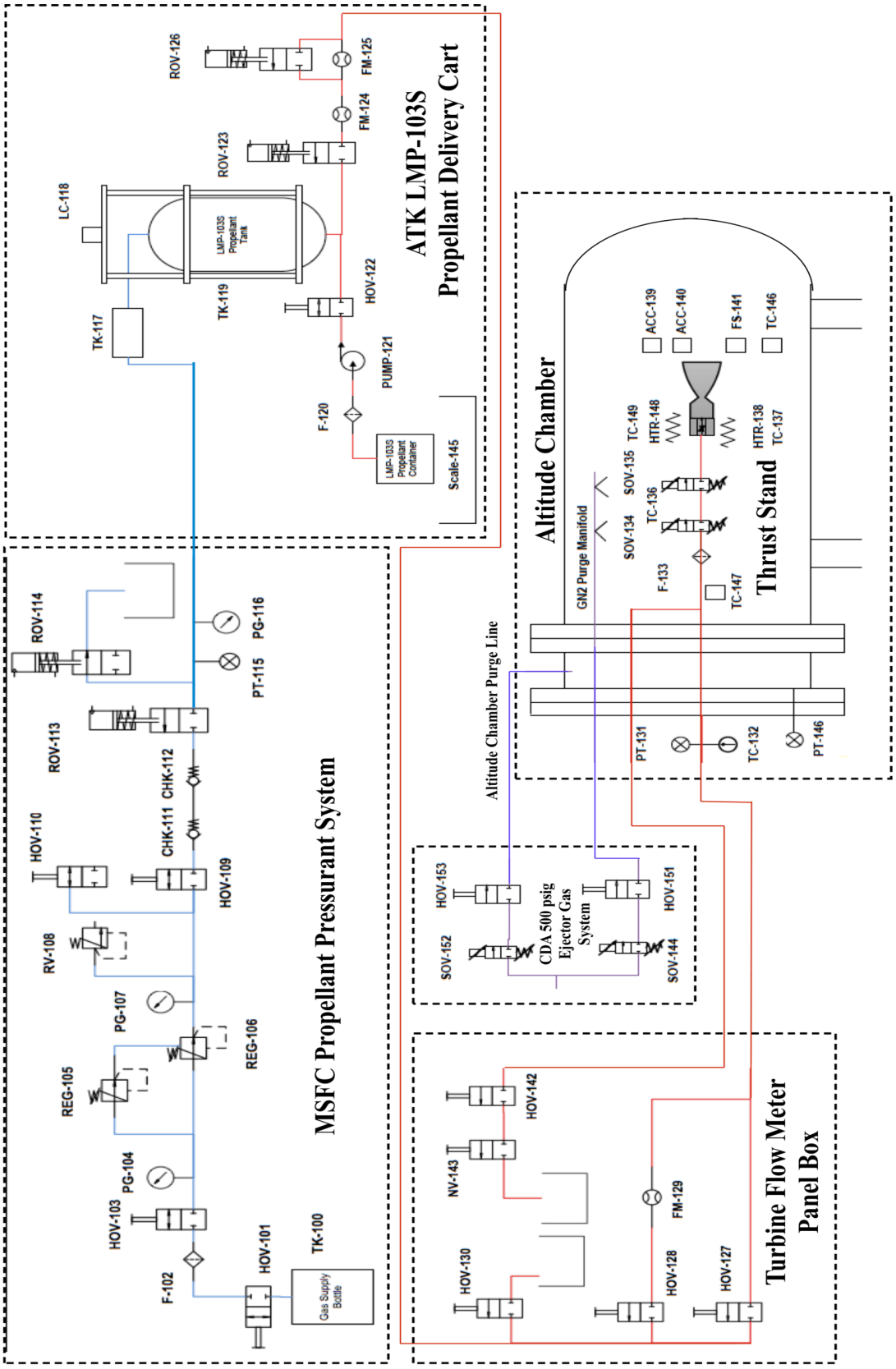

Figure 4. HPGP 22-N Thruster Instrumentation System P&ID.

Table 5. 22N Hot-Fire Test Matrix

Description	Target Inlet Pressure (kPa ga.) x10^{-2}	On-Time (s)	Off-Time (s)	Duty Cycle [%]	# Pulses
Priming	5.2	0.05	9.5	0.5	10
Single Pulse	5.2	0.1	As needed	100	3
	5.2	0.2	As needed	100	3
	5.2	0.5	As needed	100	3
	5.2	1.0	As needed	100	3
	5.2	2.0	As needed	100	3
	5.2	5.0	As needed	100	1
Single Pulse	10.3	0.1	As needed	100	3
	10.3	0.2	As needed	100	3
	10.3	0.5	As needed	100	3
	10.3	1.0	As needed	100	3
	10.3	2.0	As needed	100	3
	10.3	5.0	As needed	100	1
Single Pulse	17.2	0.1	As needed	100	3
	17.2	0.2	As needed	100	3
	17.2	0.5	As needed	100	3
	17.2	1.0	As needed	100	3
	17.2	2.0	As needed	100	3
	17.2	5.0	As needed	100	1
Single Pulse	24.1	0.1	As needed	100	3
	24.1	0.2	As needed	100	3
	24.1	0.5	As needed	100	3
	24.1	1.0	As needed	100	3
	24.1	2.0	As needed	100	3
	24.1	5.0	As needed	100	1
Pulsing	24.1	0.05	0.45	10	25
	24.1	0.02	0.48	4	25
	24.1	0.02	0.18	10	25
	24.1	0.05	0.15	25	25
	24.1	0.1	0.1	50	25
	24.1	0.15	0.05	75	25
	24.1	0.19	0.01	95	25
	24.1	0.1	0.4	20	25
	24.1	0.15	0.35	30	25
	24.1	0.3	0.2	60	25

IV. Test Results for 22-N HPGP Thruster.

H. General Discussion of the Single Pulse Test Data.

The measured single-pulse data sets (from Table 5) exhibited several issues that did not allow direct interpretation of the thruster performance from the raw data. First, the measured thrust data and sensed propellant mass were contaminated by noise sources whose magnitude was significant when compared to the mean signal level. Second, both the thrust load cell and the Coriolis flow meters exhibited significant response latency. This latency was especially pronounced with the high-mass-flow Coriolis meter. Third, the turbine flow meter exhibited large random spikes that were likely a result of a bad signal ground or common-mode noise interference. These spikes occurred throughout the test runs but were especially prevalent right after a thrust-pulse event as the mass flow dropped back towards zero. Finally, because there was no chamber pressure measurement, one could not directly calculate the characteristic velocity c^*, thrust coefficient C_F, and combustion efficiency η^* of the system; instead the chamber pressure must be derived indirectly from the measured parameters.

Figures 5 and 6 show a typical test results for 2-second and 5-second thruster burns. Here, the plotted parameters are a) measured propellant weight, b) thrust, c) mass flow from both the High-flow and Turbine Flow Meters, and d) the thruster inlet and CDA altitude pressures. Although the change in slope can be observed during the thruster burn, the measured propellant weight is extremely noisy with a signal-to-noise ratio only slightly greater than one. The high-flow Corlilis and turbine meters show only general response agreement, with the Coriolis meter signal being highly attenuated and the turbine meter signals showing large intermittent spikes shortly after the initial pressure response has trailed off. The inlet pressure measurement exhibits some "ringing," and effect that is likely due to compression of the top pressurant helium gas as the run valve opens and closes. The observed measurement properties of all of the other non-pulsed tests exhibited similar properties.

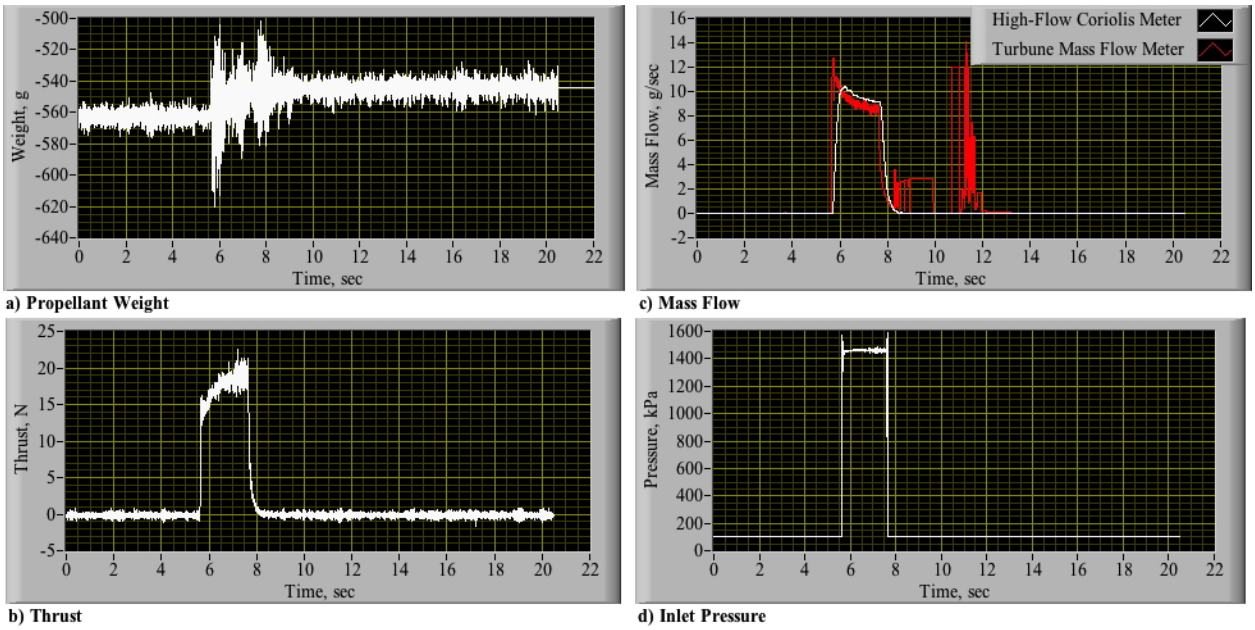

Figure 5. Unprocessed 22-N HPGP Thruster Data, 20-N, 2-Second Burn.

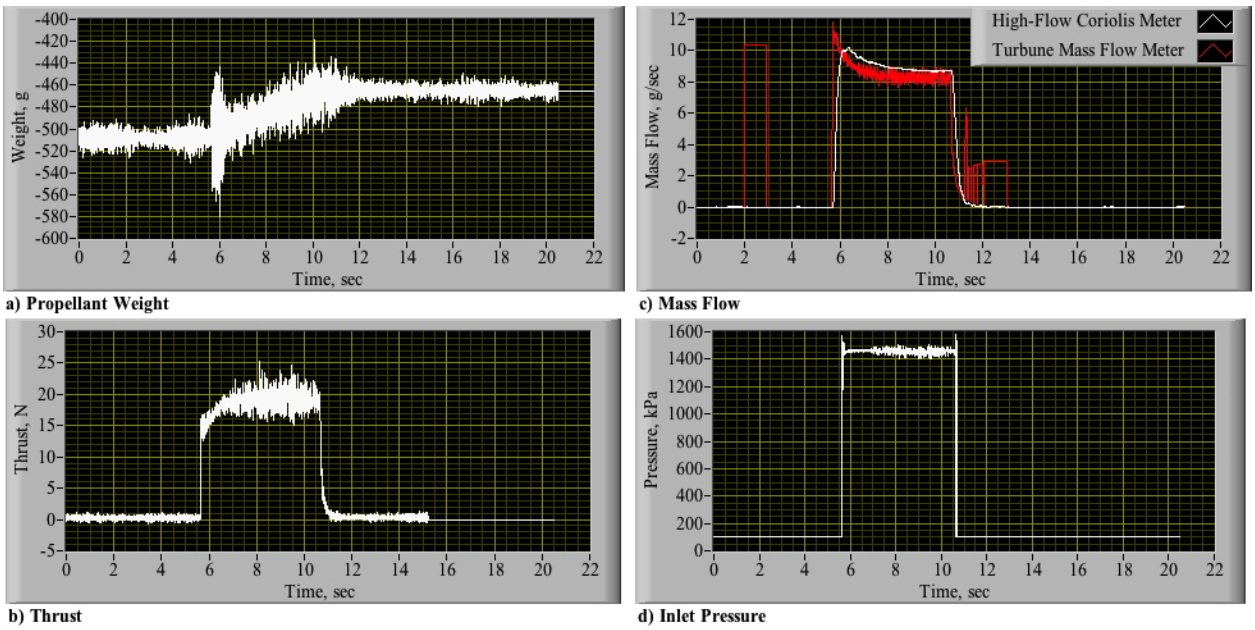

Figure 6. Unprocessed 22-N HPGP Thruster Data, 20-N, 5-Second Burn.

By comparing the thrust measurements to the inlet pressure signals, it can be observed that the slightly noisy thrust signals exhibit good initial response and jump to greater than 8N almost immediately after the run-valve is opened. However, for both cases it takes more than 1.5 seconds for the thrust signals to reach peak values. As will be demonstrated later in this section this latency is likely not a measurement artifact, but is instead a real effect that is likely produced by slow LMP-103S decomposition rates within the thruster catalyst bed. A primary result of this slow build-up reduced total impulse delivered by a thruster pulse, and a reduced mean thrust level.

I. Signal Reconstruction.

Unfortunately, all of the propellant mass-related data presented by Figs. 5 and 6 exhibit significant measurement distortions, making it difficult to directly discern the system mass flow properties without significant signal processing. Accurate knowledge of the propellant mass flow rates is essential in order to calculate both the specific impulse and characteristic velocity parameters of the thruster. To more accurately assess the system mass flows each of the mass-based measurements -- the propellant weight and Coriolis and turbine meter mass flows will be processed using Fourier convolution and de-convolution methods[xxi] to removed unwanted signal corruptions while retaining the desired deterministic signal.

1. Mass Flow Derived from Numerically Differentiated Propellant Mass.

As described in the previous section, the ATK propellant cart measured the run tank propellant weight in real time by suspending the tank from a load cell. As observed in Figs 5(a) and 6(a) the resulting measurement is extremely noisy and must be processed significantly before numerical differentiation to calculate the propellant mass flow rate. First the Frequency spectrum is calculated from the raw time history data using the Discrete Fourier transform,[xxii]

$$Y_n = \sum_{k=0}^{N} y_k e^{-j\left[\frac{2\pi}{N}\cdot n\cdot k\right]} \rightarrow n = \{0,1,2,..N/2\} \tag{1}$$

In Eq, (1) k is the sample index corresponding to time $k \bullet \Delta T$, ΔT is the sample interval of the data record, y_k is the data sample at time index k, Y_n is the complex-valued Fourier coefficient corresponding to frequency

$$f_n = \frac{n}{N \cdot \Delta T}. \tag{2}$$

N is the number of data samples in the data record, n is the harmonic order of the coefficient, and T is the record length. In order to use the Fast Fourier Transform to mechanize the calculation, sufficient "zero-padding" is included at the beginning and end of the raw time history to ensure that the signal to be processed has sufficient elements to be an even multiple of a power of two, with equal numbers of zeroes introduced to the beginning and end of the time history in order not to ensure zero time shift in the calculation.

In order to remove high frequency noise from the calculation, the resulting Fourier coefficients are subsequently set to zero for frequencies above prescribed "low pass" frequency, f_{low}. It is a well-known result that differentiation in the time domain is equivalent to multiplying each of the Fourier coefficient Y_n by $j \bullet f_n = j \bullet n/(N*\Delta T)$. Thus multiplying each coefficient by the equivalent scale factor, the resulting spectrum is then inverse-transformed to calculate the filtered and differentiated output time history. To insure that the reconstructed time series is real-valued, it is necessary to build the "upper half" of the spectrum before performing the inverse transform. Building the upper portion of the spectrum involves folding the complex conjugate of the spectrum below the Nyquist frequency[xxiii] (one-half of the sampling frequency) about the Nyquist frequency. This upper half represents the non-physical, but mathematically necessary negative frequencies of the Fourier transform.[xxiv] Figure 7 illustrates this concept. The complex-conjugate upper half of the spectrum is concatenated with the lower half of the spectrum, and the resulting frequency spectrum is transformed to the time domain via the Discrete Inverse Fourier transform,

$$y_k = \sum_{n=0}^{N/2}\left(j\cdot\left(\frac{2\pi\cdot n}{N\cdot\Delta T}\right)\cdot Y_n\cdot e^{j\cdot\left(\frac{2\pi}{N}\cdot n\cdot k\right)}\right) + \sum_{n=\frac{N}{2}+1}^{N-1}\left(-j\cdot\left(\frac{2\pi\cdot n}{N\cdot\Delta T}\right)\cdot {Y^*}_{N-n}\cdot e^{j\cdot\left(\frac{2\pi}{N}\cdot n\cdot k\right)}\right). \tag{3}$$

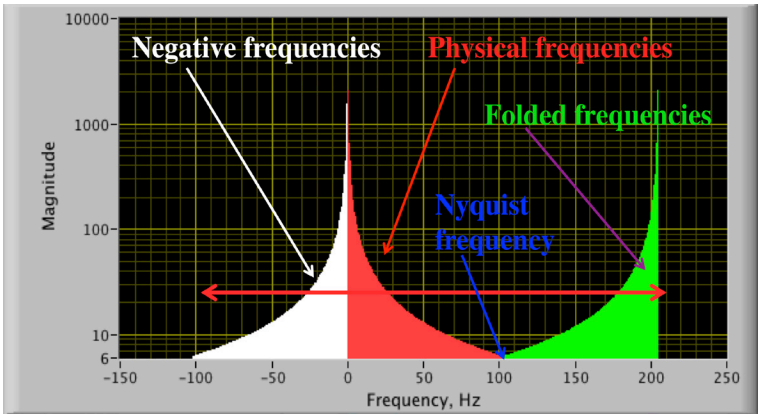

Figure 7. "Negative" Frequencies Folded onto Upper Half of the Frequency Spectrum.

2. Editing Data Spikes from Turbine Mass Flow Meter

As shown by Figure 5(b) and 6(b), the turbine mass flow meter exhibits large random spikes in the output time history. The turbine flow meter contains a free-spinning turbine rotor that turns at a speed that is proportional to the flow velocity. A critical point lies at the bottom end of the flow range, and below this minimum, the calibration factor changes with significantly flow rate change. This effect is the most likely cause of the flow spikes. Also electrostatic build up and discharge from the long cable run connecting the sensor to the DAQ system could b a contributing factor. Fortunately, because the observed spikes occur at very low "true" mass flow levels, i.e. when the thruster is not firing. Editing them from the time history trace is easy. For this spike editor, the measured thrust level is used as a threshold indicator, and any non-zero turbine meters outside of a prescribed trust range are zeroed-out.

After the threshold function has been performed, the remaining signal is low passed filtered using a modification of the convolution method described in the previous section. The described method can also be used to selectively filter out frequency bands *(high, low, notch, or band pass)* from the original noisy time history by setting the Fourier coefficients of the undesired frequency components to zero, instead of multiplying through by $j \bullet \omega$. Lowpass filtering removes "conventional" sensor noise from the mass flow signal, and also attenuates the resonant spike that occurs as mass flow enters the turbine flow path. The same low-pass filtering method is also used to filter the raw thrust signal.

3. Deconvolution of the Coriolis Flow Meter to Signal Remove Attenuation and Latency.

The Coriolis flow meter measurement is based on the principle that as a fluid moves through an oscillating tube vibrating near its resonant frequency, Coriolis forces are induced that cause the tube to twist. The amount of twist, measured using strain gauge techniques, is directly proportional to the mass flow rate of the fluid flowing through the tube. Unfortunately, this process tends to be highly damped and Coriolis sensor have know issues with frequency response.[xxv,xxvi,xxvii] In fact, the topic of Coriolis meter response time is significant enough that the Universities of Oxford and Brunel have a joint grant program[xxviii] *"to push Coriolis metering technology to its dynamic limit."* By comparing the sensed Coriolis sensor response to the turbine meter response in Figs 5(c) and 6(c), it is obvious Coriolis latency exceed *400 ms*. The resulting time shift and signal attenuation makes if difficult to use this unprocessed value for calculating the thruster I_{sp} *and* c^*.

The optimal deconvolution method developed by Whitmore and Wilson (Ref. xxiv) will be used to reconstruct the signal and restore signal fidelity up to the noise level of the system. In this method a frequency-based transfer function is calculated by dividing the Fourier spectrum of the turbine meter into the spectrum of the Coriolis meter signal spectrum. This result is subsequently curve fit with a third-order Butterworth-style[xxix,xxx] transfer function of a prescribed order and roll-off frequency. Figure 8 shows a typical comparison with a third order Butterworth filter rolling off at 4.0 Hz and a damping ratio of 0.866 overlaid on the input spectrum ratio.

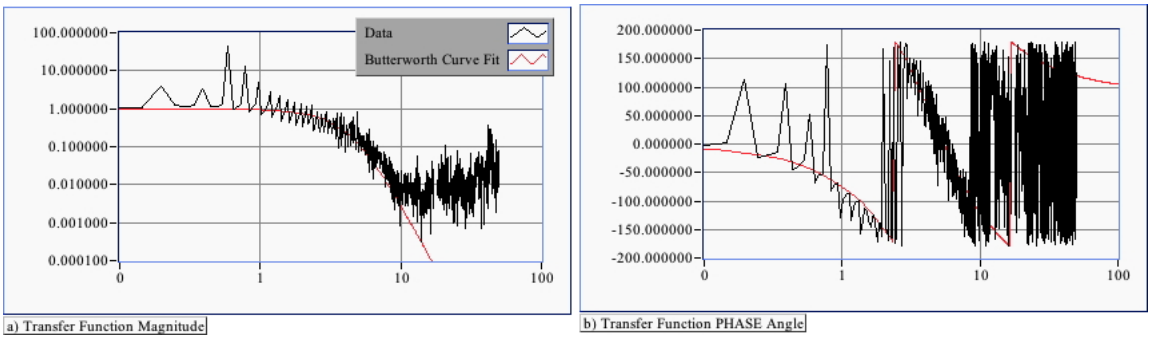

Figure 8. Turbine-to-Coriolis Flow Meter Transfer Function.

The Fourier spectrum of the high-fidelty Coriolis response is calculated by Equation (4). In Eq (4) $Y(\omega)$ is the spectrum of the measured Coriolis meter signal, $\Gamma(\omega)$ is the transfer function complex spectrum, ω is the radian frequency, and $||S/\eta||$ is the ultimate signal-to-noise ratio of the measurement. The $(*)$ superscript indicates the complex conjugate of the transfer-function spectrum.

$$\hat{Y}(\omega) = \left\{ \frac{\Gamma(\omega)^{*} \cdot \left\| S/\eta \right\|^{2}}{\left\| \Gamma(\omega) \right\|^{2} \cdot \left\| S/\eta \right\|^{2} + 1} \right\} Y(\omega) \tag{4}$$

Beyond 10 Hz the spectrum ratio (black line) tends to "flatten out" indicating the noise threshold of the Coriolis signal. Thus even the reconstructed signal will possess inherent response fidelity of only 10 Hz. At input frequencies beyond this value, the individual pulses will tend to "smear" together, and will be inseparable. Reading the magnitude graph at this frequency threshold the ultimate signal-to-noise ratio is approximately 100. Once the high-spectrum is reconstructed, the increased-fidelity is calculated using the Inverse DFT methods previously described by Section IV.I.1.

4. Example Comparison of the Reconstructed Mass Flow Values.

Figures 9(a) and 10(a) compare the filtered propellant mass of Figures 5 and 6 with the original signal, and Figures 9(b) and 10(b) compare the reconstructed mass flow time histories. For comparison purposes Figs. 9(b) and 10(b) also overlay the filtered thrust data. The three reconstructed mass flow signals agree remarkably well for both cases, and the turbine and Coriolis mass flow signals exhibit excellent response fidelity when compared to the thrust measurement. In order to differentiate the original noisy signal, the propellant mass measurement was filtered heavily at 1 Hz; thus, the response fidelity of the differentiated signal is quite low. However, because the reconstructed signal comes from numerical differentiation, the resulting mass flow estimate is inherently unbiased and provides a good "sanity check" on the magnitudes of the remaining two mass-flow signals. The observed properties shown by Figs. 9 and 10 are typical of the results exhibited by all of the Non-pulsed thruster burns.

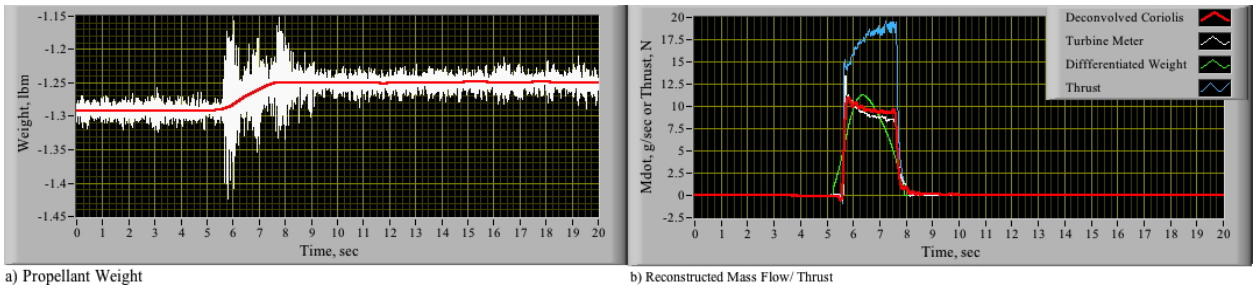

Figure 9. Reconstructed Mass and Mass Flow Signal Comparisons for 20-N, 2-Second Burn.

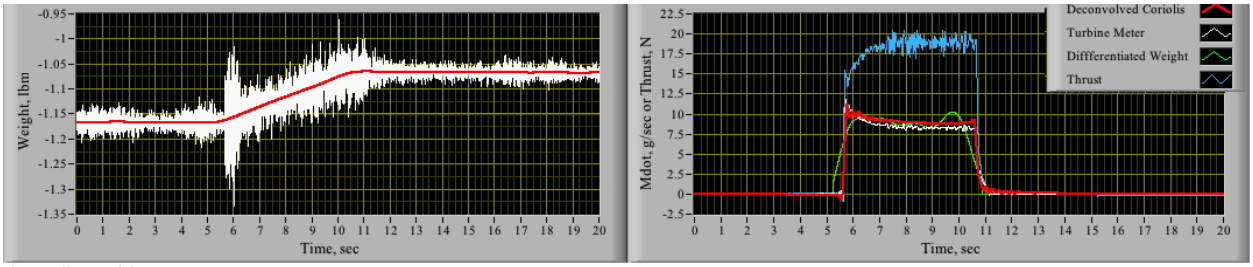

a) Propellant Weight b) Reconstructed Mass Flow/ Thrust

Figure 10. Reconstructed Mass and Mass Flow Signal Comparisons for 20-N, 2-Second Burn.

5. Thrust Signal Response Fidelity

Because the thrust signal plotted in Figs. 9(b) and 10(b) fails to reach a steady state value for greater than 1-second after mass flow has started, in a manner similar to the Coriolis meter mass flow measurement, the thrust measurement appears to have a significant response. Examination of the measurement spectra; however, show that the circumstances are otherwise. Figure 11 plots the spectra of the two signals using the data of Figure 6. The steady state magnitudes have been normalized to give the same DC-levels for this comparison plot. The thrust signal exhibits a log-linear response decay indicating little signal attenuation. However, the Coriolis meter magnitude rolls off in a significantly non-linear manner beyond 2 Hz. In fact at 10 Hz, the remaining Coriolis meter signal has a magnitude that is less than *1/50th* of the thrust signal. At 20 Hz, the Coriolis meter signal flattens out indicating that no discernable signal remains. The thrust signal does not flatten out up through 100 Hz, and captures several thrust stand harmonics at approximately 20 and 80 Hz.

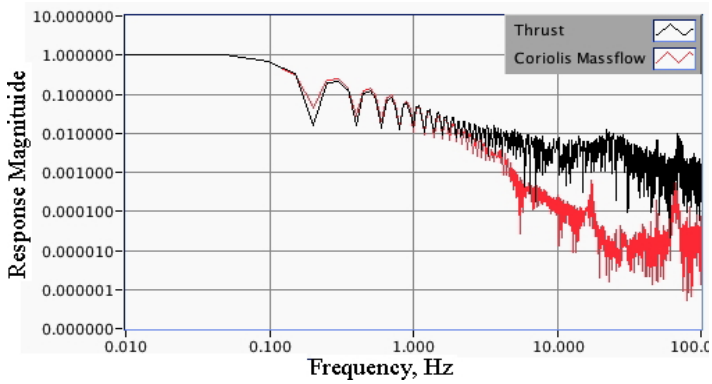

Figure 11. Reconstructed Mass and Mass Flow Signal Comparisons for 20-N, -Second Burn.

Thus, based on this analysis one must conclude that the delay in the thrust build-up is a feature of the thruster. The slow initial response is very likely a result of the time required for complete propellant decomposition within the catalyst bed. Further support of this hypothesis is offered by the very raid decay of the thrust signal once the propellant mass flow is terminated and the combustion chamber evacuates. This slow build up and rapid tail-off feature is exhibited by all of the hot-fire burns, Because the total delivered impulse is significantly effected by this slow buildup, there will be a significant reduction in effective I_{sp} of the thruster system for short-to-moderate length burns. This effect will be summarized later in this section.

6. Calculating the Chamber Pressure of the Thruster.

As was described earlier in this section, because there was no chamber pressure measurement, one could not directly calculate the characteristic velocity c^*, thrust coefficient C_F, and combustion efficiency η^* of the system; instead the chamber pressure must be derived from measured, filtered, and de-biased thrust measurements together with the 1-Dimensional De Laval flow equations.[xxxi] Values for the decomposition product thermodynamic properties including $\{M_w,\ \gamma,\ R_g,\ C_p,\ and\ T_0\}$ were taken from the data previously presented by Table 1. In this sequence of computations the nozzle expansion ratio is used to solve iteratively for the exit plane Mach number,

$$\frac{A_e}{A^*} = \varepsilon = \frac{1}{M_e}\left[\left(\frac{2}{\gamma+1}\right)\left(1+\frac{\gamma-1}{2}M_e^2\right)\right]^{\frac{\gamma+1}{2(\gamma-1)}}, \tag{5}$$

and then the exit plane pressure ratio is calculated assuming isentropic nozzle flow,

$$\frac{p_e}{P_{0e}} = \frac{1}{\left(1+\frac{\gamma-1}{2}M_e^2\right)^{\frac{\gamma}{\gamma-1}}}. \tag{6}$$

Finally the exit plane stagnation pressure is calculated.

$$\hat{P}_0 = \frac{Thrust}{A^*\left\{\gamma\cdot\sqrt{\left(\frac{2}{\gamma-1}\right)\cdot\left(\frac{2}{\gamma+1}\right)^{\frac{\gamma+1}{\gamma-1}}\cdot\left(1-\left(\frac{p_{exit}}{P_0}\right)^{\frac{\gamma-1}{\gamma}}\right)}+\left(\frac{A_{exit}}{A^*}\right)\cdot\left[\left(\frac{p_{exit}}{P_0}\right)-\left(\frac{p_{alt}}{P_0}\right)\right]\right\}}. \tag{7}$$

Equation (7) is solved iteratively for $\hat{P}_0$, a value that closely approximates chamber pressure, P_c. The symbol p_{alt} represents the vacuum test chamber altitude pressure; that is, the pressure into which the thruster-plume exits the nozzle. This parameter was recorded as a part of the CDA test facility control system data stream.

7. Calculating the Effective Specific Impulse, Characteristic Velocity, and Combustion Efficiency of the System.

The three reconstructed mass flow parameters -- Coriolis meter, turbine meter, and differentiated propellant mass -- and the filtered thrust were used to calculate the effective specific impulse of the system by integrating the respective signal to calculate total delivered impulse I_{max} and consumed propellant mass, m_{prop}. The effective specific impulse is than calculated as

$$I_{sp_{eff}} = \frac{I_{max}}{g_0\cdot m_{prop}} = \frac{\int_0^{t_{burn}} F(t)\cdot dt}{g_0\cdot\int_0^{t_{burn}}\dot{m}(t)\cdot dt}. \tag{8}$$

The characteristic velocity is calculated using the integral of the reconstructed chamber pressure and the integrated propellant mass from the three sources,

$$c^*_{eff} \equiv \frac{P_0\cdot A^*}{g_0\cdot m_{prop}} \approx \frac{\int_0^{t_{burn}}\hat{P}_0(t)\cdot A^*\cdot dt}{\int_0^{t_{burn}}\dot{m}(t)\cdot dt} \tag{9}$$

Dividing the calculated characteristic velocity by the theoretical maximum value from Table 1 approximates the combustion efficiency.

$$\eta^* = \frac{c^*_{eff}}{c^*_{\max}} \equiv \frac{\int_0^{t_{burn}}\hat{P}_0(t)\cdot A^*\cdot dt}{c^*_{\max}\cdot\int_0^{t_{burn}}\dot{m}(t)\cdot dt} \tag{10}$$

Figures 12 and 13 show typical results derived from the 20-N burn data presented in Figs 5 and 6. For the 2-second burn the effective I_{sp} is calculated as *{191.9 s, 195.7 s, and 207.5 s}* for the Coriolis meter, Turbine meter and propellant weight respectively. For the 5-second burn the corresponding values are *{206,5 s, 216.4 s, and 206,5 s}*. Figures 12 and 13 also compare the integrated mass flow values from the three available sources against the de-biased and unfiltered propellant mass measurement, and compare the measured inlet pressure against the reconstructed chamber pressure. Here the chamber pressure varies from roughly 50-65% of the inlet pressure, and agrees well with expected values for the 22-N thruster from Table 3.

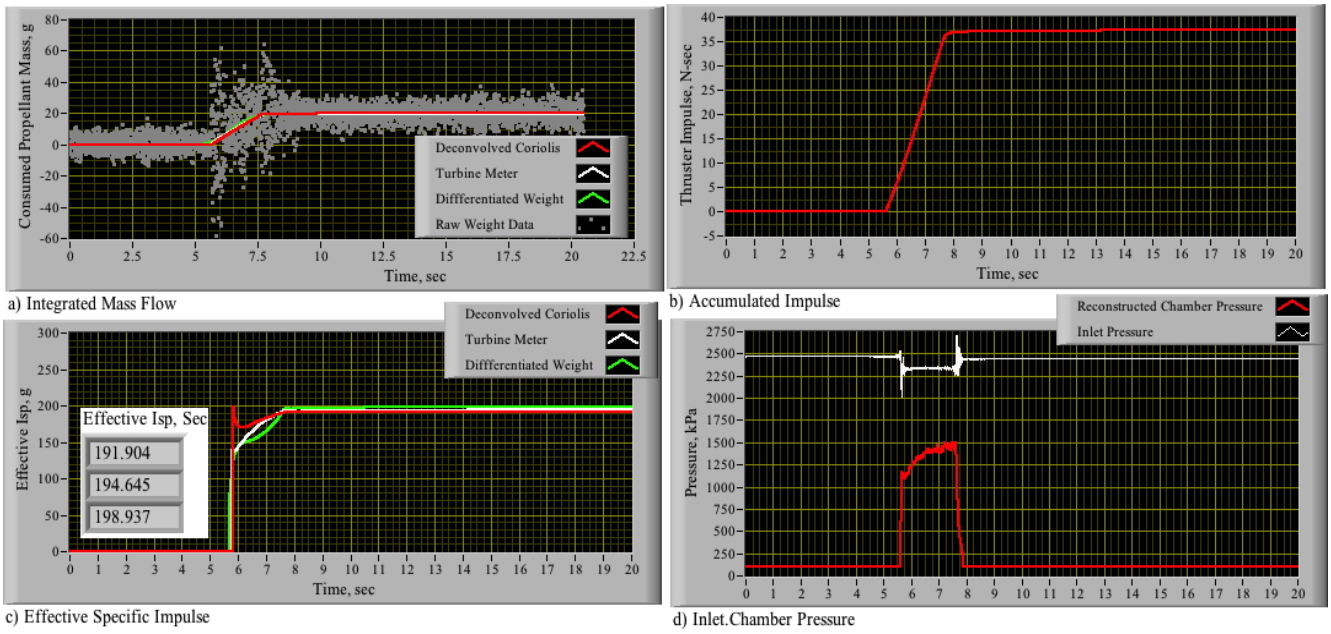

Figure 12. Effective Specific Impulse Calculation, 20-N, 2-sec Thruster Burn.

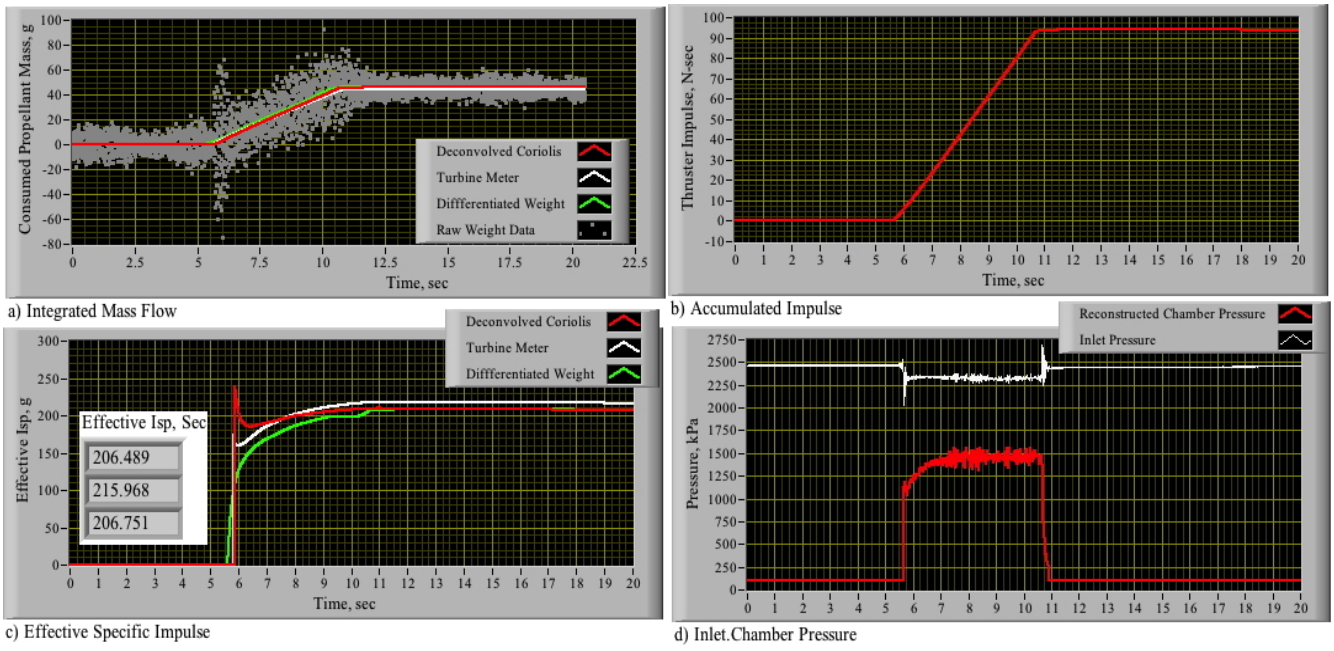

Figure 13. Effective Specific Impulse Calculation, 20-N, 5-sec Thruster Burn.

J. Single-Pulse Test Data Summary

This section summarizes the results of the single-pulse test series. For tests where multiple, separate pulses were performed, each pulse was analyzed separately. The propellant mass was filtered and differentiated assuming a truncation frequency of 1 Hz. All other parameters were filtered with a lowpass truncation frequency of 15 Hz. The Coriolis mass flow sensor was deconvolved assuming a third order Butterworth transfer function with a rolloff frequency of 2.5 Hz and the minimum-phase shift damping ratio value of 0.866. (Ref. xxx)

Figure 14 summarizes the test results from the single-pulse test series (Table 5) for all burns with at least a 1-second duration. In Figure 14(a)-(c) the calculated I_{sp}, c^*, and η^* are plotted against the filtered and de-biased thrust

level. The ECAPS estimate of the expected specific impulse range is also plotted. In Figure 14(d) the calculated thrust coefficient C_F is plotted against the thruster inlet pressure. The dashed red lines on these lots represent the approximate 95% *(2-σ)* confidence level error bounds. Those curves were calculated by taking the curve fit mean square error, multiplying through by a factor of two, and adding (+ boundary) and subtracting (- boundary) that result from the best-fit curve. The ECAPS estimate of the expected thrust coefficient for the 22-N thruster is also plotted for comparison on Figure 14(d). (*Need a reference source for this data*). The thrust coefficient is calculated by dividing the inlet pressure by a scaling factor of 1.6 to account for the pressure drop across the catalyst bed,

$$C_F = \frac{F}{A^* \cdot P_{inlet} / 1.6} \cdot \tag{11}$$

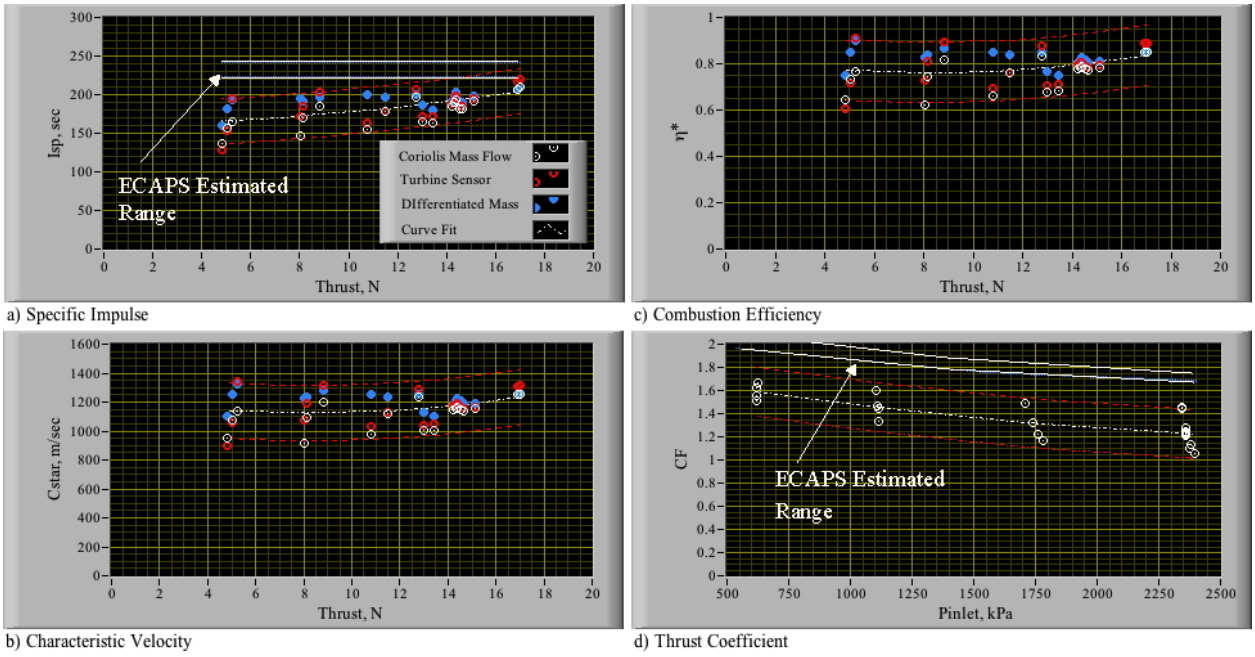

Figure 14. 22-N Single-Pulse Tests Performance Summary.

Several conclusions can be drawn with regard to the plotted data of Figure 14. First, there is observed a significant drop in the data noise as the mean thrust level rises above 14 N. Above this range, there is sufficient mass flow that the CDA test facility does a good job of accurately capturing the data. Below this thrust level mass flow levels are so low as to introduce considerable measurement variability. Also, note that the effective specific impulse and thrust coefficient levels are considerably lower -- from 20-40% -- than the expected pre-test performance levels.

A significant portion of this shortfall is likely due to the thrust build-up delay due to slow decomposition rates within the catalyst bed. Please review the discussion of Section IV.I.5. This hypothesis is supported by re-plotting the data of Figure 14, but with the estimated thruster burn time as the independent variable. Figure 15 plots these results. Figure 16 offers additional support of this assertion where the mean effective thrust level, thrust coefficient, and the differences between the ECAPS baseline and the CDA-test thrust and C_F are plotted against the propellant inlet feed pressure for each of the nominal burn times -- *0.2 s, 0.5s, 1.0 s, 2.0 s, and 5.0 s*. The thrust coefficient is calculated using the method of Eq. (11). Note that there is a distinctive drop off in thrust level as the burn duration shortens.

Finally, Figure 17 reorganizes the data of Figures 16(a) and (b) to plot the total thrust and observed thrust inlet pressure levels from Table 5 -- *{520 kPa, 1040 kpa, 1720, Kpa, and 2410 kPa)*. Figure 17(a) also plots the nominal ECAPS thrust curves for the corresponding inlet pressure levels. The data have been curve fit and extrapolated out to 8 seconds burn time. After 8 seconds only the thrust curves for the higher inlet pressure levels finally begin the approach the nominal ECAPS values. For the lower inlet pressures, the mean thrust levels remain below the ECAPS values. Consequently, one must conclude that the published ECAPS performance data applies only to steady state operating conditions, and the observed drop in thrust performance is mainly attributable to the lowered mean effective thrust levels resulting from the catalyst bed decomposition latency.

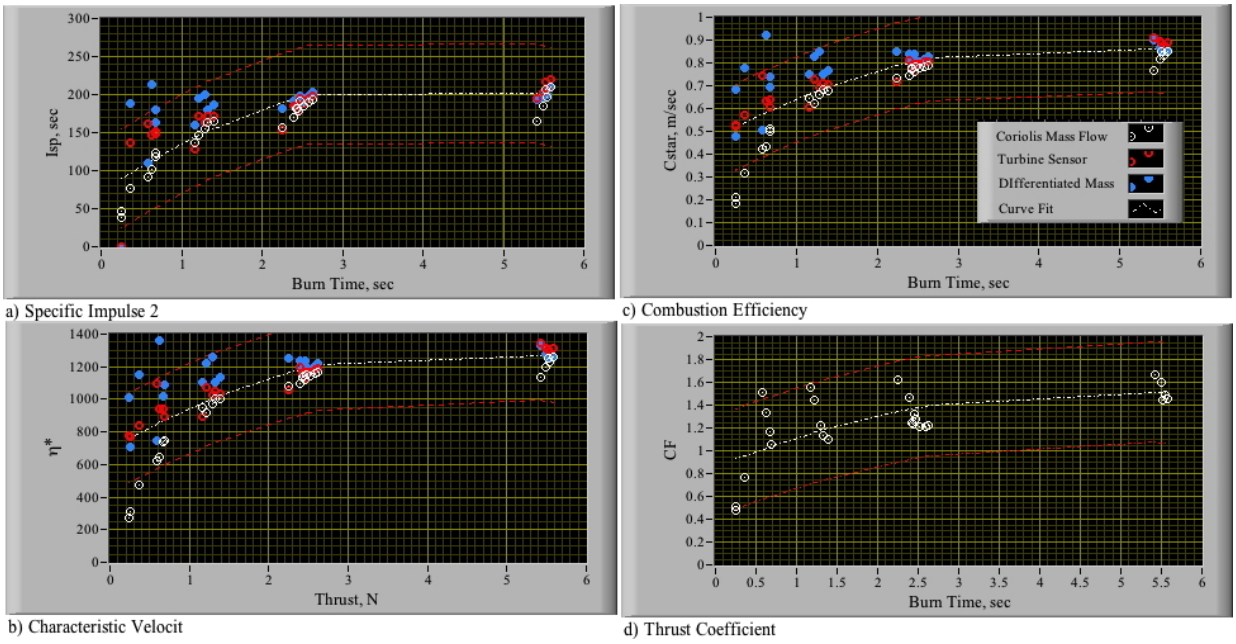

Figure 15. 22-N Single-Pulse Tests Performance Summary.

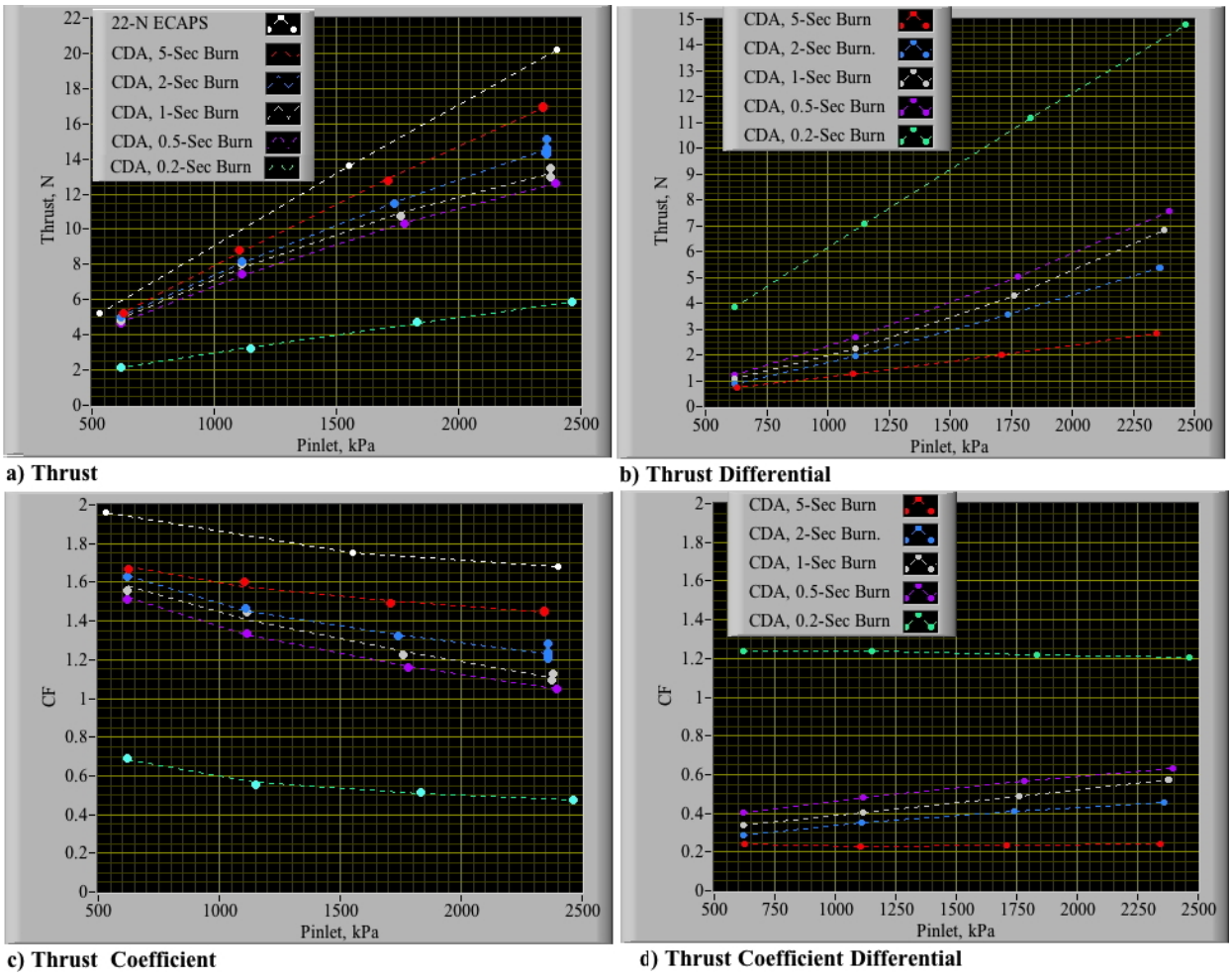

Figure 16. Comparison of Thrust, C_F Levels as a Function of Propellant Feed Pressure and Burn Time.

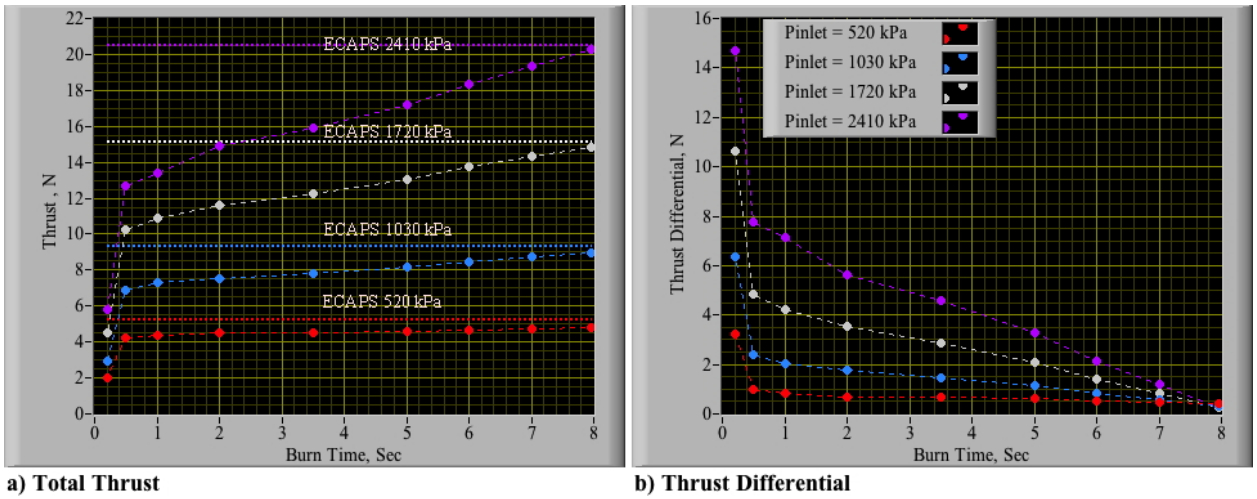

a) Total Thrust **b) Thrust Differential**

Figure 17. Total Thrust and Thrust Differential as a function of Burn Time.

It also appears that even once the effect of the startup latency is neglected, the 22-N thruster tested at MSFC has a lower overall performance level when compared to the ECAPS specs. Figure 17 plots the instantaneous specific impulse profiles calculated for each of 5-second duration burns with peak thrust levels of 5, 10, 15, and 20 Newtons (from Table 5). Here the I_{sp} time-history profile is calculated by dividing the instantaneous mass flow estimate into the thrust profile and scaling by $1/g_0$. Figure 18(a) plots the instantaneous I_{sp} calculated using the *Coriolis meter mass flow*. Figure 18(b) plots the instantaneous I_{sp} calculated using the *flow turbine meter mass flow*. Figure 18(c) plots the instantaneous I_{sp} profile calculated using *differentiated propellant mass*. Finally, Figure 18(d) plots the instantaneous I_{sp} profile calculated using the average of the three mass flow sources.

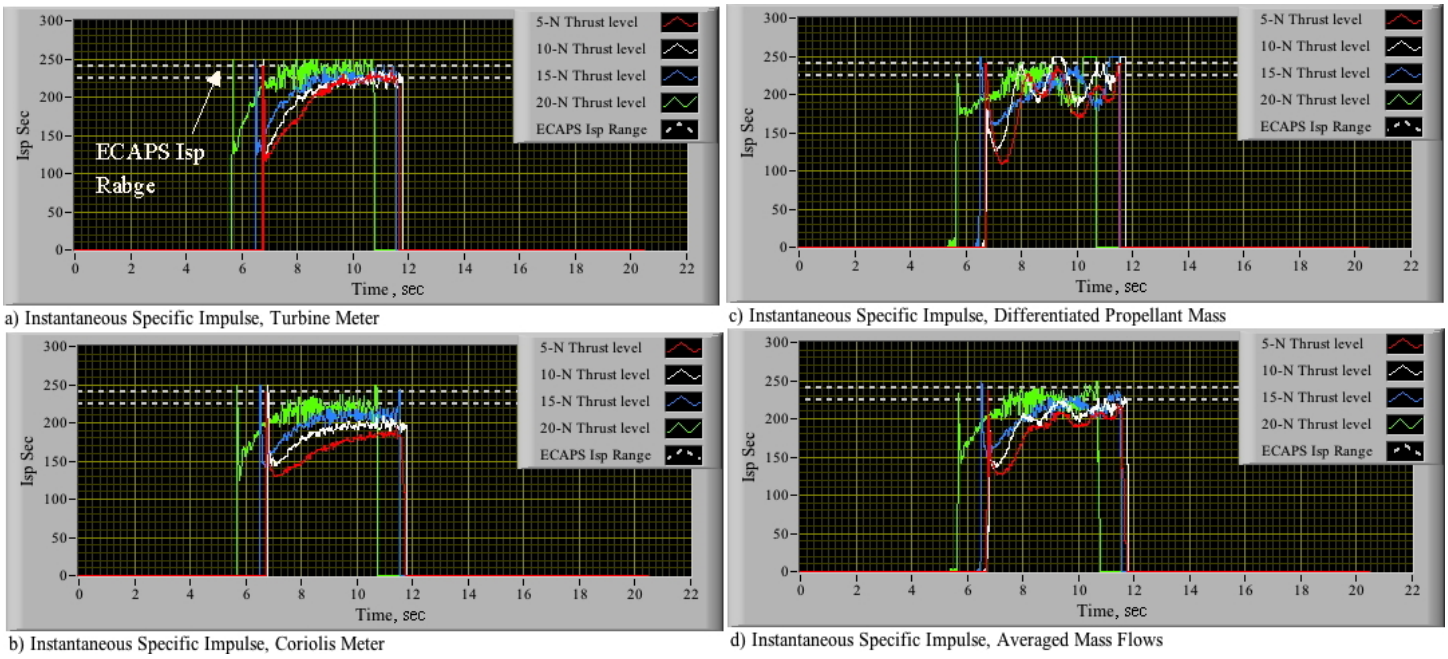

a) Instantaneous Specific Impulse, Turbine Meter

c) Instantaneous Specific Impulse, Differentiated Propellant Mass

b) Instantaneous Specific Impulse, Coriolis Meter

d) Instantaneous Specific Impulse, Averaged Mass Flows

Figure 18. Instantaneous Specific Impulse Profiles for 5-Second Pulse Burns.

When based on the filtered turbine meter mass flow, the calculated peak I_{sp} spans the expected ECAPS range from 224-241 seconds. However, the peak I_{sp} based on the reconstructed Coriolis meter mass flow lies significantly below the expected 224-241 range, and only the peak trust for the 20-N burn approaches the lower boundary. The peak I_{sp} based on the differentiated mass also lies below the expected range, but calculates slightly higher values

than does the Coriolis meter-based calculation. Not surprisingly, the differentiated propellant mass data is significantly more-noisy than are the data derived directly from mass flow, and these results must be interpreted cautiously. Clearly, the achieved maximum thrust level has a significant effect on the thruster efficiency. The readers must draw their own conclusions in the regard; however, averaged data of Figure 18(d) -- which the authors consider to be the "best available" estimate of the instantaneous I_{sp}, predicts peak values that lie than 2.

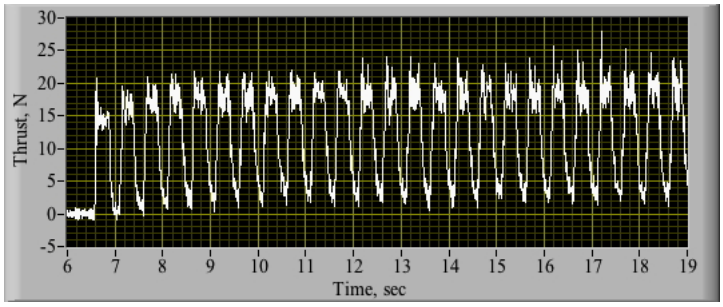

Figure 19. Example Pulsed Thruster Test Time History, Duty Cycle = 60%.

K. High-Frequency Pulsed Test Data Analysis.

Near the conclusion of the 22-N thruster testing campaign a series of pulse burns were performed in order to evaluate the minimum impulse bit I_{min} and pulse magnitude consistency. As shown by Table 5, the pulse-train frequency was either 2 or 5 Hz with duty cycles varying from 4 to 95%. Thus, "on" times varied from 0.04 seconds to 0.19 seconds, with 25 pulses performed for each test.

Due to the limited response fidelity, the mass flow measurements were unusable for this analysis and only the thrust data was available to characterize the high-frequency thruster performance. Even that data presents a challenge for dynamic analysis. In order to accurately capture the peaks at this small duty cycle times for these pulsed tests, the measurement fidelity up through 25 Hz is required. As observed on the frequency response magnitude plot of Figure 11, the linear response region of the load-sensor ends at 10 Hz, and test stand dynamics -- noted by the resonant peak near 20 Hz -- dominate the signal at that point. Thus, the poor dynamic response fidelity of the thrust load-cell and associated test stand interface will compromise performance measurements of the thruster pulse-operation.

To illustrate this point Figure 19 plots a typical unfiltered pulsed-operation thrust response with a 60% duty cycle, and a pulse frequency of 2 Hz. Note that the peak thrust levels of Figure 19 vary significantly over the time history, the intended rectangular wave pattern is quite ragged, and never returns to a zero-level between pulses. In order to overcome this problem the raw data are fit with an rectangular "pulse train" that best matches the frequency domain spectrum of the measured signal, and then the effective pulse amplitude is calculated to match the total impulse of the de-biased and integrated thrust measurement.

Defining T as the pulse train period including the "off time", t_p is the pulse time during the active duty cycle, and A_p is the effective amplitude of the pulses, the analytical harmonics of this pulse train can be calculated directly by using Eq. (12). Figure 20 also shows this best-fit pulse train overlaid on the measured time history and the corresponding frequency response comparisons between the measured data and best-fit model. On the frequency response magnitude plot, both the numerical DFT and the analytical harmonics of the pulse train given by Eq. (12) are plotted. The total impulse of this 25-cycle test was *147.02 N-s*.

$$\|Y_n\| = \frac{\sqrt{2}}{2}\frac{A_P}{\pi \cdot n}\cdot\sqrt{1-\cos\left(2\pi \cdot n \cdot \frac{t_p}{T}\right)},\ \{n = 0,1,2,...N/2+1\}\ . \tag{12}$$

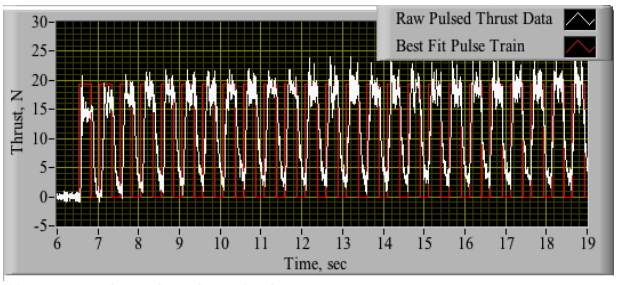

(a) Raw Input Thrust Time History Graph

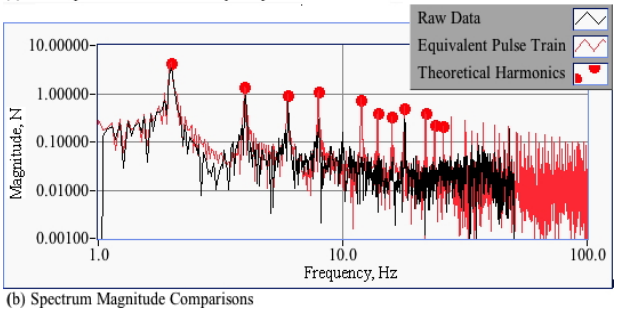

(b) Spectrum Magnitude Comparisons

Figure 20. Example Pulse Train Best-Fit Time Domain and Frequency Response Comparisons, Duty Cycle = 60%.

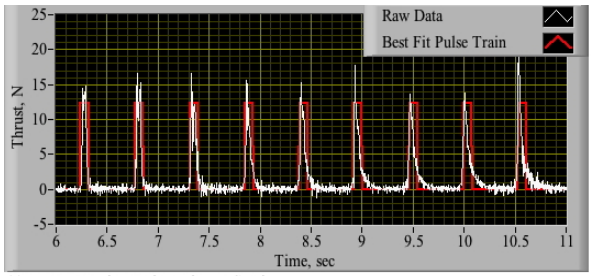

(a) Raw Input Thrust Time History Graph

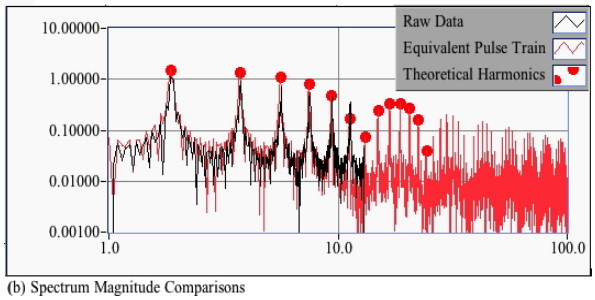

(b) Spectrum Magnitude Comparisons

Figure 21. Example Pulse Train Bet-Fit Time Domain and Frequency Response Comparisons.

Similarly, Figure 21 shows a second example, but with a significantly smaller duty cycle of 15%. The theoretical impulse bit for this test case is *5.88 N-sec*. In Figure 21(a) the peak thrust varies significantly, but the impulse delivered by each pulse is quite consistent. The pulse-train amplitude *11.69 N* is calculated to match the total impulse of the raw data*, 24.981 N-s*. Comparing the DFT of the pulse train and the theoretical harmonics to the raw data, there is excellent agreement up through 10 Hz. The theoretical impulse bit for this second test case is *1.00 N-sec.*

The data presented by Figure 22 summarizes the pulse-firing test results. In this figure several measures of performance are plotted against the active pulse-period for the thruster. The pulse period is calculated by multiplying the active duty cycle by the pulse period. Plotted data include impulse-bit, mean thrust peak amplitude, peak inlet feed pressure and calculated peak chamber pressure, and finally, the estimated peak thrust coefficient. Figure 22(a) plots the effective impulse bit calculated from the best-fit analytical model. Estimated 95% confidence interval bounds -- dashed lines -- are also plotted on this figure. These error bounds are based the residual error from the plotted 2nd order curve fit, scaled by the appropriate student-t σ-interval for N-3 degrees of freedom. (Ref. xxiii) Because the amplitude curve-fit model A_p was selected to match the measured total impulse of the measured pulse-train, and raw data and analytical impulse-bit plots both give the same mean impulse bit levels, only the error boundaries differ with the curve fit pulse train exhibiting lower variability. The minimum impulse bit from this data approaches a value of approximately *1/4th of a N-s.*

Figure 22(b) plots the equivalent rectangular pulse train amplitude and the observed mean maximum thrust amplitude of the raw data. Estimated 95% confidence intervals are also plotted. As expected, there is considerable scatter in the measured average of the maximum-pulse thrust value -- especially for very small burn times. In contrast, the calculated amplitudes A_p from pulse-train model data show little deviation from the best-fit curve. This difference in properties between the two data sets is a result of the thrust stand measurement system having insufficient fidelity to capture the discrete peak thrust events. The difference between the plotted mean curves on Fig. 22(b) gives a qualitative measure as to how much the achieved pulse shape differs from the idealized rectangular shape.

Figure 22(c) plots the mean peak inlet pressure and the corresponding peak chamber pressure. Chamber pressure is estimated using the previously described method using the pulse train amplitude A_p to estimate the effective thrust level of each pulse. The small drop off in the feed pressure as function of the pulse period is likely an effect of isentropic cooling for the higher duty cycle pulse-trains. Plotted error bounds are calculated by multiplying the curve fit residue by the appropriate student-t covariance multiplier. Because this C_F data is calculated from the impulse-bit data of Figure 22(a), there is only small scatter in the data.

Figure 22(d) plots the peak thrust coefficient calculated using the mean impulse-bit values from Figure 21(a) divided by the mean active burn time of each pulse. The peak chamber pressure from 22(c) divides this quantity and the thruster throat area used to calculate the thrust coefficient values. Finally, Figure 22 plots the C_F data of Figure 22(d), but this time the mean peak inlet pressure from Figure 22(c) is the independent variable. For comparison purposes, the quasi-steady data from Figure 16 is also plotted on this figure. ECAPS-derived steady thrust C_F estimates are also included on this plot.

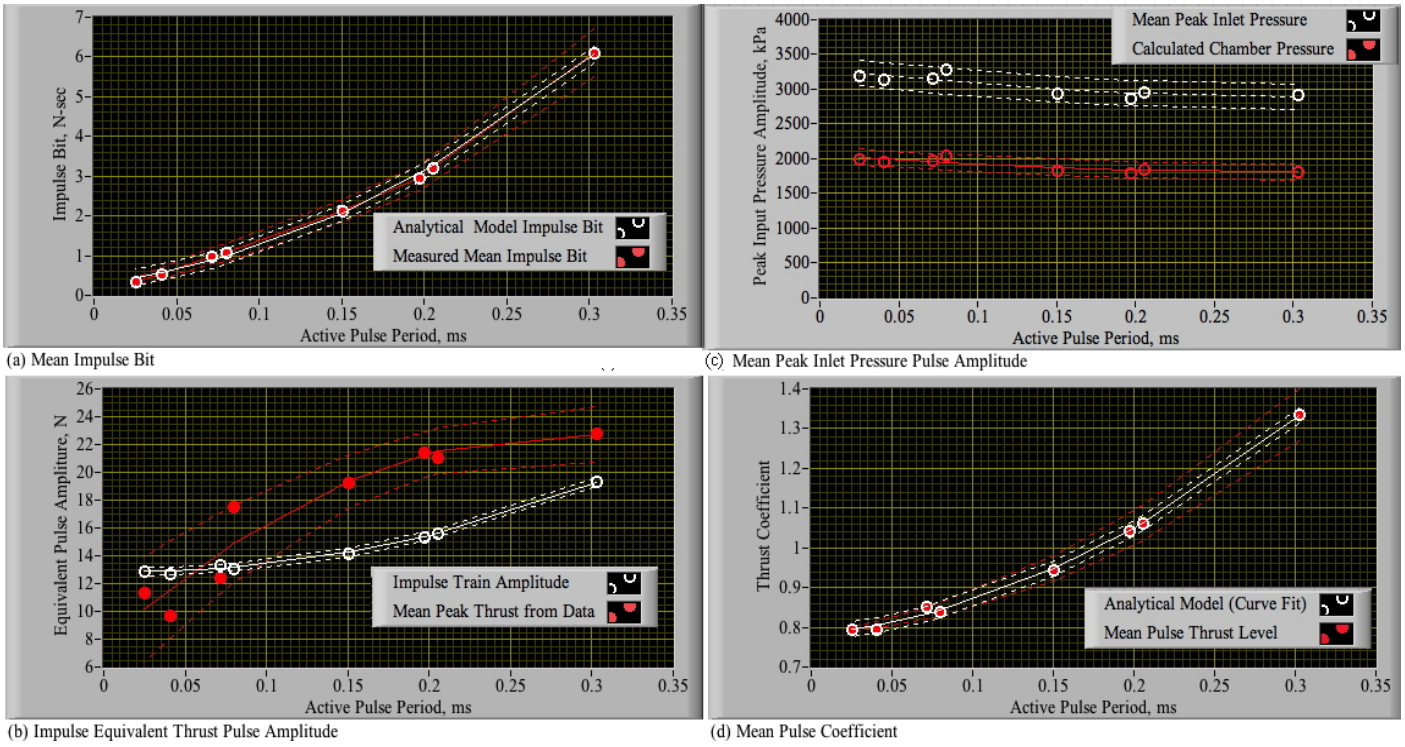

Figure 22. Pulsed Thruster Tests Data Summary.

Finally, Figure 23 plots the C_F data of Figure 22(d), but this time the mean peak inlet pressure from Figure 22(c) is the independent variable. For comparison purposes, the quasi-steady data from Figure 16 is also plotted on this figure. ECAPS-derived steady thrust C_F estimates are also included on this plot. The pulse-operation thrust coefficients are significantly lower than the quasi-steady values; and drop very rapidly as the inlet pressure increases or the burn time decreases. The large C_F drop-off as a function of pulses burn duty cycle shows that there is a significant effect of burn time on the achieved level. This observation further supports the catalyst bed latency hypothesis discussed previously in *Section IV.I.5. For the very rapid burn cycles, the chamber never has a chance to reach anywhere near a steady thrust level.*

Fortunately, the plotted impulse-bit data of Figure 22(a) and C_F data of Figure 22(d) exhibit is only small scatter with respect to burn time. This result indicates that the commanded thruster impulse is *well behaved as a function of the thruster burn time and inlet pressure, and does not vary significantly from burn-to-burn.* This predictability should allow the delivered impulse to be accurately scheduled as a function of burn time and inlet pressure for real-time flight operations. Unfortunately, because of the low fidelity of the available mass flow data in this instrumentation suite; the effects of pulsed operation on the effective specific impulse of the thruster could not be accurately quantified.

V. Conclusion

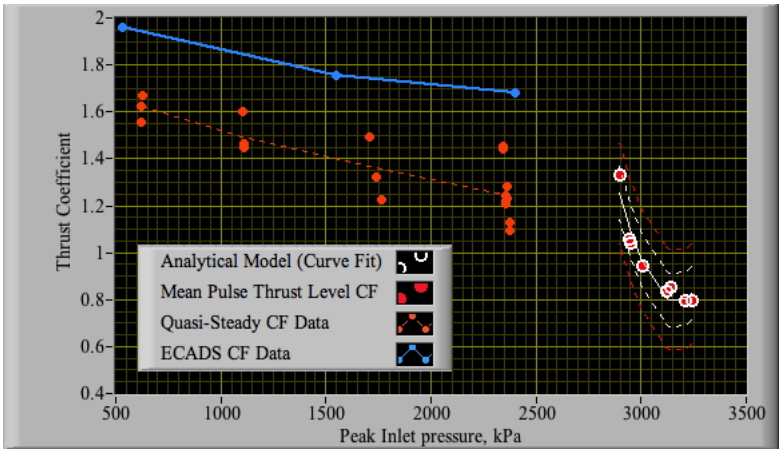

Figure 23. 22-N Thruster Comparison of Quasi-Steady and Pulsed-Operation Thrust Coefficients.

The development of practical "green" propellants to replace hydrazine for in-space propulsion has been a goal of NASA for quite some time, and is an essential element of NASA's In-Space Propulsion Systems Roadmap. This roadmap identifies difficulties associated with hydrazine as a spacecraft propellant and recommends development of "less hazardous, less toxic" alternatives. In order to expand future propulsion options and to gain valuable in-house experience with green-propellant thruster systems, NASA Marshall Flight Center recently performed a series of tests on two green thruster systems based on the high performance green propellant LMP-103S, as developed by the Swedish Space Corporation's Ecological Advanced Propulsion Systems Subsidiary.

For this test campaign NASA MSFC recently procured two HPGP thrusters with nominal 5-N (1.12 lbf) and 22-N (5 lbf) thrust capabilities. These units were laboratory-weight, but possessed overall similarity to the flight-weight hardware being built by ECAPS. In order to reduce setup time required for hot-fire testing of HPGP thrusters. Orbital ATK -- the US distributor of HPGP technologies -- provided the 5-N thruster thrust stand, propellant cart, and controller hardware for use by NASA under a non-reimbursable space act agreement (SAA). NASA purchased the 22-N thruster from ECAPS.

The HPGP thruster systems were tested in the Component Development Area (CDA) altitude test stand in late April 2015. The testing campaign had two primary objectives, 1) CDA perform facility check-outs using the 5-N thruster, and 2) perform comprehensive testing of the 22-N thruster. At the time of the testing campaign the CDA altitude simulation facility had not had a thorough check-out of the recently-installed mechanical and electrical systems, and the 5-N thruster -- previously tested and well characterized by ECAPS and Orbital-ATK -- was used to perform the facility "calibration." Following the initial system evaluations performed using the 5-N thruster, the 22-N testing was perform with minimal modifications to the test setup. The second objective was quite important to NASA as it marked the first time that a 22-N or larger HPGP thruster had been tested outside of the ECAPS facility.

This report presents comprehensive results of the 22-N thruster testing campaign. The first series of tests consisted of single discrete pulses with multiple pulses were performed for some test conditions. The thruster was allowed to cool down naturally without any mechanical or forced gas cooling between pulses. The single-pulse firings allow the quasi-steady performance of the system to be characterized. The multiple pulse firings cycled the system rapidly with different pulse duty cycles. This series of tests was intended to examine the response fidelity of the system and to allow parameters such as the minimum impulse bit and thrust and impulse-bit consistency.

Unfortunately, the instrumentation suite used for this series of tests exhibited several issues that did not allow direct interpretation of the thruster performance from the raw data. First, the measured thrust data and sensed propellant mass were contaminated by noise sources whose magnitude was significant when compared to the mean signal level. Second, both the thrust load cell and the Coriolis flow meters exhibited significant response latency. This latency was especially pronounced with the high-mass-flow Coriolis meter. Third, the turbine flow meter exhibited large random spikes that were likely a result of a bad signal ground or common-mode noise interference. These spikes occurred throughout the test runs but were especially prevalent right after a thrust-pulse event as the mass flow dropped back towards zero. Finally, because there was no chamber pressure measurement, one could not directly calculate the characteristic velocity c^*, thrust coefficient C_F, and combustion efficiency η^* of the system; instead the chamber pressure must be derived indirectly from the measured parameters.

A variety of Fourier-based signal-processing methods were used to removed unwanted signal corruptions while retaining the desired deterministic signal from key measurement parameters including thrust, propellant mass, mass flow, inlet feed pressure. Chamber pressure was calculated from filtered, and de-biased thrust measurements together with the 1-Dimensional De Laval flow equations. Detailed explanations of the applied signal-processing methods are presented.

Results from the Quasi-steady single pulse data are presented first. Several key conclusions can be drawn with regard to this data set. First, there is observed a significant drop in the data noise as the mean thrust level rises above 14 N. Above this range, there is sufficient mass flow that the CDA test facility does a good job of accurately capturing the data. Below this thrust level mass flow levels are so low as to introduce considerable measurement variability. Also the effective specific impulse and thrust coefficient levels are lower -than the expected pre-test performance levels. Test results indicate there exists an especially significant drop in the system performance as the burn time decreases. This drop is mainly attributable to the lowered mean effective thrust levels resulting from the catalyst bed decomposition latency at startup. *Only when operating in a long duration mode -- greater than 8 seconds -- does the 22-N thruster appear to march the ECAPS performance claim.*

Ignoring the thrust build up time on the measured time history traces, when based on the filtered turbine meter mass flow, the calculated peak I_{sp} spans the expected ECAPS range from 224-241 seconds. However, the peak I_{sp} based on the reconstructed Coriolis meter mass flow lies significantly below the expected 224-241 range, and only the peak trust for the 20-N burn approaches the lower boundary. The peak I_{sp} based on the differentiated mass also lies below the expected range, but calculates slightly higher values than does the Coriolis meter-based calculation. The averaged data of Figure 19(d) -- which the authors consider to be the "best available" estimate of the instantaneous I_{sp}, predicts peak values that lie near the lower boundary of the expected range -- approximately 220 seconds. The readers must draw their own conclusions in the regard, but it also appears that the 22-N thruster tested at MSFC has a lower overall performance level when compared to the ECAPS specs -- even when the decomposition latency is neglected.

Finally, the dynamic responses of the sensors operating in pulse mode were evaluated. Due to the limited response fidelity, the mass flow measurements were unusable for this analysis and only the thrust data was available to characterize the high-frequency thruster performance. Even the thrust data presents a challenge for dynamic analysis. In order to accurately capture the peaks at small duty cycle times, the raw data are fit with an rectangular "pulse train" that best matches the frequency domain spectrum of the measured signal, and then the effective pulse amplitude is calculated to match the total impulse of the de-biased and integrated thrust measurement. Unfortunately, because of the low fidelity of the available mass flow data in this instrumentation suite; the effects of pulsed operation on the effective specific impulse of the thruster could not be accurately quantified.

The calculated pulse-operation thrust coefficients are significantly lower than the quasi-steady values; and drop very rapidly as the burn time decreases or the inlet pressure increases. The large C_F drop-off as a function of the burn duty cycle shows that there is a significant effect of burn time on the achieved level. This observation further supports the previously described catalyst bed latency hypothesis. Fortunately, the impulse-bit data exhibit is only small scatter with respect to burn time. This result indicates that the commanded thruster impulse is *well behaved as a function of the thruster burn time and inlet pressure, and does not vary significantly from burn-to-burn.* This predictability should allow the delivered impulse to be accurately scheduled as a function of burn time and inlet pressure for real-time flight operations.

VI. Acknowledgments

This work was performed under funding received from the NASA Marshall Space Flight Center (MSFC) through the Alabama Space grant Consortium Summer Faculty Fellowship Program. The authors of this paper wish to acknowledge Dr. Norman F. Six Director of the MSFC Office of Education, and Mr. Todd May MSFC Space Launch Systems (SLS) Booster Development Program Manager. This program would not have been possible without from Mr. May's SLS program funding and Dr. Six is to be commended for his extraordinary efforts at pulling this program back together after nearly a 10- year hiatus. A heart felt thanks to Dr. Six for sticking with me and extending my tour of duty at MSFC to accomplish my project goals during my long (and still ongoing) convalescence after my nearly-fatal climbing accident on Mt. Ararat.

References

[i] Anon., "Total Propulsion Solutions," AeroJet, Redmond Operations, 2006-H-3391, June 2007.

[ii] Choudhary G, IIansen H, Donkin S, Kirman C. 1997. Toxicological Profile for Hydrazines. US Department of Health and Human Services Public Health Service Agency for Toxic Substances and Disease Registry (ATSDR). Atlanta, GA: 1-224.

[iii] DeSain, John D., "Green Propulsion: Trends and perspectives," Crosslink, http://www.aero.org/publications/crosslink/summer2011/04 html, [Retrieved 21 March, 2012].

[iv] Anon., **"**Hazard Analysis of Commercial Space Transportation; Vol. 1: Operations, Vol. 2: Hazards, Vol. 3: Risk Analysis,**"** U.S. Dept. of Transportation, PB93-199040, Accession No. 00620693, May 1988.

[v] Bombelli, V., "Economic Benefits for the Use of Non-toxic Monopropellants for Spacecraft Applications, AIAA-2003-4783, 39th AIAA/ASME/SAE/ASEE Joint Propulsion Conference and Exhibit, Huntsville, AL, July 2003

[vi] Venkatachalam, S., Santhosh, G., Ninan, K. N. , "An Overview on the Synthetic Routes and Properties of Ammonium Dinitramide (ADN) and other Dinitramide Salts". J. *Propellants, Explosives, Pyrotechnics*, Vol. 29, No. 3, March, 2004, pp.178–187.

[vii] Nagamachi, M. Y., Oliveira, J. I., Kawamoto, A. M., and Dutra, R., C., "ADN – The new oxidizer around the corner for an environmentally friendly smokeless propellant," J. of Aerospace Technology Management, Vol. 1, No. 2., December 2009, pp. 153-160.

[viii] Anon., "SRI International," URL: http://www.sri.com/about, [Retrieved 27 September 2012].

[ix] Bottaro, J.C., Penwell, P.E., Schmitt, R.J., 1997, "1,1,3,3- Tetraoxo - 1,2,3-Triazapropene Anion, a New Oxy Anion of Nitrogen: The Dinitramide Anion and Its Salts", J. Am. Chem. Soc., Vol. 119, pp. 9405-9410.

[x] Gordon, S., and McBride, B. J., "Computer Program for Calculation of Complex Chemical Equilibrium Compositions and

Applications," NASA RP-1311, 1994.

[xi] Neff, K., King, P., Anflo, K., and Mollerberg, "High Performance Green Propellant for Satellite Applications," AIAA-2009-4878, 45th AIAA/ASME/SAE/ASEE Joint Propulsion Conference & Exhibit AIAA 2009-4878 2 - 5 August 2009, Denver, Colorado, 2008.

[xii] Delanoe, R., "Injector Design and Test for a High Power Electrodeless Plasma Thruster, MS Thesis, KTH Royal Institute, School Electrical Engineering, Stockholm, Sweden 2011 XR-EE-SPP 2011:009, pp. 7-8, 42-43.

[xiii] Persson, M., Anflo, K., and Dinardi, A., "A Family of Thrusters For ADN-Based Monopropellant LMP-103S," AIAA-2012-3815, 48th AIAA/ASME/SAE/ASEE Joint Propulsion Conference & Exhibit 30 July - 01 August 2012, Atlanta, Georgia, 2012.

[xiv] Goldstein, Edward, "The Greening of Satellite Propulsion," Aerospace America, February, 2012, pp. 26-28.

[xv] Pokrupa, N., Anglo, K., and Svensson, O., "Spacecraft System Level Design with Regards to Incorporation of a New Green Propulsion System," AIAA-2011- 6129, 46th AIAA/ASME/SAE/ASEE Joint Propulsion Conference and Exhibit, San Diego, CA, July 31-Aug 3, 2011.

[xvi] Anflo, K., and Crowe, B., "In-Space Demonstration of an ADN-based Propulsion System," AIAA-2011-5832, 47th AIAA/ASME/SAE/ASEE Joint Propulsion Conference & Exhibit 31 July - 03 August 2011, San Diego, California, 2011.

[xvii] Anon., "*Office of the Chief technologist, Space Technlogy Roadmaps: The Future Brought to You by NASA*," http://www.nasa.gov/offices/oct/home/roadmaps/index.html, [Retrieved 29 November, 2012].

[xviii] Anon., "NASA Goes Green: NASA Selects Green Propellant Technology Demonstration Mission," http://www.nasa.gov/home/hqnews/2012/aug/HQ_12-281_Green_Propellants html, [Retrieved 12 December 2012].

[xix] Hawkins, T. W., Brand, A. J., McKay, M. B., Tinnirello, M., " Reduced Toxicity, High Performance Monopropellant at the U.S. Air Force Research Laboratory," AFRL-RZ-ED-TP-2010-219, Edwards AFB CA, April 2010.

[xx] Spores, R. A., Masse, R., and Kimbrel, S., "GPIM AF-M315E Propulsion System," AIAA_2013-3849, *49th AIAA/ASME/SAE/ASEE Joint Propulsion Conference & Exhibit*, San Jose CA, 15-17 July 2013.

[xxi] Freiberger, W. F., ed., *International Dictionary of Applied Mathematics*, Van Nostrand Company, Inc., Princeton, NJ, 1960, pp 177-178.

[xxii] Walker, James, S., *Fast Fourier Transforms*, CRC Press, Boca Raton, FL, 1991, pp. 34-47.

[xxiii] Beckwith, T. G., Marangoni, R. D., and Lienhard V, J. H., *Mechanical Measurements, 6th Ed*., Prentice Hall, 2006, pp.85-145.

[xxiv] Whitmore, Stephen A., and Wilson, Matthew D., "Wiener Deconvolution for Reconstruction of Pneumatically-Attenuated Pressure Signals," *AIAA Journal, Vol. 49, No. 5,* May 2011, pp. 890-897. DOI: 10.2514/1.J050102

[xxv] Reizner, J. R., "Coriolis Mass Flow meters in Batching Applications - The Good, the Bas, and the Ugly," *Proceedings of the World Batch Forum,* North American Conference, Chicago Il, May 16-19, 2004.

[xxvi] Henry, M.P., Clark, C., Duta, M., Cheesewright, R., Tombs, M., Response of a Coriolis mass flow meter to step changes in flow rate, *Flow Measurement and Instrumentation* 14 (2003) 109-118.

[xxvii] Henry, M., Clark, C., and Cheesewright, B., "Pushing Coriolis Mass Flow Meters to the Limit," *IEE Computing and Control Engineering, Vol. 14, No. 3,* June/July 2003, pp. 24028.

[xxviii] Anon., New Coriolis Meter Finds Hundreds of Kilograms of "Disappearing' Batch Product, *Control Engineering Europe, February 1, 2006.* http://www.ceasiamag.com/2006/02/new-coriolis-meter-finds-hundreds-of-kilograms-of-disappearing-batch-product/, [Retrieved 20 August 2015].

[xxix] Giovanni Bianchi and Roberto Sorrentino (2007), *Electronic Filter Simulation & Desig,.* McGraw-Hill Professional. pp. 17–20. ISBN 978-0-07-149467-0.

[xxx] Otnes, R., K., and Enochson, L., *Applied Time Series Analysis*, John Wiley and Sons, New York, 1978, pp. 219-260.

[xxxi] Anderson, J. D. Jr., *Modern Compressible Flow with Historical Perspective*, 3rd. ed., McGraw-Hill Higher Education, NewYork, 2003, Chapt. 4.

Small Launch Vehicles and CubeSat Control Testing

Chih-Hao Wu[1] and Jonathan E. Jones[2]
NASA Marshall Space Flight Center, Huntsville, AL, 35812

The low-cost transportation solutions to Low Earth Orbit (LEO) of the small launch vehicles are the prime focus for the NanoLaunch technology development project. In this report, the testing of the reaction control system (RCS) has been carefully designed and conducted. In particular, the angular deceleration which occurs in a spherical air bearing has been characterized. This includes the friction study of the spherical air bearing during the de-spinning process and its associated spin stabilization analysis.

Nomenclature

T = average torque in in-lbs (over several revolutions).
ω = angular velocity of the rotating system.
l_0 = constant retarding torque.
l_p = viscous damping constant.
a = turbulent damping constant.
I_0 = initial torque value.
C = integration constant.

I. Introduction

Small Launch Vehicle technology development and its associated concepts have been a focus at the National Aeronautics and Space administration (NASA) and Marshall Space Flight Center (MSFC) since 2009. The project seeks to enable US industry in the development of inexpensive and dedicated access to space. A primary objective is to reduce the overall operation cost for the technology involved. The crucial design challenge for the aerospace and mechanical engineers are to launch a small payload into Low Earth Orbit (LEO) while keeping the cost down and maintaining the system performance and reliability. NASA has invested many new cutting edge technologies such as Additive Manufacturing (AM) and Printed Electronics (i.e. Aerosol Jet Printers for Electronics) to facilitate the NanoLaunch design concepts. Theses additive manufactured parts include motor cases, solid rocket propellant, and latest super charged micron-scale capacitor utilized in the rocket motor igniters circuits. Reducing cost coupled with a fast design-to-flight cycle, and working with Accreditation Board for Engineering and Technology, Inc. (ABET) certified colleges, such as Harding University, are among the main goals of the NanoLaunch project at NASA and MSFC.

Presently, Marshall Space Flight Center (MSFC) efforts to repeat the same project success of first NASA "Solid Controlled Orbital Utility Test Systems" (SCOUT) program are summarized into two major areas by Jones [15]. First, engineers attempt to maintain affordability of the overall parts required for NanoLaunch rockets. The NanoLaunch concept is to drive overall cost down while keeping the high performance of the rocket. Second, mature launch propulsion technologies such that Nano-Propulsion is the preferred method for delivering small payloads to orbit. In short, performance and reliability will not be sacrificed while newly invented technologies, approaches, operational paradigms, and manufacturing techniques are developed to reduce the price point for orbital access.

[1] Summer Faculty Fellow, Solid Propulsion Systems, Propulsion Systems (ER50), NASA MSFC, Harding University.
[2] AST, Solid Propulsion Systems, Propulsion Systems (ER50), Huntsville, AL, 35812, NASA MSFC.

II. Initial Concept Formation

The friction characteristics of the spherical air bearing studies of Reaction Control System (RCS) begins with the conceptual drawing in Figure 1.

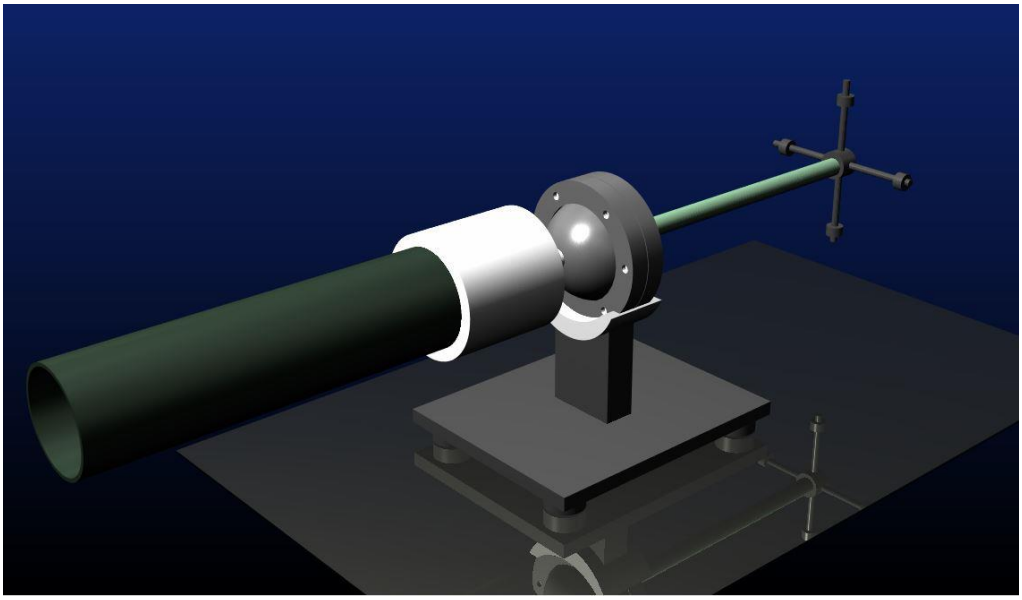

Figure 1: The initial Computer Drawing of RCS with spherical air bearing of NanoLaunch Concept.

One of the major technical challenges for the NanoLaunch project is the spin stabilization studies. A major task involved spinning a rocket while minimizing the precession and wobble before the design of experiments start. The dynamic balancing in this project required placing weights on the end of two ½"all threaded rods (spider ring) that are set perpendicular to each other. The rocket spins along its central axis, which is defined as z axis or yaw. The balancing act was accomplished through a trial and error approach. The internal imperfections of the rocket material compositions causes a dynamic imbalance of the RCS which induces a precession/wobble that requires correction. Figure 2 demonstrates the concept for the mechanism used to dynamically balance the RCS using weights.

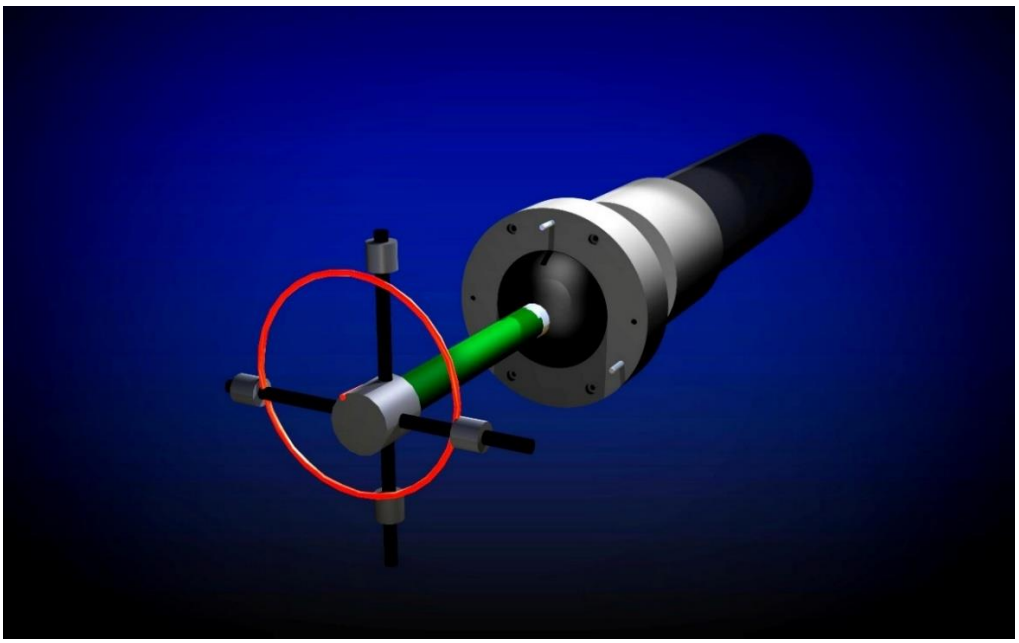

Figure 2: The computer drawing demonstrating the concept for the mechanism of how to statically and dynamically balancing a RCS.

III. Physical Construction of the Computer Drawing

Based on the initial computer drawing, the RCS for a NanoLaunch project was constructed physically in the Flat Floor of the robotics laboratory and is shown in Figure 3.

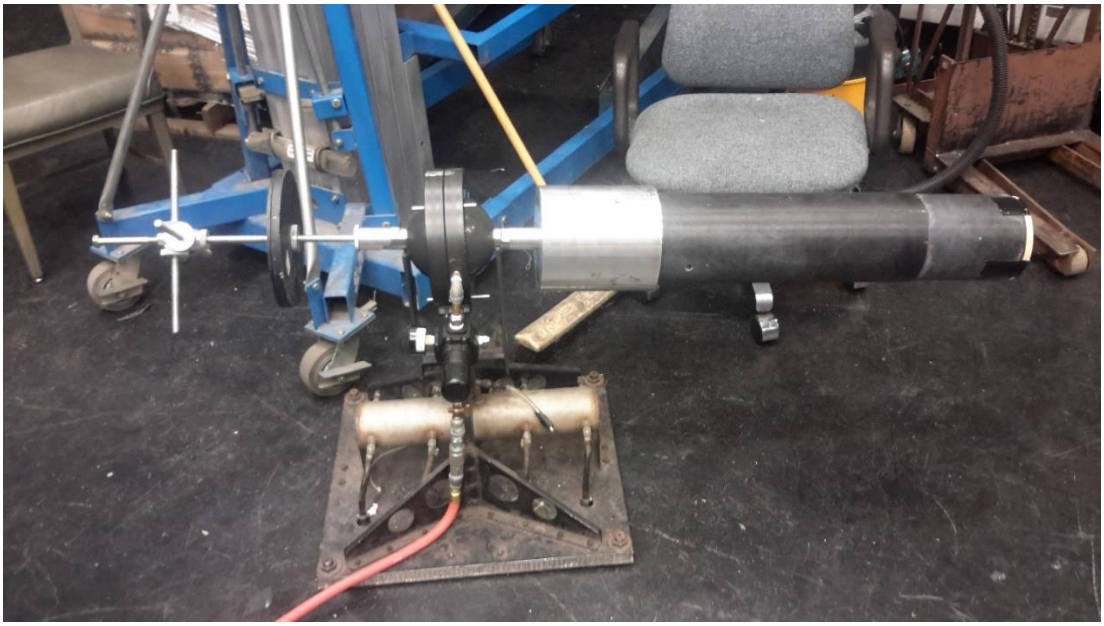

Figure 3: The Physical RCS with spherical air bearing system in Flat Floor Robotics Laboratory.

IV. Design Experiments and Final Assembly of the Test Stand

Two experiments were carefully designed to characterize the dynamic behavior of the spherical air bearing. Several devices were required to account for its angular velocity deviation versus time. A Uni-Trend Model 372 tachometer (Figure 4), a pair of Phantom v411 cameras (Figure 5) and Dewalt Cordless Drill (Figure 6) were utilized.

Figure 4: Uni-Trend Model 372 Tachometer to track angular deceleration versus time.

Figure 5: Phantom v411 widescreen digital high speed camera to track angular deceleration versus time.

The Uni-trend tachometer measured revolutions per minute (RPM) while the Phantom v411 digital high speed camera allowed the team to keep the target in frame for the truth data (the x, y, and z coordination versus time). The wide screen sensor allowed the team to get the true 1280*720 high definition (HD) images from 1 Mega Pixel (1 Mpx) cameras. Finally, Dewalt Model # DCD 760B 18 Volt Cordless ½ inch (13 mm) Compact Drill/Driver (Figure 4) provided the initial torque to spin the motor to 4 Hz for the experiment.

Figure 6: Dewalt DCD 18 Volt Cordless ½ inch Compact Drill/Driver to provided initial torque to spin motor to 4 Hz.

The final experiment setup with the high speed camera is illustrated in the Figure 7.

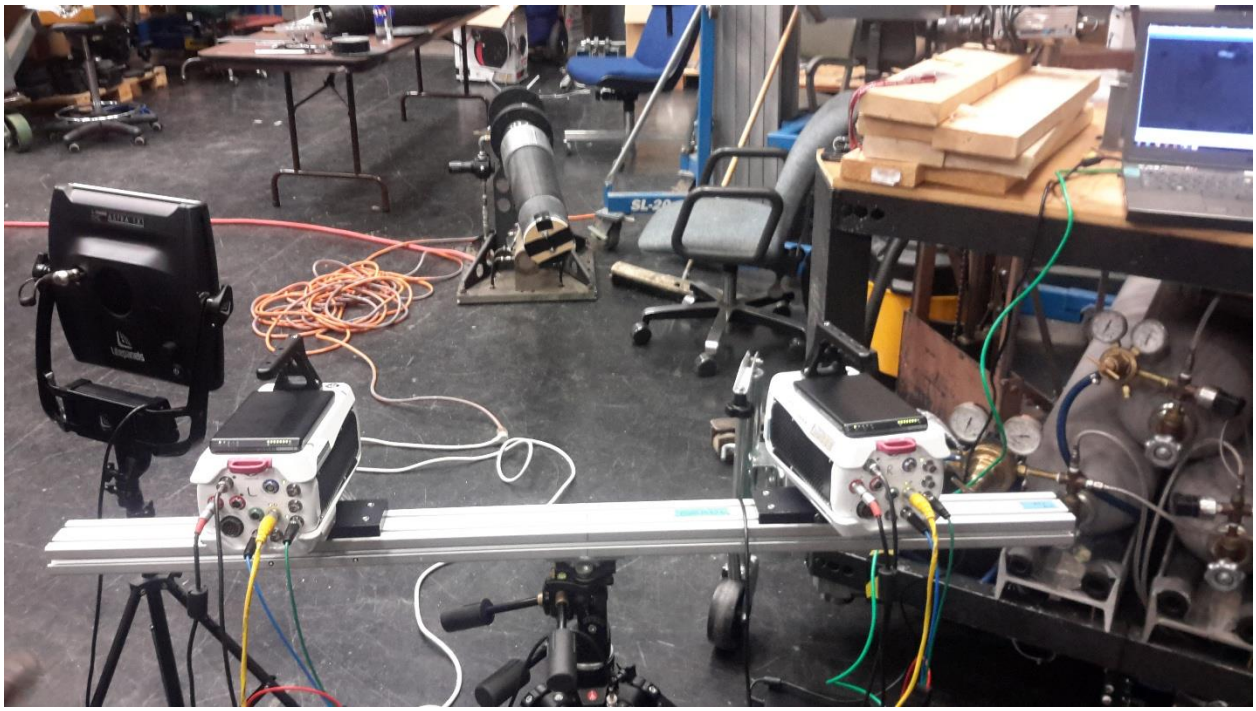

Figure 7: The final assembly for the RCS of the 6 inch air frame with two Phantom cameras and spherical air baring.

The experiments were designed to spin up the motor to 4 Hz using the Dewalt DCD 18 volt cordless drill. The angular deceleration was tracked with the tachometer. The first test collected data until the rocket motor came to a complete stop. The motor spun for about 14 minutes. The second run, only recorded data for the first 2 ½ minutes of the motor spin down. The tachometer and cameras were both used to collect the data. The next phase the project compared the data collected with the analytical model. The model characterized the relationship of the angular velocity versus time of the NanoLaunch rocket. The next objective was to provide a mathematical model of the system showing the relationship between the motor deceleration with the air drag. The experimental data were curve fit using a linear least square regression technique.

V. Mathematical Model

Theoretically, based on Boyton [14], the average retarding torque over a number of revolutions is quantified in Eq. (1). Empirical tests have shown that the retarding torque is approximated by:

$$T = a\omega^2 + l_p\omega + l_0 \tag{1}$$

where:

T = average torque in in-lbs (over several revolutions).

ω = angular velocity of the rotating system.

l_0 = constant retarding torque.

l_p = viscous damping constant.

a = turbulent damping constant.

The l_o term represents a constant retarding torque which is often referred to as a coulomb friction. The l_p term is a viscous damping term coefficient which quantifies the portion of the retarding torque which is proportional to angular velocity. Viscous drag is associated with this term which and is assumed to be proportional to the viscosity of the medium in which the item is spinning. The medium is usually air. The aw^2 term quantifies the retarding torque and is proportional to the square of angular velocity. It is usually associated with turbulent losses as air is pushed aside by protrusions on the spinning test item.

If we express Torque (T) in equation (1) as

$$T = I_0\frac{d\omega}{dt} = a\omega^2 + l_p\omega + l_0 \tag{2}$$

where I_0 represent the initial torque value. Rearranging Eq. (2) and integrate both side of the equations, we have

$$\int \frac{I_0 d\omega}{a\omega^2 + l_p\omega + l_0} = \int dt \tag{3}$$

with careful integration, we have arrived at the final form of ω with respect to t

$$\frac{2I_0}{\sqrt{4al_0 - l_p^2}}\tan^{-1}\frac{2a\omega + l_p}{\sqrt{4al_0 - l_p^2}} = t + C \tag{4}$$

where C in the above Eq. (4) represents the integration constant. Eq. (4) can be equally expressed as Eq. (5) and be observed in Figure 8 to see its pattern.

$$\omega = \frac{\sqrt{4al_0 - l_p^2}\tan[\frac{\sqrt{4l_0 - l_p^2}}{2I_0}(t - C)]}{2a} \tag{5}$$

VI. Experimental Results

A. Angular velocity versus time measurements using only the Uni-Trend Tachometer

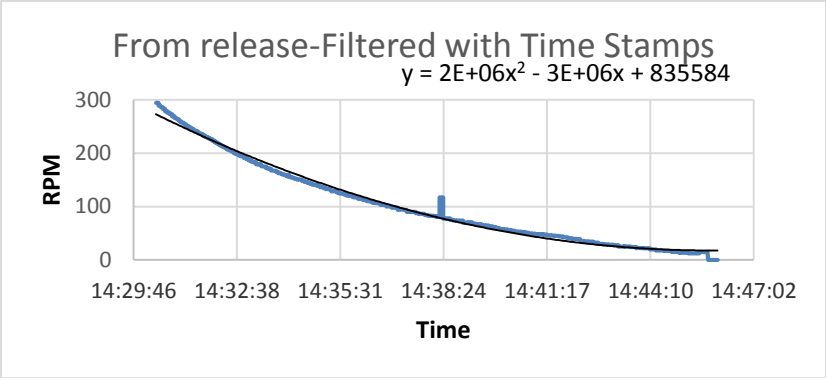

Figure 8: The filtered result of angular velocity versus time using only the Tachometer

Several observations are made from Figure 8. The solid blue line represents actual experiment data recorded through the tachometer. The de-spinning process started at 4 Hz and gradually decelerated in time. This entire cycle lasted about 14 minutes. The black line represented the polynomial curve fit using the least square method. The tachometer data was filtered to obtain the truth data set, since, it was a hand held device collecting experimental data.

B. Angular Velocity versus time measurements using both tachometer and high speed camera

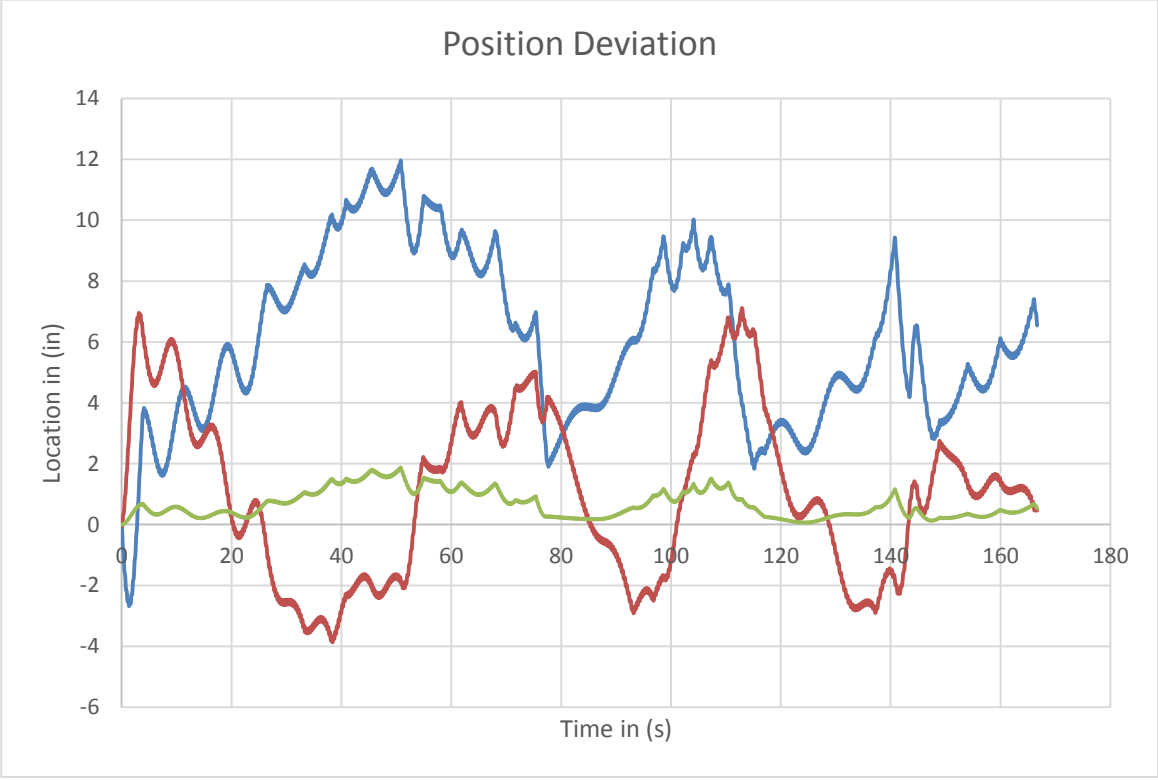

Figure 9: The position deviation plot of location versus time using high speed camera

Several observations were made from Figure 9. The solid blue line represents roll position versus time for the actual experimental truth data recorded through high speed camera. The solid red line represents pitch position versus time for the actual experimental truth data recorded through high speed camera. The solid green line represents yaw position versus time for the actual experimental truth data recorded through high speed camera. The spin down process started at 4 Hz with decreasing angular velocity gradually through the process. This entire process last 165 seconds. As can be seen in the data, the RSC control worked well in minimizing the variation in the yaw plane, but did little to reduce the roll and pitch components. Additional adaptive controls will be needed to offset the vibration/oscillatory activity in these planes, and is recommended for future work considerations.

VII. Conclusion

The friction study of the spherical air bearing is presented with detailed analysis, this includes conceptual drawings, physical experimental apparatus setup, mathematical model development, and model simulation through MATHCAD and MATLAB program. Truth data was collected for the experiment and final analysis of results were documented. The experimental setup must be improved to fix the center of the air bearing facilitating clean coordinate transfer into the frame of reference of the rocket. A least squares curve fitting approach will then be used to refine estimates of viscous damping, moments of inertia, and retarding forces on the air bearing. The air bearing can then be used to test inertial measurement units and eventually closed loop control systems.

Acknowledgments

I appreciate the opportunity to work with my mentor Dr. Jonathan Jones and thank him for his excellent guidance, motivation and support. Thanks to NASA student trainee Adam Dziubanek for his incredible help with information and logistics. Thanks to the voluntary interns Houng-Anne T. Vo and Matthew Duchock for the help they provided. And, thanks to Bobby Collins for the computer graphics.

References

[1]Hughes, P. C., *Spacecraft Attitude Dynamics*, John Wiley & Sons, New York, 1986.

[2]Humble, R., Henry, G., and Larson, W., *Space Propulsion Analysis and Design*, Space Technology Series, McGraw Hill, New York, 1995.

[3]"Fundamentals of Hybrid Rocket Combustion and Propulsion" edit by M. J. Chiaverini and K. Kuo, Volume 218, Progress in Astronautics and Aeronautics, AIAA, 2007, Reston Virginia.

[4]Chin, G., *Agile Project Management: How to Succeed in the Face of Changing Project Requirements*, AMACON, American Management Association, New York, 2004.

[5]Richardson, H. H., "A Dynamic Analysis of Externally Pressurized Air Bearings," Bachelor and Master of Science Thesis, Department of Mechanical Engineering, Massachusetts Institute of Technology, Cambridge, MA, 1955.

[6]Hamrock, B. J., Schmid, S. R., and Jacobson, B. O., *Fundamentals of Fluid Film Lubrication*, 2nd edition, Marcel Dekker, New York, 1994.

[7]Wilcock, D. F., and Booser, E. R., *Bearing Design and Application*, 1st edition, McGraw Hill, New York, 1957.

[8]Goodwin, M. J., *Dynamics of Rotor-Bearing Systems*, Unwin Hyman, London, UK, 1989.

[9]Trumpler, P. R., *Design of Film Bearings*, The MacMillan Company, New York, 1966.

[10]Hori, Y., *Hydrodynamic Lubrication*, Yokendo Ltd. Tokyo, 2006.

[11]Czolczynski, K., *Rotordynamics of Gas-Lubricated Journal Bearing Systems*, Springer-Verlag, New York, 1999.

[12]Gross, W. A., *Gas Film Lubrication*, John Wiley and Sons, Inc., New York, 1962

[13]Hamrock, B. J., *Fundamentals of Fluid Film Lubrication*, McGraw-Hill, Inc., New York, 1994.

[14]Boyton, R., Wiener, K., Hunter, N. F., and Harlow, R., Measuring Small Losses in Rotating Assemblies, *54th Annual Conference of the Society of Allied Weight Engineers, Inc.*, San Diego, CA, 1993.

[15]Jones, J. E., Kibbey, T. P., Cobb, C. B., and Harris L., Enabling Affordable, Dedicated access to Space Through Aggressive Technology Maturation, *Space Propulsion 2014*, Cologne, Germany, 2014.

[16]Zapata, E., McClesky, C., Martin, R., Lepsch, R., and Hemani T., Life Cycle Analysis of Dedicated Nano-Launch Technology, *Commercial and Government Responsive access to Space Technology Exchange (CRASTE)*, Huntsville, AL, 2014.

Mechanics Model of Plug Welding

Q. K. Zuo [1]
University of Alabama in Huntsville, Huntsville, AL, 35899

A. C. Nunes, Jr.[2]
NASA Marshall Space Flight Center, MSFC, AL, 35812

A continuum mechanics model has been developed for friction plug welding process. The model accounts for coupling of plastic deformation (material flow) and thermal heating. The model predictions of the torque, energy, and pull force on the plug were compared to the data of a recent experiment, and the agreements between predictions and data are encouraging.

Nomenclature

ω	=	plug rotation rate
R	=	radius of hole in workpiece
δ	=	thickness of workpiece layer stuck on plug
$\emptyset$	=	taper angle of plug
V_P	=	plug pull velocity
w	=	travel (penetration) distance
q	=	heat flux due to plastic heating
T	=	temperature
K	=	thermal conductivity
$L(t)$	=	radius of heat diffusion
τ	=	shear strength
P	=	pressure

I. Introduction

Plug welding is a process used to close holes left in welds by the Self-Reacting Friction Stir Welding (SR-FSW) process. In the standard Friction Stir Welding (FSW) process a rotating threaded pin is inserted into a weld seam and translated down the seam to stir the sides of the seam together. A shoulder attached to the tool above the pin prevents the weld metal from emerging out of the pressurized zone around the pin, which, if allowed, would leave a furrow, not a weld behind the tool. The pin and shoulder is pressed against the workpiece with a large force (typically tons). An "anvil" supporting the workpiece from beneath provides a reaction force to balance the tool force.

The SR-FSW process was invented for the purpose of avoiding the need for heavy anvil support, which may be difficult to provide where space is limited and is always expensive. In the SR-FSW process a shoulder is attached to the pin bottom, and the pin is pulled up through a hole in the workpiece against a second shoulder. The two shoulders, which rotate with the pin, exert a "squeeze force" on the workpiece that prevents escape of metal from the weld in SR-FSW just as the "plunge force" does with the standard FSW tool.

As the standard FSW pin is withdrawn from the weld, the weld metal flows in beneath it resulting in a completed weld. The SR-FSW pin can be removed from the workpiece only by stopping the weld and either detaching the pin bottom shoulder or detaching the pin from the upper shoulder so that the pin may be extracted from the weld. This leaves a hole in the weld. The hole is customarily filled in by a plug weld. A sketch of the plug weld process is shown in Fig. 1.

A great deal of progress has been made in understanding the FSW process. Less has been made in understanding the plug welding process. The FSW process, as complex as it is, is essentially a steady-state process. As will be seen

[1] Associate Professor, Dept. of Mechanical and Aerospace Eng. zuo@eng.uah.edu, AIAA Associate Fellow.
[2] Analyst, Materials and Processes Laboratory, Engineering Directorate.

later in this report, the plug welding process is a transient process with more parameters to be accounted for and is therefore inherently a more difficult study. The object of this research is to develop a mechanics model of the plug welding process which, once validated, can be used to improve designing of plugs and selection of weld parameters for different plate thicknesses, hole diameters, and materials.

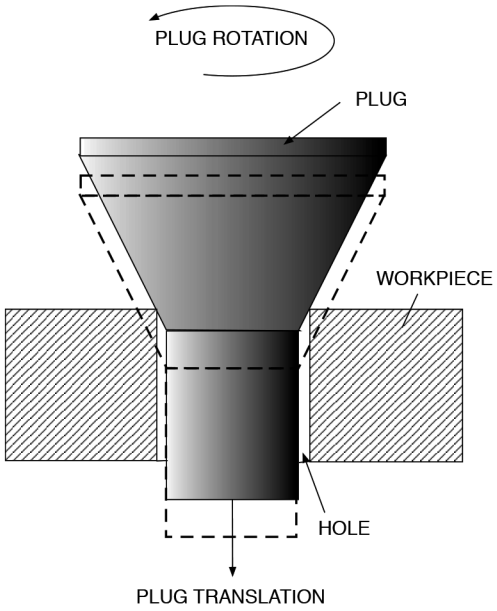

Figure 1. Sketch of plug weld process (a much-simplified plug is shown). Plug is rotated and pulled into hole in workpiece. Workpiece contact metal is extruded out along the contact surface.

II. Mathematical Model

A. Temperatures

Consider the interaction between the plug and the workpiece. Let the plug surface be represented by the plug bonded to the workpiece metal, as shown in Fig. 2. The plug moves into the paper with velocity approximately ωR, where ω is the spinning rate of the plug and R is the radius of the hole in workpiece, and the workpiece is stationary; the plug sticks at the plug/workpiece surface and a thin layer of workpiece metal of thickness δ, which may vary along the plug surface, rotates with the plug. The workpiece metal beyond the shear surface remains stationary. In this study, for simplicity, δ is treated as constant along the plug surface.

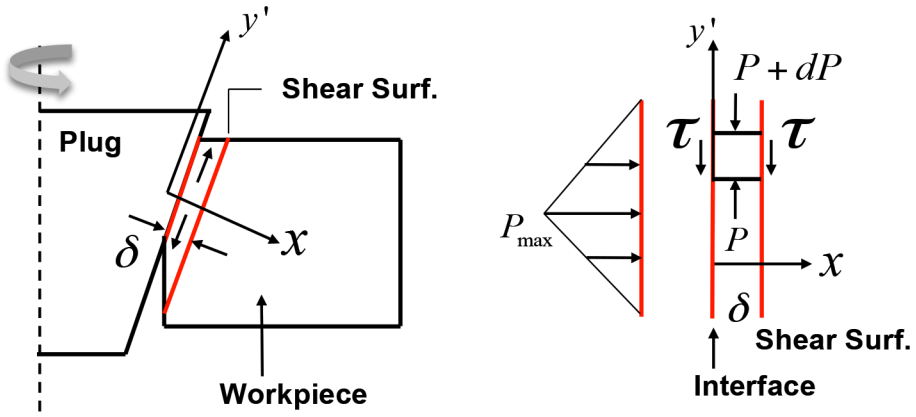

Figure 2. Simplified interface model of the plug and workpiece interaction.

If the shear stress of the weld metal at the interface temperature is τ, then the interface represents a heat source (flux) of magnitude $q = \tau\omega R$. For a constant pull velocity V_P, the depth of penetration (along the thickness of the workpiece) is $w = V_P t$, as shown in Fig. 3. Consider unit length along the circumferential direction. The area of the plug-metal interface is then $V_P t/cos(\emptyset/2)$, where $\emptyset$ is the taper angle of the plug. The rate at which the heat is generated by the heat flux q over the contact area is then

$$\dot{Q}_g = (1)\frac{V_P t}{\cos(\phi/2)} q \tag{1}$$

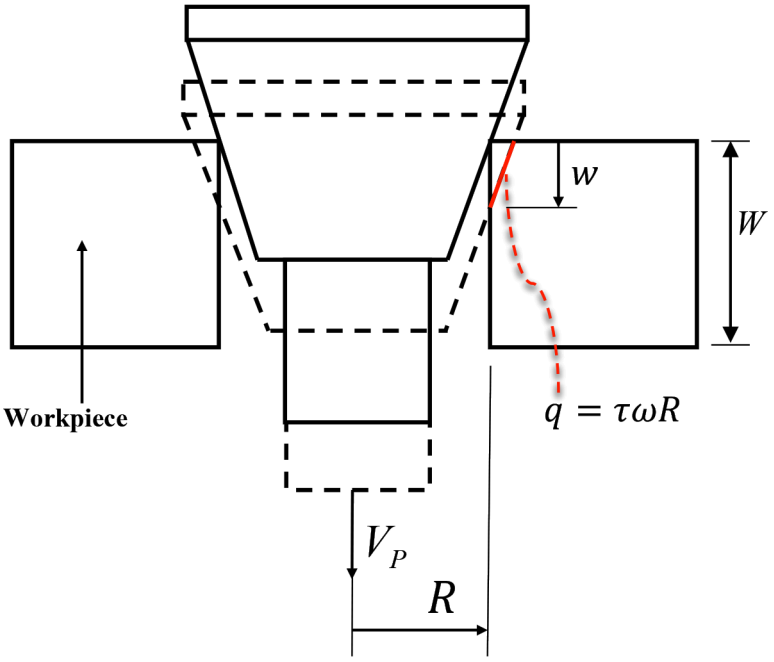

Figure 3. Plug and workpiece interaction showing contact surface and heat flux.

The heat generated is conducted into the workpiece, flowing from the interface temperature T into the ambient temperature T_∞ of the workpiece. Rather than try to solve the complex heat flow problem rigorously, a rather gross approximation is introduced. The heat from the shearing interface is taken to be substantially encapsulated in a volume bounded by an expanding radius, increasing according to a simply heat flow model, i.e. a sort of a diffusion wave. The outer boundary is circumscribed by the radius of heat diffusion from the initial contact at the top of the workpiece (see Fig. 3). The radius of heat diffusion is taken to be[1]

$$L(t) = 2\sqrt{\frac{\bar{K}}{\rho c} t} \tag{2}$$

where $\bar{K}$ is the "effective" thermal conductivity and is related to the thermal conductivity of the material K by a factor f: $\bar{K} = fK$; ρ and c are, respectively, the density and specific heat of the material. The factor f is introduced such that the heat loss to the materials beyond the radius of heat diffusion $L(t)$ is insignificant. An analysis of a heat source suddenly released at a point in infinite solids indicates that a value of $f = 1.5$ gives a radius of heat diffusion that contains more than 90% of the applied heat. Consequently, $\bar{K}$ is taken to be $1.5K$ in this study.

For a given time t the materials beyond the radius $L(t)$ are regarded as unaffected by the plastic heating. Consider unit length of workpiece (perpendicular to plane shown in Fig. 3). The volume of the material that has been affected by heating is approximated as

$$V(t) = (1)\frac{\pi}{4}L^2(t) = \pi\frac{\bar{K}}{\rho c}t \tag{3}$$

The temperature of the workpiece metal inside the heat diffusion radius is taken as the interface temperature and that beyond the radius of diffusion remains at the ambient temperature. The rate of heat absorption by the workpiece is then

$$\dot{Q}_{abs} = \rho c\dot{V}(t)(T - T_\infty) = \pi\bar{K}(T \quad T_\infty) \tag{4}$$

It follows from consideration of energy conservation that

$$\frac{\omega R V_P}{\cos(\phi/2)}\tau t = \pi\bar{K}(T - T_\infty) \tag{5}$$

To complete the model so that the sharing interface temperature can be determined a model of the flow stress as a function of the temperature needs to be prescribed.

B. Strength Model

Based on the available data[2] on the strength of the workpiece material (2219 aluminum) as a function of the temperature, a simple, piecewise linear, model $\tau = \tau(T)$ has been constructed (a detailed description of the model is reported in Ref. 3). A comparison the model results with the data is shown in Fig. 4. It is seen that the model gives a very good representation of the data.

Substitution of the strength model $\tau = \tau(T)$ into Eq. (5) yields a nonlinear algebraic equation for the interface temperature T as a function of the penetration time t, which is solved by an iterative algorithm (e.g., Newton's method). The resulting temperature $T(t)$ is then used to calculate the strength of the metal at the interface, $\tau(t)$.

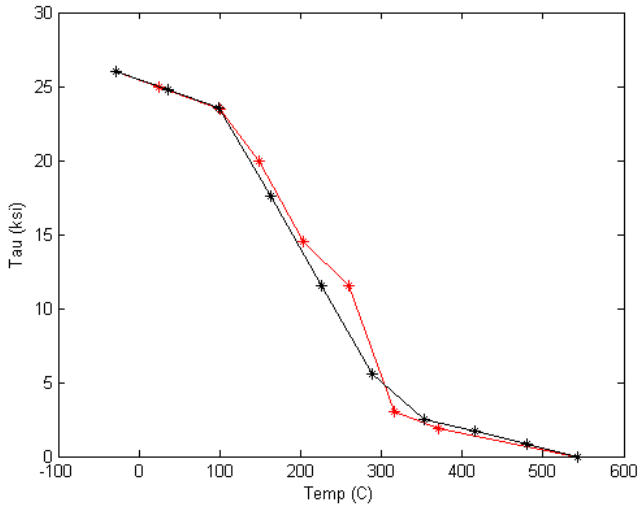

Figure 4. Comparison of the strength given by the piecewise model (black line) and the data (red stars). The model gives a very reasonable representation of the data.

C. Pressure Distribution

Consider the plastic deformation of workpiece metal between interface and the shear surface. It is seen from the micrograph of plug/workpiece contact surface, as shown in Fig. 5, that the metal between the plug-workpiece

interface and the shear surface (inside the workpiece) flows along the interface. We refer to this flow as "channel" flow. The cause of this flow is the pressure gradient in the direction of the interface.

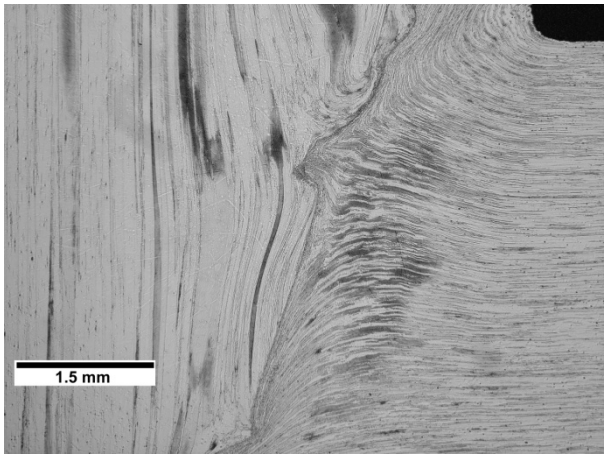

Figure 5. Micrograph (Courtesy of J.C. McClure) showing plug/workpiece contact surface. Flat elongated grains of the rolled workpiece on the left mark a workpiece-side flow against the plug surface, straight in at the center, upswept above and down swept below, as the plug forces the workpiece metal out of its way. Very close to the plug interface the workpiece grain structure vanishes and is replaced by a refined structure; this is thought to be due to passage through a shear surface (adiabatic shear band) separating metal rotating with the plug from the stationary metal of the workpiece.

As the plug is pulled through the hole of the workpiece, the width of the hole in contact with the plug expands radially under the pressure on the interface (to make room for the plug, which deforms much less than the workpiece and hence has been modeled as rigid in this work). To conserve the volume the workpiece metal in the channel must flow (or be "squeezed out") laterally (along the interface) as it expands radially. In order for the metal to flow laterally, the pressure gradient must be large enough to overcome the resistance of the metal to shearing (the shear strength).

Consider the distribution of pressure along the direction of the channel. In this simplified approximation neglecting curvature the pressure reaches maximum in the middle of the contact length and falls off to zero at the edges of the length. The contact length is $w' = w/cos(\emptyset/2)$, where $w = V_P t$ is the depth of penetration defined previously. Let the y' axis be along the interface with the origin at the middle of the contact length, as shown in Fig. 2. Then the equilibrium condition for the metal inside the channel is

$$\frac{\partial P}{\partial y'} \pm 2\frac{\tau}{\delta} = 0 \tag{6}$$

where the plus and minus signs apply to, respectively, the upper flow ($y' > 0$) and the lower flow ($y' < 0$). In the equation τ is the average shear strength of the metal in the channel. Since the thickness of the channel is very small (on the order of $100\ \mu m$), the temperature and the shear strength of the metal do not change significantly across the channel and are taken as constant in the current work. The pressure reduces to zero at the edges of the contact:

$$P\left(y' = \pm w'/2\right) = 0 \tag{7}$$

The pressure distribution is

$$P(y') = \begin{cases} P_m\left(1 - \dfrac{2y'}{w'}\right), & 0 \le y' \le \dfrac{w'}{2} \\ P_m\left(1 + \dfrac{2y'}{w'}\right), & -\dfrac{w'}{2} \le y' \le 0 \end{cases} \tag{8}$$

where $P_m = (w'/\delta)\tau$ is the maximum pressure at the center of the contact surface. A sketch of the pressure distribution along the channel is shown in Fig. 2. In this study the thickness of the channel is chosen to be $\delta = 100\ \mu m$, which is consistent with the micrograph of plug weld shown in Fig. 5.

With the shear strength and the pressure on the interface solved, the torque, power, and energy applied to the plug can be calculated in a straightforward manner (the details are reported in ref. [3]).

III. Comparison with Experimental Data

As an experimental validation the analytic model presented above was applied to some experimental plug welding data.[4] The experiment was run under the following conditions: $V_P = 27\ IPM$, $\omega = 6{,}300\ RPM$, $\emptyset = 13^o$, $R = 0.6875\ in$, $W = 0.625\ in$. In addition to the parameters specified by the experiment conditions and the strength model, the following thermal properties for aluminum 2219 were used in the calculations: $\rho = 2{,}830\ kg/m^3$, $c = 860\ J/(kg \cdot K)$, $K = 170\ W/(m \cdot K)$, and $T_m = 543\ ^oC$.

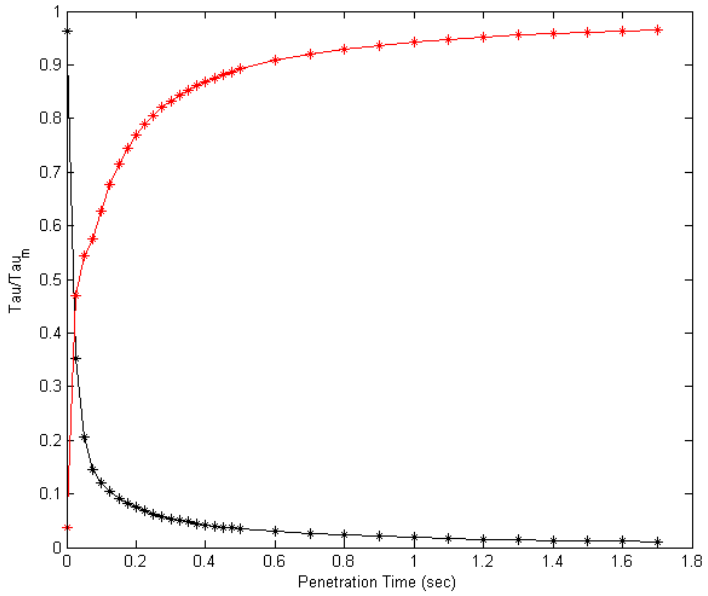

Figure 6. The normalized interface temperature (red) and material strength (black) as functions of penetration time. The temperature and strength are normalized by, respectively, the melting point ($T_m = 543\ ^oC$) and the strength of cold metal (τ_c).

The results of interface temperature T and the material strength τ, using the parameters given above, are shown in Fig. 6. It is seen that the interface, starting at the ambient temperature and very high shear strength ($\tau \approx \tau_c = 26\ ksi$), is heated up rapidly by the intense heating flux ($q = \tau\omega R$) initially. As the interface gets hotter, the shear strength reduces, leading to smaller heating flux, and hence slower increasing in the interface temperature, as expected from physics. Figure 6 clearly show the transit nature of the plug-weld process, which is accounted for in the current model.

The model predictions of the torque, energy input, and pull (plunge) force as functions of the penetration time are compared with the experimental data,[4] as shown in Figs. 7-8. Note time here is measured from when the penetration first occurs (i.e., plug starts to engage the work-piece metal). It is seen that the model gives reasonable predictions of the torque, energy input, and the pull force.

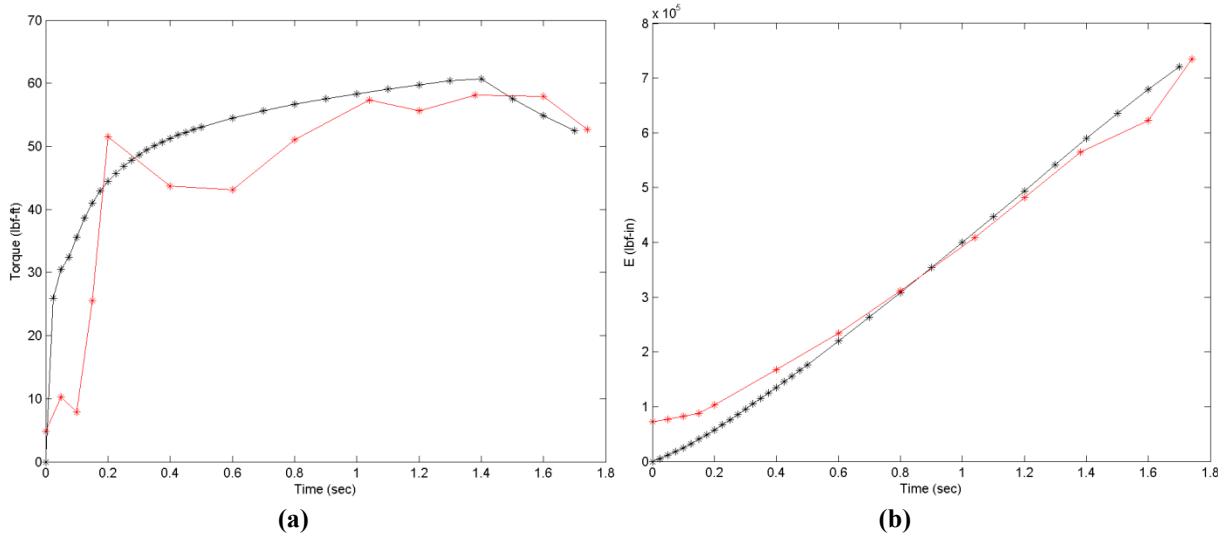

Figure 7. Comparison with the data of the predicted torque (a) and energy (b). The data is shown as red.

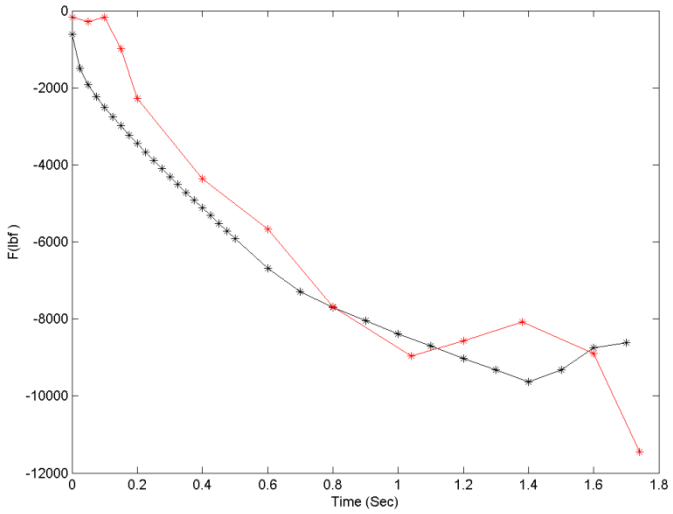

Figure 8. Comparison of the history of pull (plunge) force. The data is shown as red.

IV. Conclusion

The following are some observations and conclusions resulted from this study:

1. In plug welding processes the transient nature of heat transfer needs to be accounted for, whereas Friction Welding Process can be treated, to good accuracy, as steady-state.

2. For the plug weld experiment[4] the model predicts that the interface will reaches a temperature of $0.97T_m$ at 1.5 seconds of the travel time (penetration of the plug). This is consistent with the experiment, where local melting is believed to have occurred in the neighborhood of the bond-line (plug/workpiece interface).

3. Furthermore, comparisons of the predicted torque, energy and pull force with the data are encouraging.

It should be pointed out that much still needs to be done on the model before we can consider it a truly useful model for plug welding. The 'expanding wave" model of conduction of heat from the shearing surface seems to be physically plausible, but is a very crude assumption. With further study it may be possible to improve this model. The pressure model does not consider the deformation (plastic flow) of the plug nor local partial melting of the materials, which has been observed in the experiments. We plan to pursue these issues in the future.

Acknowledgments

We are grateful to Po-Shou Chen and Justin Littell for the experimental data of plug welding and for explaining various features observed in the experiments. We also thank Judy Schneider and Carolyn Russell for technical discussions and organizational support.

References

[1]Crank, J., *The Mathematics of Diffusion*, Oxford University Press, 1975, Chap. 1.
[2]Davis, J.R., et al., *Metals Handbook* (10th Edition), Vol 2 (Properties and Selections: Nonferrous Alloys and Special-Purpose Materials, ASM International, 1990, pp. 79-81.
[3]Zuo, Q.K., "Mechanics Model of Plug Welding", *Report to NASA Marshall Space Flight Center (EM 32)*, 2015 (unpublished).
[4]Cleghorn, D., Hepburn, F., Girgis, A., Chen, P. and Littell, J., "SLS 0.625" Friction Pull Plug Weld Development", *NASA Technical Report* (to be published).

APPENDIX A—MARSHALL FACULTY FELLOWSHIP PROGRAM ANNOUNCEMENT

MARSHALL FACULTY FELLOWSHIP PROGRAM

JUNE 8, 2015 – AUGUST 14, 2015

Application Deadline May 18, 2015

- The Marshall Space Flight Center is offering Faculty Fellowships for qualified STEM faculty at U.S. colleges and universities to conduct research with NASA colleagues during a ten-week residential program in Huntsville, Alabama.
- Faculty Fellows will receive stipends of $15,000 (Assistant Professor, Research Faculty), $17,000 (Associate Professor), or $19,000 (Professor).
- A relocation allowance of $1,500 will be provided to those fellows who live more than fifty miles from MSFC and a $500 travel supplement for one round-trip.
- Applicants must be U.S. citizens who hold full-time teaching or research appointments at accredited U.S. universities or colleges.
- During the ten-week program, fellows are required to conduct their research on-site at the Marshall Space Flight Center.

Women and under-represented minorities, and persons with disabilities are encouraged to apply.

APPENDIX B—NASA MARSHALL FACULTY FELLOWSHIP PROGRAM
Program Description

Objectives

- To nourish research collaborations between MSFC and US colleges and universities;
- To Provide research opportunities for college and university faculty;
- To encourage the exchange of ideas between fellows and MSFC employees;
- To encourage collaborative research with other government agencies and the private sector; and
- To establish effective education and outreach activities to foster greater awareness of this program.

Faculty Fellowships

Fellowships are awarded to qualified STEM faculty members and other related disciplines for collaborative NASA-university research projects. Fellows will conduct research beneficial to the fellow and MSFC.

Marshall Collaborator

A Marshall Collaborator will be identified to serve as the co-investigator and day-to-day contact. At the end of the ten-week period, the Faculty Fellow will prepare a final report summarizing the summer effort, including results and recommending follow-up work.

Compensation

Stipends for Faculty Fellows are set as follows: for the 10-week period:

Assistant Professors and Research Faculty	$15,000
Associate Professors	$17,000
Professors	$19,000

A Relocation allowance of $1,500 will be provided to fellows who live more than fifty miles from the Marshall Center.

A travel supplement of $500 will be provided to those fellows receiving the relocation allowance.

Duration

The duration of the fellowship is ten continuous weeks.

Selection

The applicants selected to be Faculty Fellows will be chosen by the Marshall group which has been assigned the area of investigation (concentration) chosen by the applicants.

Eligibility

- US Citizen
- Full time teaching or research appointments at accredited US universities or colleges.
- Fellowships are awarded for one summer period, but Fellows may apply again for a second year.
- If an individual has participated in this program for two consecutive years, s/he must not participate for two years before coming eligible to participate again.
- Women, under-represented minorities, and persons with disabilities are encouraged to apply.

Regulations

- The program is residential, Fellows are required to conduct their research, during the ten-week program, on-site at the Marshall Space Flight Center.
- Participants cannot receive remuneration from other entities or other programs or other university or government sources during the Faculty Fellowship 10-week period.
- An oral presentation by the Fellow to the Marshall group with which s/he has been affiliated is required, near the end of the Fellowship period.
- A written Final Report is required at the end of the Fellowship.
- A written evaluation of the program by the Fellow is expected at the end of the Fellowship.

Application Deadline: February 28, 2016

REPORT DOCUMENTATION PAGE

Form Approved
OMB No. 0704-0188

1. REPORT DATE *(DD-MM-YYYY)*	2. REPORT TYPE	3. DATES COVERED *(From - To)*
01–12–2015	Technical Memorandum	

4. TITLE AND SUBTITLE
Marshall Space Flight Center Faculty Fellowship Program

5a. CONTRACT NUMBER

5b. GRANT NUMBER

5c. PROGRAM ELEMENT NUMBER

6. AUTHOR(S)
N.F. Six, Program Manager/Compiler

5d. PROJECT NUMBER

5e. TASK NUMBER

5f. WORK UNIT NUMBER

7. PERFORMING ORGANIZATION NAME(S) AND ADDRESS(ES)
George C. Marshall Space Flight Center
Huntsville, AL 35812

8. PERFORMING ORGANIZATION REPORT NUMBER
M–1405

9. SPONSORING/MONITORING AGENCY NAME(S) AND ADDRESS(ES)
National Aeronautics and Space Administration
Washington, DC 20546–0001

10. SPONSORING/MONITOR'S ACRONYM(S)

11. SPONSORING/MONITORING REPORT NUMBER
NASA/TM—2015–218216

12. DISTRIBUTION/AVAILABILITY STATEMENT
Unclassified-Unlimited
Subject Category 31
Availability: NASA STI Information Desk (757–864–9658)

13. SUPPLEMENTARY NOTES
Prepared by the Academic Affairs Office, Office of Human Capital

14. ABSTRACT
The summer research projects conducted by the Faculty Fellows at Marshall Space Flight Center included propulsion studies on green propellants, gas bubble dynamics in solids, and simulation of fluid and thermal transients; materials investigations of sandwich structures in composites, plug and friction stir welding; and additive manufacturing strength characterization and thermosets curing in space. Three studies involved instrumentation, increasing the resolving power of spectral interferometry, measuring emissivity and sensing strain in structures. Other research included fluid dynamics—water hammer effect, human factors—interpersonal space requirements for close proximity, control systems—for small launch vehicles, and astrophysics—Earth weather modification by solar eclipsing, and detection of a warm-hot intergalactic medium (WHIM) filament.

15. SUBJECT TERMS
space transportation, launch vehicles, spacecraft propulsion, propellants, mechanical engineering, WHIM filament

16. SECURITY CLASSIFICATION OF:			17. LIMITATION OF ABSTRACT	18. NUMBER OF PAGES	19a. NAME OF RESPONSIBLE PERSON
a. REPORT	b. ABSTRACT	c. THIS PAGE			STI Help Desk at email: help@sti.nasa.gov
U	U	U	UU	184	19b. TELEPHONE NUMBER *(Include area code)* STI Help Desk at: 757–864–9658

National Aeronautics and
Space Administration
IS20
George C. Marshall Space Flight Center
Huntsville, Alabama 35812